



Terms and Conditions of Use of Digitised Theses from Trinity College Library Dublin

Copyright statement

All material supplied by Trinity College Library is protected by copyright (under the Copyright and Related Rights Act, 2000 as amended) and other relevant Intellectual Property Rights. By accessing and using a Digitised Thesis from Trinity College Library you acknowledge that all Intellectual Property Rights in any Works supplied are the sole and exclusive property of the copyright and/or other IPR holder. Specific copyright holders may not be explicitly identified. Use of materials from other sources within a thesis should not be construed as a claim over them.

A non-exclusive, non-transferable licence is hereby granted to those using or reproducing, in whole or in part, the material for valid purposes, providing the copyright owners are acknowledged using the normal conventions. Where specific permission to use material is required, this is identified and such permission must be sought from the copyright holder or agency cited.

Liability statement

By using a Digitised Thesis, I accept that Trinity College Dublin bears no legal responsibility for the accuracy, legality or comprehensiveness of materials contained within the thesis, and that Trinity College Dublin accepts no liability for indirect, consequential, or incidental, damages or losses arising from use of the thesis for whatever reason. Information located in a thesis may be subject to specific use constraints, details of which may not be explicitly described. It is the responsibility of potential and actual users to be aware of such constraints and to abide by them. By making use of material from a digitised thesis, you accept these copyright and disclaimer provisions. Where it is brought to the attention of Trinity College Library that there may be a breach of copyright or other restraint, it is the policy to withdraw or take down access to a thesis while the issue is being resolved.

Access Agreement

By using a Digitised Thesis from Trinity College Library you are bound by the following Terms & Conditions. Please read them carefully.

I have read and I understand the following statement: All material supplied via a Digitised Thesis from Trinity College Library is protected by copyright and other intellectual property rights, and duplication or sale of all or part of any of a thesis is not permitted, except that material may be duplicated by you for your research use or for educational purposes in electronic or print form providing the copyright owners are acknowledged using the normal conventions. You must obtain permission for any other use. Electronic or print copies may not be offered, whether for sale or otherwise to anyone. This copy has been supplied on the understanding that it is copyright material and that no quotation from the thesis may be published without proper acknowledgement.



Theoretical and computational aspects of electronic transport at the nanoscale

By

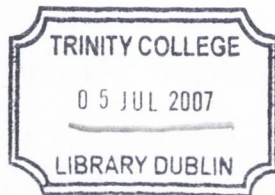
Alexandre Reily Rocha

A thesis submitted for the degree of
Doctor of Philosophy



School of Physics
Trinity College Dublin

January 2007



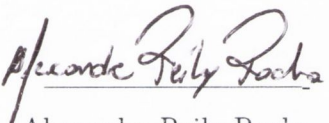
THESIS
8084

Declaration

I Alexandre Reily Rocha hereby declare that this dissertation has not been submitted as an exercise for a degree at this or any other University.

It comprises work performed entirely by myself during the course of my Ph.D. studies at Trinity College Dublin. I was involved in a number of collaborations during that time and where it is appropriate my collaborators are dully acknowledged for their contributions.

A copy of this thesis my be landed or copied by the Trinity College Library upon request by a third party provided it spans single copies made for study purposes only, subject to normal conditions of acknowledgement.


Alexandre Reily Rocha

Abstract

The problem of electronic transport in systems comprising only a handful of atoms is one of the most exciting branches of nanoscience. The aim of this work is to address the issue of non-equilibrium transport at the nanoscale. At first, we lay down the theoretical framework based on Keldysh's non-equilibrium Green function formalism. We show how this formalism relates to the Landauer-Büttiker formalism for the linear regime and how the current through a nanoscopic system can be related to a rate equation for which a steady state solution can be found. This formalism can be applied with different choices of Hamiltonian. In this work we choose to work with the Hamiltonian obtained from density functional theory which provides an accurate description of the electronic structure of nanoscopic systems. The combination of NEGFs and DFT results in *Smeagol*, a state-of-the-art tool for calculating materials-specific electronic transport properties of molecular devices as well as interfaces and junctions.

Smeagol is then used to study the magnetoresistance in magnetic point contacts and whether asymmetries in the $I - V$ characteristics can be explained solely by electronic effects. We show how new exchange and correlation functionals must be used to accurately portray the electronic transport properties of point contacts with adsorbed impurities. We also introduce the new concept of molecular spin valves. In other words we investigate the possibility of using organic molecules sandwiched between magnetic electrodes to create novel GMR devices which combine spintronics and the relatively new field of molecular electronics. We show that organic molecules can be engineered to produce large magnetoresistance ratios and by further choosing the end-groups even greater enhancement of these ratios can be achieved. We also show how to accurately model spin-polarised scanning tunnelling microscopy using *Smeagol*.

Finally we show how computer simulations can give powerful insights into the transport properties of macromolecules (most notably DNA). We show the main mechanism for transport in DNA molecules attached to gold electrodes and conclude that it is a wide-gap semiconductor.

For my parents, Célia and Jeová Rocha,
my grandmother Phyllis Reily and in
memory of my grandfather, Duncan
Alexander Reily.

People who had a great influence in my life
and in my choice of an academic career.

Acknowledgements

During the period I was in Dublin a number of people were extremely important in helping me with this work.

Initially I would like to thank my supervisor Stefano Sanvito. We both took a gamble when without knowing each other I decided to be his first PhD student and he decided to be my supervisor. We started off quite literally under a rail bridge and with merely three computers (other things that went on during that first year better remain untold). Today four years later he has established himself and his odd collection of students and post-docs as one of the best computational materials science groups in the country and certainly is a strong contender in the world stage. I like to think I am part of the history of this group and of what we have achieved in a little over four years. Stefano's insights into physics and his views on "what's hot and what's not" guided me through the course of this work. In the end, I have to say, I couldn't expect for a better outcome.

The funding agencies made it all possible, Enterprise Ireland (Grant # EI-SC/2002/10), Science Foundation Ireland (Grant # SFI05/RFP/PHY0062) both paid my fees and maintenance, and also provided support for attending conferences. The same can be said about the Irish Academy of Sciences which provided for our constant visits to the University of Lancaster and for our collaborators to come to Dublin. This brings me to the people involved in the development of *Smeagol* - the main topic of this thesis. I can say that it had many parents and I couldn't possibly forget the valuable contributions from Jaime Ferrer and Víctor García-Suárez from Universidad de Oviedo in Spain and from Colin Lambert and Steve Bailey from Lancaster University (UK). We should all be proud of this offspring.

The calculations included in this thesis were performed in different computational facilities: the Trinity Centre for High Performance Computing (Jimmy Tang, Bob, Dermot and Geoff), the Irish Centre for High End Computing and CINECA (Italy). I am grateful for the support their technical staff provided for setting up *Smeagol*.

The computational spintronics group in Trinity comprises an odd bunch of people. There is Ruairi, the poker gambler. Maria who is quiet, but always so hardworking

and purposeful when she speaks. Cormac who has a knowledge for trivia only surpassed by Wikipedia. Will, who taught me about scuba diving and ate my Kit-Kats. Ivan, who is very meticulous and always pointed out flaws and bugs in *Smeagol* (usually very politely). Das whom I shared an apartment with for a year and was always available to answer my questions about SIESTA. Finally there is Nicola, who introduced me to *Family Guy*. I can say that now I know why the dinosaurs died out. Unfortunately he decided to leave physics for a more profitable career in industry and the food back in Italy.

Coffee breaks are a part of the PhD program and the people who were always ready to have a cup of coffee and chat away the afternoon will be missed once I've left Trinity College: Dave, Andrew and Eireann - the crowd from the other groups. I don't know if they actually did any work, or what exactly their PhD's were about, but they were definitely good fun to hang around with. Andrew is an extremely critical (sarcastic as well which is great) and intelligent person and conversations with him were very entertaining. Dave turned out to be more than a colleague, I consider him a good friend. And what we must remember is that it is all *just a theory*. I met people at the very end of my Ph.D., Fred and Brian who I couldn't possibly forget as well as Miguel and Tom, our system administrators. They went out of their way to solve my computer problems (this acknowledgement was obviously written weeks before going to print, but I am quite sure I had some last-minute printer problems).

From the family side there is my aunt Suzel who lives in Belfast and now her husband Antônio. She was the family point of contact in Ireland. I spent many a weekend in her house (old and new), and although I am completely tone deaf (she is an ethnomusicologist) she has not disowned me (yet).

I would also like to thank my wife Clarissa for her immense love and support throughout our experience in Ireland. We've been through some rough times as one would expect from a project of this magnitude. Yet I have come out almost unscathed at the other end (Let us wait for the *viva* shall we?). If it weren't for her I would have gone crazy long ago and would have ended up committed to an institution (some might say that wouldn't necessarily be a bad idea).

From the start my parents have supported me in my personal decisions even when I picked this weird career - physics in Brazil is not exactly regarded as traditional. When I was growing up my mother taught me to savour new cultures and visit new places (Ireland is not Easter Island, but sounds exotic!). My father overcame hardship to become a successful doctor and researcher. In many aspects I have tried to use them as an example. I would like to thank them for teaching me how to be

independent and how to be critical.

My grandmother is probably disappointed that I don't work at a *Synchrotron* facility anymore (it's been four years now!). There is no more buzzword she can show off to her friends at church. Perhaps she'll satisfy herself with *nanoscience* from now on.

Finally I would like to thank a person who defined the ideology for my entire family, the man behind it all, pulling the all strings. Long ago he came up with a master plan for defining our way of thinking for generations to come. He succeeded! We are becoming academics as he once was. We can't get away from it! Unfortunately, he could not see this/his work coming full cycle. Most people strive to do better than their parents and grandparents, but I don't think that is achievable, because, in my case, my grandfather has set the bar too high. I do hope, however, that this work is the beginning of something that would eventually make him proud.

Contents

Acknowledgements	iii
General Introduction	1
Molecular-Electronics	2
Electron transport through molecules	2
The bonding with the contacts	4
Spin-Electronics	5
Giant-magnetoresistance	5
Transition metals and spin valves	6
Spin valves	7
Spin polarisation of a device	9
Why spins and molecules?	10
Why is tool for computational electronic transport so important?	13
Dissertation Layout	15
1 Electronic Transport using Non-equilibrium Green Functions	17
1.1 Setting up the transport problem	17
1.2 The Landauer formalism: equilibrium transport	21
1.3 A simple model for transport under bias	23
1.3.1 Charging effects	27
1.3.2 Asymmetries	29
1.4 Non-Equilibrium Transport	31
1.4.1 Non-equilibrium Green functions (NEGF) for an open system	31
1.4.2 Steady-state and self-consistent procedure	34
1.5 Spin polarised systems: Collinear versus non-collinear spins	38
1.6 Leads' self-energies	42
1.6.1 Surface Green's functions	42
1.6.2 The " K_1 problem"	45
1.6.3 Finding the singularities of K_1	47

1.6.4	Solution of the “ K^1 problem”	49
1.7	Conclusion	55
2	<i>Smeagol</i>: Density Functional Theory and NEGF’s	57
2.1	Introduction: The many-body problem	57
2.1.1	An attempt at solving the many-electron problem	59
2.2	Density Functional Theory	60
2.2.1	Limitations of LDA and GGA	64
2.2.2	The calculation of the Kohn-Sham states	67
2.3	The SIESTA code	69
2.4	The <i>Smeagol</i> code	73
2.4.1	Parallelising <i>Smeagol</i>	78
2.4.2	An overview of <i>Smeagol</i> capabilities	82
2.5	Test Cases	83
2.5.1	Au capacitor: Hartree potential and bias ramp	83
2.5.2	Au atomic chains	84
2.5.3	Nickel point contacts using non-collinear spins	87
2.5.4	Platinum single atom chains: k-point sampling	90
2.5.5	1,4-benzene-dithiolate on Au electrodes	94
2.6	Conclusion	98
3	GMR and Asymmetries in point contacts	99
3.1	Introduction	99
3.2	Magnetoresistance in Nickel point contacts: an <i>ab initio</i> study	101
3.2.1	Impurity-free MPCs: relaxation and transport I	102
3.2.2	Effects of different exchange-correlation potentials (V_{XC}) in impurity-free Ni point contacts	106
3.2.3	Oxygen-rich MPCs: relaxation and transport II	110
3.2.4	Effects of different exchange-correlation potentials (V_{XC}) for oxygen-rich Ni point contacts	113
3.3	Conclusion	117
4	Organic Spin valves	119
4.1	Introduction	119
4.2	Triphenyl-dithiolate: metallic regime	121
4.3	Octane-dithiolate: tunnelling regime	129
4.4	1,4-benzene-(S, Se, Te): end-group engineering	133

4.5	Asymmetric molecules	136
4.6	Modelling scanning tunnelling microscopy with <i>Smeagol</i>	140
4.7	Conclusion	148
5	Transport through DNA: where physics and biology meet	149
5.1	Introduction	149
5.1.1	What is DNA?	150
5.1.2	Is DNA a conductor?	153
5.2	Calculations	157
5.2.1	Describing Au in DFT with <i>s</i> orbitals only	158
5.2.2	Infinite DNA strands	159
5.2.3	Two-base-pair DNA	160
5.2.4	Transport through A-DNA molecules	164
5.3	Conclusions	166
	General Conclusion	169
	Future work	170
	Bibliography	173
	Appendices	
A	Extensions to <i>Smeagol</i>	189
B	Publications stemming from this work	195
C	The <i>Smeagol</i> Manual	197

List of Figures

1	Energy level lineup between a molecule and two current voltage probes.	3
2	Sketch of a Au atomic chain sandwiching a π -bonded molecule	4
3	Band structure, density of states and Fermi surface for fcc Cobalt. . .	7
4	Artistic impression of a GMR device: two magnetic materials sandwiching a non-magnetic one	8
1.1	Modelling the transport problem	18
1.2	Schematic representation of incoming and outgoing wavefunctions scattered by a potential $V(\mathbf{r})$	21
1.3	Single-level depiction of a molecule between jellium electrodes	24
1.4	Diagram illustrating the level alignment of a molecule with respect to electrodes under bias.	26
1.5	I-V characteristics for a simple model for transport with a single energy level.	28
1.6	I-V characteristics for a simple model for transport including charging effects	29
1.7	I-V characteristics for a simple model for transport including asymmetric coupling to the electrodes.	30
1.8	Integration path for calculating the non-equilibrium density matrix: complex plane and real axis.	39
1.9	One-dimensional array of atoms with non-collinear spins.	40
1.10	Schematic diagram of the Hamiltonian for an infinite current/voltage probe	43
1.11	Examples of singularities in H_1	46
1.12	Schematic representation of the decimation procedure	51
2.1	Anti-ferromagnetic NiO structure.	65
2.2	Band structure of bulk NiO using density functional theory in the local spin density approximation	65

2.3	Band structure of bulk NiO using density functional theory using LDA+U and SIC	66
2.4	Numerical localised atomic orbital basis set for Ni generated by SIESTA.	71
2.5	Real-space ramp added to the Hartree potential to account for the applied bias	75
2.6	Hartree potential for a parallel plate capacitor: the potential is defined up to a constant	76
2.7	Flow-chart of the <i>Smeagol</i> algorithm	77
2.8	Types of parallelism in SISTA	80
2.9	Hartree potential and charge density of an infinite parallel-plate capacitor.	84
2.10	Potential iso-surfaces of an infinite capacitor	85
2.11	Transmission coefficients for a gold monoatomic chain	86
2.12	Schematic representation of the Ni point contact	88
2.13	Transmission coefficient as a function of energy for nickel quantum point contacts.	89
2.14	Platinum point contact with hydrogen molecule	91
2.15	Total energy calculation as a function of tip separation for platinum point contact	92
2.16	Transmission coefficients of a H ₂ molecule between platinum contacts.	93
2.17	Benzene-dithiolate molecule between gold electrodes.	94
2.18	$I - V$ characteristics as a function of energy for different voltages for 1,4-benzene-dithiolate molecule attached to a [111] gold surface.	95
2.19	Transmission as a function of energy for different voltages for 1,4-benzene-dithiolate molecule attached to a [111] gold surface.	96
2.20	$I - V$ characteristics for 1,4-benzene-dithiolate molecule attached to a [001] gold surface.	97
2.21	Transmission as a function of energy for different voltages for 1,4-benzene-dithiolate molecule attached to a [111] gold surface.	97
3.1	Ball-and-stick representation of a Ni point contact	102
3.2	Total energy curves for relaxation of a nickel point contact.	103
3.3	Projected density of states for Ni point contact	104
3.4	Transmission coefficients for Ni point contact	105
3.5	Transmission coefficients for Ni point contact.	106
3.6	Orbitals in an infinite Ni mono-atomic wire.	107
3.7	DFT-calculated band structures for one-dimensional nickel chain.	108

3.8	Transmission coefficients for Ni point contact using LDA+U.	109
3.9	Ball-and-stick sketch of a Ni point contact with oxygen.	111
3.10	Total energy curves for relaxation of a nickel point contact with oxygen.	112
3.11	Transmission coefficients for Ni point contact with oxygen.	113
3.12	Band structure and PDOS for NiO wire using LDA.	114
3.13	Band structure and PDOS for ferromagnetic NiO nanowire using LDA+U.	114
3.14	Band structure and PDOS for non-magnetic NiO nanowire using LDA+U.	115
3.15	Band structure and PDOS for anti-ferromagnetic NiO nanowire using LDA+U.	116
3.16	Transmission coefficients using LDA+U for Ni point contact with O.	117
4.1	A molecular spin valve device.	120
4.2	Atomic arrangement and total density of states of an tricene-dithiol molecule.	122
4.3	Characteristic curve and transmission for tricene-dithiolate.	123
4.4	Transmission coefficients as a function of the number of benzene rings.	124
4.5	Projected density of states for tricene-dithiolate.	125
4.6	Scheme of the spin-transport mechanism: real world.	126
4.7	Local charge density for 1,4-triphenyl-dithiolate attached to nickel leads in the parallel alignment of the electrodes.	127
4.8	Local charge density for 1,4-triphenyl-dithiolate attached to nickel leads in the anti-parallel alignment of the electrodes.	128
4.9	Scheme for spin-transport mechanism: ideal world.	129
4.10	Sketch and total density of states of an alkane-dithiol molecule.	130
4.11	Transport properties of octane-dithiolate.	131
4.12	Local charge density for octane-dithiolate attached to nickel.	132
4.13	Distance dependence of the zero-bias transmission coefficients of octane- dithiolate.	133
4.14	Total energy curve as a function super-cell size in a) 1,4-benzene- Selenium and b) 1,4-benzene-Tellurium.	134
4.15	Transport properties of 1,4-phenyl-Selenium molecule on Ni surface.	135
4.16	Transport properties of 1,4-phenyl-Selenium molecule on Ni surface.	136
4.17	Transport properties of 1,4-phenyl-Tellurium molecule on Ni surface.	137
4.18	Ball-and-stick representation of a 1,4-benzene-tellurium-thiolate molecule attached to Ni [001] surfaces.	138
4.19	$I - V$ characteristics of 1,4-benzene-tellurium-thiolate molecule sand- wiched between two Ni [001] surfaces.	138

4.20	Giant-magnetoresistance ratio as a function of applied bias for 1,4-benzene-tellurium-thiolate.	139
4.21	Transmission coefficients as a function of energy for 1,4-benzene-tellurium-thiolate.	140
4.22	Scanning tunnelling microscopy configurations for 1,4-benzene-thiol-thiolate.	141
4.23	Local charge density of 1,4-benzene-thiol-thiolate probed by magnetic STM.	142
4.24	Characteristic curves for 1,4-benzene-thiol-thiolate.	143
4.25	Transmission coefficients as a function of energy for the parallel configuration and different positions of the STM tip on the molecule.	144
4.26	Giant magnetoresistance ratio as function of bias for different arrangements of the STM tip.	144
4.27	Transmission as a function of energy for BDTT attached to a Ni [001] surface for forward bias in configuration III.	145
4.28	Projected density of states of the combined system surface/BDTT/tip.	145
4.29	Transmission as a function of energy for benzene-thiolate-tellurium on nickel.	146
4.30	Theoretically calculated STM image of a benzene-thiol-thiolate molecule attached to a Ni surface probed by a Ni STM tip. a) Majority spin current, b) minority spin current and c) total current. The molecule lies along the diagonal depicted by the red line.	147
5.1	Sketch of the four nitrogenated basis that form DNA: (a) Adenine, (b) Thymine, (c) Guanine and (d) Cytosine.	150
5.2	Structural formula for a nucleotide showing the phosphate backbone and the pentose. The base is one of (a-d) in figure (5.1).	151
5.3	The molecular selectivity properties of DNA nitrogenated basis'.	151
5.4	Side and top views of one full turn (10 base pairs) for B-DNA.	152
5.5	Side and top views of one full turn (11 base pairs) for A-DNA.	153
5.6	Ball-and-stick model of a) a two-base-pair, and b) an eleven-base-pair A-DNA arrangements.	158
5.7	Band structures of fcc bulk gold.	159
5.8	Density of states of Poly-(dC)-Poly-(dG) A-DNA molecules.	160
5.9	Local charge density iso-surfaces in A-DNA.	161
5.10	Projected density of states for two-base-pair DNA connected to gold electrodes.	161

5.11	Projected charge density around the Fermi level for a two-base-pair DNA molecule attached to gold electrodes.	162
5.12	Current as a function of bias for a two-base-pair DNA strand.	162
5.13	Transmission as a function of energy for a two-base-pair attached to gold electrodes.	163
5.14	Energy dependent transmission coefficients between two [001] gold surfaces with sulphur atoms attached to the hollow sites.	164
5.15	Projected density of states of a thiolated A-DNA structure attached to gold electrodes.	165
5.16	Iso-surface plot of the local density around the Fermi level. a) Side view and b) top view.	166
5.17	Transmission as a function of energy for a 11-base pair DNA strand attached to gold electrodes.	166
A.1	Schematic representation of redistribution of the Hamiltonian into groups of communicators	190
A.2	Schematic representation of the calculation of the density matrix.	192

List of Tables

1	Spin-polarisation of typical magnetic metals	10
2	Valence band spin-orbit splitting for various semiconductors.	11
3	Nuclear magnetic moments of selected atoms.	12
2.1	Benchmarking of <i>Smeagol</i> over TCP/IP	81
2.2	Timing of <i>Smeagol</i> for <i>k</i> -point calculation.	82
5.1	Initial atomic configurations and their respective basis sets for each element in the DNA calculation. Elements denoted by prime are involved in hydrogen bonds.	157

General Introduction

The study of electronic transport through devices comprising only a handful of atoms is becoming one of the most fascinating branches of modern solid state physics. This area was initiated with the advent of the scanning tunnelling microscope (STM) [1] and at present comprises a multitude of applications which span over several disciplines and encompass different technologies, from building blocks for revolutionary computer architectures and disposable electronics, to diagnostic tools for genetically driven medicine. Clearly many of these devices will soon change and enhance the quality of our daily life.

Recently there has been a growing interest in making electronic devices using organic molecules. This field, which takes the suggestive name of molecular-electronics [2], aims at replacing standard semiconductors with organic materials. These have the advantages of being produced with low-temperature low-cost chemical methods, instead of expensive high-temperature solid-state growth (e.g. molecular beam epitaxy) and patterning (lithography) techniques. In addition the endless possibilities of chemical synthesis, end-group and side-chain engineering give good expectation for new concept devices.

The standard set up for a molecular electronics device is to sandwich either a single molecule or an organic monolayer between metallic electrodes. This setup was first proposed by Aviran and Ratner [3], but was only experimentally accomplished much later by Reed and coworkers [4].

From the electronic side negative differential resistance [5] and rectification [6] have already been proved at the molecular level and fully functional molecular transistors [7], memories [8] and logic gates [9, 10] have been demonstrated suggesting a possible road-map to the post-silicon era. These should produce future generations of computers, together with magnetic data storage devices exceeding the Terabit/in² storage limit. The readout of such high-density data storage media will be achieved using nanoscale devices with magnetic atomic point contacts [11, 12].

At the same time hybrid molecular devices are becoming increasingly popular in multifunctional sensor design, demonstrating a sensitivity with orders of magni-

tude superior to those achieved with conventional methods. These molecular devices include for example carbon nanotube detectors for NO_2 [13], nerve agents [14], nanowire-based virus detectors [15] and chemical sensors [16]. The near future should see the development of on-chip nanolabs able to sense a particular signature of gene or protein expression and therefore be able to diagnose various diseases. These will be formidable tools for the study of biological systems and in the field of preventive medicine [17].

Still the field of biological sciences provides us with a seemingly unlikely candidate for molecular electronics devices. Desoxyribonucleic acid (DNA) has interesting molecular recognition properties [18] which can be used to integrate devices into useful circuits by self-assembly [19]. The quest for conducting DNA [20, 21, 22, 23] and its application in electronics can lead to a new family of devices based on biologically active molecules.

Molecular-Electronics

Electron transport through molecules

Transport through molecules and in general through low dimensional objects is somehow different to that in standard metals or semiconductors. This is mainly due to the collapse of the Fermi surface into a single or a small number of energy levels (the highest occupied molecular orbital - HOMO). The nature and lineup of the HOMO with the Fermi energy of the current/voltage probes determine most of the transport properties. Let us consider the simple case of a two probe device. Following a simple model proposed by Datta [24] the typical energy level lineup is schematically presented in figure 1.

In absence of any coupling (figure 1a) both the energy levels of the molecule and the Fermi level of the electrodes will align with a common vacuum level. In this case the system is characterised by the work function of the electrodes and both the ionisation potential (IP) and the electron affinity (EA) of the molecule. In this setup the molecule can exchange electrons with the electrodes only if the typical temperature is comparable to either $IP - WF$ or $WF - EA$ where WF is the metal work function. This condition is normally not satisfied. Local charge neutrality of the whole system and integer occupation of the molecule is therefore guaranteed.

In contrast, the interaction between the molecular levels and the extended wavefunctions of the metallic contacts has the effect of broadening and shifting the molecular levels. In the extreme limit of large coupling extended states spanning through

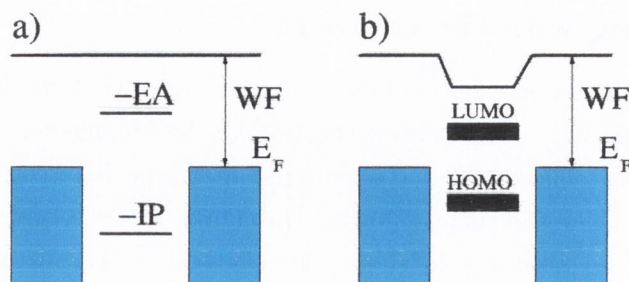


Figure 1: Energy level lineup between a molecule and two current voltage probes. In the weak coupling limit a) the molecule is characterised by the ionisation potential (IP) and the electron affinity (EA), which line up with the metal Fermi energy (WF is the work function of the contact). In the case of strong coupling b) between the molecule and the leads the molecular levels shift and broaden. It is then more appropriate to discuss transport in terms of HOMO and LUMO states.

the entire system (electrode plus molecule) can develop and the molecular device will behave as a good metal. In this limit the molecular levels cannot be associated any longer to the elementary removal energies of the isolated molecule and a description in terms of fractionally occupied HOMO and LUMO (lowest unoccupied molecular orbital) is more appropriate.

The effect of an applied bias V is that of shifting the chemical potentials of the two current/voltage probes relative to each other by eV , with e the electronic charge. As a rule of thumb current will flow whenever a molecular level (either the HOMO or the LUMO) is positioned within such a bias window. The appearing of molecular levels in the bias window when the potential is increased typically leads to changes in the slope of the I - V characteristics, in steps in the differential conductance $dI/dV(V)$ and in peaks in its derivative $d^2I/dV^2(V)$. This means that fingerprints of the molecular spectrum can be found in the measurement of its electrical properties.

Since the seminal work of Reed *et al.* [4], several experiments have been performed on a variety of molecules [5, 6, 7, 25, 26, 27]. Although the feasibility of single molecule devices has been shown, a number of issues have been raised by these experiments. Probably the most important of them is the nature of the contact between the molecule and the surface of the electrodes. Present experimental methods cannot establish the bonding at the atomic level and the reproducibility of the I - V curves remains poor at best. However, more recently some statistically representative experiments have been performed [27, 28] and some features seem to be robust.

The bonding with the contacts

One of the fundamental aspects of molecular electronics is that the bonding between a molecule and the current/voltage probes can be engineered to a degree usually superior to that achievable in conventional inorganic heterostructures. This can dramatically change the current flowing through a device. Consider for instance the simple case of an atomic gold chain, described by s orbitals only, sandwiching a π -bonded molecule (see figure 2).

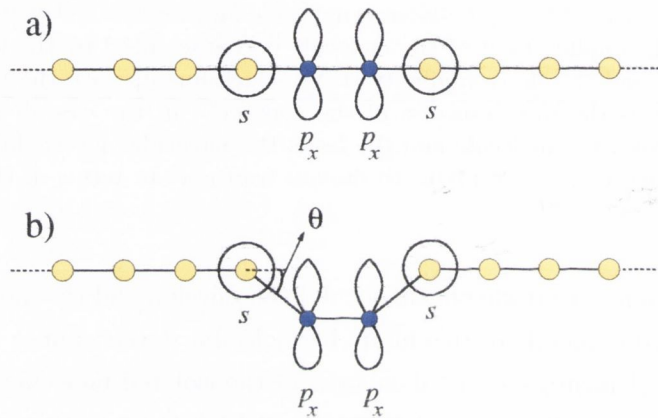


Figure 2: Au atomic chain sandwiching a π -bonded molecule (say an S_2 molecule). a) the molecule is aligned with the Au chain and the transmission is suppressed because the matrix element $\langle s|H|p_x \rangle$ vanishes. In contrast when the molecule forms some angle θ with the Au chain b) then a component of the hopping integral along the bond develops and current can flow.

Let us assume that the relevant molecular state (the one close to the Fermi level of the gold chain) is formed by p_x orbitals, i.e. by those perpendicular to the chain axis. When the molecule is positioned along the axis of the chain the hopping integral between the molecule and the chain $\langle s|H|p_x \rangle$ vanishes regardless of the separation between the two. This is simply the result of the particular symmetry of the problem since s and p_x orbitals do not share the same angular momentum about the bond axis [29]. As a consequence the current is identically zero.

In contrast if the molecule is not coaxial with the chain (figure 2b), then there is a component of the p_x orbital along the bond axis and the hopping integral becomes

$$E_{sp\sigma} = \gamma_{sp\sigma} \sin \theta, \quad (1)$$

where $\gamma_{sp\sigma}$ is the $sp\sigma$ hopping integral and θ the bond angle. This dependence of the hopping integral on the bond orientation may have dramatic consequences

on the transport properties. Hence, the I - V characteristics of a molecule can be engineered by simply changing the details of the bonding with the electrodes. This is considerably more complicated in extended interfaces (for instance between two metals), since disorder, interdiffusion and roughness have the effect of averaging out the atomistic details of the bonding. It is important to remark that even when molecular layers are grown a good level of tuning of the bonding properties still exists. For instance the bonding site and the bond angle usually depend on the layer density (coverage) [30], and these can be further tuned by changing the anchoring groups [28].

Ultimately this means that molecules present great potential but also introduce new complications, specially from the fabrication point of view. Greater control and characterisation is necessary when designing devices. Most of the effects are yet unknown and the phase space that one has to explore - the number of configurations of molecules on surfaces - is extremely large.

Spin-Electronics

Giant magnetoresistance (GMR)

Very few scientific discoveries have moved from an academic laboratory to industrial mass production as quickly as the giant magnetoresistance effect (GMR) [31, 32], the forerunner of spintronics and now exploited in any read-head for standard hard drives. GMR is the change of the electrical resistance of a magnetic device when an external magnetic field is applied and it is essentially associated to a change in the magnetic state of the device itself. The revolutionary scientific message revealed by the GMR effect is that the electron spin, as well as the electronic charge, can be used in electronic applications. This idea, of employing the spin degree of freedom of the electrons as a new way of storing or transmitting information is yet to be fully explored. However it is already setting a new paradigm.

More recently, the electron spin has made its appearance in semiconductor physics with the potential of bringing memory and logic functionalities on the same chip [33, 34, 35]. The electron spin is the ultimate logic bit. In semiconductors spin preserves coherence over extremely long times [36] and distances [37], thus it offers the tantalising prospect of being used for quantum logic [38].

Ultimately, spin looks like an attractive degree of freedom to be used in logic because the energy scale relevant for its typical dynamics is order of magnitudes smaller than that involved in manipulating the electron charge in standard transis-

tors. This can translate in devices exhibiting ultra-low power consumption and high speed. Moreover the sole existence of magnetic materials with high Curie temperature suggests the possibility of powerless non-volatility.

Transition metals and spin valves

Magnetic transition metals and their permalloys occupy an important place in the field of spin-electronics. This is essentially due to their high Curie temperature (for commercially useful magnetic materials it must exceed ~ 500 °K [39]), and the possibility of engineering the various magnetic properties by alloying. The ferromagnetism in $3d$ transition metals can be understood by simply looking at their electronic structure.

The nominal atomic configurations of Ni, Co and Fe are respectively $4s^23d^8$, $4s^23d^7$ and $4s^23d^6$. Therefore in forming a solid one expects the Fermi level (E_F) to be in a region of density of states (DOS) with dominant d character. Since the d shells are rather localised the DOS is large around E_F and the material becomes Stoner unstable thus developing a ferromagnetic ground state. The band energies $\epsilon_{\vec{k}\sigma}$ for the two different spin orientations ($\sigma = \uparrow, \downarrow$) are shifted with respect to each other by a constant $\Delta = \epsilon_{\vec{k}\downarrow} - \epsilon_{\vec{k}\uparrow}$, with Δ approximately 1.4 eV in Fe, 1.3 eV in Co and 1.0 eV in Ni. More sophisticated density functional theory (DFT) calculations show that such picture is a good approximation of the real electronic structure of Ni, Co and Fe.

In addition to the formation of a net magnetic moment a consequence of the spin-splitting of the band structure is that the Fermi surface for the two spin directions is rather different. This difference is more pronounced in the case of strong ferromagnet, where only one of the two spin-split d manifolds is fully occupied (majority band) while the other has some fractional occupation (minority band). An example of this situation is fcc Co (the high temperature phase), whose electronic structure is presented in figure (3).

The main feature of the band-structure of Co (and indeed of the other $3d$ magnetic transition metals) is the presence of a broad (delocalised) and only weakly spin-split s band, and of a narrow (localised) and largely spin-polarised d band. The former has almost free electron-like character for energies both below (note the parabolic behaviour of the bands around Γ for $E \sim -9$ eV) and above E_F . In contrast the latter is only about 5 eV wide and cuts close to the Fermi level. Because of the spin-splitting of the d manifold, Δ , the majority spin band has an almost spherical Fermi surface (see figure 3c1), while the minority one has a rather complicated structure,

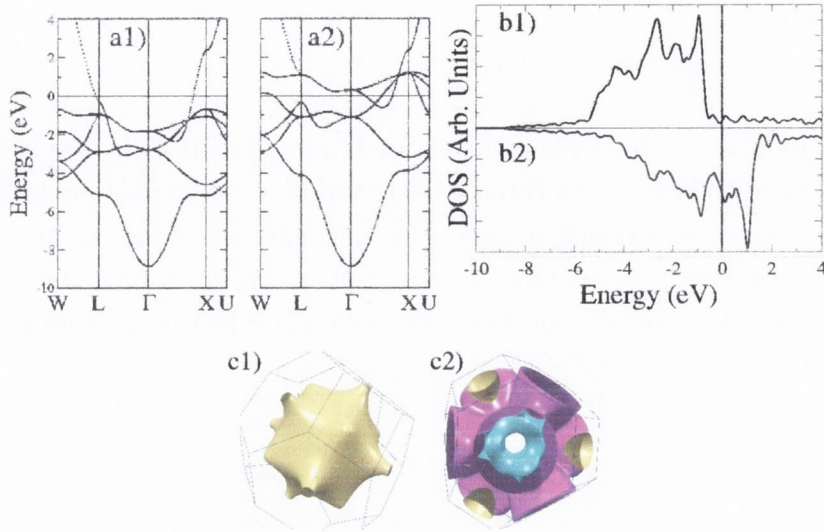


Figure 3: a) Band structure, b) density of states, and c) Fermi surface for fcc Co. The figures a1), b1) and c1) refers to the majority spin electrons, while a2), b2) and c2) to the minority. The pictures a) and b) have been obtained with density functional theory using the code SIESTA [40], and c) from an *spd* tight-binding Hamiltonian [41].

mostly arising from the *d* manifold (see figure 3c2). The different structure of the Fermi surface for majority and minority spins and the fact that these differences arise from a different orbital character are the main ingredients for understanding the transport properties of magnetic transition metal heterostructures.

Spin valves

The prototype of all spin devices is the spin-valve. This is formed by two magnetic layers (normally transition metals) separated by a non-magnetic spacer (either metal or insulator). One of the two magnetic layers is free to rotate in small magnetic fields, while the other usually is pinned by exchange coupling with either an antiferromagnet or by strong magnetic anisotropy. The current passing through a spin-valve depends on the mutual orientation of the two magnetic layers and it is typically higher for a parallel alignment (PA) than for an antiparallel alignment (AA). Thus a spin-valve behaves essentially as a spin polariser/analyser device. The quantity that defines the effectiveness of the spin-filtering effect is the GMR ratio R_{GMR} defined as (“optimistic

definition”)

$$R_{\text{GMR}} = \frac{I_{\text{PA}} - I_{\text{AA}}}{I_{\text{AA}}} \quad (2)$$

An intuitive understanding of the spin-filtering produced by a spin-valve can be obtained by looking at the Fermi level lineup of the materials forming the device. Let us consider for example a Co/Cu/Co spin-valve (see figure 4), and assume that the two spin-bands do not mix. This is the two spin fluid approximation, which is valid in the case of weak spin-orbit scattering and collinear magnetism [42].

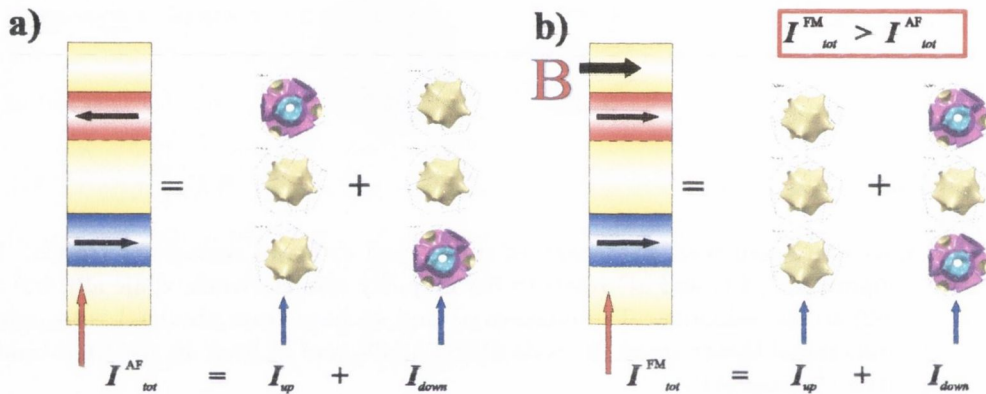


Figure 4: Sketch of a GMR device, two magnetic materials sandwiching a non-magnetic one. (a) In the absence of a magnetic field, the magnetic moments of the two electrodes are aligned anti-parallel to each other, (b) whereas when a small magnetic field is applied, the two magnetic moments align with each other. The overall change in resistance due to the applied magnetic field is equal to the GMR

In the AA a spin electron propagates in the majority spin band in the bottom layer and in the minority band in the top one (and *vice versa* for the other spin orientation). Consequently electrons always travel across the Fermi surfaces of Cu and of both the spin-bands of Co. In contrast, in the PA the two spin currents are rather different. The majority current is made from electrons that have travelled within the Fermi surfaces of Cu and that of the majority spin of Co, while the down spin current from electrons that have travelled within the Fermi surfaces of Cu and that of the minority spin of Co. This leads to two different current paths for the AA and the PA. Since the two spin currents in parallel add to form the total current and since generally the resistances of majority and minority electrons are different in a magnetic transition metal, the current passing through the PA and AA configurations

¹An alternative definition (“pessimistic definition”) using $I_{\text{PA}} + I_{\text{AA}}$ in the denominator is sometimes used.

are different. Importantly the larger the mismatch between the two spin currents, the larger the GMR ratio.

Spin polarisation of a device

An important question is how to quantify the relative difference between the two spin currents in a magnetic device and how to relate this property to the elementary electronic structure of the materials forming the device. For that purpose we define the spin-polarisation P of a material/device as

$$P = \frac{I_{\uparrow} - I_{\downarrow}}{I_{\uparrow} + I_{\downarrow}}, \quad (3)$$

where I_{σ} is the spin- σ contribution to the current. I_{σ} and P are not directly observable and must be calculated or inferred from indirect measurements. Unfortunately the way to relate the spin-current I_{σ} to the electronic structure of a material is not uniquely defined and depends on the particular experiment carried out.

As brilliantly pointed out by Mazin [43], the relation between the spin-polarisation of a magnetic material and its electronic structure depends critically on the transport regime that one is considering (ballistic, diffusive, tunnelling, etc). As a first approximation the current I is simply proportional to $N_{\text{F}}v_{\text{F}}^n$, where N_{F} and v_{F} are the DOS at the Fermi level and the Fermi velocity respectively. Different transport regimes weight the contribution of the Fermi velocity differently, and one has $n = 2$ for diffusive transport, $n = 1$ for ballistic transport and $n = 0$ for tunnelling.

Therefore the spin-polarisation P becomes

$$P_n = \frac{N_{\text{F}}^{\uparrow}(v_{\text{F}}^{\uparrow})^n - N_{\text{F}}^{\downarrow}(v_{\text{F}}^{\downarrow})^n}{N_{\text{F}}^{\uparrow}(v_{\text{F}}^{\uparrow})^n + N_{\text{F}}^{\downarrow}(v_{\text{F}}^{\downarrow})^n}. \quad (4)$$

Typical values of P_n for several magnetic metals are reported in table 1.

Notably the spin-polarisation of a device can be different from that of the materials forming it. This is connected to the fact that the bonding at the interface between two different materials can be strongly spin-selective. For instance if the bonding between two materials has mainly s -character, then one expects strong scattering for d -like electrons. As a consequence the spin-polarisation of the current will be determined by the spin-polarisation of the almost free s -electrons. This is usually much smaller than that of the d -electrons and it may even have the opposite sign. For instance it has been demonstrated that the sign of the magnetoresistance of a magnetic tunnelling junction can be altered by simply replacing the insulator forming the barrier [47].

	P_n (%)	$n=2$	$n=1$	$n=0$
Fe		20	30	60
Ni		0	-49	-82
CrO ₂		100	100	100
La _{0.67} Ca _{0.33} MnO ₃		92	76	36
Tl ₂ Mn ₂ O ₇		-71	-5	66

Table 1: Spin-polarisation of typical magnetic metals according to the various definitions given in the text. The data are taken from literature as follows: Ni and Fe [43], CrO₂ [44], La_{0.67}Ca_{0.33}MnO₃ [45] and Tl₂Mn₂O₇ [46].

Why spins and molecules?

What are the advantages of using molecules instead of inorganic materials for performing spin-physics? These are essentially two. On the one hand there are intrinsic molecular properties and in particular the weak spin-orbit and hyperfine interactions. On the other hand there are the properties connected to the formation of interfaces between magnetic metals and molecules. We will return to the interfacial properties in much greater detail in chapter 4, here we focus our attention only on the intrinsic aspects.

It is only until recently that spin has entered the realm of molecular electronics. The driving idea behind the first pioneering experiment of Tsukagoshi and coworkers [48], who injected spin polarised electrons into carbon nanotubes, is that the spin-orbit interaction is very weak in carbon-based materials. The fact that SO interaction, the main source of spin dephasing, is small in addition to the rather weak hyperfine interaction suggests extremely long spin relaxation times. Therefore coherent spin propagation over large distances becomes possible. A rather conservative estimate of the spin diffusion length from the Tsukagoshi's experiment indicated 130 nm as a lower bound of the spin-diffusion in carbon nanotubes. These findings have stimulated a growing activity in the area and several experiments dealing with molecular tunnelling junctions [49], spin-transport through polymers [50, 51] and optical pump/probe experiments through molecular bridges [52] have recently appeared.

Spin-orbit interaction is a relativistic effect which couples the electron spin \vec{S} with its angular momentum \vec{L} . The spin-orbit Hamiltonian in general can be written as

$$H_{\text{SO}} = V_{\text{SO}}(\vec{r}) \vec{S} \cdot \vec{L}, \quad (5)$$

where $V_{\text{SO}}(\vec{r})$ is a term which contains the gradient of the electrostatic potential. Although it is rather intuitive to realize that the strength of this interaction grows with the atomic number Z (in fact it is proportional to Z^4), its actual value in the solid state depends on various factors such as the crystal symmetry and the material composition. Importantly the spin-orbit effect is responsible for spin-precession and the loss of spin-coherence. In organic materials usually the spin-orbit interaction is rather small. This is mostly due to the small atomic number of carbon - the main constituent of these molecules. In table 2 we compare the spin-orbit splitting Δ_{SO} of the valence band of several semiconductors [53] with that of carbon in the diamond structure [54]. The table shows that in carbon the spin-splitting of the valence band

	Δ_{SO} (meV)
Si	44
Ge	290
GaAs	340
AlAs	280
InAs	380
GaP	80
InP	111
GaSb	750
AlSb	670
InSb	980
C	13

Table 2: Valence band spin-orbit splitting for various semiconductors.

is approximately one order of magnitude smaller than in ordinary III-V or group IV semiconductors and one should expect a considerably longer spin-lifetime [36, 37].

Another important interaction, which generally leads to spin-decoherence, is the hyperfine interaction between electron and nuclear spins. This has the form

$$H_{\text{hyp}} = A_{\text{hyp}} \vec{s} \cdot \vec{S}_{\text{N}}, \quad (6)$$

where \vec{s} and \vec{S}_{N} are respectively the electronic and nuclear spin, and A_{hyp} is the hyperfine coupling strength. The hyperfine interaction is a source of spin de-coherence [55] because the random flipping of nuclear spins can cause that of an electron spin. However, in III-V semiconductors hyperfine interaction was also proved to be a tool for controlling nuclear spins via optically polarised electron spins [56]. In organic

materials usually the hyperfine interaction is weak. The main reason for this is that most of the molecules used for spin-transport are π -conjugate molecules where the transport is mostly through molecular states localised over the carbon atoms. Carbon, in its most abundant isotopic form, ^{12}C , has nuclear spin $S_{\text{N}}=0$, and therefore is not hyperfine active. Moreover the π -states are usually delocalised and H_{hyp} can be, anyway, rather small. In table 3 we report the value of the nuclear spin for various atomic species with their relative isotopic abundance.

Isotope	IA (%)	S_{N}
^1H	99.98	1/2
^2H	0.02	1
^{12}C	98.93	0
^{13}C	1.1	1/2
^{14}N	99.632	2
^{15}N	0.368	1/2
^{16}O	99.757	0
^{18}O	0.205	0
^{19}F	100	1/2
^{69}Ga	60.108	3/2
^{71}Ga	39.892	3/2
^{75}As	100	3/2
^{28}Si	92.2297	0
^{29}Si	4.6832	1/2
^{30}Si	3.0872	0

Table 3: Nuclear spin for elements present in typical organic molecules and in both Si and GaAs. Here we report the nuclear spin for the most abundant isotopes, together with their relative isotopic abundance (IA).

Estimates of the spin-lifetime of organic materials from transport experiments are at the moment only a few. Moreover in most cases these are extracted from spin-valve measurements by fitting to the Jullier's formula [57]. This procedure does not distinguish the source of spin-flip, which may or may not be located inside the molecule, but at the interface with the magnetic electrodes. Therefore these measurements are likely to offer a conservative estimate of the spin-lifetime. Nevertheless the results for the spin diffusion length reported in the literature are rather encouraging for carbon nanotubes (130nm) [48], polymers (200nm) [51], or Alq_3 molecules (5nm) [58].

The molecular world has all the ingredients that spin-electronics needs. The conductivity of polymers can be changed by more than ten orders of magnitude [59] and elementary molecules can be designed with the desired electronic structure. Molecules can be anchored to metals in numerous ways and the bonding angle can be further engineered by the coverage density [30]. The spin-relaxation times can be extremely long and furthermore both paramagnetic and ferromagnetic molecules are available [60].

Why a tool for computing electronic transport is so important?

In addition to this large experimental activity, an equally large effort has been devoted to the development of efficient computational methods for evaluating I - V characteristics of nanoscale devices. This is quite a remarkable theoretical challenge since advanced quantum transport algorithms must be combined with state of the art electronic structure methods. Ideally these tools should be able to include strong correlation as well as inelastic effects, and they should be suitable for describing large systems (easily scalable methods). Furthermore in order to compare directly to experiments the detailed knowledge of the atomic configuration is needed.

Moreover the interface between molecular electronics and spintronics requires tools that can deal with the transport properties of magnetic systems at the nanoscale. Magnetic materials present a challenging perspective for present methods based on DFT because of the localised nature of the d orbitals. A computational tool which fulfils this gap is still lacking.

Modern theory of quantum transport has developed a range of methods for calculating transport in nanoscale conductors under a time-independent external bias. Broadly speaking these can be divided into two main classes: 1) steady state algorithms, and 2) time dependent schemes. The first are based upon the assumption that, regardless of the details of a possible transient, a steady state is always achieved. The current through the entire device is calculated as a balance of currents entering and leaving a given scattering region, either using scattering theory [61, 62, 63, 64, 65, 66, 67, 68, 69, 70, 71, 72], or by solving a master equation [73, 74, 75]. A multitude of variations over this generic scheme are available [69], depending on the underlying assumption leading to the steady state, the details of the electronic structure method employed, and the way in which the external potential is introduced in the calculation. Interestingly most of the methods can be demon-

strated to be formally equivalent for non-interacting electrons [76], although their equivalence is not demonstrated for the interacting case. Among these algorithms a particular place is occupied by implementations of the non-equilibrium Green function (NEGF) [61, 62, 63, 64] method within density functional theory (DFT) [77, 78]. This approach, which is based on equilibrium DFT to describe the electronic structure, has the advantage of being conceptually simple, and computationally easy and versatile to implement [79, 80, 81, 82, 83].

The main question one wishes to answer with a non-equilibrium approach as opposed to an equilibrium one (linear regime [84]) are the effects of the external bias on the electronic structure and consequently on the electronic transport properties.

In this thesis a detailed description of our recently developed quantum transport code *Smeagol* [71, 72] is presented. *Smeagol* is a DFT implementation of the non-equilibrium Green function method, which has been specifically designed for magnetic materials. The main core of *Smeagol* is our original technique for constructing the leads self-energies [65], which avoids the standard problems of recursive methods [61] and allows us to describe devices having current/voltage probes with a complicated electronic structure. For that reason, it has been specially designed for treating magnetic systems and the problem of magnetotransport. In addition *Smeagol* has been constructed to be a modular and scalable code, with particular emphasis on heavy parallelisation, to facilitate large scale simulations. In its present form *Smeagol* includes the following capabilities

- Full parallelisation up to 128 processors.
- Fully spin polarised including non-collinear spins.
- Ability to calculate both molecules and surfaces: finite and periodic boundary conditions in the transverse direction (orthogonal to the transport).
- Ability to perform large scale calculations up to 100 atoms per processor.
- Inclusion of new exchange and correlation functionals such as LDA+U [85] and self-interaction corrected LDA [86].
- Ability to calculate currents and transmission coefficients with a high degree of accuracy (some results span over five orders of magnitude; see chapter (4) for details).

Dissertation Layout

In this thesis we will highlight the computational tool developed to tackle problems in electronic transport through nanostructures. As we have already mentioned, the importance of simulations which can make quantitative predictions about materials specific systems can lead to a deeper understanding of electronic transport at the nanoscale as well as guide experimental efforts towards devices working under optimal conditions.

In chapter 1 we will address the theoretical foundations of NEGF for a general Hamiltonian, setting up the non-equilibrium transport problem for a non-periodic open system. We will also derive the main equations and how to map the total Hamiltonian of the infinite system into a finite effective Hamiltonian that can be used to calculate the Green function and consequently the density matrix. We will also discuss the effects of the leads and a novel method to solve stability issues related to localised states in the electrodes, usually present in magnetic systems.

In chapter 2 the NEGF formalism will be related to density functional theory. The single-particle Kohn-Sham Hamiltonian is used together with non-equilibrium Green functions to calculate the electronic transport properties of nanoscopic systems. This powerful combination is what we call *Smeagol*. The *Smeagol* algorithm is shown and a description of its implementation within the SIESTA DFT [40] code will be given. Moreover, in this chapter some key examples demonstrate some of *Smeagol*'s capabilities.

In the following chapters some important results obtained with *Smeagol* are presented. In chapter 3 the focus is on nickel magnetic point contacts (MPC). Initially a self-consistent tight-binding Hamiltonian is used to calculate the transport properties of Ni MPCs. We are particularly interested in addressing asymmetries in the $I - V$ characteristics of these systems, and to study the possibility that such asymmetries can originate solely from electronic arguments and the presence of a domain-wall (DW) in the constricted region. We have also studied the effects of oxygen in Ni MPCs using DFT. In this case we considered the effects of different exchange-correlation potentials on the transport properties.

In chapter 4 *Smeagol* is used to understand GMR effects in molecular spintronics devices. The concept of organic spin valves is introduced [87, 88]. We show that organic molecules sandwiched between nickel electrodes present GMR in excess of 600 %. We also study the possibility of tailoring the GMR by choosing the appropriate molecule and by selecting different anchoring groups attached to the electrodes.

Expanding over the idea of end-group engineering we propose a novel device, a magnetic diode using an asymmetric molecule. Finally asymmetries are also addressed in a typical spin-polarised STM-like setup.

In chapter 5 we move slightly away from magnetic systems and go deeply into organic materials. Some insights into the conductivity of DNA connected to gold electrodes will be presented. The issue of DNA conductivity is yet to be resolved and *Smeagol* can give valuable contributions to this problem. The number of atoms involved in the calculations and the effects of the electrodes on the transport make it impossible for any other computational tool to tackle the problem. This gives us the chance to highlight *Smeagol* as a tool for large scale electronic transport.

Reaching the end of this dissertation, the final conclusions will be drawn together with some thoughts for future work in this field. The possible paths that should be followed from a perspective of developing *Smeagol* will be highlighted. We will point out some of the problems that still need to be addressed in materials science and nanotechnology.

Chapter 1

Non-equilibrium Green Functions and the Transport Problem

1.1 Setting up the transport problem

The new paradigm imposed by nanotechnology is the need for a complete quantum mechanical description of electronic transport. At the atomic level a classical description of physical systems gives way to quantum mechanics - and in some cases, special relativity. As we have already mentioned, decreasing the sizes of electronic devices presents tantalising perspectives, however the road ahead might be quite bumpy. Firstly, new fabrication methods need to be devised as we are reaching the limits in size resolution for current ones. Secondly, when modelling atomic scale circuits, one must introduce a treatment in terms of wave functions and transmission probabilities, an aspect usually ignored in conventional electronic engineering.

The typical system one wishes to study in atomic scale transport problems is presented in figure (1.1a). It is a two-probe device consisting of two charge reservoirs bridged by a nanoscale object, namely a molecule or a surface. In a real world scenario this component would be integrated, in a variety of ways, with a number of similar components for logic and/or data storage applications. There are a number of questions that need to be answered before we can attempt to mass produce these nanoscale devices. In fact, we still understand very little about the electronic transport properties of a single atomic size device.

A clearer understanding is imperative if we want to use such systems for technological applications. Therefore throughout this work, we will focus on a single device, a task difficult enough as it is.

Figure (1.1) pictures the same problem from three different perspectives. From a thermodynamic point of view the system comprises two bulk leads and a central region. The latter includes the actual device and, for reasons that will be clear later,

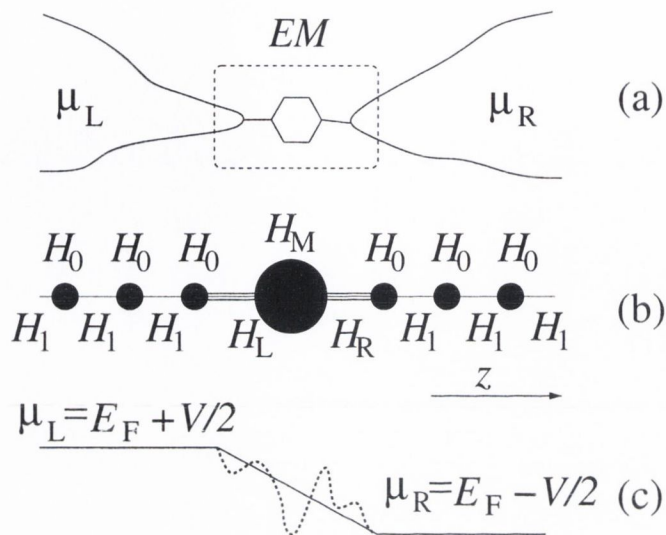


Figure 1.1: Schematic representation of the transport problem from three different perspectives: (a) thermodynamical, (b) quantum mechanical and (c) electrostatical.

part of the leads. Therefore we call such central region an “extended molecule” (EM).¹ The two current/voltage leads are kept at two different chemical potentials respectively μ_L and μ_R and are able to exchange electrons with the EM. Note that when the applied bias is zero ($\mu_L = \mu_R$), this system of interacting electrons is in thermodynamic equilibrium and may be regarded as a grand canonical ensemble. When the bias is applied however $\mu_L \neq \mu_R$ and the current will flow. The prescription for establishing the steady state is that of adiabatically switching on the coupling between the leads and the EM [63, 89, 90].

One important aspect that is missing from figure (1.1a) is the battery. A battery is connected to the ends of the charge reservoirs and a potential difference is applied. Effectively this bias is what keeps the two chemical potentials μ_L and μ_R different. The effect will be of charge flowing across the device, from one reservoir into another to try to counter-balance the effect of the external bias: the current.

At the Hamiltonian level the system under investigation is described by an infinite hermitian matrix \mathcal{H} .² We assume that our system has a rather regular structure, in particular the electrodes. This is by no means the general case but an assump-

¹Hereafter we refer to “molecule” as any system comprising a finite number of atoms, e. g. a segment of a carbon nanotube. This includes also extended surfaces, finite along the transport direction, such as in tunnelling junctions.

²Throughout this work we use calligraphic symbols to denote infinite matrices and capitalised characters for finite ones

tion that makes the problem solvable. First notice that the two semi-infinite current/voltage probes are defect-free crystalline metals. These have a regular periodic structure and a unit cell along which the direction of the transport can be defined. The second assumption is that the transport problem will be formulated in terms of a linear combination of atomic orbitals (LCAO). Despite the rather general choice of basis it is clear that the total Hamiltonian for the system is going to be rather sparse. Given the sparsity of the total Hamiltonian it is convenient to introduce the concept of principal layer (PL). A principal layer is the smallest cell that repeats periodically in the direction of transport. It is constructed in such a way to interact only with the nearest neighbour PLs. This means that *all* the matrix elements between atoms belonging to two non-adjacent PLs vanish.

For example take a linear chain of hydrogen atoms described by a nearest neighbour tight-binding model then one atom forms the PL. However if nearest and next nearest neighbour elements are included then the PL will contain two atoms, etc (for examples see section 1.6.2). A more general case would be that of a PL formed by N_{species} types of atoms (atomic species) with N_{atoms}^i atoms of species i and each species comprising of N_{orbitals}^i orbitals (basis functions).

We then define H_0 as the $N \times N$ matrix describing all interactions within a PL, where

$$N = \sum_i^{N_{\text{species}}} N_{\text{atoms}}^i \times N_{\text{orbitals}}^i, \quad (1.1)$$

is the total number of degrees of freedom (total number of basis functions) in the PL. Similarly H_1 is the $N \times N$ matrix describing the interaction between two PLs. Finally H_M is the $M \times M$ matrix describing the extended molecule and H_{LM} (H_{RM}) is the $N \times M$ matrix containing the interaction between the last PL of the left-hand side (right-hand side) lead and the extended molecule. The final form of \mathcal{H} is

$$\mathcal{H} = \begin{pmatrix} \cdot & \cdot & \cdot & \cdot & \cdot & \cdot & \cdot & \cdot & \cdot & \cdot & \cdot \\ \cdot & 0 & H_{-1} & H_0 & H_1 & 0 & \cdot & \cdot & \cdot & \cdot & \cdot \\ \cdot & \cdot & 0 & H_{-1} & H_0 & H_{LM} & 0 & \cdot & \cdot & \cdot & \cdot \\ \cdot & \cdot & \cdot & 0 & H_{ML} & H_M & H_{MR} & 0 & \cdot & \cdot & \cdot \\ \cdot & \cdot & \cdot & \cdot & 0 & H_{RM} & H_0 & H_1 & 0 & \cdot & \cdot \\ \cdot & \cdot & \cdot & \cdot & \cdot & 0 & H_{-1} & H_0 & H_1 & 0 & \cdot \\ \cdot & \cdot & \cdot & \cdot & \cdot & \cdot & \cdot & \cdot & \cdot & \cdot & \cdot \end{pmatrix}. \quad (1.2)$$

For a system which preserves time-reversal symmetry $H_{-1} = H_1^\dagger$, $H_{ML} = H_{LM}^\dagger$ and $H_{MR} = H_{RM}^\dagger$. In this form \mathcal{H} has the same structure as the Hamiltonian of a one-dimensional system as shown in figure 1.1b. However this is not the most general

situation and does not apply if a magnetic field is present for example. Also note that \mathcal{H} is tridiagonal.

For a non-orthogonal basis set the overlap matrix \mathcal{S} has exactly the same structure of \mathcal{H} . Therefore we adopt the notation S_0, S_1, S_{LM}, S_{RM} and S_M for the various blocks of \mathcal{S} , in complete analogy with their Hamiltonian counterparts. Here the principal layer, defined for \mathcal{H} is used for both the \mathcal{S} and the \mathcal{H} matrix, even though the range of \mathcal{S} can be considerably shorter than that of \mathcal{H} .

Let us now discuss the electrostatics of the problem (figure 1.1c). The main consideration here is that the current/voltage probes are made from good metals and therefore preserve local charge neutrality. For this reason the effect of an external bias voltage on the leads will produce a rigid shift of the whole spectrum, i.e. of all the on-site energies. In contrast a non-trivial potential profile will develop over the extended molecule, which needs to be calculated self-consistently. Importantly the resulting self-consistent electrostatic potential must match that of the leads at the boundaries of the EM. If this does not happen, the potential profile will develop a discontinuity with the generation of spurious scattering. Therefore, in order to achieve a good match of the electrostatic potential, several layers of the leads are usually included in the extended molecule. Their number ultimately depends upon the screening length of the leads, but in most situations a few (between two and four) atomic planes are sufficient.

Moreover, even in the case of extremely short screening length, it is good practice to include a few planes of the leads in the extended molecule because the electrodes generally have reconstructed surfaces, which might undergo additional geometrical reconstructions when bonding to a nanoscale device (e.g. molecules attached to metallic surfaces through corrosive chemical groups).

In order to find the electron's wavefunction and determine the full quantum mechanical properties of the problem one, in principle, needs to diagonalise \mathcal{H} . However, the Hamiltonian is clearly neither finite nor translationally invariant (the terms $H_{LM}, H_{ML}, H_{MR}, H_{RM}, H_M$ break translational symmetry). Hence, Bloch's theorem cannot be applied for the entire system and we need to diagonalise an infinite matrix; clearly an impossible task.

This issue must be addressed in a different way. A possible way is to assume that states deep inside the electrodes are associated to Bloch states of the infinite system. These states are scattered by the potential created by the central EM. One can then use a Green function [61, 63] or a wavefunction approach [91, 92] to calculate the ground state electronic properties (including the wavefunction) of an open system.

The resulting wavefunction can be considered as a combination of Bloch states for the region inside the electrodes and localised atomic-like states for the region in and around the EM.

Even if one is able to calculate the Hamiltonian \mathcal{H} (and the electron wavefunction) the problem of transport still needs to be addressed. We do so by looking at two different limits. Firstly the limit of infinitesimally small bias: the linear regime. In this limit, we can formulate a quantum mechanical description of our problem lying at or close to equilibrium conditions. We assume that under an external applied bias the Hamiltonian $\mathcal{H}(V)$ does not significantly change from that of the ground-state $\mathcal{H}(V=0)$. This approach will be presented in section 1.2 where we show using the Landauer-Büttiker formalism [84] that the transport properties, most notably the conductance can be associated with the transmission probabilities of the scattered part of the electronic wavefunction.

Secondly, we will present, in section (1.3), a very simple model of transport across a single energy level in order to understand changes to the system's Hamiltonian under bias - an effect we neglected in the previous situation case. The total current at steady state can be associated to the rate of transfer of electrons across the EM. These two simple cases will lead to a deeper understanding of the transport problem. We will then join these two concepts into a more general framework which we present in section (1.4).

1.2 The Landauer formalism: equilibrium transport

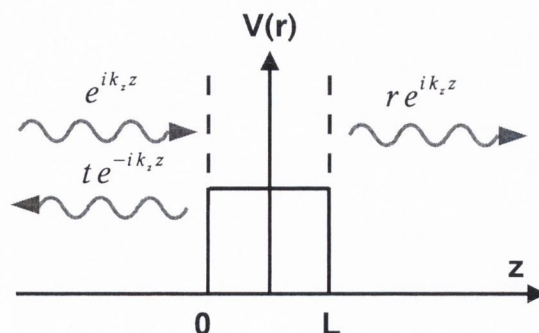


Figure 1.2: Schematic representation of incoming and outgoing wavefunctions scattered by a potential $V(r)$

The Landauer-Büttiker formalism [84] associates the conductance of a device with

the quantum mechanical transmission probabilities of the one electron wave function as it approaches an arbitrary scattering potential [61]. There are two underlying assumptions in this formulation namely: the electrodes must be both in thermal equilibrium devoid of correlation effects.

The problem can be formulated in terms of incoming, $|\Phi_{in}\rangle$ and outgoing, $|\Phi_{out}\rangle$ electron wavefunctions propagating along a one dimensional wire (scattering channel) and scattered by a potential connecting the two leads. Due to the periodic nature of the wire, these wavefunctions have the form of Bloch waves and in absence of a scattering potential, each one contributes with $2e^2/h = G_0$ to the total conductance [84]. We then define the scattering channel as the asymptotic part of the wavefunction deep inside the leads. If the system is multi-dimensional (quasi- 1D, 2D or 3D), several possible Bloch waves with the same energy can propagate through the leads (multi-channel problem). Once the i -th channel in the left hand-side reaches the scattering region it can be transmitted to any channel into the right hand-side lead or back scattered into any channels of the left hand-side lead.

Figure (1.2) provides a simple example of the transport problem formulated in terms of in-scattering and out-scattering channels: free electrons with energy E are injected from the left and are scattered by a step potential

$$V(z) = \begin{cases} V & , < z < L \\ 0 & , \text{elsewhere} \end{cases} \quad (1.3)$$

As we can see, an incoming electron with wave-vector k_z is partially backscattered with wave-vector $-k_z$ and partially transmitted. The total wavefunction for this problem reads

$$|\Phi_{Total}\rangle = |\Phi_{in}\rangle + |\Phi_{0L}\rangle + |\Phi_{out}\rangle, \quad (1.4)$$

with

$$\langle z|\Phi_{Total}\rangle = \begin{cases} \langle z|\Phi_{in}\rangle = e^{ik_z z} + r e^{-ik_z z} & 0 \leq z \\ \langle z|\Phi_{0L}\rangle = A e^{\kappa_z z} + B e^{-\kappa_z z} & 0 \leq z \leq L \\ \langle z|\Phi_{out}\rangle = t e^{ik_z z} & z > L \end{cases} \quad (1.5)$$

where the wave-vector k_z is given by

$$k_z = \frac{\sqrt{2mE}}{\hbar}, \quad (1.6)$$

whereas

$$\kappa_z = \frac{\sqrt{2m(V-E)}}{\hbar}, \quad (1.7)$$

can be real (evanescent) or imaginary (propagating) depending on whether $V > E$ or $V < E$ respectively. The coefficients A , B , t and r are determined by imposing

the continuity of the total wavefunction and its derivative at the boundaries of the step potential. Finally

$$|r|^2 + |t|^2 = 1, \quad (1.8)$$

i.e., the flux is conserved.

Alternatively the scattering process can be described in terms of the scattering matrix, S , which relates the wavefunction of the incoming and outgoing electrons with respect to the step potential *i. e.*, channels entering ($|\Phi_{in}\rangle$) or leaving ($|\Phi_{out}\rangle$) the region $0 \leq x \leq L$:

$$|\Phi_{in}\rangle = S|\Phi_{out}\rangle \quad (1.9)$$

where

$$S = \begin{pmatrix} r & t' \\ t & r' \end{pmatrix}, \quad (1.10)$$

and t and r are the transmission and reflexion coefficients respectively for incoming waves from the left whereas t' and r' are the counter parts for incoming waves from the right. In the more general multi-channel problem r , t , r' and t' are matrices.

Following Landauer [84], we can define the total conductance as ³

$$\Gamma = \frac{e^2}{h} \sum_{\sigma} \sum'_{ij} T_{ij}^{\sigma} = \frac{e^2}{h} \sum_{\sigma} Tr [t_{\sigma} t_{\sigma}^{\dagger}] = \frac{G_0}{2} \sum_{\sigma} Tr [t_{\sigma} t_{\sigma}^{\dagger}] \quad (1.11)$$

where \sum'_{ij} indicates that the sum is performed over all channels at the Fermi energy (E_F) (the open channels) and we have introduced the spin index σ ($\sigma = \uparrow, \downarrow$). We can clearly see that the conductance is written in terms of the conductance quantum G_0 . Most importantly we note that the conductance has been directly associated with the coefficients of the out-scattered wavefunctions of our simple problem. Hence the energy-dependent transmission probability

$$T^{\sigma}(E) = Tr [t_{\sigma}(E) t_{\sigma}^{\dagger}(E)].^4 \quad (1.12)$$

1.3 A simple model for transport under bias

Before laying the theoretical framework which is the main subject of this dissertation we will take some time to introduce a simple model for electronic transport under bias.

³In the case presented here we are already considering the more general situation of a non spin-degenerate system, so the Hilbert space spans over the spin degrees of freedom σ as well. For that reason the universal quantum of conductance, G_0 is divided by two.

⁴In our simple problem this reduces to $T(E) = |t(E)|^2$.

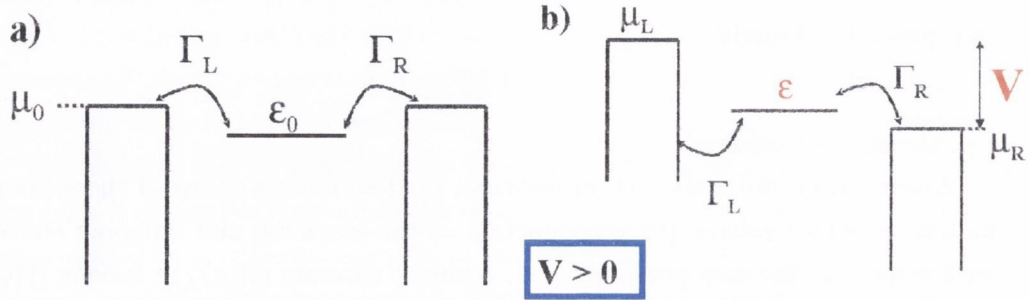


Figure 1.3: Schematic picture of a single energy level - representing a molecule - sandwiched between two jellium reservoirs each with a chemical potential μ_0 . The coupling between the molecular state and the leads is given by Γ_L and Γ_R .

We model our system by sandwiching a molecule between two charge reservoirs. We represent a molecule as a single energy level ϵ_0 . The electrodes are modelled as jellium (constant density of states) with chemical potential set at μ_0 (in the case of thermodynamic equilibrium the chemical potential μ_0 coincides with the Fermi level E_F). When the molecule is attached to the electrodes, the strength of the coupling to the left- and right-hand-side lead is given by Γ_L and Γ_R respectively (see figure (1.3)), *i. e.* the hopping probabilities are Γ_L/\hbar and Γ_R/\hbar . We can write an effective Hamiltonian for our system as the original on-site energy and include the effects of the coupling to the electrodes in terms of a imaginary part added to it

$$\epsilon' = \epsilon_0 + i\frac{\Gamma_L}{2} + i\frac{\Gamma_R}{2}. \quad (1.13)$$

In doing so we only need to focus on the molecule, assuming that the electrodes are not affected by changes due to the attached molecule.

While the density of states of the isolated molecule is a delta function

$$\delta(E - \epsilon_0) = \lim_{\eta \rightarrow 0^+} = \frac{1}{\pi} \frac{\eta}{(E - \epsilon_0)^2 + \eta^2}, \quad (1.14)$$

that of the coupled system is given by a Lorentzian with broadening $\Gamma = \Gamma_L + \Gamma_R$,

$$DOS = \frac{1}{\pi} \Im \left(\frac{1}{E - \epsilon'} \right) = \frac{1}{2\pi} \frac{\Gamma_L + \Gamma_R}{(E - \epsilon)^2 + \left(\frac{\Gamma_L + \Gamma_R}{2}\right)^2}. \quad (1.15)$$

This broadening can be associated with the inverse lifetime of the electron on the molecule. In other words, the stronger the coupling the quicker the electron flows from (to) the electrode into (from) the molecule.

Initially, at $V=0$, the position of the chemical potential for both left and right

electrodes, μ_0 , is the same.⁵ When a bias is applied the chemical potential of the left electrode is shifted by $\frac{eV}{2}$ whereas that of the right hand-side lead changes by $-\frac{eV}{2}$. We assume, in this case, that the drop in the potential occurs at the two interfaces between the molecules and the electrodes. Therefore the position of the energy level remains unchanged. The new chemical potential of the left- and right-hand-side electrodes are now given by $\mu_L = \mu_0 + \frac{V}{2}$ and $\mu_R = \mu_0 - \frac{V}{2}$ respectively (see figure 1.3b)).

We now need to calculate the current under bias. Suppose the molecule is attached solely to the left electrode and $\epsilon < \mu_L$. Then electrons will flow from the left electrode into the molecule until the energy level is in thermodynamical equilibrium with the lead. The opposite happens if $\epsilon > \mu_L$, *i. e.*, electrons flow out of the molecule into the electrode until equilibrium is reached. At equilibrium, the occupation of the molecular state is driven by the chemical potential of the left electrode. It can be written as

$$N_L = 2f(\epsilon, \mu_L) \quad (1.16)$$

where $f(\epsilon, \mu_L)$ is the Fermi distribution at energy ϵ and chemical potential μ_L

$$f(\epsilon, \mu_L) = \frac{1}{e^{(\epsilon - \mu_L)/k_B T} + 1}, \quad (1.17)$$

k_B is the Boltzmann constant [93] and T is the temperature.

Analogously we can use the same arguments to calculate the occupation when the molecule is attached to the right-hand-side lead only

$$N_R = 2f(\epsilon, \mu_R). \quad (1.18)$$

Up to this point there is no current flowing through the system. The molecule is only connected to either the left- or the right-hand-side electrode and it is therefore in thermal equilibrium with either electrode. Once the molecule is connected to both left and right electrodes and bias is applied, we have three possible situations.

The first case is when $\epsilon_0 > \mu_L > \mu_R$, the molecular energy level is initially empty and above both chemical potentials. In this situation there are no electrons available for conduction and there will be no current (figure (1.4a)). The second case corresponds to $\epsilon_0 < \mu_R < \mu_L$. This time there are electrons which can flow from the

⁵For the sake of simplicity we are assuming that both left and right electrodes are made of the same material. We will show latter on in this chapter that one can use different electrodes with different chemical potentials. Once the molecule is attached to the left and to the right leads, there will be an equilibration of the chemical potential leading to a compensating electric field.

⁶The factor two in the equation indicates spin degeneracy. A non-spin-degenerate case could be derived analogously.

left electrode into the molecule, however there are no empty states available in the right lead. Therefore Pauli exclusion principle prevents current from flowing (figure (1.4b)). The third and most interesting scenario is when

$$\mu_R < \epsilon_0 < \mu_L, \quad (1.19)$$

i. e., the molecular state lies between the two chemical potentials. While electrons coming from the left electrode populate the molecule they can also leave for the right lead. Consequently current flows (see figure (1.4c)).

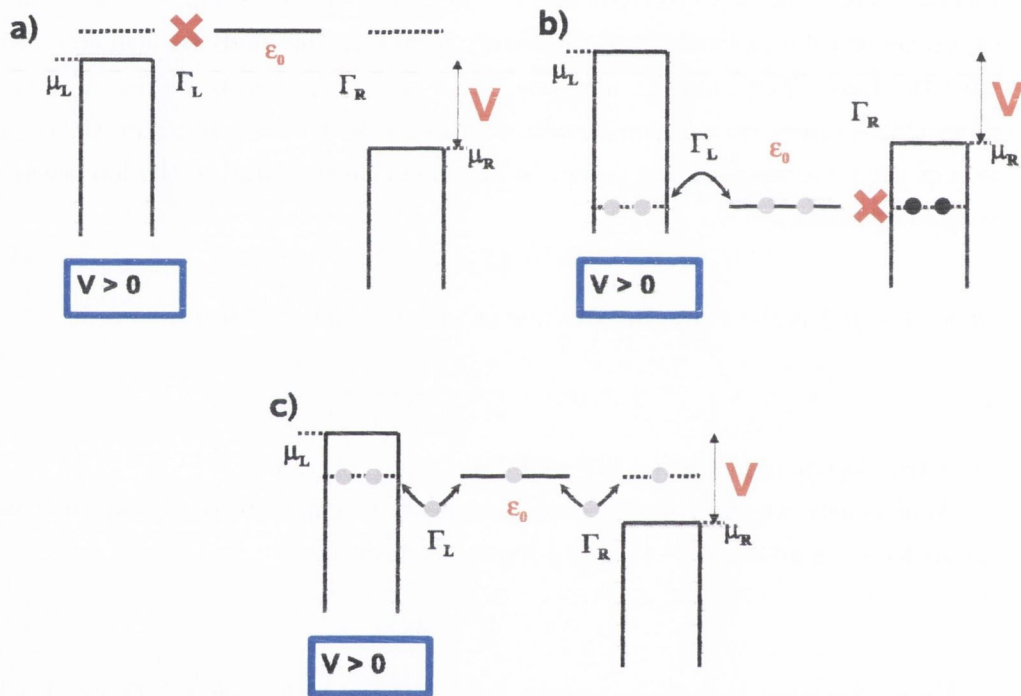


Figure 1.4: Diagram illustrating different positions of a molecular state with respect to the chemical potential of the semi-infinite electrodes. a) The energy level is higher than chemical potentials both in the right (μ_R) and in the left (μ_L) reservoirs \rightarrow no current. b) The energy level is lower than both chemical potentials \rightarrow no current. c) The energy level lies between μ_L and μ_R \rightarrow current.

Bearing in mind that the time-averaged non-equilibrium charge on the molecule corresponds to a value N in between N_L and N_R , then the current flowing from the left-hand-side lead to the molecule is simply

$$I_L = \frac{e\Gamma_L}{h} (N_L - N). \quad (1.20)$$

This equation shows that the current flowing into the molecule is proportionate to the number of excess electrons, *i. e.* to the charge difference $N_L - N$. Analogously,

the net current flowing from the molecule into the right electrode is

$$I_R = \frac{e\Gamma_R}{h} (N_R - N). \quad (1.21)$$

Initially, immediately after the coupling between the molecule and the leads has been switched on, the number of electrons flowing in and out of the molecule is going to vary as the molecule is reaching a steady state (a situation that will ultimately depend on the coupling to the left and right reservoirs). At steady state the number of electrons per unit time flowing from the left lead into the molecule and from the molecule into the right lead must be equal. By setting $I_L = I_R$ we obtain an expression for the occupation of the molecular level at the steady state

$$N = \frac{\Gamma_L f(\epsilon_0, \mu_L) + \Gamma_R f(\epsilon_0, \mu_R)}{\Gamma_L + \Gamma_R}. \quad (1.22)$$

Consequently, we can write an equation for the total current

$$I = \frac{2e}{h} \frac{\Gamma_L \Gamma_R}{\Gamma_L + \Gamma_R} (f(\epsilon_0, \mu_L) - f(\epsilon_0, \mu_R)). \quad (1.23)$$

In figure 1.5 we show the $I - V$ characteristics for different positions of the molecular state ϵ_0 . We can clearly see that, as long as the states lie outside the bias window, there is no current. However, for sufficiently high biases ϵ_0 will eventually be within the bias window and current will flow. In fact, the size of the gap in the current/voltage curve is given by $4|\mu_0 - \epsilon_0|$. Also note that the maximum current allowed through the junction is independent from the position of the energy level

$$I_{\max} = \frac{2e}{h} \frac{\Gamma_L \Gamma_R}{\Gamma_L + \Gamma_R} \quad (1.24)$$

1.3.1 Charging effects

The simple picture provided in the previous section shows how a balancing act between charge flowing in and out of the molecule will lead to electronic transport in conditions out of equilibrium. In order to make our model more realistic we can include changes to the Hamiltonian arising from changes in the occupation of the energy level. In simple terms, we would like to correct the on-site potential of the molecule to account for the electrostatic potential (classical) and possibly electron-electron (quantum) interactions.

As a simple approximation we assume that the energy level has the following form

$$\epsilon = \epsilon_0 + U_{\text{SCF}}, \quad (1.25)$$

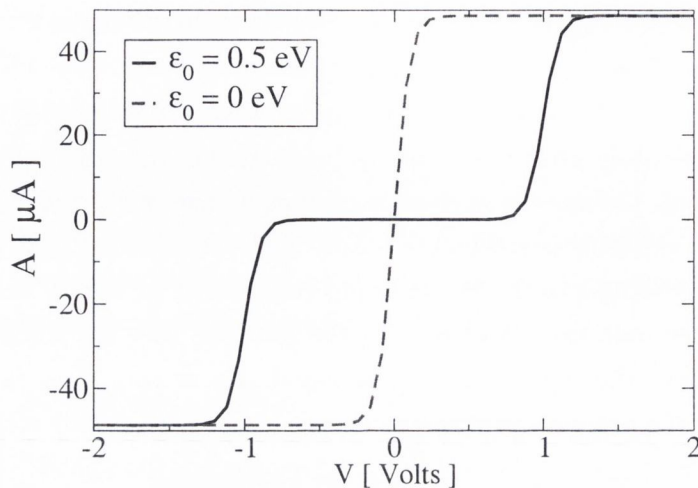


Figure 1.5: Current as a function of voltage for a molecule - represented by a single energy level - within two electrodes. In this case $\Gamma_L = \Gamma_R = 1$ eV and the molecular energy level is positioned either at the initial chemical potential μ_0 (dashed curve) or above it (solid line). The on-site energy is set to 0 and 0.5 eV respectively and $\mu_0 = 0$ eV. The case of $\epsilon_0 < \mu_0$ is the same as $\epsilon_0 > \mu_0$.

where the shift U_{SCF} is given by

$$U_{\text{SCF}} = U(N - 2f(\epsilon_0, \mu_0)). \quad (1.26)$$

We can clearly see that the term $f(\epsilon_0, \mu_0)$, the Fermi distribution for chemical potential μ_0 , corresponds to the initial occupation of the molecule at zero bias whereas N is the electronic population at a certain bias V (to be evaluated self-consistently). Therefore the term U_{SCF} indicates that the molecular state will shift - up or down - to account for changes in its population.

The non-equilibrium population N can be calculated in similar fashion to equation (1.22) if we replace ϵ_0 with ϵ . Now we need to calculate both quantities N and U_{SCF} self-consistently by iterating over equations (1.22), (1.25) and (1.26). This procedure must be repeated for each value of the external bias.

In figure 1.6 we show the $I - V$ characteristics when we include charging effects. We can clearly see that, instead of a sharp jump in the current once the bias exceeds $\frac{4}{e}|\epsilon_0 - \mu_0|$, the linear dependence of the on-site potential on the occupation leads to a linear $I - V$ characteristics, persisting until the maximum current for that particular state has been reached.

We can understand such behaviour using a very simple pictorial description. Let us assume for the sake of simplicity that initially our energy level is higher than the chemical potential μ_0 . Within the bias gap, the molecular state remains essentially

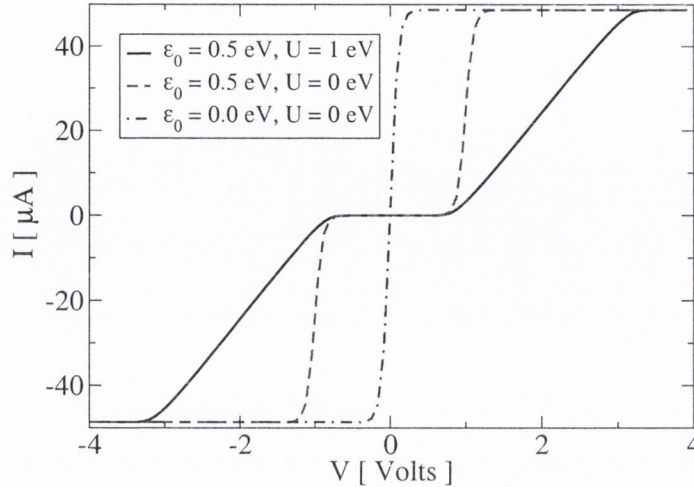


Figure 1.6: Current as a function of voltage for a molecule - represented by a single energy level - sandwiched between two electrodes. In this case $\Gamma_L = \Gamma_R = 1$ eV and the molecular energy level is positioned either at the initial chemical potential μ_0 (dashed-dotted line) or above it (solid). The on-site energy is set to 0 and 0.5 eV respectively and $U = 1$ eV. For comparison we also show the curve presented in figure (1.5) with $U = 0$ eV. Note that for $\epsilon = \mu_0 = 0$ eV charging has no effect in the $I - V$.

unchanged since there are no electrons providing additional charge. However when the energy level lies within the bias window it will start to charge, *i.e.*, its occupation which was originally zero will change. Once this happens the potential (equation (1.25)) shifts up accordingly to compensate for such an effect, and consequently the current drops because the position of that energy level is never completely within the bias window. The linear behaviour is essentially given by the linear dependence of the self-consistent potential on the occupation. When the bias is equal to $2|\mu_0 - \epsilon_0| + 2U$ (the factor 2 comes from the fact that we shift one electrode by $V/2$ and the other by $-V/2$), the potential cannot shift any higher and the current will reach its maximum value. As we mentioned earlier the maximum for the current is only given by the coupling to the electrodes Γ_L and Γ_R .

1.3.2 Asymmetries

If we analyse equation (1.23) in the case of no-charging effects ($\epsilon = \epsilon_0$), we will see that no matter what the coupling terms Γ_L and Γ_R are, the current will always be symmetric with respect to the applied bias. In fact, interchanging $\Gamma_L \rightleftharpoons \Gamma_R$ leaves the total current and the occupation unchanged.

In order to introduce asymmetries in the $I - V$ characteristics we must take

into consideration effects due to changes in the electron occupation in addition to different coupling strengths. Once that is done we can see that although the pre-factor in equation (1.23) remains the same, term

$$f(\epsilon, \mu_L) - f(\epsilon, \mu_R) \quad (1.27)$$

containing the Fermi functions now depends on the position of the molecular energy level ϵ . As discussed before, this energy level must be calculated self-consistently in the case of charging effects.

By expanding equation (1.25) using equations (1.26) and (1.22) we obtain

$$\epsilon = \epsilon_0 + U \left(\frac{\Gamma_L f(\epsilon, \mu_L) + \Gamma_R f(\epsilon, \mu_R)}{\Gamma_L + \Gamma_R} - 2f(\epsilon_0, \mu) \right). \quad (1.28)$$

Hence, with the introduction of charging effects we can clearly see that the position of the energy level ϵ is not invariant by interchanging $\Gamma_L \rightleftharpoons \Gamma_R$. Consequently asymmetries in the $I - V$ will arise due to both charging and asymmetric coupling.

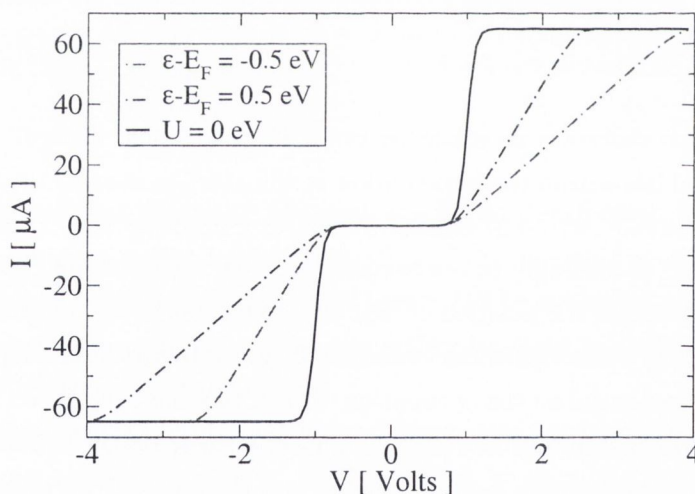


Figure 1.7: Current as a function of voltage for a molecule - represented by a single energy level - within two electrodes. In this case $\Gamma_L \neq \Gamma_R$ and the molecular energy level is positioned either at the Fermi level (solid curve), above (dashed) and below (dotted) the Fermi level. The on-site energy is set to 0, 1 and -1 eV respectively and we have included the effects of charging following equations (1.26) and (1.25) with $U = 1$ eV.

In figure (1.7) we show the effects of asymmetric coupling on the current either considering or not charging effects. We can clearly see that charging of the molecular level induces an asymmetric $I - V$ characteristics. This behaviour depends on the position of the molecular state ϵ_0 as well as the coupling constants.

Although over-simplified, this model brings into light a number of interesting aspects in electronic transport through molecular systems. We have shown that charging effects might have considerable implications for transport, more specifically, the combination of asymmetric coupling to the electrodes and charging leads to asymmetric current/voltage curves. A more realistic description of our system might eventually lead to rectification, an important mechanism in modern electronics.

Obviously, this model cannot account for realistic systems. In order to model material-dependent devices one must be able of describing the electronic properties of such systems with a large degree of accuracy. Moreover, charging must be correctly described if we wish to propose novel devices for logic applications.

In the next section we extend the ideas developed so far introducing an atomistic description of both the electrodes and the molecule. The electronic structure and consequently all other parameters describing our device are calculated with *ab initio* techniques. Hence, our simple model becomes a specific case in a more general theoretical framework know as non-equilibrium Green function formalism [90, 61].

1.4 Non-Equilibrium Transport

1.4.1 Non-equilibrium Green functions (NEGF) for an open system

As pointed out in the introduction we are dealing with an infinite-dimensional non-periodic Hermitian problem. The problem can be written down in terms of the retarded Green's function \mathcal{G}^R for the whole system by solving the Green function equation

$$[\epsilon^+ \mathcal{S} - \mathcal{H}] \mathcal{G}^R(E) = \mathcal{I}, \quad (1.29)$$

where \mathcal{I} is an infinitely-dimensional identity matrix, $\epsilon^+ = \lim_{\delta \rightarrow 0^+} E + i\delta$ and E is the energy. The same equation explicitly using the block-diagonal structure of both the Hamiltonian and the overlap matrix (we drop the symbol "R" indicating the retarded quantities) is of the form

$$\begin{pmatrix} \epsilon^+ \mathcal{S}_L - \mathcal{H}_L & \epsilon^+ \mathcal{S}_{LM} - \mathcal{H}_{LM} & 0 \\ \epsilon^+ \mathcal{S}_{ML} - \mathcal{H}_{ML} & \epsilon^+ \mathcal{S}_M - \mathcal{H}_M & \epsilon^+ \mathcal{S}_{MR} - \mathcal{H}_{MR} \\ 0 & \epsilon^+ \mathcal{S}_{RM} - \mathcal{H}_{RM} & \epsilon^+ \mathcal{S}_R - \mathcal{H}_R \end{pmatrix} \begin{pmatrix} \mathcal{G}_L & \mathcal{G}_{LM} & \mathcal{G}_{LR} \\ \mathcal{G}_{ML} & \mathcal{G}_M & \mathcal{G}_{MR} \\ \mathcal{G}_{RL} & \mathcal{G}_{RM} & \mathcal{G}_R \end{pmatrix} = \begin{pmatrix} \mathcal{I} & 0 & 0 \\ 0 & I_M & 0 \\ 0 & 0 & \mathcal{I} \end{pmatrix}, \quad (1.30)$$

where we have partitioned the Green's functions \mathcal{G} into the infinite blocks describing the left- and right-hand side leads \mathcal{G}_L and \mathcal{G}_R , those describing the interaction between the leads and extended molecule \mathcal{G}_{LM} , \mathcal{G}_{RM} , the direct scattering between the leads \mathcal{G}_{LR} , and the finite block describing the extended molecule G_M . We have also introduced the matrices \mathcal{H}_L , \mathcal{H}_R , \mathcal{H}_{LM} , \mathcal{H}_{RM} and their corresponding overlap matrix blocks, indicating respectively the left- and right-hand-side leads Hamiltonian and the coupling matrix between the leads and the extended molecule. H_M is an $M \times M$ matrix and I_M is the $M \times M$ unit matrix. The infinite matrices, \mathcal{H}_L and \mathcal{H}_R describe the leads and have the following block-diagonal form

$$\mathcal{H}_L = \begin{pmatrix} \ddots & \ddots & \ddots & \ddots & \vdots \\ 0 & H_{-1} & H_0 & H_1 & 0 \\ \dots & 0 & H_{-1} & H_0 & H_1 \\ \dots & \dots & 0 & H_{-1} & H_0 \end{pmatrix}, \quad (1.31)$$

with similar expressions for \mathcal{H}_R and the overlap \mathcal{S} matrix counterparts. In contrast the coupling matrices between the leads and the extended molecule are infinite-dimensional matrices whose elements are all zero except for a rectangular block coupling the last PL of the leads and the extended molecule. For example we have

$$\mathcal{H}_{LM} = \begin{pmatrix} \vdots \\ 0 \\ H_{LM} \end{pmatrix}. \quad (1.32)$$

The crucial step in solving equation (1.30) is to write down the corresponding equation for the Green's function involving the EM and surface PL's of the left and right leads and then evaluate the retarded Green function for the extended molecule G_M^R . This can be done by returning to our initial assumptions about the electrostatics of the problem (section (1.1)); the potential drop occurs entirely across the extended molecule and there are no changes to the electronic structure of the charge reservoirs arising from neither the coupling to the molecule nor through the external bias. Bearing that in mind we can focus solely on the scattering region and treat the effect of electrodes in terms of an effective interaction.

This can be achieved by eliminating the degrees of freedom of the electrodes one by one from deep into the leads all the way to the interface with the EM. Effectively, one can renormalise the total Hamiltonian using a procedure that can be shown to be exact [65]. The final expression for G_M^R has the form

$$G_M^R(E) = [\epsilon^+ S_M - H_M - \Sigma_L^R(E) - \Sigma_R^R(E)]^{-1}, \quad (1.33)$$

where we have introduced the retarded self-energies for the left- and right-hand side lead

$$\Sigma_L^R(E) = (\epsilon^+ S_{ML} - H_{ML}) G_L^{0R}(E) (\epsilon^+ S_{LM} - H_{LM}) \quad (1.34)$$

and

$$\Sigma_R^R(E) = (\epsilon^+ S_{MR} - H_{MR}) G_R^{0R}(E) (\epsilon^+ S_{RM} - H_{RM}). \quad (1.35)$$

Here G_L^{0R} and G_R^{0R} are the retarded *surface* Green function of the leads, i.e. the leads retarded Green functions evaluated at the PL neighbouring the extended molecule when this one is decoupled from the leads. Formally G_L^{0R} (G_R^{0R}) corresponds to the right lower (left higher) block of the retarded Green's function for the whole left-hand side (right-hand side) semi-infinite lead. These are simply

$$\mathcal{G}_L^{0R}(E) = [\epsilon^+ \mathcal{S}_L - \mathcal{H}_L]^{-1} \quad (1.36)$$

and

$$\mathcal{G}_R^{0R}(E) = [\epsilon^+ \mathcal{S}_R - \mathcal{H}_R]^{-1}. \quad (1.37)$$

Note that \mathcal{G}_L^{0R} (\mathcal{G}_R^{0R}) is not the same as \mathcal{G}_L^R (\mathcal{G}_R^R) defined in equation (1.30). In fact the former are the Green functions for the semi-infinite leads in isolation, while the latter are the same quantities for the leads attached to the scattering region. Importantly one does not need to solve equations (1.36) and (1.37) for calculating the leads surface Green functions and a closed form avoiding the inversion of infinite matrices can be provided [65]. We will return to this discussion in more detail in section (1.6.2).

Let us conclude this section with a few comments on the results obtained. The retarded Green's function G_M^R contains all the information about the electronic structure of the extended molecule attached to the leads. In its close form given by the equation (1.33) it is simply the retarded Green's function associated to the effective Hamiltonian matrix H_{eff}

$$H_{\text{eff}} = H_M + \Sigma_L^R(E) + \Sigma_R^R(E).^7 \quad (1.38)$$

Note that H_{eff} is not Hermitian since the self-energies are not Hermitian matrices. This means the total number of particles in the extended molecule is not conserved, as expected by the presence of the leads. Moreover, since G_M^R contains all the information about the electronic structure of the extended molecule in equilibrium with

⁷Note that this is a more general case of equation (1.13). In the one level problem we set $H_M = \epsilon_0$ and $\Sigma_{L/R} = \Delta + i\Gamma_{L/R}/2$, with $\Delta = 0$. The real part of the self-energies shift the on-site energy level while the Γ 's provide the level broadening.

the leads, it can be directly used for extracting the zero-bias conductance G of the system. In fact one can simply apply the Fisher-Lee [61, 94] relation and obtain

$$G = \frac{2e^2}{h} \sum_{\text{Tr}} [\Gamma_L G^{\text{R}\dagger\text{M}} \Gamma_R G_M^{\text{R}}], \quad (1.39)$$

where

$$\Gamma_\alpha(E) = i[\Sigma_\alpha^{\text{R}}(E) - \Sigma_\alpha^{\text{R}}(E)^\dagger], \quad (1.40)$$

($\alpha=L,R$). In equation (1.39) all the quantities are evaluated at the Fermi energy E_F . Clearly $\text{Tr}[\Gamma_L G_M^{\text{R}\dagger} \Gamma_R G_M^{\text{R}}](E)$ is simply the energy dependent total transmission coefficient $T(E)$ of standard scattering theory [84].

Finally note that what we have elaborated so far is an alternative way of solving a scattering problem. In standard scattering theory, as discussed in section (1.2), one first computes the asymptotic current carrying states deep into the leads (scattering channels) and then evaluates the quantum mechanical probabilities for these channels to be reflected and transmitted through the extended molecule [84]. The details of the scattering region are often reduced to a matrix describing the effective coupling between the two surface PLs of the leads which can be solve using a Green function [65] or transfer matrix approach [92]. In contrast the use of (1.39) describes an alternative though equivalent approach, in which the leads are projected out to yield a reduced matrix describing an effective EM. The current through surface PL's perpendicular to the transport direction are the same,⁸ the two approaches are equivalent and there is no clear advantage in using either one or the other. However, when the Hamiltonian matrix of the scattering region H_M is not known *a priori*, then the NEGF method offers a simple way of setting up a self-consistent procedure.

1.4.2 Steady-state and self-consistent procedure

Consider now the case in which the matrix elements of the Hamiltonian of the system are not known explicitly, but only their functional dependence upon the charge density $n(\vec{r})$, $\mathcal{H} = \mathcal{H}[n]$, is known. This is the most common case in standard mean field electronic structure theory, such as DFT [77, 78]. If no external bias is applied to the device (linear response limit) the Hamiltonian of the system can be simply obtained from a standard equilibrium DFT calculation and the procedure described in the previous section can be used without any modification. However, when an external bias V is applied, the charge distribution on the extended molecule will differ from

⁸Some caution should be taken in selecting the plane for evaluating the conductance when the basis set is not complete as in the case of LAO basis sets. See for instance [95] and [96].

the one at equilibrium since both the net charge and the electrical polarisation are affected by the bias. This will determine a new electrostatic potential profile with different scattering properties.

These modifications will affect only the extended molecule, since our leads preserve local charge neutrality. This means that the charge density and therefore the Hamiltonian of the leads are not modified by the external bias applied. As discussed at the beginning the only effect of the external bias over the current/voltage electrodes is a rigid shift of the on-site energies. The Hamiltonian then takes the form

$$\mathcal{H} = \begin{pmatrix} \mathcal{H}_L + \mathcal{S}_L eV/2 & \mathcal{H}_{LM} & 0 \\ \mathcal{H}_{ML} & H_M & \mathcal{H}_{MR} \\ 0 & \mathcal{H}_{RM} & \mathcal{H}_R - \mathcal{S}_R eV/2 \end{pmatrix}, \quad (1.41)$$

Note that the coupling matrices between the leads and the extended molecule are also not modified by the external bias, since by construction the charge density in the surface planes of the extended molecule matches exactly that of the leads.

The Hamiltonian of the extended molecule

$$H_M = H_M[n] \quad (1.42)$$

depends on the density matrix, which is calculated using the lesser Green function [61, 62, 63, 64, 71, 89, 90]

$$D_M = \frac{1}{2\pi i} \int dE G_M^<(E), \quad (1.43)$$

so a procedure must be devised to compute this quantity.

In equilibrium, $G^<(E) = -2i \text{Im} [G^R(E)] f(E - \mu)$, so it is only necessary to consider the retarded Green function, given by equation (1.33). Out of equilibrium, however, the presence of the leads establishes a non-equilibrium population in the extended molecule and $G^<$ is no longer equal to $-2i \text{Im} [G^R] f(E - \mu)$. The non-equilibrium Green function formalism [61, 62, 63, 64, 89, 90] provides the correct expression (see appendix C in [71]):

$$G_M^<(E) = iG_M^R(E)[\Gamma_L f(E - \mu_L) + \Gamma_R f(E - \mu_R)]G_M^{R\dagger}(E) \quad (1.44)$$

where $\mu_{L/R} = \mu \pm eV/2$, $f(x)$ is the Fermi function for a given temperature T ,

$$\Sigma_{L/R} = \Sigma_{L/R}(E, V), \quad (1.45)$$

and

$$\Gamma_{L/R} = \Gamma_{L/R}(E, V). \quad (1.46)$$

Our main assumption about the leads is that the effect of the bias induces a rigid shift in the electronic structure, hence it is easy to see that

$$\Sigma_{L/R}(E, V) = \Sigma_{L/R}(E \mp eV/2, V = 0) \quad (1.47)$$

and consequently

$$\Gamma_{L/R}(E, V) = \Gamma_{L/R}(E \mp eV/2, V = 0). \quad (1.48)$$

In other words, we can calculate the self-energies and the Γ matrices for zero bias and apply a shift of $\mp \frac{V}{2}$ to the electronic structure to mimic the applied bias.⁹

Finally, $G_M^R(E)$ is given again by equation (1.33) where now we replace $\Sigma_{L/R}(E)$ with $\Sigma_{L/R} = \Sigma_{L/R}(E \pm eV/2)$.

The self consistent procedure is as follows. First a trial charge density

$$n^0(\vec{r}) = \langle \vec{r} | D_M^0 | \vec{r} \rangle \quad (1.49)$$

is used to compute H_M from equation (1.42). Then Γ_L , Γ_R and G_M^R are calculated from equations (1.47), (1.48), and (1.33). These quantities are used to compute $G_M^<$ in equation (1.44), which is fed back into equation (1.43) to find a new density n^1 . This process is iterated until a self-consistent solution is achieved, which is when

$$\text{Max} \| D_M^j - D_M^{j+1} \| < \delta, \quad (1.50)$$

where $\delta \ll 1$ is a tolerance parameter.

Finally, the current I can be calculated using [97]

$$I = \frac{e}{h} \int dE \text{Tr}[\Gamma_L G_M^{R\dagger} \Gamma_R G_M^R] (f(E - \mu_L) - f(E - \mu_R)). \quad (1.51)$$

Note that the term $\text{Tr}[\Gamma_L G_M^{R\dagger} \Gamma_R G_M^R]$ is analogous to the conductance for the linear regime (Eq. (1.11)). Hence we can associate

$$T(E, V) = \text{Tr}[\Gamma_L G_M^{R\dagger} \Gamma_R G_M^R], \quad (1.52)$$

with the transmission coefficient, which in the more general non-equilibrium case is bias-dependent as well as energy-dependent. Koentopp and Burke have shown that the Landauer-Büttiker formula only holds in the case of interacting electrons in the

⁹We can see that this is indeed the case by taking the Hamiltonian of an infinite system H and applying a constant potential V . The resulting eigenvalue equation is $H + VS = ES$ which becomes $H = (E - V)S$. It is then clear that the eigenvectors for this problem are unchanged when compared to the zero bias case and the eigenvalues are shifted by a constant V (assuming that the potential has converged deep inside the electrodes and all we see is a constant bias). Subsequently the charge density n remains the same provided we shift the Fermi level (chemical potential) by V .

limit of zero bias when the exchange and correlation term in the Hamiltonian is local. In the case of non-local potentials a correction due to the response to the external electric field in the exchange-correlation potential must be added [?].

Let us conclude this section with a note on how to perform the integrals of equations (1.43) and (1.51). The one for the current is trivial since the two Fermi functions effectively cut the integration to give a narrow energy window between the chemical potentials of the leads. In addition the transmission coefficients, with the exception of some tunnelling situations, is usually a smooth function of the energy.

In contrast, the integration leading to the density matrix (1.43) is more difficult, since the integral is unbound and the Green function has poles over the real energy axis. This however can be drastically simplified by adding and subtracting the term $G_M^R \Gamma_R G_M^{R\dagger} f(E - \mu_L)$ to equation (1.44) to yield after some rearrangements

$$G_M^<(E) = i \left[G_M^R(E) (\Gamma_L + \Gamma_R) G_M^{R\dagger}(E) f(E - \mu_L) + G_M^R(E) \Gamma_R G_M^{R\dagger}(E) (f(E - \mu_R) - f(E - \mu_L)) \right]. \quad (1.53)$$

We can note that

$$\begin{aligned} \Gamma_L + \Gamma_R &= i \left[\Sigma_L^R - \Sigma_L^{R\dagger} + \Sigma_R^R - \Sigma_R^{R\dagger} \right] = \\ &= i \left[(-\epsilon S_M + H_M + \Sigma_L^R + \Sigma_R^R) - (-\epsilon S_M^\dagger + H_M^\dagger + \Sigma_L^{R\dagger} + \Sigma_R^{R\dagger}) \right] \\ &= i \left[(G_M^{R\dagger})^{-1} - (G_M^R)^{-1} \right]. \end{aligned} \quad (1.54)$$

Therefore, by substituting equation (1.54) into equation (1.53) we obtain

$$G_M^<(E) = - \left(G_M^R - G_M^{R\dagger} \right) f(E - \mu_L) + i G_M^R \Gamma_R G_M^{R\dagger} (f(E - \mu_R) - f(E - \mu_L)), \quad (1.55)$$

which in turn reduces to

$$G_M^<(E) = -2i \text{Im} [G_M^R] f(E - \mu_L) + i G_M^R \Gamma_R G_M^{R\dagger} (f(E - \mu_R) - f(E - \mu_L)).^{10} \quad (1.56)$$

Based on the new form of $G_M^<(E)$, it is now possible to rewrite the integral (1.43) as the sum of two contributions $D = D_{\text{eq}} + D_V$

$$D_{\text{eq}} = -\frac{1}{\pi} \int dE \text{Im} [G_M^R] f(E - \mu_L), \quad (1.57)$$

and

$$D_V = \frac{1}{2\pi} \int dE G_M^R \Gamma_R G_M^{R\dagger} [f(E - \mu_R) - f(E - \mu_L)]. \quad (1.58)$$

¹⁰Considering G_M^R to be a symmetric matrix.

D_{eq} can be interpreted as the density matrix at equilibrium, *i.e.* the one obtained when both the reservoirs have the same chemical potential μ_L , while D_V contains all the corrections due to the non-equilibrium conditions. Computationally, D_V is bound by the two Fermi functions of the leads, in similar fashion to the current I , and therefore one needs to perform the integration only in the energy range between the two chemical potentials (see figure (1.8a)). In contrast D_{eq} is unbound, but the integral can be performed in the complex plane using a standard contour integral technique [98], since G_M^R is both analytical [99] and smooth.¹¹ Despite being unbound, in the lower part of the energy axis the integral of equation (1.57) only requires the inclusion of all occupied states (those below the Fermi level) of the extended molecule and of the bands of the electrodes. At energies below a certain threshold, the integrand goes to zero quite quickly. Hence we can choose a finite value for the lower limit of integration ensuring all the available states below E_F are counted. The point denoted **EnergLowestBound** - a parameter of the calculation - in Fig. (1.8) indicates that limit.

The integration in all cases is performed using a Gaussian quadrature (Gauss-Legendre) method [100].

1.5 Spin polarised systems: Collinear versus non-collinear spins

The Green function method described in the previous section can be generalised to magnetic systems or to other systems where the spin degree of freedom has to be taken into consideration (open-shell systems). We consider two different cases. The first is when spin up (majority) and spin down (minority) electrons are completely decoupled from each other in the sense that there is no spin-flip. This is the case of collinear-spin systems and in transport theory is known as the “two-spin fluid” approximation [101]. In this situation, the Hamiltonian, overlap matrix and all other operators have the form

$$A = \left(\begin{array}{c|c} A^\uparrow & 0 \\ \hline 0 & A^\downarrow \end{array} \right), \quad (1.59)$$

where the A^σ block describes the spin σ sub-band.

¹¹In the same way, we could add and subtract a term $G_M^R \Gamma_L G_M^{R\dagger} f(E - \mu_R)$ to equation (1.43) and work through the algebra to obtain equations which are analogous to (1.57) and (1.58). In practice, numerical errors arise when calculating the Green function which might lead to slight differences in the density matrix calculated by these two methods. In order to minimise the effects of numerical errors we perform an average of the density matrices obtained in the two possible ways.

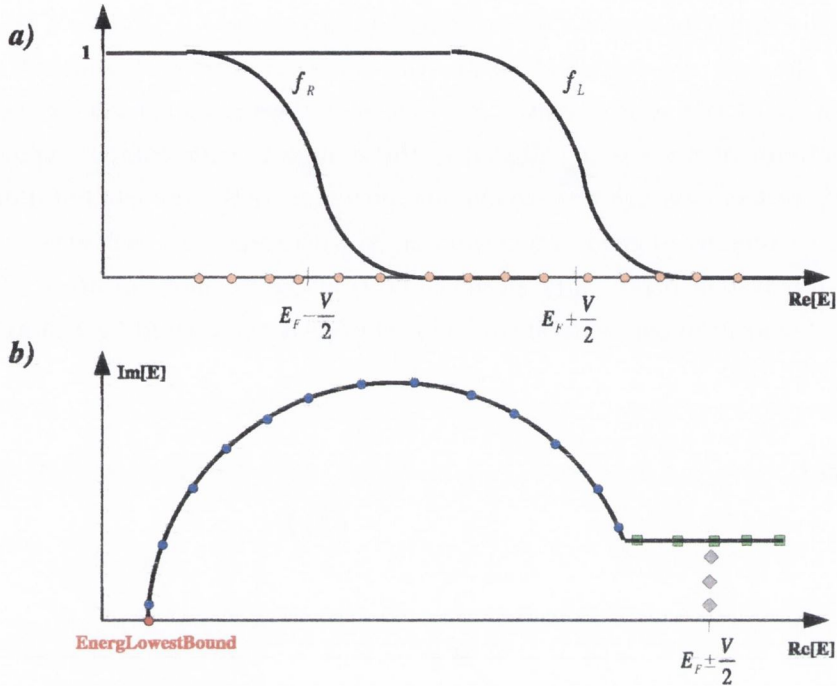


Figure 1.8: Diagram of the Green function integration leading to the non-equilibrium charge density. The non-equilibrium part must be performed along the real energy axis, but it is bound by the left- and right-hand side Fermi distribution functions, f_L and f_R . b) The integral for the equilibrium component is performed over a semicircular path in the complex energy plane. Here we show the lower limit of integration (below the lowest band of the electrodes), the energy mesh along the two segments of the curve and the poles of the Fermi distribution.

In this case we can work with two completely independent systems. Because majority and minority spins are effectively decoupled we can separate the two spins and calculate all quantities independently. The formalism described in section (1.4) still holds, but we need to introduce a new index which spans over the spin degree of freedom, σ . Operators such as the Hamiltonian, overlap matrix, Green function and density matrix are now written in the form

$$A_{ij}^{\sigma\sigma'} = A_{ij}^{\sigma\sigma'} \delta_{\sigma\sigma'} = A_{ij}^{\sigma} \quad (1.60)$$

Once convergence is achieved the total transmission and the total current are simply given by

$$T = \sum_{\sigma} T^{\sigma} = T^{\uparrow} + T^{\downarrow} \quad (1.61)$$

$$I = \sum_{\sigma} I^{\sigma} = I^{\uparrow} + I^{\downarrow}, \quad (1.62)$$

i. e., the contributions of the two spins add in parallel.

In the case we described above, the spins are always considered to be in an eigenstate of the spin operator S_z . We might want to consider cases where the magnetic moments are not aligned in the same way (non-collinear spins). In other words, we can envisage a situation where the magnetic moments of different atoms in our system are aligned at a certain angle with respect to each other. An example of such a system is presented in figure (1.9) where we show an array of atoms with a spiral-shaped magnetic moment. This is exactly the case in for example a domain wall [102, 103].

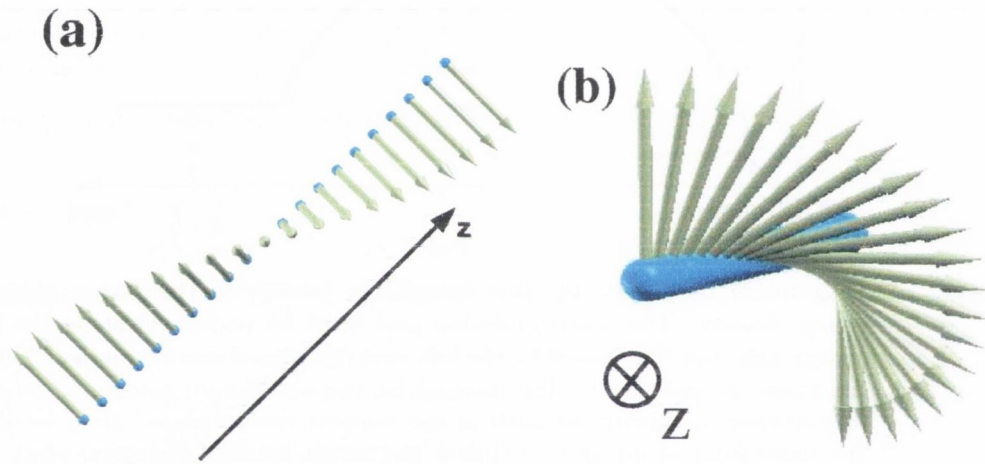


Figure 1.9: Infinite mono-atomic wire with arrows showing the direction of the magnetic moments for each atom. a) Diagonal and b) top views of the wire. Note that the magnitude of the spins are kept constant, but the magnetic moments are allowed to point in different directions.

In this case our operators have the following form ¹²

$$A = \begin{pmatrix} A^{\uparrow\uparrow} & A^{\uparrow\downarrow} \\ A^{\downarrow\uparrow} & A^{\downarrow\downarrow} \end{pmatrix} \quad (1.63)$$

The off-diagonal terms couple the up and down spins and are related to the angles between the magnetic moments.

Now, instead of working with different spins we use the NEGF formalism for a general spin direction. The total Hamiltonian has dimensions $2N \times 2N$. We can then define the Green function for this system in the form of equation (1.63),

$$G = \begin{pmatrix} G^{\uparrow\uparrow} & G^{\uparrow\downarrow} \\ G^{\downarrow\uparrow} & G^{\downarrow\downarrow} \end{pmatrix}, \quad (1.64)$$

¹²Except for the overlap matrix which still retains the form of equation (1.59).

where

$$G^{\uparrow\uparrow} = \begin{pmatrix} ES_L^{\uparrow} - H_L^{\uparrow\uparrow} - \Sigma_L^{\uparrow\uparrow} & ES_{LM}^{\uparrow} - H_{LM}^{\uparrow\uparrow} & 0 \\ ES_{ML}^{\uparrow} - H_{ML}^{\uparrow\uparrow} & ES_M^{\uparrow} - H_M^{\uparrow\uparrow} & ES_{MR}^{\uparrow} - H_{MR}^{\uparrow\uparrow} \\ 0 & ES_{RM}^{\uparrow} - H_{RM}^{\uparrow\uparrow} & ES_R^{\uparrow} - H_R^{\uparrow\uparrow} - \Sigma_R^{\uparrow\uparrow} \end{pmatrix}, \quad (1.65)$$

$$G^{\uparrow\downarrow} = \begin{pmatrix} -H_L^{\uparrow\downarrow} - \Sigma_L^{\uparrow\downarrow} & -H_{LM}^{\uparrow\downarrow} & 0 \\ -H_{ML}^{\uparrow\downarrow} & -H_M^{\uparrow\downarrow} & -H_{MR}^{\uparrow\downarrow} \\ 0 & -H_{RM}^{\uparrow\downarrow} & -H_R^{\uparrow\downarrow} - \Sigma_R^{\uparrow\downarrow} \end{pmatrix}, \quad (1.66)$$

$$G^{\downarrow\uparrow} = \begin{pmatrix} -H_L^{\downarrow\uparrow} - \Sigma_L^{\downarrow\uparrow} & -H_{LM}^{\downarrow\uparrow} & 0 \\ -H_{ML}^{\downarrow\uparrow} & -H_M^{\downarrow\uparrow} & -H_{MR}^{\downarrow\uparrow} \\ 0 & -H_{RM}^{\downarrow\uparrow} & -H_R^{\downarrow\uparrow} - \Sigma_R^{\downarrow\uparrow} \end{pmatrix}, \quad (1.67)$$

$$G^{\downarrow\downarrow} = \begin{pmatrix} ES_L^{\downarrow} - H_L^{\downarrow\downarrow} - \Sigma_L^{\downarrow\downarrow} & ES_{LM}^{\downarrow} - H_{LM}^{\downarrow\downarrow} & 0 \\ ES_{ML}^{\downarrow} - H_{ML}^{\downarrow\downarrow} & ES_M^{\downarrow} - H_M^{\downarrow\downarrow} & ES_{MR}^{\downarrow} - H_{MR}^{\downarrow\downarrow} \\ 0 & ES_{RM}^{\downarrow} - H_{RM}^{\downarrow\downarrow} & ES_R^{\downarrow} - H_R^{\downarrow\downarrow} - \Sigma_R^{\downarrow\downarrow} \end{pmatrix}. \quad (1.68)$$

By using the Green function defined in equation (1.64) we can apply equations (1.57) and (1.58) as we did in section (1.4) after redefining the self-energies as

$$\Sigma_L = \left(\begin{array}{ccc|ccc} \Sigma_L^{\uparrow\uparrow} & 0 & 0 & \Sigma_L^{\uparrow\downarrow} & 0 & 0 \\ 0 & 0 & 0 & 0 & 0 & 0 \\ 0 & 0 & 0 & 0 & 0 & 0 \\ \hline \Sigma_L^{\downarrow\uparrow} & 0 & 0 & \Sigma_L^{\downarrow\downarrow} & 0 & 0 \\ 0 & 0 & 0 & 0 & 0 & 0 \\ 0 & 0 & 0 & 0 & 0 & 0 \end{array} \right), \quad (1.69)$$

and

$$\Sigma_R = \left(\begin{array}{ccc|ccc} 0 & 0 & 0 & 0 & 0 & 0 \\ 0 & 0 & 0 & 0 & 0 & 0 \\ 0 & 0 & \Sigma_R^{\uparrow\uparrow} & 0 & 0 & \Sigma_R^{\uparrow\downarrow} \\ \hline 0 & 0 & 0 & 0 & 0 & 0 \\ 0 & 0 & 0 & 0 & 0 & 0 \\ 0 & 0 & \Sigma_R^{\downarrow\uparrow} & 0 & 0 & \Sigma_R^{\downarrow\downarrow} \end{array} \right). \quad (1.70)$$

Γ_L and Γ_R can be calculated in an analogous way.

Finally, the density matrix (equation (1.43)) and the current (Eq. (1.51)) can be calculated using the procedure described previously.

Finally, let us conclude this section with a note on the Spin-Orbit (SO) interaction. Spin-Orbit coupling is a relativistic correction to the Schrödinger equation [104, 105] which increases with atomic number. While for materials formed from light atoms such an effect is negligible, for heavier atoms it plays an increasingly important role. In the case of 3d transition metals for example it is the cause of magnetic

anisotropies [106] of the order of 10-100 μeV and in semiconductors it causes the edges of the valence and the conduction band to spin-split [107].

When we consider the SO effect the spin is no longer a good quantum number. In turn one needs to consider the total angular momentum \vec{J} ($\vec{J} = \vec{S} + \vec{L}$: the sum of spin and orbital angular momenta). In essence, the SO coupling leads to off-diagonal terms in the Hamiltonian in similar fashion to Eq. (1.63). Therefore, the formalism described so far can be naturally extended to include SO effects in the transport properties of nanostructures provided we can write a Hamiltonian for the scattering region [108].

Hence, we have shown that the NEGF method can be generalised to include periodic boundary conditions in the transverse direction. This is particularly useful when dealing with transport through surfaces and hetero-junctions.

1.6 Leads' self-energies

1.6.1 Surface Green's functions

Let us now return to the question of how to calculate the self-energies for the leads. From equations (1.34) and (1.35) it is clear that the problem is reduced to that of computing the retarded surface Green functions for the left- (G_L^{0R}) and right-hand side (G_R^{0R}) lead respectively. This does not require any self-consistent procedure since the Hamiltonian is known and it is equal to that of the bulk leads plus a rigid shift of the on-site energies. However the calculation should be repeated several times since the Σ 's are energy dependent. Therefore it is crucial to have a stable algorithm.

There are a number of techniques in the literature to calculate the surface Green functions of a semi-infinite system. These range from recursive methods [61, 109] to semi-analytical constructions [65]. Here we have generalised the scheme introduced by Sanvito *et. al.* [65] to non-orthogonal basis sets. This method gives us a prescription for calculating the retarded surface Green function exactly. The main idea is to construct the Green function for an infinite system as a summation of Bloch states with both real and imaginary wave-vectors, and then to apply the appropriate boundary conditions to obtain the Green function for a semi-infinite lead.

As explained in section (1.1) the Hamiltonian and the overlap matrices are arranged in a tridiagonal block form, having respectively H_0 and S_0 on the diagonal, and H_1 and S_1 as the first off diagonal blocks (see figure 1.10)). Since we are dealing with an infinite periodic quasi-one-dimensional system, the Schrödinger equation can

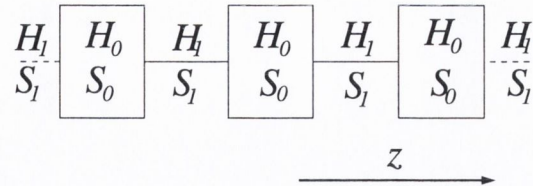


Figure 1.10: Infinite periodic system used as current/voltage probe and schematic diagram of the Hamiltonian. H_0 and S_0 are the matrices describing the Hamiltonian and the overlap within a PL, while H_1 and S_1 are the same quantities calculated between two adjacent PLs. The arrow indicates the direction of transport (here along the z axis).

be solved for Bloch states

$$\psi_z = n_k^{1/2} e^{ikz} \phi_k \quad (1.71)$$

and reads

$$[K_0 + K_1 e^{ik} + K_{-1} e^{-ik}] \phi_k = 0, \quad (1.72)$$

where $z = a_0 j$ with j integer and a_0 the separation between principal layers, k is the wave-vector along the direction of transport (in units of π/a_0), ϕ_k is a N -dimensional column vector and n_k a normalisation factor. Here we introduce the $N \times N$ matrices

$$K_0 = H_0 - ES_0, \quad (1.73)$$

$$K_1 = H_1 - ES_1, \quad (1.74)$$

$$K_{-1} = H_{-1} - ES_{-1}. \quad (1.75)$$

Since the Green's functions are constructed at a given energy our task is to compute $k(E)$ (both real and complex) instead of $E(k)$ as conventionally done in band theory. A numerically efficient method to solve the "inverse" secular equation $k = k(E)$ is to map it onto an equivalent eigenvalue problem. It is simple to demonstrate [65] that the eigenvalues of the following $2N \times 2N$ non-Hermitian matrix

$$M = \begin{pmatrix} -K_1^{-1}K_0 & -K_1^{-1}K_{-1} \\ I_N & 0 \end{pmatrix} \quad (1.76)$$

for a given energy E are $e^{ik(E)}$ and that the upper N components of the eigenvectors are the vectors ϕ_k . Clearly for the solution of this eigenvalue problem one needs to invert K_1 . However, since K_1 is determined by the details of the physical system, the choice of basis set and of principal layer may be singular or severely ill-conditioned. This problem often originates from the fact that a few states within a PL do not couple to states in the nearest-neighbouring PLs, but it can also be due to the symmetry

of the problem. For example in the case of *ab initio* derived matrices this becomes unavoidable when one considers transition metals, where the strongly localised *d* shells coexist with rather delocalised *s* electrons. A possible solution to this problem is to consider an equivalent *generalised* eigenvalue problem, which does not require matrix inversion. However this solution is not satisfactory for two reasons. First the matrices still remain ill-conditioned and the general algorithm is rather unstable. Secondly for extreme cases we have discovered that the generalised eigenvalue solver cannot return meaningful eigenvalues (divisions by zero are encountered when dealing with some “critical” closed-channel, *k* imaginary). We therefore decide to use an alternative approach constructing a regularisation procedure for eliminating the singularities of K_1 . This must be performed before starting the actual calculation of the Green functions. We will return on this aspect in section 1.6.2. For the moment we assume that K_1 has been regularised and it is neither singular nor ill-conditioned.

When using orthogonal basis sets the knowledge of *k* and $\{\phi_k\}$ is sufficient to construct the retarded Green function for the doubly-infinite system, which has the form [65]

$$G_{zz'} = \begin{cases} \sum_l^N \phi_{k_l} e^{ik_l(z-z')} \tilde{\phi}_{k_l}^\dagger V^{-1} & z \geq z' \\ \sum_l^N \phi_{\bar{k}_l} e^{i\bar{k}_l(z-z')} \tilde{\phi}_{\bar{k}_l}^\dagger V^{-1} & z \leq z' \end{cases}, \quad (1.77)$$

where the summation runs over both real and imaginary k_l . In equation (1.77) k_l (\bar{k}_l) are chosen to be the right-moving or right-decaying (left-moving or left-decaying) Bloch states, i.e. those with either positive group velocity or having *k*-vector with positive imaginary part (negative group velocity or negative imaginary part). $\{\phi_{k_l}\}$ are the corresponding vectors, and V is defined in reference [65]. Finally $\{\tilde{\phi}_{k_l}\}$ is just the dual of $\{\phi_{k_l}\}$ obtained from

$$\tilde{\phi}_{k_l}^\dagger \phi_{k_m} = \delta_{lm} \quad (1.78)$$

$$\tilde{\phi}_{\bar{k}_l}^\dagger \phi_{\bar{k}_m} = \delta_{lm} \quad (1.79)$$

$$(1.80)$$

In the case of a non-orthogonal basis set the same expression is still valid if V is now defined as follows

$$V = \sum_l^N \left(H_1^\dagger - E S_1^\dagger \right) \left[\phi_{k_l} e^{-ik_l} \phi_{k_l}^\dagger - \phi_{\bar{k}_l} e^{-i\bar{k}_l} \phi_{\bar{k}_l}^\dagger \right]. \quad (1.81)$$

Finally the surface Green functions for a semi-infinite system can be obtained from those of the doubly-infinite one by an appropriate choice of boundary conditions.

For instance if we subtract the term

$$\Delta_z(z' - z_0) = \sum_{l,h}^N \phi_{\bar{k}_h} e^{i\bar{k}_h(z-z_0)} \phi_{\bar{k}_h}^\dagger \phi_{k_l} e^{ik_l(z_0-z')} \phi_{k_l}^\dagger V^{-1}, \quad (1.82)$$

from $G_{zz'}$ of equation (1.77) we obtain a new retarded Green function vanishing at $z = z_0$. Note that $\Delta_z(z' - z_0)$ is a linear combination of eigenvectors (wavefunctions) and therefore does not alter the causality of G .

In this way we obtain the final expression for the retarded surface Green functions of both the left- and right-hand side lead

$$G_L^0 = \left[I_N - \sum_{l,h} \phi_{\bar{k}_h} e^{-i\bar{k}_h} \phi_{\bar{k}_h}^\dagger \phi_{k_l} e^{ik_l} \phi_{k_l}^\dagger \right] V^{-1}, \quad (1.83)$$

$$G_R^0 = \left[I_N - \sum_{l,h} \phi_{k_h} e^{ik_h} \phi_{k_h}^\dagger \phi_{\bar{k}_l} e^{-i\bar{k}_l} \phi_{\bar{k}_l}^\dagger \right] V^{-1}. \quad (1.84)$$

Once these operators have been calculated it is easy to obtain the self-energies from equations (1.34) and (1.35). These need to be computed at the beginning of the calculation only for a given energy mesh.

1.6.2 The “ K_1 problem”

The method presented in section (1.6.1) to calculate the leads Green’s functions depends crucially on the fact that the coupling matrix between principal layers $K_1 = H_1 - ES_1$ is invertible and not ill-defined. However this is not necessarily the case since singularities can be present in K_1 as the result of poor coupling between PLs or because of symmetry reasons. Note also that since $K_1 = H_1 - ES_1$ the rank of K_1 may also depend on the energy E .

We now give a few examples illustrating how these singularities arise. Let us consider for the sake of simplicity an orthogonal nearest neighbour tight-binding model with only one s -like basis function per atom. In this case $K_1 = H_1$ is independent of energy. In figure (1.11) we present four possible cases for which H_1 is singular, by no means the only ones. In the picture the dots represent the atomic position, the lines the bonds and the dashed boxes enclose a PL. All the bonds are assumed to have the same strength, thus all hopping integrals γ are identical.

In the first case (figure (1.11a)) the PL coincides with the primitive unit cell of the system and therefore it is the smallest principal layer that can be constructed. However since every second atom in the cell does not couple with its mirror in the

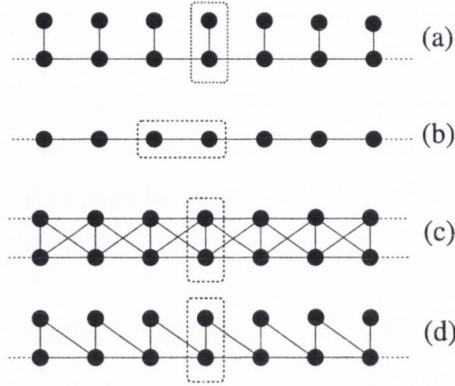


Figure 1.11: Four different structures for which H_1 is singular: (a) lack of bonding, (b) super-cell, (c) over-bonding, (d) odd bonding. Each black dot represents an atom and each line a bond. The dashed boxes enclose a principal layer.

two adjacent cells H_1 has the form

$$H_1 = \begin{pmatrix} \gamma & 0 \\ 0 & 0 \end{pmatrix} \quad (1.85)$$

and therefore is singular. This is the case of “lack of bonding” between principal layers. It is the most common case and almost always present when dealing with transition metals, since localised d shells coexist with delocalised s orbitals.

Figure (1.11b) presents a different possibility. Here the PL is a super-cell constructed from two unit cells and every atom in the PL couples with atoms located in only one of the two adjacent PLs. In this case

$$H_1 = \begin{pmatrix} 0 & 0 \\ \gamma & 0 \end{pmatrix}, \quad (1.86)$$

which is again singular. Clearly in this specific case one can reduce the principal layer into the primitive unit cell solving the problem (H_1 become a scalar γ). However in a multi-orbital scheme the super-cell drawn may be the smallest PL possible and the problem will appear. Again this is a rather typical situation when dealing with transition metals.

The case of “over-bonding” is shown in figure (1.11c). Again the PL coincides with the primitive unit cell, but now every atom in the PL is coupled to all the atoms in the two adjacent PLs. In this case

$$H_1 = \begin{pmatrix} \gamma & \gamma \\ \gamma & \gamma \end{pmatrix}, \quad (1.87)$$

which is not invertible either. This situation is usually driven by symmetry.

Finally the “odd-bonding” case is presented in figure (1.11d). Also in this case the PL coincides with the primitive unit cell, however the upper atom in the cell is coupled only to atoms in the right nearest neighbour principal layer. The H_1 matrix is then (we label as “1” the upper atom in the cell)

$$H_1 = \begin{pmatrix} 0 & \gamma \\ 0 & \gamma \end{pmatrix}, \quad (1.88)$$

i.e. it is also singular.

Clearly the above categorisation is basis dependent, since one can always find a unitary rotation transforming a generic H_1 in a new matrix of the form of equation (1.88).

1.6.3 Finding the singularities of K_1

We now present the first step of a scheme for regularising K_1 , and indeed the whole Hamiltonian and overlap matrix, by removing their singularities. In the cases of “lack of bonding”, “super-cell” and “odd-bonding” presented in the previous section the singularities of $K_1 = H_1$ were well defined since an entire column was zero. However more generally, and in particular in the case of multiple zetas basis set, K_1 is singular without having such a simple structure (for instance as in the “over-bonding” case). This is the most typical situation and a method for identifying the singularities is needed.

The ultimate goal is to perform a unitary transformation of both \mathcal{H} and \mathcal{S} in such a way that the off-diagonal blocks of the leads Hamiltonian and overlap matrix (H_1 and S_1) assume the form

$${}^N_{N-R} [0, A] = \begin{pmatrix} 0 & 0 & \cdots & A_{1,N-R+1} & \cdots & A_{1,N} \\ 0 & 0 & \cdots & A_{2,N-R+1} & \cdots & A_{2,N} \\ 0 & 0 & \cdots & A_{3,N-R+1} & \cdots & A_{3,N} \\ \vdots & \vdots & \vdots & \vdots & \vdots & \vdots \\ 0 & 0 & \cdots & A_{N,N-R+1} & \cdots & A_{N,N} \end{pmatrix}, \quad (1.89)$$

i.e. they are $N \times N$ block matrices of rank R , whose first $N - R$ columns vanish. In this form the problem is re-conducted to the problem of “odd-bonding” presented in the previous section.

This can be achieved by performing a generalised singular value decomposition (GSVD) [110]. The idea is that a pair of $N \times N$ matrices, in this case H_1 and S_1 , can be written in the following form

$$H_1 = U \Lambda_1 [0, W] Q^\dagger, \quad (1.90)$$

$$S_1 = V \Lambda_2 [0, W] Q^\dagger, \quad (1.91)$$

with U , V and Q unitary $N \times N$ matrices and W being a $R \times R$ non-singular triangular matrix where R is the rank of the $2N \times N$ matrix $\begin{bmatrix} H_1 \\ S_1 \end{bmatrix}$ ($R \leq N$). The matrices Λ_1 and Λ_2 are defined as follows:

$$\Lambda_1 = \begin{matrix} & & K & L \\ & & \left(\begin{array}{cc} I_K & 0 \\ 0 & C \end{array} \right) & \\ & K & & \\ & L & & \\ N-K-L & & \left(\begin{array}{cc} 0 & 0 \end{array} \right) & \end{matrix}, \quad (1.92)$$

$$\Lambda_2 = \begin{matrix} & & K & L \\ & & \left(\begin{array}{cc} 0 & C' \\ 0 & 0 \end{array} \right) & \\ & L & & \\ N-L & & & \end{matrix} \quad (1.93)$$

where L is the rank of S_1 , $K + L = R$, I_K is the $K \times K$ unit matrix and C and C' are $L \times L$ matrices to be determined.

Clearly the two matrices H_1 and S_1 have the two common generators W and Q . Then, one can perform a unitary transformation of both H_1 and S_1 by using Q , obtaining

$$H_1^Q = Q^\dagger H_1 Q = Q^\dagger U \Lambda_1 [0, W] = \begin{matrix} & N-R & R \\ N & \left[\begin{array}{cc} 0 & \bar{H}_1 \end{array} \right] & \end{matrix}, \quad (1.94)$$

$$S_1^Q = Q^\dagger S_1 Q = Q^\dagger V \Lambda_2 [0, W] = \begin{matrix} & N-R & R \\ N & \left[\begin{array}{cc} 0 & \bar{S}_1 \end{array} \right] & \end{matrix}. \quad (1.95)$$

Here \bar{H}_1 and \bar{S}_1 are the $N \times R$ non-vanishing blocks of the GSVD transformed matrices H_1 and S_1 respectively.

In an analogous way the same transformation for H_1^\dagger , S_1^\dagger , H_0 and S_0 leads to

$$H_1^{Q\dagger} = Q^\dagger H_1^\dagger Q = \begin{matrix} & N \\ N-R & \left[\begin{array}{c} 0 \\ \bar{H}_1^\dagger \end{array} \right] & \end{matrix} \quad (1.96)$$

$$S_1^{Q\dagger} = Q^\dagger S_1^\dagger Q = \begin{matrix} & N \\ N-R & \left[\begin{array}{c} 0 \\ \bar{S}_1^\dagger \end{array} \right] & \end{matrix} \quad (1.97)$$

$$H_0^Q = Q^\dagger H_0 Q, \quad (1.98)$$

$$S_0^Q = Q^\dagger S_0 Q, \quad (1.99)$$

where the transformed matrices H_0^Q and S_0^Q are not necessarily in the form of equation (1.89).

We are now in the position of writing the final unitary transformation for the total (infinite) Hamiltonian \mathcal{H} and overlap \mathcal{S} matrices describing the whole system (leads

plus extended molecule). These are given by $Q^\dagger \mathcal{H} Q$ and $Q^\dagger \mathcal{S} Q$ with the infinite matrix Q defined as

$$Q = \begin{pmatrix} \ddots & \cdot & \cdot & \cdot & \cdot & \cdot & \cdot & \cdot & \cdot & \cdot \\ \cdot & 0 & Q & 0 & \cdot & \cdot & \cdot & \cdot & \cdot & \cdot \\ \cdot & \cdot & 0 & Q & 0 & \cdot & \cdot & \cdot & \cdot & \cdot \\ \cdot & \cdot & \cdot & 0 & I_M & 0 & \cdot & \cdot & \cdot & \cdot \\ \cdot & \cdot & \cdot & \cdot & 0 & Q & 0 & \cdot & \cdot & \cdot \\ \cdot & \cdot & \cdot & \cdot & \cdot & 0 & Q & 0 & \cdot & \cdot \\ \cdot & \cdot & \cdot & \cdot & \cdot & \cdot & \cdot & \cdot & \cdot & \ddots \end{pmatrix}, \quad (1.100)$$

where I_M is the $M \times M$ unit matrix. Note that this unitary transformation rotates all the H_1 matrices (the S_1 matrices in the case of \mathcal{S}), but leaves H_M (S_M) unchanged. Finally the matrices coupling the extended molecule to the leads transform as follows

$$\begin{aligned} H_{LM}^Q &\rightarrow Q^\dagger H_{LM}, \\ H_{ML}^Q &\rightarrow H_{ML} Q, \\ H_{RM}^Q &\rightarrow Q^\dagger H_{RM}, \\ H_{MR}^Q &\rightarrow H_{MR} Q, \end{aligned} \quad (1.101)$$

and so do the corresponding matrices of \mathcal{S} .

1.6.4 Solution of the “ K^1 problem”

Now that both \mathcal{H} and \mathcal{S} have been written in a convenient form we can efficiently renormalise them out. The key observation is that the two (infinite) blocks describing the leads have now the following structure (the \mathcal{S} matrix has an analogous structure and it is not shown here explicitly)

$$\begin{aligned} \mathcal{H}_{L/R}^Q &= \begin{pmatrix} \ddots & \vdots & \vdots & \vdots & \vdots \\ \cdots & Q^\dagger H_0 Q & Q^\dagger H_1 Q & 0 & \cdots \\ \cdots & Q^\dagger H_{-1} Q & Q^\dagger H_0 Q & Q^\dagger H_1 Q & \cdots \\ \cdots & 0 & Q^\dagger H_{-1} Q & Q^\dagger H_0 Q & \cdots \\ \vdots & \vdots & \vdots & \vdots & \ddots \end{pmatrix} = \\ &= \begin{pmatrix} \ddots & \vdots & \vdots & \vdots & \vdots \\ \cdots & Q^\dagger H_0 Q & \begin{bmatrix} 0 & \bar{H}_1 \end{bmatrix} & 0 & \cdots \\ \cdots & \begin{bmatrix} 0 \\ \bar{H}_1^\dagger \end{bmatrix} & \begin{pmatrix} C & B \\ B^\dagger & D \end{pmatrix} & \begin{bmatrix} 0 & \bar{H}_1 \end{bmatrix} & \cdots \\ \cdots & 0 & \begin{bmatrix} 0 \\ \bar{H}_1^\dagger \end{bmatrix} & \begin{pmatrix} C & B \\ B^\dagger & D \end{pmatrix} & \cdots \\ \vdots & \vdots & \vdots & \vdots & \ddots \end{pmatrix}, \end{aligned} \quad (1.102)$$

where the matrices D , B and C are respectively $R \times R$, $N \times (N - R)$ and $(N - R) \times (N - R)$.

Note that the degrees of freedom (orbitals) contained in the block C of the matrix $H_0^Q = Q^\dagger H_0 Q$ couple to those of only one of the two adjacent PLs. This situation is the generalisation to a multi-orbital non-orthogonal tight-binding model of the “odd bonding” case discussed at the beginning of this section (figure 1.11d). These degrees of freedom are somehow redundant and they will be eliminated. We therefore proceed with performing Gaussian elimination [65] (also known as “decimation”) of all the degrees of freedom associated to all the blocks C .

The idea is that the Schrödinger equation $Q^\dagger[\mathcal{H} - ES]Q\Psi = 0$ can be re-arranged in such a way that a subset of degrees of freedom (in this case those associated to orbitals in a PL that couple only to one adjacent PL) do not appear explicitly. The procedure is recursive. Let us suppose we wish to eliminate the l -th row and column of the matrix $\mathcal{K}^Q = Q^\dagger[\mathcal{H} - ES]Q$. This can be done by re-arranging the remaining matrix elements according to

$$\mathcal{K}_{ij}^{Q(1)} = \mathcal{K}_{ij}^Q - \frac{\mathcal{K}_{il}^Q \mathcal{K}_{lj}^Q}{\mathcal{K}_{ll}^Q}. \quad (1.103)$$

The dimension of the resulting new matrix $\mathcal{K}^{Q(1)}$ (“1” indicates that one decimation has been performed) is reduced by one with respect to the original \mathcal{K}^Q . This procedure is then repeated and after r decimations we obtain a matrix

$$\mathcal{K}_{ij}^{Q(r)} = \mathcal{K}_{ij}^{Q(r-1)} - \frac{\mathcal{K}_{il}^{Q(r-1)} \mathcal{K}_{lj}^{Q(r-1)}}{\mathcal{K}_{ll}^{Q(r-1)}}. \quad (1.104)$$

Let us now decimate all the matrix elements contained in all the sub-matrices C . We obtain a new tridiagonal matrix $\mathcal{K}^{Q(\infty)}$ (“ ∞ ” means that an infinite number of decimations have been performed) of the form

$$\mathcal{K}^{Q(\infty)} = \begin{pmatrix} \cdot & \cdot & \cdot & \cdot & \cdot & \cdot & \cdot & \cdot & \cdot & \cdot & \cdot \\ 0 & \Theta^\dagger & \Delta & \Theta & 0 & \cdot & \cdot & \cdot & \cdot & \cdot & \cdot \\ \cdot & 0 & \Theta^\dagger & \Delta & T_1 & 0 & \cdot & \cdot & \cdot & \cdot & \cdot \\ \cdot & \cdot & 0 & T_1^\dagger & D_1 & K_{LM}^Q & 0 & \cdot & \cdot & \cdot & \cdot \\ \cdot & \cdot & \cdot & 0 & K_{ML}^Q & K_M & \Theta_{MR} & 0 & \cdot & \cdot & \cdot \\ \cdot & \cdot & \cdot & \cdot & 0 & \Theta_{RM} & D_2 & \Theta & 0 & \cdot & \cdot \\ \cdot & \cdot & \cdot & \cdot & \cdot & 0 & \Theta^\dagger & \Delta & \Theta & 0 & \cdot \\ \cdot & \cdot & \cdot & \cdot & \cdot & \cdot & 0 & \Theta^\dagger & \Delta & \Theta & 0 \\ \cdot & \cdot & \cdot & \cdot & \cdot & \cdot & \cdot & \cdot & \cdot & \cdot & \cdot \end{pmatrix}, \quad (1.105)$$

where $K_{LM}^Q = H_{LM}^Q - ES_{LM}^Q$, $K_{ML}^Q = H_{ML}^Q - ES_{ML}^Q$ and $K_M = H_M - ES_M$. The crucial point is that the new matrix $\mathcal{K}^{Q(\infty)}$ is still in the desired tridiagonal form, but now

the coupling matrices between principal layers Θ are not singular. These are now $R \times R$ matrices obtained from the decimation of the non-coupled degrees of freedom of the matrices K_1^Q . Moreover the elimination of degrees of freedom achieved with the decimation scheme is carried out only in the leads. The electronic structure of these is not updated during the self-consistent procedure for evaluating the Green's function, and therefore the information regarding the decimated degrees of freedom are not necessary. In contrast the degrees of freedom of the scattering region are not affected by the decimation or the rotation. Therefore the matrix K_M is unaffected by the decimation.

In the decimated matrix $\mathcal{K}^{Q(\infty)}$ new terms appear (D_1, D_2, T_1 and Θ_{MR}). These arise from the specific structure of the starting matrix $Q^\dagger[\mathcal{H} - ES]Q$ and from the fact that the complete system (leads plus scattering region) is not periodic. In fact assuming that j is the last principal layer of the left-hand side lead and l is the first layer of right-hand side lead, the decimation is carried out up to $j - 1$ to the left and starts from l to the right of the scattering region. This allows us to preserve the tridiagonal form of \mathcal{K} and at the same time to leave K_M unchanged. A schematic picture of the decimation strategy is illustrated in figure 1.12.

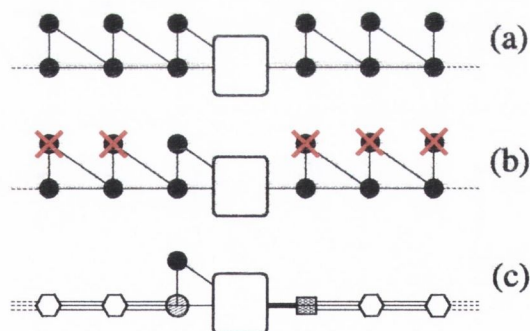


Figure 1.12: Schematic representation of the decimation strategy for the rotated \mathcal{K} matrix. Every symbol (dots, boxes ..) represents a collection of degrees of freedom (a matrix block) and every line the coupling. (a) Original structure after the rotation Q . In the periodic leads the upper black dots represent the blocks C of the matrix of equation (1.6.4). The large white rectangular box represents the scattering region. (b) The degrees of freedom marked with the red crosses are decimated. (c) Final structure after decimation. The new white symbols represent the leads degrees of freedom of the principal layers adjacent to the scattering region as they appear after the decimation.

In practical terms all the blocks of the infinite matrix of equation (1.105) can be calculated by decimating auxiliary finite matrices. In particular

1. Δ , Θ and D_2 are calculated by decimating both the C matrices of the following finite $2N \times 2N$ matrix

$$\left(\begin{array}{c|c} \left(\begin{array}{cc} C & B \\ B^\dagger & D \end{array} \right) & [0 \quad \bar{K}_1] \\ \hline \left[\begin{array}{c} 0 \\ \bar{K}_1^\dagger \end{array} \right] & \left(\begin{array}{cc} C & B \\ B^\dagger & D \end{array} \right) \end{array} \right) \longrightarrow \left(\begin{array}{cc} D_2 & \Theta \\ \Theta^\dagger & \Delta \end{array} \right), \quad (1.106)$$

where $\bar{K}_1 = \bar{H}_1 - E\bar{S}_1$ and

$$\left(\begin{array}{cc} C & B \\ B^\dagger & D \end{array} \right) = H_0^Q - ES_0^Q. \quad (1.107)$$

2. D_1 and T_1 are calculated by decimating only the upper C matrix of the same finite $2N \times 2N$ matrix

$$\left(\begin{array}{c|c} \left(\begin{array}{cc} C & B \\ B^\dagger & D \end{array} \right) & [0 \quad \bar{K}_1] \\ \hline \left[\begin{array}{c} 0 \\ \bar{K}_1^\dagger \end{array} \right] & \left(\begin{array}{cc} C & B \\ B^\dagger & D \end{array} \right) \end{array} \right) \longrightarrow \left(\begin{array}{cc} D_2 & T_1 \\ T_1^\dagger & D_1 \end{array} \right), \quad (1.108)$$

where D_1 is $N \times N$, while T_1 is $R \times N$.

3. Θ_{MR} is a $M \times R$ matrix obtained by decimating the C block of the following $(N + M) \times (N + M)$ matrix

$$\left(\begin{array}{c|c} 0_M & K_{MR}^Q \\ \hline K_{RM}^Q & \left(\begin{array}{cc} C & B \\ B^\dagger & D \end{array} \right) \end{array} \right) \longrightarrow \left(\begin{array}{cc} 0_M & \Theta_{MR} \\ \Theta_{RM} & D_2 \end{array} \right), \quad (1.109)$$

where 0_M is the M -dimensional null matrix.

Finally we are now in the position for calculating the self-energies. These are obtained from the surface Green's functions for the rotated and decimated leads (specified by the matrices Δ and Θ) and have the following form

$$\Sigma_L = K_{ML}^Q \left(-D_1 - T_1^\dagger G_L T_1 \right)^{-1} K_{LM}^Q \quad (1.110)$$

and

$$\Sigma_R = \Theta_{MR} [G_R^{-1} - (D_2 - \Delta)]^{-1} \Theta_{RM}. \quad (1.111)$$

Clearly our procedure not only regularises the algorithm for calculating the self-energies, giving it the necessary numerical stability, but also drastically reduces the degrees of freedom (orbitals) needed for solving the transport problem. These go

Albeit, it is clear that the diagonal part of the leads' Hamiltonians have a slightly different structure, a similar decimation procedure can be done on the total Hamiltonian. The resulting \mathcal{K}^Q is written using matrices calculated in analogous form. In practice:

1. Δ , Θ and D_2 are calculated by decimating both the C matrices of the following finite $2N \times 2N$ matrix

$$\left(\begin{array}{c} \left(\begin{array}{cc} C & B \\ B^\dagger & D \end{array} \right) \\ \left[0 \quad \bar{K}_1^\dagger \right] \end{array} \right) \left(\begin{array}{c} \left[\begin{array}{c} 0 \\ \bar{K}_1 \end{array} \right] \\ \left(\begin{array}{cc} C & B \\ B^\dagger & D \end{array} \right) \end{array} \right) \longrightarrow \left(\begin{array}{cc} \Delta & \Theta \\ \Theta^\dagger & D_2 \end{array} \right), \quad (1.117)$$

where $\bar{K}_1 = \bar{H}_1 - E\bar{S}_1$ and

$$\left(\begin{array}{cc} C & B \\ B^\dagger & D \end{array} \right) = H_0^Q - ES_0^Q. \quad (1.118)$$

2. D_1 and T_1 are calculated by decimating only the lower C matrix of the same finite $2N \times 2N$ matrix

$$\left(\begin{array}{c} \left(\begin{array}{cc} C & B \\ B^\dagger & D \end{array} \right) \\ \left[0 \quad \bar{K}_1^\dagger \right] \end{array} \right) \left(\begin{array}{c} \left[\begin{array}{c} 0 \\ \bar{K}_1 \end{array} \right] \\ \left(\begin{array}{cc} C & B \\ B^\dagger & D \end{array} \right) \end{array} \right) \longrightarrow \left(\begin{array}{cc} D_1 & T_1 \\ T_1^\dagger & D_2 \end{array} \right), \quad (1.119)$$

where D_1 is $N \times N$, while T_1 is $R \times N$.

3. Θ_{ML} is a $M \times R$ matrix obtained by decimating the C block of the following $(N + M) \times (N + M)$ matrix

$$\left(\begin{array}{c} \left(\begin{array}{cc} C & B \\ B^\dagger & D \end{array} \right) \\ K_{ML}^Q \end{array} \right) \left(\begin{array}{c} K_{LM}^Q \\ 0_M \end{array} \right) \longrightarrow \left(\begin{array}{cc} D_2 & \Theta_{LM} \\ \Theta_{ML} & 0_M \end{array} \right), \quad (1.120)$$

where 0_M is the M -dimensional null matrix.

It is easy to see that the self-energies for the system using this particular transformation are

$$\Sigma_L = \Theta_{ML} [G_L^{-1} - (D_2 - \Delta)]^{-1} \Theta_{LM}. \quad (1.121)$$

and

$$\Sigma_R = K_{MR}^Q \left(-D_1 - T_1^\dagger G_R T_1 \right)^{-1} K_{RM}^Q. \quad (1.122)$$

1.7 Conclusion

In this chapter we have presented a comprehensive description of the non-equilibrium Green function formalism applied to transport. We have shown how to describe the transport problem specially under the effects of an external applied bias. The Green function can be used to calculate the steady state charge density and a self-consistent procedure can be put in place provided the system's Hamiltonian is a functional of this charge density - or the density matrix.

We have also shown that it is not necessary to treat the entire open system, but on the contrary we can focus on the scattering region and add the effects of the electrodes in terms of self-energies which are only statically (non-self-consistently) affected by the external potential. These self-energies, specially in the case of localised d orbitals might be difficult to compute and singularities in the Hamiltonian usually arise. Using the generalised singular value decomposition (GSVD) with non-orthogonal basis sets we can pin point all the states which are uncoupled and an automatic regularisation procedure is used to remove such singularities. This final procedure is very robust and leads to the decimation of a large number of states which are not directly linked to the transport properties or the density matrix of the scattering region, but indirectly influence its calculation.

The procedure presented in this chapter is very general. In principle, one could use any Hamiltonian form to calculate the Green function. In the next chapter we will present an implementation of this method within density functional theory which provides a framework for calculating accurate electronic structures and hence precise electronic transport properties.

Chapter 2

Smeagol: Density Functional Theory and NEGF's

2.1 Introduction: The many-body problem

In solid state physics one is interested in systems comprising many atoms, and consequently many electrons. Therefore the description of the electronic structure of molecules and solids entails the correct characterisation of a large number of particles: electrons and nucleons. In all but a handful of cases the number of particles involved is prohibitive. In fact, the problem involving many electrons is unsolvable analytically, and exact numerical solutions are computationally feasible for a few electrons. As often is the case one must rely on approximations and ultimately on numerical methods to obtain the desired properties.

In many-particle systems one must solve an eigenvalue problem for the energy E in the form

$$\hat{\mathcal{H}}\Psi = E\Psi \quad (2.1)$$

where $\hat{\mathcal{H}}$ is the quantum mechanical Hamiltonian of the form:

$$\begin{aligned} \hat{\mathcal{H}} = & \sum_i^{N_e} \frac{-\hbar^2}{2m_e} \nabla_{\vec{r}_i}^2 + \sum_I^{N_N} \frac{-\hbar^2}{2M_I} \nabla_{\vec{R}_I}^2 + \frac{1}{2} \sum_{I \neq J}^{N_N} \frac{e^2 Z_I Z_J}{|\vec{\mathbf{R}}_I - \vec{\mathbf{R}}_J|} - \\ & - \frac{1}{2} \sum_{i,I}^{N_e, N_N} \frac{e^2 Z_I}{|\vec{\mathbf{r}}_i - \vec{\mathbf{R}}_I|} + \frac{1}{2} \sum_{i \neq j}^N \frac{Z e^2}{|\vec{\mathbf{r}}_i - \vec{\mathbf{r}}_j|}, \end{aligned} \quad (2.2)$$

where $\vec{\mathbf{x}}_i$ is the position operator for the i -th electron and $\vec{\mathbf{R}}_I$ the analogous position operator for I -th nucleus.¹ In equation (2.2), the first term represents the kinetic energy of the electrons of mass m_e , the second the kinetic energy of the nuclei - with

¹We consider the nucleus as a point charge $Z_I |e|$, with $|e|$ the electronic charge.

mass M_I ; the third the Coulomb interaction between different nuclei; the fourth, the electrostatic attraction between *nuclei* and electrons and finally the fifth term is the electron-electron interaction.

In most solid state problems N_e and N_N are of the order of 10^{23} - 10^{26} particles. Therefore the many-body wavefunction

$$\Psi = \Psi \left(\vec{x}_1, \vec{x}_2, \dots, \vec{x}_i, \dots, \vec{x}_{N_e}; \vec{X}_1, \vec{X}_2, \dots, \vec{X}_i, \dots, \vec{X}_{N_N} \right)^2 \quad (2.3)$$

is a function of an insurmountable number of variables.

In order to solve such a problem we must start by making a few assumptions that allow us to reduce the number of variables involved. The first assumption comes from the fact that the masses of the nuclei are much larger than those of the electrons. In that case we can assume that the Hamiltonian is separable. From a classical perspective this is equivalent to considering the nuclei to move at a much slower speed than the electrons. From the electrons' reference point they are almost stationary. Hence, one can separate the electronic wavefunction from that of the nuclei

$$\Psi = \Psi^e(\{\vec{x}_i\}) \times \Psi^N(\{\vec{X}_i\}). \quad (2.4)$$

Within this approximation (the Born-Oppenheimer approximation [105]) if one knows the positions of the nuclei, he will only need to worry about solving for the electronic part of the wavefunction. Hence, the Schrödinger equations (2.1) and (2.2) reduce to

$$\hat{\mathcal{H}}\Psi = [\hat{\mathcal{H}}^e + \hat{\mathcal{H}}^N] \Psi^e \Psi^N, \quad (2.5)$$

$$\hat{\mathcal{H}}^e \Psi^e = E(\{\vec{X}_i\}) \Psi^e, \quad (2.6)$$

$$\hat{\mathcal{H}}^e = \hat{T}_e(\{\vec{x}_i\}) + \hat{V}_{ee}(\{\vec{x}_i\}) + \hat{V}_{eN}(\{\vec{x}_i\}; \{\vec{X}_i\}), \quad (2.7)$$

where

$$\hat{T}_e(\{\vec{x}_i\}) = \sum_i^{N_e} \frac{-\hbar^2}{2m_e} \nabla_{\vec{r}_i}^2 \quad (2.8)$$

$$\hat{V}_{ee}(\{\vec{x}_i\}) = \frac{1}{2} \sum_{i \neq j}^N \frac{e^2}{|\vec{r}_i - \vec{r}_j|} \quad (2.9)$$

$$\hat{V}_{eN}(\{\vec{x}_i\}; \{\vec{X}_i\}) = -\frac{1}{2} \sum_{i,I}^{N_e, N_N} \frac{e^2 Z_I}{|\vec{r}_i - \vec{R}_I|}. \quad (2.10)$$

²Throughout this chapter we assume that the coordinates \vec{x}_i comprise both the position \vec{r}_i as well as the spin coordinates \vec{s}_i (\vec{X}_I , \vec{R}_I and \vec{I}_I respectively for the nuclei).

The total electronic energy $E(\{\vec{\mathbf{X}}_i\})$ is a function of the position of the nuclei and is calculated for a particular atomic configuration. Such configuration is usually obtained by calculating the atomic forces and relaxing their coordinates using classical equations of motion.

2.1.1 An attempt at solving the many-electron problem

Finding the solution of equation (2.6) is still far from being easy. The main difficulty comes from the second term in this equation, \hat{V}_{ee} . Because of this term the problem we cannot write the total many-electron wavefunction as a product of single-particle wavefunctions. In other words, it is not possible to separate the coordinates for each electron and to treat them separately.

One possibility of solving this problem comes from noting that the total electronic wavefunction must be anti-symmetric, since electrons are fermions. Therefore we can propose a solution which is an anti-symmetric product of single particle wavefunctions $\phi_i(\{\vec{\mathbf{x}}_j\})$.

$$\Psi_{HF}^e = \frac{1}{N!} \begin{vmatrix} \phi_1(\vec{\mathbf{x}}_1) & \phi_2(\vec{\mathbf{x}}_1) & \cdots & \phi_N(\vec{\mathbf{x}}_1) \\ \phi_1(\vec{\mathbf{x}}_2) & \phi_2(\vec{\mathbf{x}}_2) & \cdots & \phi_N(\vec{\mathbf{x}}_2) \\ \vdots & \vdots & & \vdots \\ \phi_1(\vec{\mathbf{x}}_N) & \phi_2(\vec{\mathbf{x}}_N) & \cdots & \phi_N(\vec{\mathbf{x}}_N) \end{vmatrix} = \frac{1}{N!} \det[\phi_i(\vec{\mathbf{x}}_j)]. \quad (2.11)$$

The method that uses the single Slater determinant of form (2.11) as a solution for the wavefunction is known as the Hartree-Fock method [105, 111]. The basis functions $\{\phi_i(\{\vec{\mathbf{x}}_j\})\}$ are usually written in terms of linear combinations of Gaussian-type orbitals, *i. e.* localised orbitals. These orbitals are then used to calculate the minima of

$$\delta \left\{ \langle \Psi^e | \hat{\mathcal{H}}^e | \Psi^e \rangle - E \langle \Psi^e | \Psi^e \rangle \right\} = 0. \quad (2.12)$$

The equation (2.12) expresses the variational principle over the energy [112].

If a system is periodic, Bloch's theorem [93] significantly reduces the number of degrees of freedom of the problem. However, in large scale electronic structure calculations and in particular in molecular electronics problems Hartree-Fock methods can be extremely expensive in computational terms. The size of a Hartree-Fock calculation increases with N^5 , where N is the system size (the number of basis functions).³ The largest computational overhead is related to the calculation of the Fock

³There are other drawbacks inherent to Hartree-Fock calculations, such as the poor description of single-particle states and the complete absence of electron correlations [111].

matrix, the many-body Hamiltonian of a system of N identical particles [105]. On the one hand the use of Slater- or Gaussian-type orbitals reduces this computational overhead since many of the single and two-body integrals may be performed analytically. On the other hand, the number of Gaussian functions necessary for a good description of each orbital is relatively large.

An extension to the Hartree-Fock method is an approach known as Configuration Interaction [113], where an appropriate linear combination of Slater determinants is used, including a number of orbitals describing excited states. However, wavefunction-based methods such as these are prohibitively expensive except for relatively small systems. In large scale atomic calculations where one deals with hundreds or perhaps thousands of atoms, and where translational symmetry may be broken, a new approach is required; a formulation of quantum mechanics that significantly reduces the number of variables, but still enables us to calculate electronic properties with high degrees of accuracy.

2.2 Density Functional Theory

One possible way of tackling the many-body problem in terms of one particle wave functions is offered by Density Functional Theory (DFT) [111, 114]. In 1964, Hohenberg and Kohn [77] demonstrated a theorem in which the problem of finding the many-body wavefunction is reduced to that of calculating the equilibrium charge density $n(\vec{x})$. The Hohenberg-Kohn theorem states that the ground-state energy E of an N -electron system is an unique functional of the charge density n ,

$$E = E[n] = \hat{T}[n] + \hat{V}_{\text{ext}}[n] + \hat{V}_{Ne}[n] + \hat{V}_{ee}[n], \quad (2.13)$$

where we define the charge density n as

$$n^{\sigma_1}(\vec{r}_1) = N_e \int |\Psi^e(\vec{x}_1, \vec{x}_2, \dots, \vec{x}_{N_e})|^2 d\sigma_2 d\sigma_3 \dots d\sigma_{N_e} d\vec{r}_2 d\vec{r}_3 \dots d\vec{r}_{N_e}, \quad (2.14)$$

$$n(\vec{r}) = \int n^\sigma(\vec{r}) d\sigma = n^\uparrow(\vec{r}) + n^\downarrow(\vec{r}) \quad (2.15)$$

provided

$$\langle \Psi^e | \Psi^e \rangle = 1 \quad (2.16)$$

and

$$\int n^\sigma(\vec{r}) d\sigma d\vec{r} = N_e. \quad (2.17)$$

Moreover, the ground state density minimises such a functional.

The four terms on the right hand-side of equation (2.13) make up for the kinetic energy \hat{T} , the external applied electric field \hat{V}_{ext} as well as the electron-nucleus and electron-electron interaction (\hat{V}_{eN} and \hat{V}_{ee} respectively).

Once the ground state charge density has been determined all ground-state quantities describing the system, such as the many-particle wavefunction are also univocally determined.

It is interesting to note that DFT is a completely novel formulation of quantum mechanics. Previously one would consider either the Hamiltonian or the Lagrangian formulations. In the former case, the wavefunction is the quantity sought. This could be obtained by either solving the wave equation (Schrödinger's formalism) or by diagonalising a Hamiltonian and solving the eigenvalue problem (Heisenberg). In the later case, the Lagrangian formulation, one seeks to minimise the action in order to find the propagation of a particular state. Both formulations have been shown by Feynman to be equivalent [115].

For time-independent problems⁴ DFT provides yet another approach where the main quantity we are interested in is the classical electron charge density. In this case the number of parameters involved is reduced to three (the value of the charge density in real-space) whereas in the two cases discussed above one needs to deal with the coordinates of each particle.

Hence, if the density functional is known we will be able to solve the variational problem for the electron density and obtain all the ground-state properties of our system. Unfortunately, the exact functional is not known and the Hohenberg-Kohn theorem alone does not provide a procedure on how to find the ground state charge density. Therefore one must rely on approximations.

In 1965, Kohn and Sham [78] assumed that the problem of finding the ground state charge density can be mapped onto that of solving a set of single particle Schrödinger-like equations:

$$\left[-\frac{\hbar^2}{2m} \nabla^2 + V_{\text{eff}}(\vec{\mathbf{x}}) \right] \psi_i(\vec{\mathbf{x}}) = \epsilon_i \psi_i(\vec{\mathbf{x}}). \quad (2.18)$$

The set of eigen-states $\{\psi_i\}$ which are solutions to the above eigenvalue problem are known as Kohn-Sham states. The effective potential V_{eff} corresponds to the effective single particle potential seen by an electron due to its interaction with the

⁴An analogous version to the Hohenberg-Kohn theorem was developed to include time-dependent potentials. This is known as the Runge-Gross theorem [116]. This way one can calculate optical excitations in atoms and molecules in the adiabatic limit [117].

other $N - 1$ Kohn-Sham states.⁵ This potential is defined as

$$V_{\text{eff}}(\vec{x}) = V(\vec{x}) + V_H(\vec{x}) + V_{XC}(\vec{x}). \quad (2.19)$$

The first term in equation (2.19) is the external potential and includes the potential originating from the nuclei as well as an external applied electric field if present. The term V_H corresponds to the classical Coulomb potential (Hartree potential) for an electron density $n(\vec{r})$. This term is obtained by solving the Poisson equation for the scalar potential

$$-\nabla^2 V_H(\vec{r}) = n(\vec{r}). \quad (2.20)$$

Finally,

$$V_{XC}(\vec{x}) = \frac{\delta E_{XC}}{\delta n} \quad (2.21)$$

is the exchange-correlation potential defined as the functional derivative of the exchange-correlation energy, E_{XC} with respect to the electron density. This last term contains all the remaining contributions to the potential that we do not know exactly. Finally, the total energy of the system is given by the sum over all the occupied states of the Kohn-Sham (KS) single particle energies ϵ_i up to the total number of electrons N_e ,

$$E_{\text{Tot}} = \sum_i^{N_e} \epsilon_i. \quad (2.22)$$

Consequently we define the Fermi energy for this system as the highest occupied Kohn-Sham eigenvalue, ϵ_{N_e} . Furthermore one can generalise equation (2.22) to include temperature

$$E_{\text{Tot}} = \sum_i f(\epsilon_i - E_F) \epsilon_i \quad (2.23)$$

with the Fermi distribution f defined in (1.17).

The Kohn-Sham eigenfunctions $\{\psi_i(\vec{x})\}$ can be used to calculate n ,

$$n(\vec{r}) = \sum_i^{\text{occupied}} |\psi_i(\vec{r})|^2 = \sum_i |\psi_i(\vec{r})|^2 f_i, \quad (2.24)$$

where f_i is the occupation number ($0 \leq f_i \leq 1$) and provided that

$$\langle \psi_i | \psi_i \rangle = 1. \quad (2.25)$$

The solutions of the Kohn-Sham equations in principle give the ground state properties of the system. However, the term described in equation (2.21) is not know

⁵In practice, "standard" DFT methods also include spurious interactions of the electron with its own charge density. This effect is know as the self-interaction (SI) and can be important for strongly-correlated systems [86].

exactly and some kind of approximation is needed. The two types of approximations which are generally used are the local density approximation⁶⁷ (LDA) [78, 118] and the generalised gradient approximation (GGA) [119, 120, 121]. In the first case, one considers E_{XC} to be that of a uniform electron gas of the partial density $n(\mathbf{r})$. Within this approximation, the exchange and correlation energy is given by

$$E_{XC}^{LSDA} = \int d^3r n(\mathbf{r}) e_{xc}(n^\uparrow, n^\downarrow), \quad (2.26)$$

where e_{xc} is the exchange-correlation energy density (energy per unit volume) for a uniform electron gas [122, 123]. In equation (2.26) we take the more general spin polarised case by introducing different charge populations for spin *up* (\uparrow) and spin *down* (\downarrow) whereby the total charge density is defined as the sum of the two (Eq. (2.15)).

The second case is an extension of the former and introduces terms depending on the gradient of the charge density. One of the forms used for V_{XC} in GGA is the Perdew-Burke-Ernzerhof (PBE) form [121]

$$E_{XC}^{GGA} = \int d^3r \mathcal{F}(n^\uparrow, n^\downarrow, \nabla n^\uparrow, \nabla n^\downarrow) \quad (2.27)$$

Note that both LDA and GGA are local approximations while the exact exchange-correlation potential may be non-local.

These choices of V_{XC} have been widely used in a variety of problems ranging from semi-conductors to metals, from solids to molecules. Today, density functional theory is widely employed in the description of bulk materials and molecules in physics, chemistry, biology and even geology. These approximations usually yield reasonably good bond lengths. In particular, GGA is widely used in chemistry to calculate bond lengths in organic molecules and reaction paths with great success [124, 125].

While in the chemical sciences GGA consistently gives more accurate results the same is not true in physics and materials science. In some cases, albeit being a cruder approximation, LDA results compare better to experiments (usually in the case of simple metals where the density is uniform).

Finally, we end this section with a few notes on the Kohn-Sham orbitals, the eigenstates $\psi_i(\mathbf{r})$ of equation (2.18). Strictly speaking, these orbitals are not single-particle states. Therefore they can not be interpreted as molecular orbitals of our

⁶⁷Local spin density approximation (LSDA) in the case of spin polarised systems.

⁷Recently the issue of uniqueness of the spin-polarised LDA (LSDA) potentials has come into question, although the uniqueness is recovered in the case of non-collinear spins. It is not the aim of this work to discuss these issues here. The reader should refer to [?, ?] and references therein.

many-body problem. Moreover, DFT, as mentioned earlier, is a ground state theory. Despite these claims, the calculation of band structures, both conduction and valence, and molecular energy levels using DFT-based Hamiltonians is widespread in the scientific community and in many cases, it yields accurate results. Therefore, one must always be aware of such limitations when dealing with DFT calculations.

To a large extent the electronic transport properties of nanoscopic systems is determined by three factors: the band structure of the electrodes, the position of the energy levels of the scattering region and the level alignment between the two. Therefore, we can, for practical purposes associate the accuracy of a transport calculation using DFT Hamiltonians to the accuracy of band structure calculations and/or molecular energy levels.

2.2.1 Limitations of LDA and GGA

Despite the success of density functional theory and the reasonably accurate descriptions obtained using LDA and GGA there are a number of problems for which these approximations fail. In some cases the discrepancies between experimentally obtained properties and DFT calculations are so large that they hinder even a qualitative analysis of the results. One of the most notorious cases is that of the transition metal oxides. Take for example the case of bulk nickel oxide (NiO). LDA calculations yield a metallic ground state whereas experiments show that it is an anti-ferromagnetic Mott insulator [126]. Figure (2.1) shows the real magnetic configuration of NiO in the rock-salt structure. In the ground state AF2 magnetic phase atoms align ferromagnetically within [111] planes and antiferromagnetically between the planes.

In both LDA and GGA, the exchange-correlation potential is a local functional of the charge density. Furthermore, they are accurate when the charge density is a smoothly varying function. Hence, for systems where strong correlation effects are important, *i. e.*, where the charge density changes sharply, these approximations most likely fail.

Anisimov *et al.* [127, 128] proposed a correction, based on the Hubbard model. The general idea is to correct for localisation effects by replacing the LDA XC energy with the Hubbard- U energy (a function of the Coulomb repulsion parameter U and the exchange parameter J) that depends on the orbital occupations. The authors postulated the correction which needs to be added to the total LDA energy

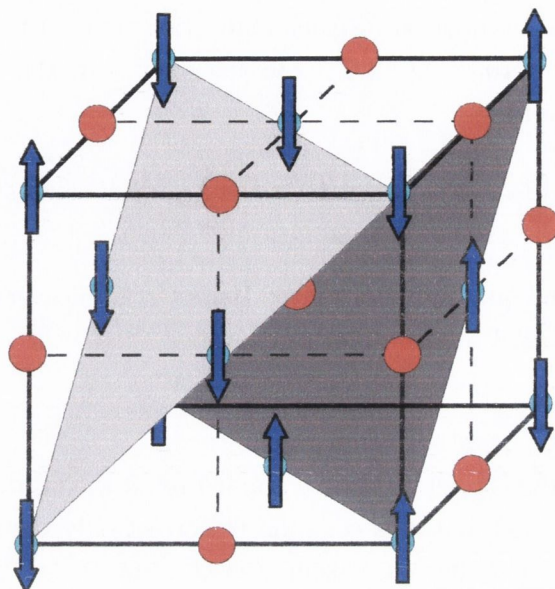


Figure 2.1: Schematic representation of rock-salt NiO in the AF2 anti-ferromagnetic configuration. The oxygen atoms are represented as red spheres and the Ni atoms as blue arrows pointing in the direction of the local magnetisation. The Ni atoms are ferromagnetically aligned within the $[111]$ planes of the structure whereas the coupling between planes is anti-ferromagnetic.

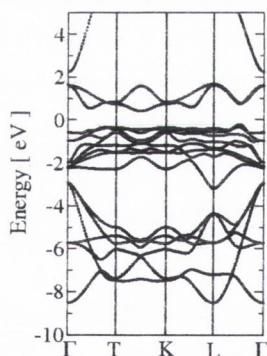


Figure 2.2: Band structure of bulk NiO using density functional theory in the local spin density approximation in the AF2 magnetic configuration. Majority and minority spin bands are identical.

$$\begin{aligned} \Delta E = & \frac{1}{2} \sum_{m,m',\sigma} U n_{m\sigma} n_{m'-\sigma} + \frac{1}{2} \sum_{m,m',\sigma} (U - J) n_{m\sigma} n_{m'\sigma} - \\ & U [N^\uparrow (N^\uparrow - 1) / 2 + N^\downarrow (N^\downarrow - 1) / 2 + N^\uparrow N^\downarrow] + \\ & J [N^\uparrow (N^\uparrow - 1) / 2 + N^\downarrow (N^\downarrow - 1) / 2], \end{aligned} \quad (2.28)$$

where N^\uparrow (N^\downarrow) is the total number of spin-up (spin-down) electrons and $n_{m\sigma}$ is

the self-consistent occupation for each state with spin σ ($\sigma = \uparrow, \downarrow$) and m quantum number (for d shells $m = \{-2, 2\}$). In the same way, the correction to the LDA potential is of the form

$$\Delta V_{m\sigma} = U \sum_{m'} (n_{m'-\sigma} - n_{-\sigma}^0) + (U - J) \sum_{(m \neq m')} (n_{m'\sigma} - n_{\sigma}^0) + (U - J) \left(\frac{1}{2} - n_{\sigma}^0 \right) \quad (2.29)$$

for each spin σ and quantum number m . Here n_{σ}^0 is the average orbital occupations of the correlated shell

$$n_{\sigma}^0 = \frac{1}{2l+1} N^{\sigma}, \quad (2.30)$$

and l is the orbital quantum number [129].

In principle, the correction can be applied to all the orbitals (in that case U and J would be matrices), but it is common to correct only the more localised orbitals such as the d and f shells. As Anisimov *et al.* note, U does not correspond exactly to the atomic Hubbard U term [130], because it also should include screening effects in the solid.

This method is usually referred to as the LDA+ U method and depends on two parameters U and J which are usually fitted, *i. e.*, they are inputs to any calculation. Hence, one could claim that computations using a LDA+ U functional are no longer fully *ab initio*. However, a physically appropriate choice of parameters leads to a good description of the electronic properties of strongly correlated materials such as the transition metal oxides.

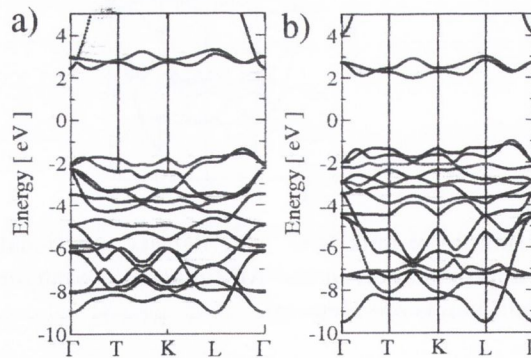


Figure 2.3: Band structure of bulk NiO using LSDA in the AF2 configuration using a) LDA+ U and b) ASIC. In the antiferromagnetic case majority and minority band structures are identical.

An *ab initio* method for correcting the localised states comes in the form of self-interaction correction [122]. The effective potential (Hartree and exchange-correlation potentials) of equation (2.18) in both LDA and GGA include an integral

over the charge density. Therefore the effective potential seen by an electron includes the contributions of all the other electrons, but it also includes interactions with itself (the self-interaction). Perdew and Zunger [122] proposed a scheme for removing the contribution coming from the electron's SI by using the Kohn-Sham orbitals. This approach works well for molecules, however, in the limit of infinite systems, such as solids, such correction should go to zero (the self-interaction of a Bloch state vanishes for $N \rightarrow \infty$).⁸

A novel approach was proposed by Filippetti and Spaldin [131] where the correction is introduced as atomic corrections instead, an approximation that reduces the computational overhead and in the case of solids gives quantitatively satisfactory results [86]. Hereafter we shall refer to this approach as Atomic-SIC (ASIC). In both the cases of the Perdew-Zunger method as well as ASIC, there are no phenomenological parameters and it is a fully first-principles approach.

In figure (2.3) we show the results for the LDA+U ($U = 8$ eV and $J = 1$ eV) and ASIC methods. We can clearly see that in both cases the gap opens with respect to the LDA gap in the anti-ferromagnetic case (approximately 4 eV), and gets closer to experimental observations.

There are also functionals, where part (B3LYP) or all (EXX) of the exchange term from the Hartree-Fock method replaces the LDA term (keeping the correlation term intact). For a review see [112] and references therein.

2.2.2 The calculation of the Kohn-Sham states

So far we have not discussed the method for calculating the Kohn-Sham states ψ_i . One possible approach is to directly solve the Schrödinger-like Kohn-Sham wave equation (2.18) using a real-space approach [117, 132], *i. e.*, writing the wavefunction and Hamiltonian over some numerical grid.

Another possibility is to write the Kohn-Sham orbitals over a given basis set. Using a linear combination of basis functions the problem reduces to that of finding the expansion coefficients that minimise equation (2.18). One possible choice of basis set is a combination of plane waves [133]

$$\psi_i(\vec{r}) = \sum_{\mathbf{k}} A_i^{(\mathbf{k})} e^{\mathbf{k} \cdot \vec{r}}. \quad (2.31)$$

⁸In practice, for solids, the Perdew-Zunger approach over-corrects band gaps and other electronic properties of the system.

⁹The reader should be aware that the \mathbf{k} vectors presented in equation (2.31) are not the momentum quantum numbers arising from Bloch's theorem for translationally invariant systems.

where usually one sums over as many \mathbf{k} vectors as one deems necessary to appropriately describe ψ_i . Plane-waves might seem a natural since it is equivalent to a complex Fourier expansion of the real-space wavefunction. Due to this property the problem can be treated in reciprocal space using many of the properties of Fourier transforms [134]. In addition, the availability of the fast Fourier transform algorithm [100] makes calculations rather efficient in practice. Moreover, there is only one parameter controlling the quality of the basis set namely the maximum number of \mathbf{k} vectors used. This obviously depends on the specific calculation and varies according to the system under study. The larger the number of vectors the more accurate the calculation, but also the more memory and numerically intensive it is.

A drawback of using plane-waves is its requirement of a large number of basis functions in order to describe localised states. Moreover, plane-wave codes describe the vacuum (a region where there is no charge density) on the same footing as the molecule. Hence, calculations of large scale molecular systems is hindered in plane-wave numerical implementations of DFT.

A possible way around this problem is that of using a localised basis. These can be Gaussian- or Slater-type orbitals or they can be made to resemble even more an atomic character. The KS orbitals are expanded as

$$\psi_i(\vec{\mathbf{r}}) = \sum_l c_l^i \phi_l(\vec{\mathbf{r}}) \quad (2.32)$$

where $\{\phi_l(\mathbf{r})\}$ is a set of functions with an atomic character. For example, for a H_2 molecule we would choose our basis functions as the solutions of the isolated atom centred on both hydrogens.

There are a number of advantages in using a localised basis set. One of these is that the range of interaction is finite, consequently Hamiltonian matrix elements go to zero for orbitals that are far apart. Therefore the Hamiltonian and overlap matrix, $S_{ij} = \langle \phi_i | \phi_j \rangle$ become relatively sparse saving memory and computer time.

Another important point will be discussed in section (2.4). The Hamiltonian and Overlap matrices in a localised basis representation are in a tight-binding-like form, very much the form needed by the NEGF formalism presented in chapter 1.

This choice of basis set is exactly the one made in SIESTA (Spanish Initiative for Electronic Structure Calculations with Thousands of Atoms) [40, 135], our DFT program of choice for electronic structure calculations.

2.3 The SIESTA code

There are a number of robust packages already available for doing DFT calculations. It is not the scope of this project to produce a new package for DFT, but possibly to introduce changes to an existing one in order to allow us to perform non-equilibrium transport calculations. The SIESTA code [40] appears as a reasonable choice because it is based on a localised basis set and it is readily available. It is important to note, however, that the NEGF framework (and in particular our implementation of it) is more general, *i. e.*, it does not depend on the choice of DFT package. In fact, the Hamiltonian used need not be the one originating from DFT, it could for example be a tight-binding Hamiltonian [70] or even a many-body one [?, ?]. On the other hand, the Kohn-Sham Hamiltonian seems like a natural choice because the total energy and the Hamiltonian are written in terms of the charge density and consequently the density matrix, a quantity that is readily available in the NEGF formalism (equation (1.43)). Furthermore, a DFT implementation based on an LCAO basis set is consistent with the derivation of NEGF described in chapter 1.

The basis set in SIESTA is a numerical basis obtained by solving the Schrödinger equation of the isolated atom immersed in a hard-wall potential. It reads

$$\phi_{n,l,m}(r, \theta, \varphi) = R_{n,l}(r) Y_{l,m}(\theta, \varphi) \quad (2.33)$$

where $R_{n,l}$ is the radial function for orbital n and $Y_{l,m}$ is the real spherical harmonic for the orbital angular momentum l and magnetic quantum number m .¹⁰ The radial part of the wave function satisfies the normalisation relation

$$\int |R_{n,l}(r)|^2 r^2 dr = 1. \quad (2.34)$$

Most of the time, we are interested in the properties stemming only from the outermost electrons in the atom.¹¹ One possible approximation is to separate the core electrons (the electrons closest to the nucleus) from the valence electrons. In that case, the potential as seen from the valence electrons is that of the nucleus screened by the core electrons. The so called pseudopotential [136] is not only much smoother than the all-electron potential (it does go as $1/r$ for $r \rightarrow 0$), but it also enables us to focus on a reduced number of particles for our problem. Hence, the basis set $\{\phi_i\}$ where $i = \{n, l, m\}$, characterises only a subset of electrons in a given

¹⁰Both the radial and angular parts of the wavefunctions are real, hence so is the basis function ϕ .

¹¹One can consider that the bonding, electronic and transport properties of materials are mostly influenced by valence electrons.

atom, for example 3d and 4s in Nickel. The remaining electrons are accounted for in the pseudopotential [136].

The pseudopotential is initially written in semi-local form (a different radial potential for each angular momentum) and then it is transformed to its full non-local form as proposed by Kleinman and Bylander [137].

In order to achieve the necessary variational freedom, one can also include empty orbitals (say 4p in Ni). Moreover SIESTA also includes the possibility of using a multiple- ζ basis set. Each ζ orbital retains the same spherical harmonics as the original atomic orbital, but the radial form is given by a new function constructed with the split-valence method [138]. Using this method, the radial part of our second- ζ retains the tail of the first- ζ outside a split-radius r_l^s and has a polynomial form inside:

$$R_{n,l}^{2\zeta} = \begin{cases} r^l (a_l - b_l r^2) & \text{if } r < r_l^s \\ R_{n,l}^{1\zeta}(r) & \text{if } r \geq r_l^s \end{cases} \quad (2.35)$$

The constants a_l and b_l are determined by matching the wavefunction and its first derivative.

The opposite is also possible. The radial function $R(r)_{n,l}$ remains unchanged while one takes the spherical harmonics with higher orbital angular momentum. These are known as polarised orbitals.¹²

$$\phi_{n,l',m} = R_{n,l} Y_{l+1,m}, \quad (2.36)$$

with $-(l+1) < m < l+1$. These extra basis functions enlarge the variational freedom in the minimisation procedure and allow one to construct basis functions with an angular momentum larger than the largest allowed by the pseudopotential. Usually, the dimension of the basis set is larger than the total number of electrons (in the case the number of basis functions equals that of valence electrons we talk about the “minimal” basis function).

Figure (2.4) shows the radial part of different basis functions for a Ni atom. We can clearly see that the wavefunctions go to zero for $r > r_c$, the cutoff radius.¹³ This property ensures the sparsity of the Hamiltonian.

The overlap matrix is defined as

$$S_{ij} = \int d\vec{r} \phi_i(\vec{r} - \vec{\mathbf{R}}_I) \phi_j(\vec{r} - \vec{\mathbf{R}}_J) \quad (2.37)$$

¹²The corrections to the basis function due to a constant electric field in first order perturbation theory will only have angular momentum components $l' = l \pm 1$. These polarised orbitals help to account for changes in the orbitals due to bond formation.

¹³The cutoff radius r_c can be different for each orbital.

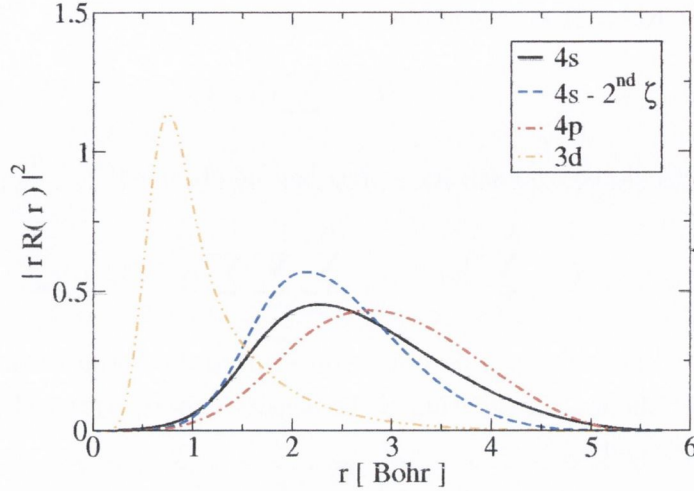


Figure 2.4: Numerical localised atomic orbital basis set for Ni generated by SIESTA. For $r > r_c$ the cutoff radiae, the basis functions go to zero.

with $i = \{i', I\}$, $j = \{j', J\}$ and $\vec{\mathbf{R}}_I$ is the position of the I -th atom.

Using an initial charge density n_0 (usually the charge density of the isolated atoms comprising the system), the potential is calculated in real space. The Hartree potential is calculated by solving the Poisson equation (2.20) in reciprocal space using a Fast Fourier Transform (FFT) algorithm. It requires the potential to be periodic, but it can make use of very efficient optimised FFT methods. The exchange and correlation potential can be calculated using either (2.26) or (2.27), and (2.21).

Once the potential has been obtained, the Kohn-Sham Hamiltonian matrix is computed by evaluating integrals of the form

$$\begin{aligned}
 H_{ij} = & -\frac{\hbar}{2m} \int d\vec{\mathbf{r}} \phi_i(\vec{\mathbf{r}} - \vec{\mathbf{R}}_I) \nabla^2 \phi_j(\vec{\mathbf{r}} - \vec{\mathbf{R}}_J) + \\
 & + \int d\mathbf{r} \phi_i(\vec{\mathbf{r}} - \vec{\mathbf{R}}_I) V_{\text{eff}}(\vec{\mathbf{r}}) \phi_j(\vec{\mathbf{r}} - \vec{\mathbf{R}}_J). \quad (2.38)
 \end{aligned}$$

For periodic systems, one must also include the coupling to the periodic mirrors of the unit cell

$$H_{ij}(\vec{\mathbf{k}}) = \sum_l H_{ij}^l e^{i\vec{\mathbf{k}} \cdot \vec{\mathbf{r}}_l}, \quad (2.39)$$

where $\vec{\mathbf{r}}_l$ is the position vector between the 0-th and the l -th unit cells. An analogous equation can be written for the total overlap matrix S .

The Hamiltonian is then diagonalised to obtain the coefficients c_i^l for the i -th eigenvector ψ_i as defined in equation (2.32).

Once the Kohn-Sham eigenvectors

$$\psi_i(\vec{\mathbf{r}}) = \sum_l c_l^i \phi_l(\vec{\mathbf{r}}) \quad (2.40)$$

have been calculated, the density matrix can be obtained

$$D = \sum_l^{N_{E_F}} |\psi_l\rangle\langle\psi_l| = \sum_l^{N_{E_F}} \sum_i \sum_j c_l^i c_l^{j*} |\phi_i\rangle\langle\phi_j|, \quad (2.41)$$

where N_{E_F} is the number of occupied states up to the Fermi level.

Therefore the matrix elements of the density matrix expressed over the localised basis set are equal to

$$D_{ij} = \sum_l c_l^i c_l^{j*} f(\epsilon_l - E_F). \quad (2.42)$$

The electron charge density is just the diagonal elements of the density matrix in the real-space representation

$$\langle\vec{\mathbf{r}}|D|\vec{\mathbf{r}}\rangle = n(\vec{\mathbf{r}}) = \sum_{i,j} \phi_i(\vec{\mathbf{r}}) D_{ij} \phi_j(\vec{\mathbf{r}}). \quad (2.43)$$

The steps presented above are iterated until a self-consistent solution for the charge density is obtained. In other words, we start with a initial charge density n_0 which is used to calculate the effective potential $V_{\text{eff}}(\vec{\mathbf{r}})$. We then calculate the Hamiltonian elements H_{ij} . By diagonalising this Hamiltonian we find the KS eigenstates $|\psi_l\rangle$ which provide a new density matrix calculated using equation (2.41). This density matrix is subsequently projected onto the basis set to calculate a new electron charge density n_1 . This procedure is repeated until the convergence criteria is satisfied

$$\|n^j - n^{j+1}\| < \delta, \quad (2.44)$$

where δ is a tolerance parameter.

Recently there have been a number of extensions to SIESTA such as the inclusion of different approximations for the exchange-correlation potential (LDA+U [129] and SIC [86]) and Spin-Orbit interaction [108].

Although SIESTA is a state of the art DFT package, it cannot treat open systems, *i. e.*, it can only treat finite or periodic Hamiltonians. If one wishes to calculate the transport properties of devices using density functional theory, a novel approach must be taken to evaluate the electronic structure of an infinite non-periodic system. Most importantly, one must avoid the problem of diagonalising the Kohn-Sham Hamiltonian, which in the case of an open system is infinite.

2.4 *Smeagol*: electronic transport at the atomic and molecular scale



So far we have presented two seemingly dissimilar theoretical frameworks. On the one hand the method presented in chapter (1) deals with the electronic transport problem for an open system. The method itself is very general and up to this point no assumption was made about the character of the single-particle Hamiltonian \mathcal{H} appearing in equation (1.1) except that it is a function of the charge density.

On the other hand, we have just presented the DFT formalism where the electronic structure of extended periodic systems and finite molecules can be calculated. The limitations of present implementations include their inability of treating systems with no translational invariance and the effects of an external electric field; and consequently it is impossible to calculate the electronic transport properties of devices.

Therefore it is natural to interface the two formalisms into a single tool. In other words, use density functional theory to calculate a single-particle tight-binding-like Hamiltonian and then use the NEGF formalism for obtaining the associated non-equilibrium density matrix which includes the effects of the semi-infinite leads as well as the external bias.

As we discussed in section (2.3) SIESTA is readily available as a DFT tool, it produces a single-particle Kohn-Sham Hamiltonian in a localised basis representation and it is capable of treating large scale systems (> 100 atoms). The same cannot be said about an implementation of NEGF; a numerical tool which is versatile and which can treat the transport properties of many classes of problems was not yet available.

Hence we set out to develop *Smeagol* [71, 72], a computer software which uses DFT-NEGF to accurately predict the electronic transport properties of molecular devices [87], heterostructures [139] and tunnelling junctions [140] to name but a few.

In many cases we are interested in the magnetotransport properties, therefore

one must also be able to treat spin-polarised systems satisfactorily. This is also one of the main goals of *Smeagol*. One of its features is the calculation of the surface Green function using a semi-analytic approach and the solution of the K_1 problem (section (1.6)).

While SIESTA provides the Kohn-Sham Hamiltonian, *Smeagol* has been made to interface with it and to calculate the non-equilibrium charge density of an open system via Green functions.

In order to interface SIESTA with our transport code we need to make three major changes. First, we must include in our calculations the fact that our system is connected to semi-infinite leads on either side instead of being periodic. This can be done by simply adding the self-energies described in equations (1.34) and (1.35) to the KS Hamiltonian. These self-energies are obtained by a separate calculation for an infinitely long system as sketched in figure (1.10) and described in subsection (1.6.1). The Hamiltonian and Overlap matrix elements for each PL and their respective coupling terms between each PL are saved and subsequently read - during the *Smeagol* calculation - to calculate the surface Green function and the self-energies for a given range of energies. These terms are stored either in memory or on disk for future use. This clearly assumes that the leads are not affected by changes of the electronic structure of the scattering region when bias is applied.

The second change has to do with the Hartree potential, the classical electrostatic part of the energy functional. We must introduce a linear external potential associated with the external bias. The solution of the Poisson equation (equation (2.20)) is defined up to a linear term. This term is determined by the boundary conditions at the edges of the cell. In our case, we wish to set the potential on the left- and right-hand-side boundaries to match those of bulk (the electrodes) plus a shifted induced by the external potential.

$$V_H(\vec{x}) = \begin{cases} \frac{V}{2} + \phi_{\text{bulk}}(0) & z = 0 \\ -\frac{V}{2} + \phi_{\text{bulk}}(0) & z = L \end{cases} \quad (2.45)$$

where L is the length of the cell and $\phi_{\text{bulk}}(0)$ is the Hartree potential of bulk at the edge of the PL. In this approximation the only effect of the external potential V on the leads is a global shift of the electronic structure.

Since total Hartree potential can be separated into a periodic part plus the desired slope a constant slope can be added separately. The periodic part ϕ_H can be solved using the same FFT method used by SIESTA while the slope is added afterwards

resulting in the total Hartree potential for a bias V

$$V_H(\mathbf{x}) = \phi_H(\mathbf{x}) + \frac{V}{L}(z - a) + b \quad (2.46)$$

where a corresponds to the centre of the cell and b sets the zero of $V_H(\mathbf{x})$.

Figure (2.5) shows a sketch of a general device described by *Smeagol*: the scattering region is enclosed by the dashed line. In practice, the ramp is included in the form of a saw-like potential. The inclusion of the self-energies accounts for the break in translational symmetry.

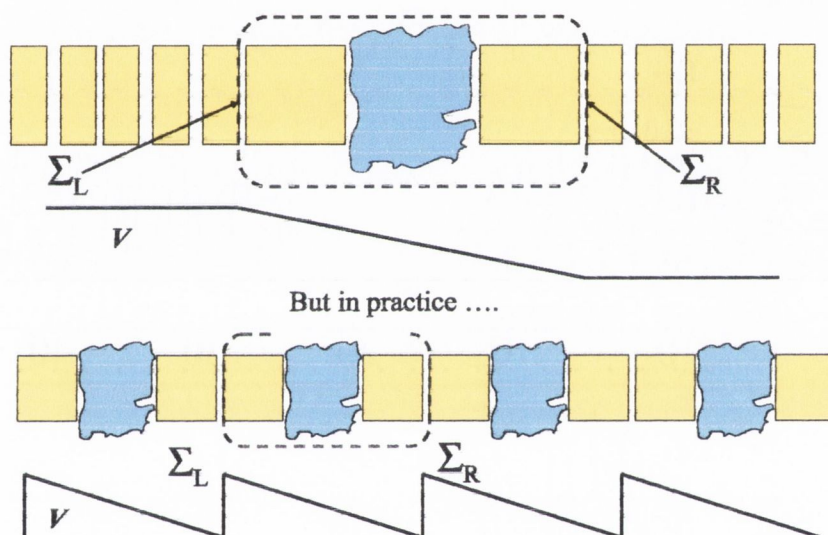


Figure 2.5: Real-space ramp added to the Hartree potential in SIESTA during the self-consistent cycle. a) The device described by *Smeagol*: one scattering region, two semi-infinite electrodes, and the bias across the extended molecule. Note that outside the interaction region the bias is constant. b) The way the electrostatic problem is solved in practice in SIESTA: a saw-like potential is added to V_H and the problem is solved using FFT's with periodic boundary conditions. Translational symmetry is broken by introducing the self-energies with the correct shift in the electronic structure.

Another change in the way the Hartree potential is handled is related to the constant b . The solution via FFT's discards the $\mathbf{k} = 0$ component of the Fourier transform which set the total charge in the cell. This means that in principle two different calculations might give different values for the constant b (V_H is obtained from the Poisson equation and can be rigidly shifted). This is not desirable because we need to match the potential at the edges of the cell to that of bulk. This issue is illustrated in figure (2.6) for a parallel plate gold capacitor compared to that of bulk gold. Here two infinite gold plates are set a distance of $\sim 12 \text{ \AA}$ apart. We

can see that moving away from the vacuum (central) region the system converges (the peak-to-peak oscillations remain constant) quite quickly. At the edges of the cell ($d = 0$ and 45 \AA) the potential resembles that of bulk gold. However when we superimpose the two potential profiles we can clearly see a mismatch (indicated by the blue arrow in the graph). Because the total DFT potential is defined up to a constant we can, without loss of generality, impose a constant shift to the Hartree potential across the entire cell. This way, the potential at the edges of the cell match that of the bulk electrodes and we can introduce the self-energies from a separate calculation.

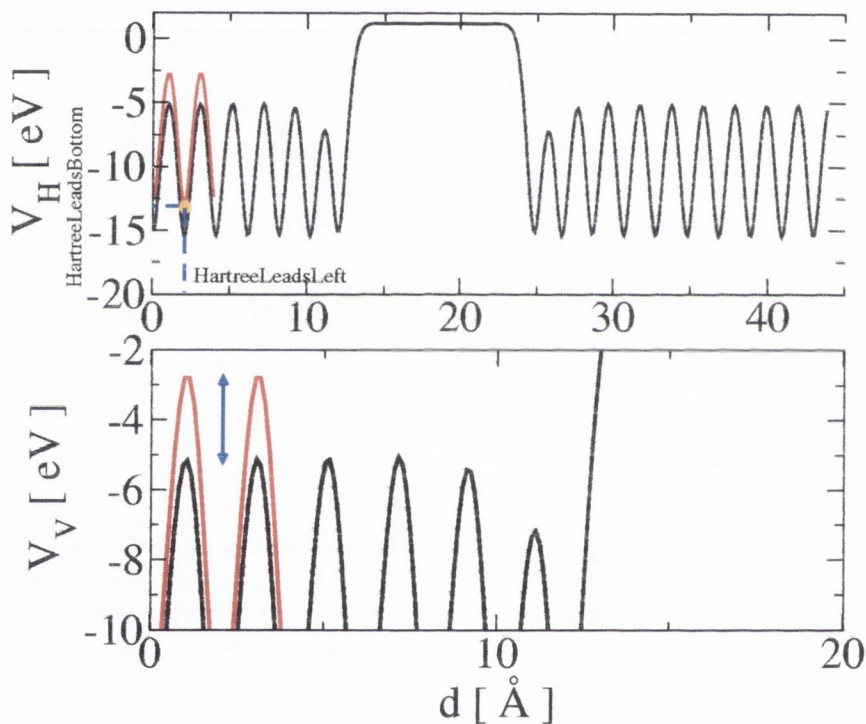


Figure 2.6: Hartree potential for a parallel plate capacitor (black line) and Hartree potential for one unit cell of bulk gold (red line). The blue arrow indicates the constant shift in the potential b which must be added to the calculation for the potential in electrodes and in the EM to match. Top and bottom panels represent the same figure with different scaling in the y axis.

In order to determine the constant b , a plane inside the scattering region is selected. The position of this plane along z is denoted *HartreeLeadsLeft* in figure (2.6) (a similar plane is selected for the right-hand-side denoted *HartreeLeadsRight*). The potential for the electrodes is obtained from a separate calculation and the value of the potential is a parameter of the NEGF calculation. During the self-consistent

cycle the Hartree potential of the EM is calculated and the average value over the plane at HartreeLeadsLeft is compared to the one at an equivalent plane for the potential on the leads. The difference between these two values is deemed to be the value of b .

The third and final step consists in substituting the DFT procedure for calculating the density matrix with the NEGF technique. Once the Hamiltonians and overlap matrices are obtained, we can use our method to calculate the non-equilibrium density matrix using equation (1.43).

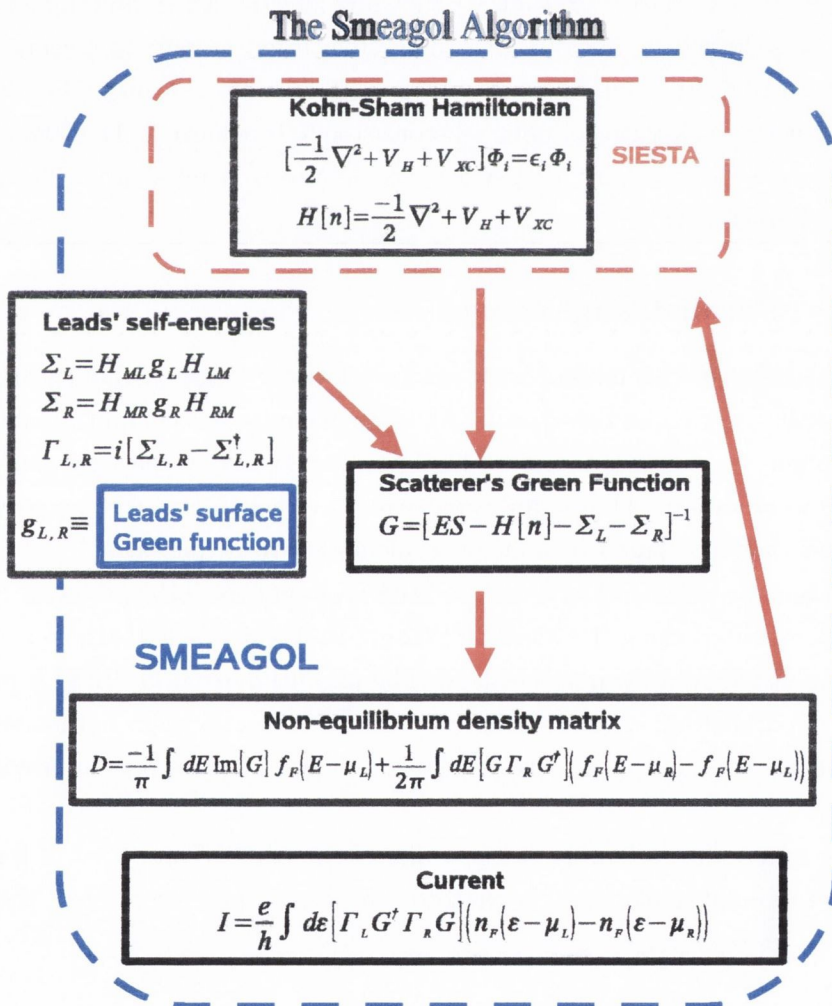


Figure 2.7: Flow-chart of the *Smeagol* program, highlighting the interconnection between *Smeagol* and SIESTA. It is clear that the code has been developed to interact with SIESTA in a modular fashion, making it portable to other *ab initio* computational tools.

In summary, we can calculate the density matrix for an open system within DFT and apply the method to a range of problems, for many different materials and geometries. Note that as far as the algorithm is constructed the specific form of the Hamiltonian is irrelevant, once it is written in a LCAO basis set and it is a functional of the charge density. *Smeagol*, in fact, is built in a modular fashion which gives us the option of using a different DFT software at the price of only minor changes. Hence interfacing *Smeagol* with other LCAO DFT codes or other Quantum Chemistry tools such as HF is relatively simple.

In figure (2.7) we show a general fluxogram of *Smeagol* and how it interfaces with SIESTA. We can clearly see that SIESTA provides the KS Hamiltonian and *Smeagol* introduces the self-energies turning the system from periodic to a central scattering region attached to semi-infinite electrodes. The codes exchange Hamiltonians and density matrices iteratively until self-consistency is achieved. Then *Smeagol* is used to calculate the transport properties such as the transmission coefficients and the $I - V$ characteristics.

2.4.1 Parallelising *Smeagol*

The systems we wish to deal with can be relatively large. Although SIESTA - and in general, other codes based on LCAOs - is generally less computationally intensive than plane wave codes, there are limits to the size of systems we can tackle on a simple workstation. These limitations can be either due to the memory needed or the time one is prepared to wait for a calculation to be performed.¹⁴

Either way, a parallel approach to SIESTA might solve the problem. SIESTA has been parallelised using the Message Passing Protocol (MPI) [141], so it can be used in most distributed memory clusters. The parallel version of SIESTA provides two types of parallelism: over k -points and over basis functions. In both cases the initial Hamiltonian in sparse form is distributed over all processors, improving memory usage.

For a periodic system we start by discretising the BZ into a set of k -points $\{k_i\}$. When the number of points is relatively large each processor solves the eigenvalue problem for equation

$$\left(\sum_{j=0}^N H_j e^{i\vec{k}\cdot\vec{r}_j} - E \sum_{j=0}^N S_j e^{i\vec{k}\cdot\vec{r}_j} \right) = 0 \quad (2.47)$$

¹⁴With present computational capabilities, one could treat a maximum of about 200 atoms on a single processing unit.

in series using a different k -point. The resulting eigenvectors $|\psi_i^{k_i}\rangle$ and eigenvalues $\epsilon_i^{k_i}$ are then regrouped to perform the integral (sum) over k -points in equation the equation for the density matrix

$$D = \int_{\mathbf{k}} d\mathbf{k} \sum_i |\psi_i^{\mathbf{k}}\rangle \langle \psi_i^{\mathbf{k}}| \sim \frac{1}{V_{\mathbf{k}}} \sum_{\mathbf{k}} \sum_i^{N_{\mathbf{k}}} |\psi_i^{\mathbf{k}}\rangle \langle \psi_i^{\mathbf{k}}| \quad (2.48)$$

where $N_{\mathbf{k}}$ is the number of k -points used in discretising the reciprocal space (for solving the problem numerically) and $V_{\mathbf{k}}$ is the volume of the Brillouin zone (BZ). This method is known as parallel over k (POK). This form of parallelism is highly scalable; the number of point-to-point communications is relatively small and the total number of CPUs¹⁵ can go up to a few hundred depending on the total number of k points. The main drawback of this method is that it requires the number of k -points to be bigger than the number of processors. For small systems, specially metals, the number of k -points can reach a few thousand, but for larger unit cells or molecules, where we have only one k -point, one must rely on a different kind of parallelism.

When the number of k points is smaller than the number of processors - for instance, a Γ point calculation - we perform the diagonalisation itself in parallel in what is known as the parallel over orbitals (POO) method. Unfortunately diagonalisation algorithms in parallel, in general, are not very efficient. The need for a large number of communication tags between CPUs leads to poor scalability specially in networks where the interconnects are slow, e.g. TCP/IP. At best, this type of parallelism, scales conveniently (around linear scaling) up to 6 CPUs for a TCP/IP network and 12-16 CPUs over InfinibandTM. Therefore, it is always preferable to use the POK whenever possible.

Diagrams of the two procedures are shown in figure (2.8). In the POK method the full Hamiltonian for each k -point is sent to a number of CPUs which is subsequently diagonalised and regrouped to calculate the density matrix. In the POO the Hamiltonian is diagonalised using a parallel algorithm (ScaLapack [142]).

As mentioned in section (2.4), *Smeagol* bypasses the diagonalisation procedure by performing the integrals of equations (1.57) and (1.58). The main computational bottleneck in *Smeagol* is performing these integrals. This includes performing the matrix inversion in equation (1.33) for each energy. Numerically, an integral is nothing more than a sum. Therefore we can calculate each term of such sum independently in parallel and collect the results at the very end. This scheme is called parallel over energy (POE).

¹⁵The central processing unit (CPU) is commonly known as the processor.

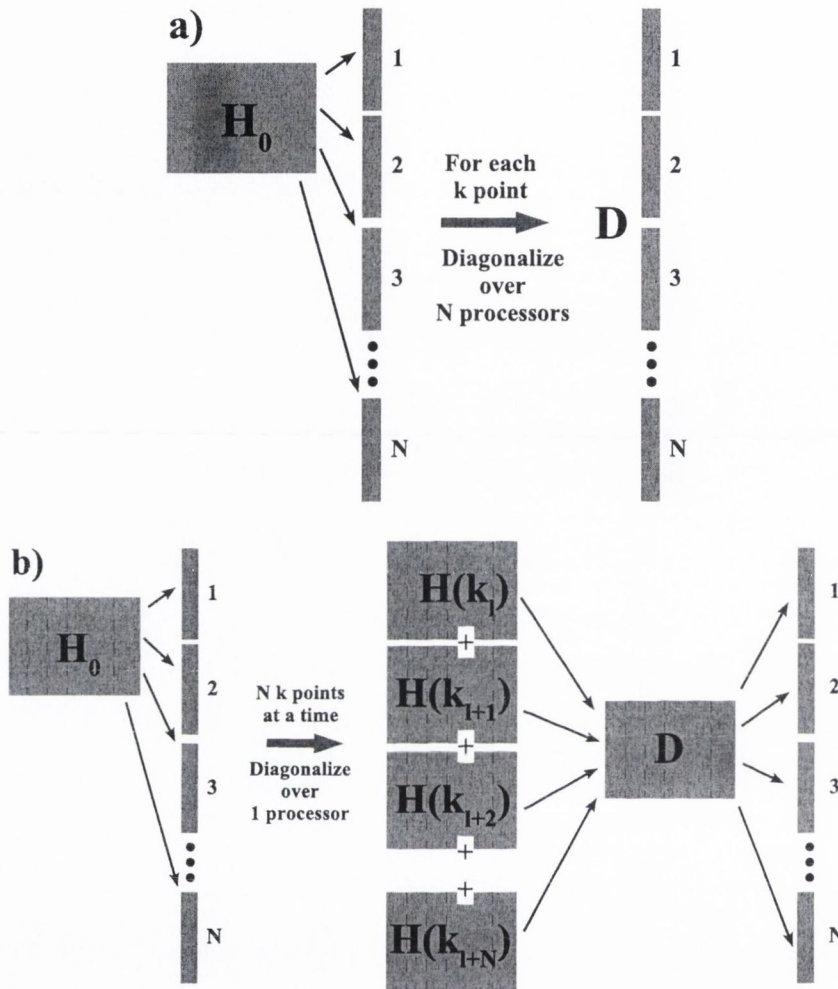


Figure 2.8: Two choices of parallelism in SIESTA. a) Parallel over orbitals (POO): the total Hamiltonian is diagonalised in parallel and the density matrix is calculate. b) Parallel over k -points (POK): the Hamiltonian for each k -point is diagonalised in series, each in a different CPU. The eigenvectors are regrouped to calculate the density matrix.

In many ways, this scheme is similar to the POK method whereby the inversion at each energy is calculated over a different processor and $D_{\text{eq}}(E_i) + D_V(E_i)$ is subsequently computed. Finally, once all the energy points have been calculated all the processors sum the results (with the appropriate weighting factors) to obtain the total density matrix.

In tables (2.1) and (2.2) we show how *Smeagol* scales as a function of the number of processors for two different types of interconnect.¹⁶ We can clearly see how the to-

¹⁶The calculations were performed, in both cases, on AMD-64bit-Opteron clusters with 4 Gb

tal CPU time¹⁷ remains relatively unchanged, an indication that the communication overhead is small. Consequently, as the number of processors increases the wall-time (the actual real time taken for the calculation) decreases almost as $1/N$. This is true for both types of interconnects (only slight differences are observed) which ensures good scalability (the slight increase in total wall-time is observed due to communication overheads). Most importantly there is no significant difference between different types of communication switches (in fact we observe better results using TCP/IP over Infiniband).

Although we observe a significant increase in the total CPU time ($\sim 26\%$), the NEGF segment of the calculation only increases by approximately 10%. This is mostly due to the calculation of the potential in real space. Firstly, with the increase in the number of processors the NEGF part of the calculation loses importance (from approximately 70% to 50% of the total time of the calculation). Secondly, the distribution of the grid over the processors can be controlled by the user. For consistency, the default values were set throughout, but the appropriate choice of parameters can lead to decreased communication between compute nodes and significant improvements in performance.

Number of CPUs	8	16	32	64
Time [s]				
Total CPU Time	33951.188	26094.441	28490.203	33923.216
CPU Time NEGF subroutine	25771.792	21587.093	22871.922	25728.925
Total Wall-time	4243.898	1630.902	890.318	530.050
Wall-time NEGF subroutine	3221.474	1349.193	714.747	402.01

Table 2.1: Timing of *Smeagol* for k -point (4 k -points) calculation using 16, 32, 64 and 128 processors at 0 bias for a 85 atom unit cell ($N = 826$) over TCP/IP.

The *Smeagol* method can be easily parallelised up to 100 processors using the same scheme as in the parallel over k method. A description of a more scalable of RAM per node (2 CPUs per node) and 2.3 GHz clock-speed. We used the Pathscale [143] compiler with the following compilation flags in both cases: `-m64 -mtune=opteron -mieee-fp -zerouv -OPT:Ofast -O2 -march=opteron -mcpu=opteron -ipa`.

¹⁷The CPU time corresponds to the sum over all processing units of the time taken for a set of operations

Number of CPUs	8	16	32	64
Time [s]				
Total CPU Time [s]	29575.384	31497.067	36839.019	46331.667
CPU Time NEGF subroutine	21074.052	21876.695	23434.525	26718.410
Total Wall-time	3696.9	1968.6	1151.2	723.9
Wall-time NEGF subroutine	2634.2	1367.2	732.3	417.4

Table 2.2: Timing of *Smeagol* for k -point (4 k -points) calculation using 16, 32, 64 and 128 processors at 0 bias for a 85 atom unit cell ($N = 826$) over InifinibandTM.

method for parallelising *Smeagol* up to 4096 processors is presented in the appendix A.

2.4.2 An overview of *Smeagol* capabilities

As a tool for calculating accurate materials specific transport properties at the atomic scale, *Smeagol* has a number of features including but not limited to:

- The use of *ab initio* Hamiltonians expressed in a LCAO basis and the flexibility to use both DFT and HF methods.
- Full parallelisation in energy (POE) up to 128 processors (see appendix A for parallelisation up to 4096 processors - energy and orbital space).
- Fully spin polarised including non-collinear spins.
- Ability to calculate both molecules and surfaces: finite and periodic boundary conditions in the transverse direction (orthogonal to the transport).
- Ability to perform large scale calculations up to 100 atoms per processor.
- Inclusion of new exchange and correlation functionals such as LDA+U [85] and self-interaction corrected LDA [86].
- Ability to calculate currents and transmission coefficients with a high degree of accuracy (some results span over five orders of magnitude; see chapter (4) for details).

2.5 Test Cases

This section is divided in five subsections, each one of them devised to show one of *Smeagol's* capabilities. In the first subsection we deal with a parallel-plate capacitor with vacuum as a dielectric medium. This simulation clarifies how *Smeagol* deals with the Hartree potential. In subsection (2.5.3) we show calculations for magnetic materials (one of *Smeagol's* main capabilities) and in particular we show how it is possible to address systems with non-collinear spins. In subsections (2.5.4) and (2.5.5) we turn to the more realistic problems of hydrogen-rich Platinum point contacts and organic molecules sandwiched by metallic electrodes. In both cases, there have been extensive experimental investigations and we show how *Smeagol* is capable of addressing some issues relating to these systems.

2.5.1 Au capacitor: Hartree potential and bias ramp

One important test for *Smeagol* is to check that the self-consistent Hartree potential is correctly obtained. For that purpose, we performed calculations for two semi-infinite gold surfaces separated by 12.27 Å, thus creating an ideal parallel plate capacitor.

The two gold surfaces are oriented along the (100) direction and the unit cell has only one atom in the cross section. The extended molecule comprises seven atomic planes in the direction of the transport, which is enough for achieving a good convergence of the Hartree potential (the Thomas-Fermi screening length in gold is ~ 0.6 Å [144]). For the calculation we use 100 k -points in the full Brillouin zone in the transverse direction, a single zeta basis set for the s , p and d orbitals and standard local density approximation (LDA) of the exchange and correlation potential.

In figure (2.9) we present the planar average of the Hartree (electrostatic) potential V_H , the difference between the planar average of Hartree potential at finite bias and that at zero bias ΔV , and the difference $\Delta\rho$ between the planar average of the charge density along the direction of the transport for a given bias and that at zero bias. The quantities shown in the picture are those expected from the classical physics of a parallel plate capacitor. In the leads the electrostatic potential shows oscillations with a period corresponding to that of the separation between the gold planes, but with a constant average. In contrast in the vacuum region the potential is much higher, since there are no contributions from the nuclei, but it is uniform. If we eliminate the oscillations, by subtracting the zero bias potential from that obtained at finite bias (figure 2.9b), we obtain a constant potential profile in the leads and a linear drop in the vacuum region. Finally the macroscopic average of the charge

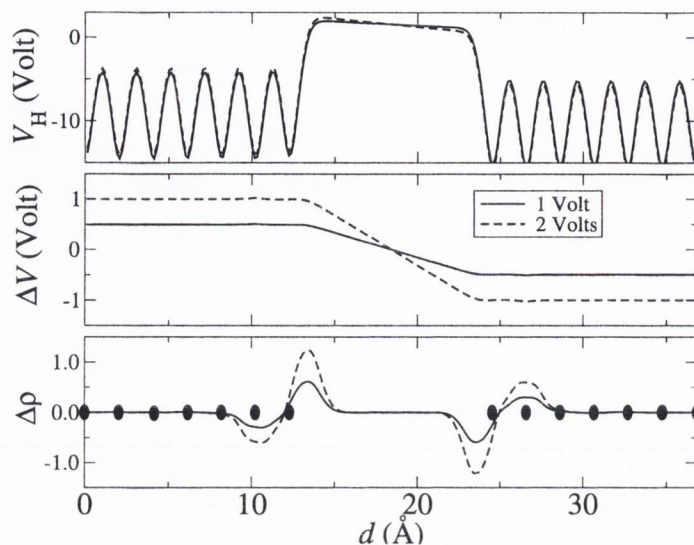


Figure 2.9: a) Planar average of the Hartree potential V_H for an infinite parallel-plate capacitor. b) Difference between the planar average of the Hartree potential at a given bias and that at zero bias ΔV . c) Difference $\Delta\rho$ between the planar average of the charge density along the direction of the transport for a given bias and that at zero bias. The dots indicates the position of gold planes.

density shows charge accumulation on the surfaces of the capacitor and local charge neutrality in the leads region as expected from a capacitor.

Similarly we can look at the equipotential surfaces in the vacuum region by plotting the iso-surfaces of constant potential along the central part of the capacitor. The result is shown in figure (2.10). We can clearly see that they represent planes parallel to the capacitor plates. Exactly as one would expect when the total electrostatic potential in the vacuum region is

$$V_H(\mathbf{r}) = V \cdot z \quad \forall x, y. \quad (2.49)$$

This result shows that the solution of the Hartree potential is consistent with the potential drop across a vacuum region of two infinite plates as described by classical electromagnetism [145]. Furthermore, we have shown that *Smeagol* can efficiently perform k-point calculations highlighting its potential for transport calculations through - magnetic or not - interfaces, a field of great interest [139, 140].

2.5.2 Au atomic chains

Metallic quantum point contacts (PC) present conductance quantisation behaviour even at room temperature [64, 146, 147, 148, 149]. While conductance quantisation

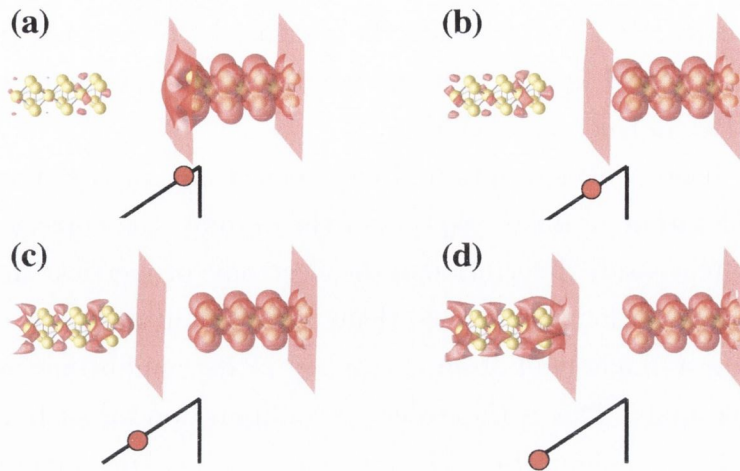


Figure 2.10: (a-d) Iso-surfaces of constant potential along the vacuum region of the capacitor for different positions perpendicular to the capacitor plates. For each panel we also present schematically the potential at which the iso-surface is calculated.

in semiconductor point contacts can be observed in constrictions a few hundred Angstroms wide [150, 151], the same effect can be achieved in metallic systems only at the atomic scale. The quantisation of conductance arises in one-dimensional systems due to the cancellation of the Fermi velocity and the density of states in the expression for the conductance [84]. This depends only on the number of bands available in the constriction (up to the number of valence electrons). A system is said to be 1D when the width of the constricted region is comparable to the Fermi wavelength. In the case of semiconductors that would be 200 \AA for GaAs and in the case of metals a few Angstroms ($\sim 5 \text{ \AA}$ for Gold). Hence, we can clearly see that observing such an effect in metallic systems entails measurements in atomically thin constrictions.

In break junction experiments [147], two metal surfaces are brought into contact and subsequently separated. During the elongation process and just before the junction ruptures the conductance displays flat plateaus and abrupt jumps (step-like curves). The experiments are repeated a number of times and the results recorded. In order to show conductance quantisation in atomically thin PCs one uses histograms to obtain statistically representative data of transmission curves as a function of the elongation process [147]. These histograms are obtained by summing all the conductance curves recorded in the course of an experiment. The steps observed in conductance curves are displayed as peaks in the histogram. Proof that Au PCs present one quantum of conductance is given by a sharp peak at $1 G_0 = 2e^2/h$.

Recently, Rodrigues *et al.* have shown that the crystallographic orientation of the tips plays an important role in the determination of the transport properties of

these PCs [149]. The authors used atomically resolved high resolution transmission electron microscopy (HRTEM) to image the elongation process of gold point contacts. It is clear from HRTEM images that the point contacts retain the crystallographic bulk structure (fcc in the case of gold).

Hence, the theoretical description of electronic transport in atomic chains must take into consideration atomistic aspects of the system: the correct arrangement of the atoms and an accurate description of the electronic properties. As an example we have performed calculations for a [100]-oriented gold quantum point contact (see inset of figure (2.11)). A single gold atom is trapped at its equilibrium position between two [100] fcc pyramids. This is the expected configuration for such a specific crystal orientation, and the configuration likely to form in breaking junction experiments [152] for small elongation of the junction. It has also been confirmed by atomic resolution TEM images [146, 149, 153]. In this case we have used LDA and a single zeta basis set for s , p and d orbitals. The unit cell of the extended molecule now contains 141 atoms (seven planes of the leads are included) and we consider periodic boundary conditions with 16 k -points in the 2-D Brillouin zone.

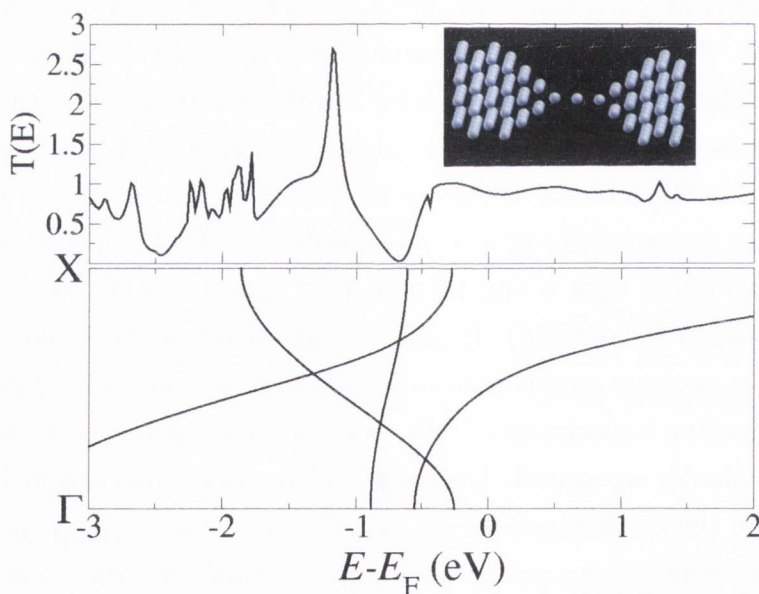


Figure 2.11: The transmission coefficient as a function of energy (upper panel) for a gold atomic point contact sandwiched between two gold tips oriented along the [100] direction. In the lower panel the band-structure for a monoatomic gold chain with lattice constant equal to the Au-Au separation in bulk gold. The inset shows a ball-and-stick representation of the atomic positions of the PC (the extended molecule).

In figure 2.11 we present the zero-bias transmission coefficient as a function of

energy. Recalling that the linear response conductance is simply $G = G_0 T(E_F)$ (in this case we have complete spin-degeneracy) our calculation shows one quantum conductance for this point contact. Interestingly the transmission coefficient is a rather smooth function $T \sim 1$ for a rather broad energy range around E_F . This means that the $G = 1G_0$ result is stable against the fluctuations of the position of the Fermi level, which may be encountered experimentally.

The large plateau at $T \sim 1$ ($-0.5 \text{ eV} < E - E_F < 2 \text{ eV}$) indicates the presence of a single conductance channel for energies around and above E_F . This is expected from the band-structure of a straight monoatomic gold chain with lattice parameter equal to the Au-Au separation in bulk gold (see figure (2.11b)), which presents only one s band for such energy range. Therefore we conclude that the transport at the Fermi level is dominated by a single low-scattering s channel. Notably for energies 1 eV below E_F the transmission coefficient shows values exceeding one, which are due to contributions from d orbitals. In gold mono-atomic chains these are substantially closer to E_F than in bulk gold and participate to the transport. These results are in good agreement with previously reported calculations [92, 154] and experimental data [146, 147, 149]. Additional examples of *Smeagol's* calculations for PCs carried out by the authors can be found in the next sections of this text and elsewhere in the literature [155, 156].

2.5.3 Nickel point contacts using non-collinear spins

The transport properties of magnetic transition metal point contacts have been the subject of several recent investigations [11, 157, 158, 159, 160, 161]. Technologically these systems are attractive since they can be used as building blocks for read heads in ultra-high density magnetic data storage devices. From a more fundamental point of view they offer the chance to investigate magnetotransport at the atomic level. Magnetic point contacts are effectively spin-valve-like devices, with the spacer now replaced by a narrow constriction where a sharp domain wall can nucleate [162].

A simple argument based on the assumption that all the valence electrons can be transmitted with $T \sim 1$ gives an upper bound for the GMR of the order of a few percent (250 % in the case of nickel). This however may be rather optimistic since one expects the d electrons to undergo quite severe back-scattering. Indeed small values of GMR for Ni point contacts have been measured [159]. Surprisingly at the same time other groups have measured huge GMR for the same system [11, 157, 163, 164]. Although mechanical effects can be behind these large values [160], the question on whether or not a large GMR of electronic origin can be found in magnetic point

contacts remains.

Therefore we investigate the zero bias conductance of a four atom long monoatomic Ni chain sandwiched between two Ni (001) surfaces (see figure (2.12)). This is an extreme situation rarely found in actual break junctions [165]. However an abrupt domain wall (one atomic spacing long) in a monoatomic chain is the smallest domain wall possible, and it is expected to show the larger GMR. For this reason our calculations represent an upper bound on the GMR obtainable in Ni only devices, and they also serve as a test of the *Smeagol* capability for dealing with non-collinear spins.

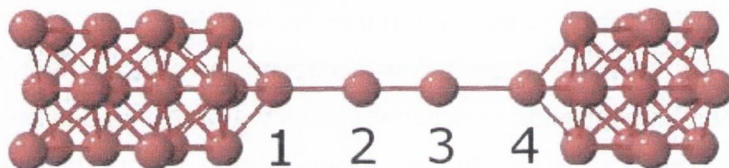


Figure 2.12: Schematic representation of the Ni point contact simulated. In the symmetric case the domain wall is located between the second and the third atom, while in the asymmetric it is placed between the third and the fourth. The direction of the current is from 1 to 4 for positive bias.

In this calculation we use a double zeta basis set for s , p and d orbitals and consider finite leads (no periodic boundary conditions are applied) with either four or five atoms in the cross section. We then investigate two possible situations. In the first one we place the domain wall symmetrically with respect to the leads, i.e. between the second and the third atom of the chain. In the second (asymmetric) the domain wall is positioned between the third and the fourth atom. Furthermore we perform spin-collinear and spin-non-collinear calculations for both cases. Interestingly all our non-collinear calculations always converge to a final collinear solution. This confirms expectations based on simple s - d model [166], suggesting that the strong exchange coupling between the conduction electrons and those responsible for the ferromagnetism, stabilise the collinear state if the magnetisation vectors of the leads are collinear.

In figure (2.13) we present the transmission coefficient as a function of the energy for both the symmetric and asymmetric case and the parallel state. For collinear calculations the contributions from majority and minority spins are plotted separately, while we have only one transmission coefficient in the non-collinear case. Clearly in

all the cases the non-collinear solution agrees closely with the collinear one, i.e.

$$T_{\text{collinear}}^{\uparrow} + T_{\text{collinear}}^{\downarrow} = T_{\text{non-collinear}}. \quad (2.50)$$

This is expected since the final magnetic arrangement of the non-collinear calculation is actually collinear, and it is a good test for our computational scheme.

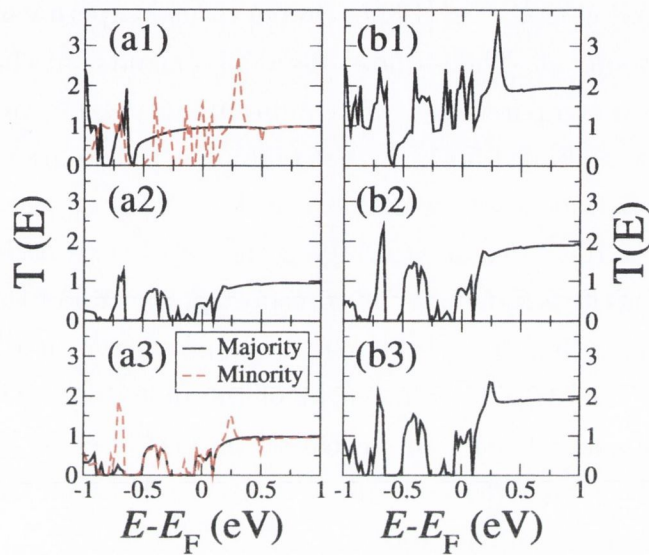


Figure 2.13: Transmission coefficient as a function of energy for the nickel quantum point contacts of figure 2.12. The right-hand side panels (a) are for collinear calculations and the left-hand-side (b) are for non-collinear; (1) parallel state, (2) antiparallel with symmetric domain wall, (3) antiparallel with asymmetric domain wall. Note that in the non-collinear case we do not distinguish between majority and minority spins. In panel (a2) majority and minority spins are degenerate.

Turning our attention to the features of the transmission coefficient it is evident that, at the Fermi level, T in the parallel state is larger than that in the antiparallel. This difference however is not large and the GMR ratio is about 60% with little difference between the symmetric and asymmetric domain wall. This is mainly due to the much higher transmission of the un-polarised s electrons compared with that of the d . Note that the conductance approaches $2e^2/h$ for energies approximately 0.5 eV above the Fermi level. For such energies in fact no d electrons contribute to the density of states of both the spin sub-bands, and only s electrons are left. These are then transmitted with $T \sim 1$ as in the case of Au chains investigated previously.

We will come back to the issue of large MR in magnetic point contacts in chapter 3 where we consider a number of magnetic configurations as well as impurities.

2.5.4 The importance of k-point sampling in Platinum single atom chains

The conductance of atomic metallic point contacts is an area of great interest. As we have discussed in the previous section, quantised conductance in metals was first observed in atomically thin gold nanowires. Since then a number of works have been performed over a number of different metals [167, 168].

Recently van Ruitenbeek *et al* [169] have performed experiments on Pt PCs in a hydrogen-rich environment. The authors observed a significant change in the transport behaviour when compared to *clean* conditions (cryogenic vacuum). For clean Pt point contacts a peak at $1.5 G_0$ in the conductance histograms is predominant, but in a hydrogen-rich atmosphere a sharp peak at $1 G_0$ appears instead. This is an indication that a H_2 molecule is bridging the gap between the two tips and it becomes the bottleneck that defines the transport properties of the whole system.

Despite indications that H_2 is bridging the point contact, it is impossible to experimentally probe the atomic arrangement of the molecules. Theoretical tools to model the molecule and calculate the transport properties come in hand for corroborating the assumption that the molecule actually lies between the two tips and for establishing the molecular orientation.

In order to address this issue we used *Smeagol* to perform calculations on Pt PCs. We used a double zeta basis set for both Pt and H. Our system consisted of two pyramidal tips connected by a hydrogen molecule. Initially we performed relaxations on the system by fixing the edges of the unit cell and allowing central region to relax. The total energy curve was calculated as a function of the unit cell size. We considered two configurations, namely the axis of the hydrogen molecule lying either along the axis of the tip - which we shall call bridge configuration (BC) - or perpendicular to it - called perpendicular configuration (PPC). Figure (2.14 shows the different atomic configurations in our calculations.

Figure (2.15) shows the total energy curve for different configurations of the hydrogen molecule on the tip as a function of distance between the two pyramids. We can see that, at small tip separations the hydrogen molecules remain dissociated in the pyramids instead of lying in between the two tips. That is clear from the lower energy for the CZ curve. As we simulate the pulling of the two tips - as we would expect in an STM or break junction experiment - a crossing point in which the BC becomes more energetically favourable can be seen. This trend seems to suggest that the Hydrogen molecule, as the tips are separated, tends move from the pyramids to the tips eventually lying along the axis of the point contact. This result, *i. e.* a

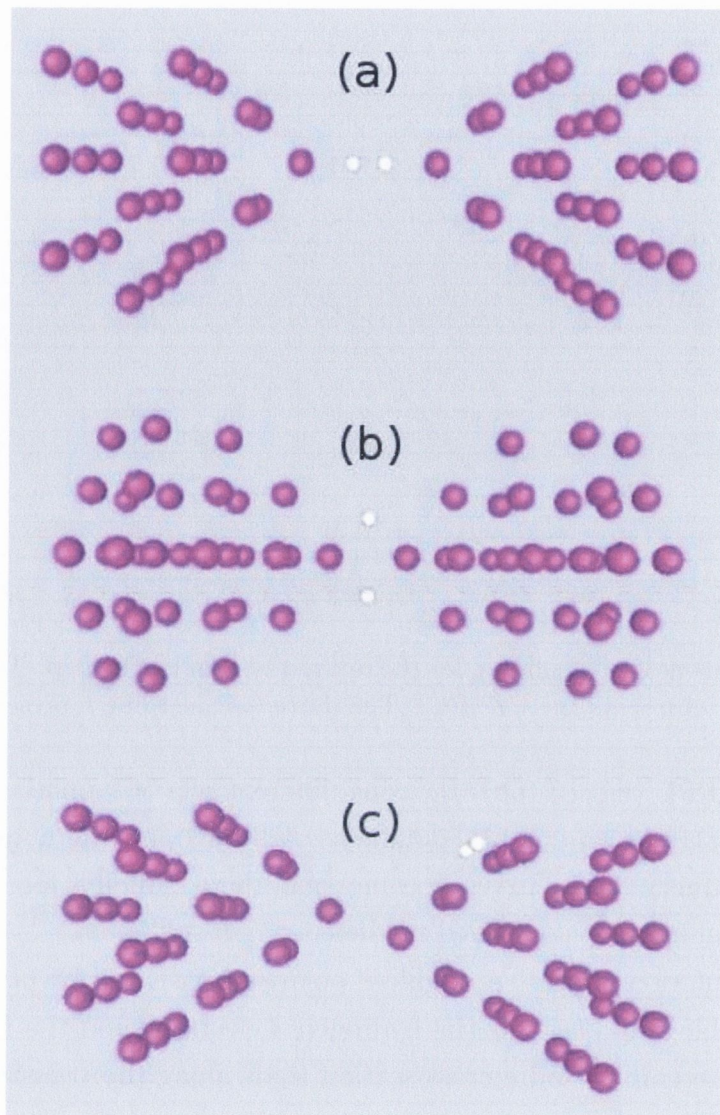


Figure 2.14: Sketch of a Platinum point contact with one hydrogen molecule in between the two tips. There are two possible configurations (a) bridge configuration (BC) and (b) perpendicular configuration (PC). c) We also consider the possibility that the H_2 molecule is adsorbed onto one of the tips (CZ).

configuration favouring the BC has also been obtained by other theoretical works [170, 171, 172].

In order to obtain the correct electronic structure of the electrodes, it is imperative to consider the boundary conditions along the transverse direction. Platinum, albeit non-magnetic, has d states which are close to the Fermi level. Therefore the band structure of bulk Pt has flat bands close to E_F . In order to ensure the correct description of these states we must use a reasonable k -point sampling in the transverse BZ. In figure (2.16) we show transmission curves for both the BC (fig.

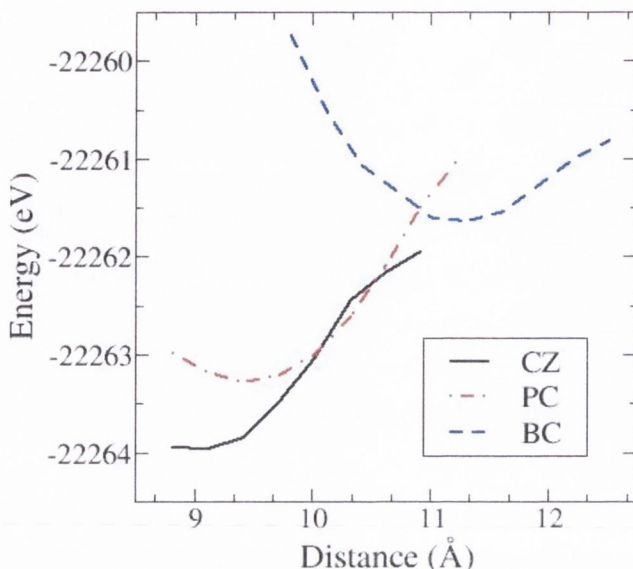


Figure 2.15: Total energy calculation for the relaxed system tip/H₂/tip. The solid (dashed) line represents the CZ (BC). The dotted-dashed line represents the PPC

(2.16a1-3)) and PPC (fig. (2.16b1-3)) using different sets of k -points. We can clearly see that as we introduce periodic boundary conditions and the number of k -points increases, the transmission curves become smoother. Finally, for 12 k -points the curves become sufficiently converged to the correct result.

For our calculations we use a double- ζ polarised basis set for platinum s , p and d orbital, a double zeta basis for the hydrogen s electrons and the LDA functional. As a first step we employ finite cross section leads along the transversal directions, composed of alternated planes containing 4 and 5 atoms each. The resulting transmission coefficients show many peaks and gaps throughout all the energy range and particularly sharp variations around the Fermi energy, as can be seen in figures 2.16 (a1) and (b1). When thicker slabs composed of alternating planes of 9 and 12 atoms are employed the results do not improve and the large oscillations still remain, as shown in figures 2.16 (a2) and (b2). It is apparent from these figures that while $T(E)$ shows a long plateau at positive energies, it presents strong oscillations at the Fermi energy and, therefore, it is uncertain to infer the conductance of the junction from $T(E_F)$.

This is in stark contrast with the case of gold, where the d -levels lie below E_F , and $T(E)$ is smooth regardless of the size of the leads cross section. For platinum the presence of d -states at the Fermi energy opens mini-bands and mini-gaps, which translate into strong oscillations in $T(E \sim E_F)$. These mini-bands and mini-gaps

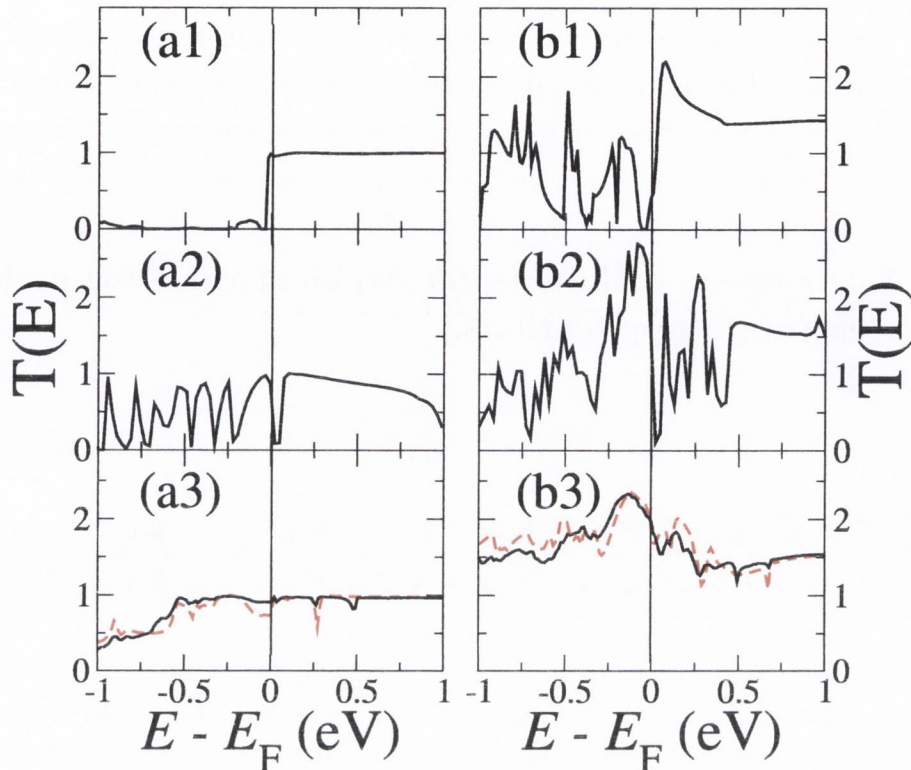


Figure 2.16: Transmission coefficients for an H_2 molecule sandwiched between fcc platinum leads near the equilibrium distances (~ 9.5 and 11 \AA). The left hand side (a) corresponds to the configuration where the molecule lies parallel to the current flow and the right hand side (b) to the configuration where the molecule lies perpendicular. The leads are made of alternating slabs of 4-5 atoms (1) and 9-12 atoms (2) without periodic boundary conditions along the perpendicular directions (xy), and 9-9 atoms with periodic boundary conditions along xy (3). In the last case the dashed and continuous lines have been obtained with 4 and 12 k points, respectively.

arise from interference effects of the d -states along the transverse direction. Consequently, oscillations in $T(E)$ should disappear when bulk electrodes are used. Indeed, this is what we find when slabs made of 3×3 atomic planes and periodic boundary conditions are employed, as shown in figures 2.16 (a3) and (b3). We moreover show how $T(E)$ converges when the number of transverse k points is increased from 4 to 12. Although some small variations and peaks still remain when 4 k points are used, the transmission at the Fermi level is essentially converged. Note that the parallel case has $T \sim 1$ for a long range of energies around E_F , which remains essentially unperturbed for small variations of the coordinates or the distance between the electrodes. This explains the sharp peak observed in the experimental conductance histograms [169].

As we can see, in materials where d states play a role in the electronic proper-

ties, the correct calculation of the transmission coefficients involves using periodic boundary conditions. Moreover, we have shown that we can use *Smeagol* to solve experimental conundrums and provide useful insight into the world of metallic point contacts. Our point here was just to use an example of one possible *Smeagol* application. A more detailed description of this work can be found elsewhere [155, 156].

2.5.5 1,4-benzene-dithiolate on Au electrodes for molecular electronics applications.

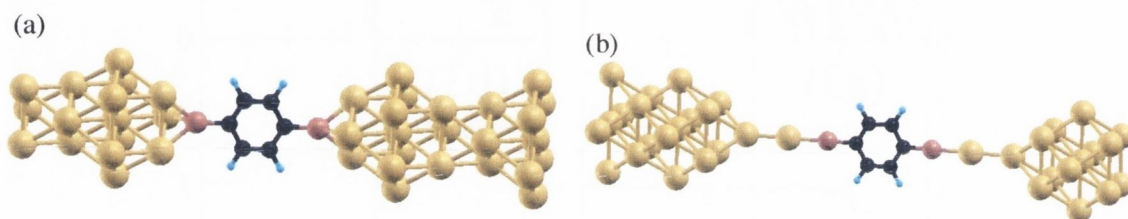


Figure 2.17: Ball-and-stick representation of a 1,4-benzene-dithiolate molecule attached to a a) [111] and b) [001] gold surface. Colour legend: C - black; H - light blue; S - red; Au - gold.

Recently there has been increasing interest in molecular electronics, *i. e.* in the ability to drive current through molecules and possibly their use as electronic devices. Integrating these devices could lead to applications ranging from sensors to new information data storage devices. The first experiments in molecular electronics were performed by Reed *et al.* [4]. The authors used a gold break junction setup to create a gap where a single 1,4-benzene-dithiol molecule (BDT) is trapped. A ball-and-stick model of the BDT molecule is shown in figure (2.17). The sulphur atoms (thiol groups) from both ends of the benzene ring bond strongly to the gold surface. The authors observed a strongly non-linear $I - V$ characteristics and a conductance gap of approximately 2 Volts.

After this seminal experiment many works in the field have followed, most of which use a similar set up with a choice of different organic molecules [27]. These experiments have shown interesting properties such as negative differential resistance [5], rectification [6] and transistor behaviour [7].

Partly due to the availability of experimental results, BDT attached to gold electrodes has become the benchmark for any transport calculation using *ab initio* methods [79, 98, 173]. All theoretical predictions give currents much higher (usually two orders of magnitude) than experimental observations. So far, no code has

been able to account for the differences in the conductance, but they all seem to give comparable results. This discrepancy has been so far attributed to our lack of knowledge about the atomic arrangement of the molecule and the tip. It has been argued that the position of the molecule on the gold surface has an effect on the transport properties.

We set out to perform our own calculations for benzene-dithiol using *Smeagol*. In particular, we wish to show how *Smeagol* can cope with the calculation of $I - V$ characteristics for different configurations of the electrodes. We have studied the effects of different surfaces, namely [111] and [001] on the $I - V$ characteristics of this molecule. In all cases we have modelled gold using a single- ζ s , p and d basis set whereas for both carbon and sulphur we used a double- ζ basis (s , p and d as well) with polarisation orbitals. Finally for hydrogen, a single- ζ polarised s wavefunction. In all cases finite boundary conditions were used.

The first situation considered was the case of a molecule attached to the hollow site in the [111] gold surface as our electrodes. Figure (2.17a) shows a ball-and-stick sketch of the system under consideration. The sulphur atom was positioned on the hollow site of the [111] surface of gold at distances according to values obtained in the literature for *ab initio* molecular dynamics calculations [174, 175].

As we apply a bias (see fig. (2.18)) we observe a small gap of about $0.5V$ before the onset of relatively high currents ($\sim 2 \mu A$).

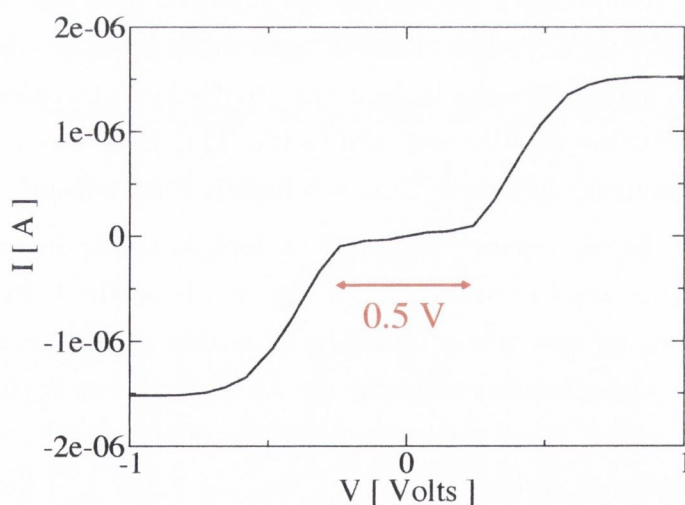


Figure 2.18: $I - V$ characteristics as a function of energy for different voltages for 1,4-benzene-dithiolate molecule attached to a [111] gold surface.

In figure (2.19) we present the transmission coefficients as a function of bias. We can clearly see that the transmission at zero bias (black curve) is quite small and there is a gap slightly below the Fermi level. Once we start to apply the bias the

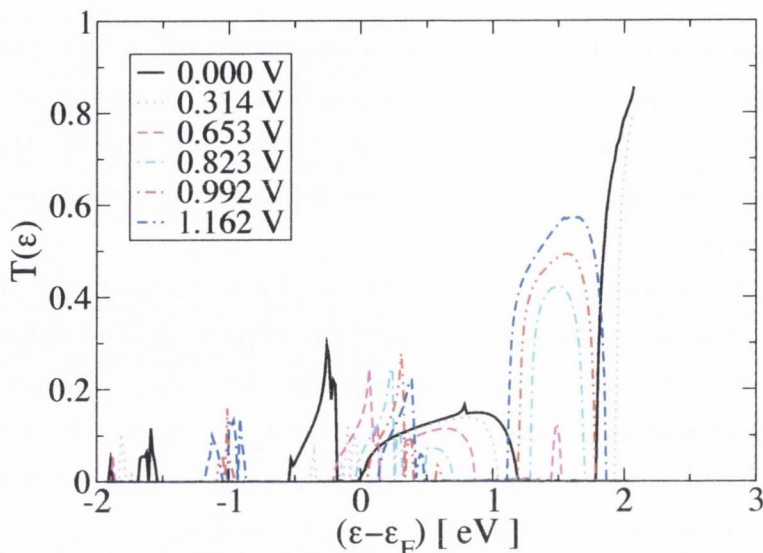


Figure 2.19: Transmission as a function of energy for different voltages for 1,4-benzene-dithiolate molecule attached to a [111] gold surface.

state positioned approximately -0.2 eV below the Fermi level starts to shift. Once the bias is sufficiently large (~ 250 meV) that state lies within the bias window and the system starts to conduct.

In the case of the [001] surface we place the sulphur atom on top of a single gold atom. This arrangement simulates a break junction experiment. While the two gold surfaces are being pulled apart gold atoms are removed from the surface forming a wire (the gold-gold bond is weaker than the gold-sulphur bond). Hence one expects the coupling to be quite different. In fact, the $I - V$ characteristics shown in figure (2.20) presents a different profile compared to the [111] case. From the onset of bias, the system is conducting, and there is no conductance gap around zero bias.

The reason for the discrepancy is clear if we look at the transmission coefficients for different bias presented in figure (2.21). At zero bias, the Fermi level is pinned to a resonance and, as one starts to apply bias, this state becomes immediately conducting. The transmission coefficient for such resonance is close to $1 G_0$, the quantum of conductance, hence the currents for the [001] case are considerably larger than that in the previous case.

We can see that in both cases we have high conductance and in one particular case we see no gap at all. The explanation given earlier about the position of the atoms on the surface might seem likely at first, however, the experimental results seem quite robust. In particular, the typical gap observed in the experiments has also been measured in slightly different molecules [176]. One aspect not taken into account here

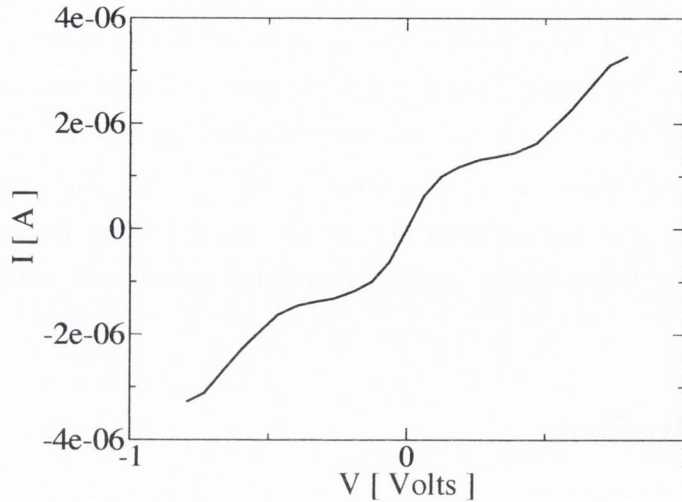


Figure 2.20: $I - V$ characteristics for 1,4-benzene-dithiolate molecule attached to a [001] gold surface.

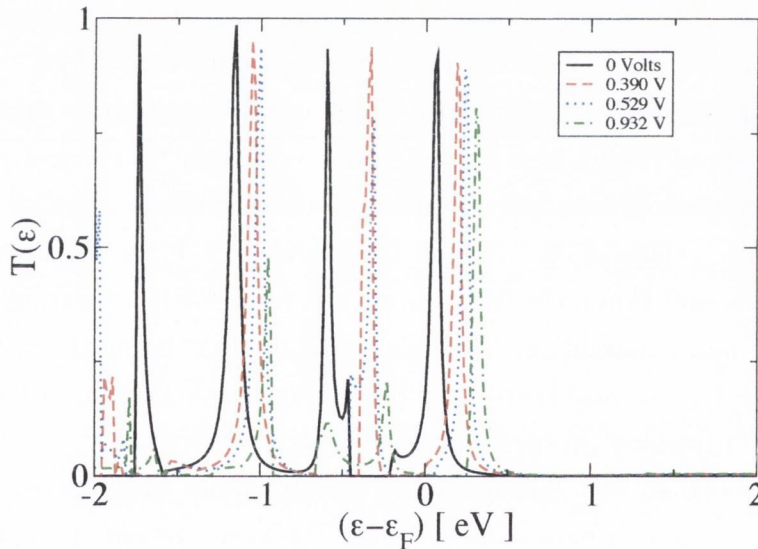


Figure 2.21: Transmission as a function of energy for different voltages for 1,4-benzene-dithiolate molecule attached to a [111] gold surface.

are the periodic boundary conditions, which might give rise to mini-gaps. However, other calculations including k -point sampling show similar behaviour [177].

A final comment on this issue is required. A possible explanation for the large disagreement between the experimental and theoretical results was given by Toher *et al.* [178]. The authors proposed that charging effects are not correctly taken into consideration by LDA and GGA because neither approximation possess the derivative discontinuity of the potential [177]. This mainly originates from the fact that LDA and GGA are not self-interaction free. This is of particular importance

in the case of weak coupling. In further work - using *Smeagol* - the authors showed that the energy levels of the self-interaction-corrected BDT molecule are driven down with respect to the Au Fermi energy. This in turn decreases the current.

More recent experimental data obtained in a more controlled set of experiments [27] seem to suggest that the conductance is higher than obtained by Reed and coworkers although still one order of magnitude smaller than theoretically predicted values. Results by Toher *et al.* are in reasonable agreement with this new set of results.

2.6 Conclusion

In this chapter we have presented the formalism for solving the ground state properties of a many-particle system using DFT. In particular, we have shown how DFT with an appropriate choice of exchange-correlation potential can give us an accurate description of the electronic structure of molecules and solids. Furthermore, we have shown how it is possible to take the Kohn-Sham Hamiltonian $H[n]$ - which is both a functional of the charge density and a single particle operator - and use it to calculate the non-equilibrium Green function and consequently the electronic transport properties of a nanoscopic system out of equilibrium (with an external bias applied).

The symbiotic relationship between DFT and NEGF has been realised within *Smeagol* our non-equilibrium electronic transport tool. We have highlighted *Smeagol*'s algorithm and main capabilities. We have presented how it interfaces with SIESTA, our choice of DFT code, and how it has been fully parallelised in order to cope with large scale computational problems in nanoscience.

As we have seen so far, *Smeagol* is a powerful tool. We can use it to perform calculations on a range of nanoscale systems. We have presented results on systems ranging from metallic point contacts to molecular electronic devices. In all cases we are able to obtain quantitative results that can be closely related to experimental observations and previous calculations.

In the next chapters we will use *Smeagol* to its full, exploring issues such as magnetic point contacts, molecular electronics using DNA and molecular spintronics, The latter is a field of particular interest to us because of our seminal work in the field [70, 88].

Chapter 3

Giant Magnetoresistance and $I - V$ Asymmetries in Nickel Magnetic Point Contacts

3.1 Introduction

The use of the GMR effect in industrial applications has already led to the construction of the present generation of magnetic data storage devices. However, in order to reach storage densities of the order of Terabit/in² a substantial down-scaling of the read/write devices is needed. One possible avenue to this target is given by magnetic point contacts (MPC's), where the lateral size of the typical contacts approaches the atomic scale.

Recent experiments have shown that nanoscaled magnetic point contacts may present huge magnetoresistance (HGMR) [11, 12, 157, 163, 179, 164] reaching up to a few hundred thousand percent (using the optimistic definition of MR). This result alone can be seen as a major leap toward nanoscopic magnetic memory read/write devices. In addition, it is important to report that electro-deposited nickel point contacts present highly asymmetric $I-V$ characteristics typical of a diode-like behaviour [179, 164]. A complete explanation of both these effects is still lacking.

To date there is a large debate around the origin of the large magnetoresistance effects in MPC's. On the one hand, it has been argued that magnetic field-induced mechanical effects can produce a large GMR (LGMR) - $\sim 100 - 500\%$. In fact, either magnetostriction, dipole-dipole interactions between the apexes [180] and magnetically induced stress relief [181] may have the effect of compressing the nanocontact once a magnetic field is applied. This enlarges the cross section of the MPC and consequently the resistance of the junction decreases. On the other hand, there are also strong indications that mechanical effects alone are not able to account for whole

magnetoresistance. Specifically García *et. al.* have shown that the behaviour of MPC's does not comply with mechanical changes, in particular with magnetostriction effects [11, 157].

In our opinion, three important works demonstrated that LGMR in magnetic point contacts can be attributed to an electronic origin. First van Hoof *et. al.* [182] showed that the resistance of an abrupt domain wall (DW) can be rather large, giving rise to a GMR of the order of 60%. The calculations were performed using realistic band-structure for Stoner ferromagnets (Fe, Ni and Co) and the current was calculated in linear response limit. Along the same lines Tataru *et. al.* [183] demonstrated that later confinement can enhance the GMR. In this work values of the order of 300% were obtained in ultra-small point contacts, in good agreement with experiments. Finally, Bruno [162] demonstrated that if the magnetic moments on the apexes of a magnetic constriction are not aligned parallel to each other then a DW will be formed inside the constricted region. The main features of this DW are quite different from those of the well known Bloch [102, 184] and Néel [103] walls. In particular, the crucial point is that the length of the DW is predicted to be as long as the diameter of the constriction. This result suggests that the DW trapped in an atomic scale MPC may be very sharp, only a few atomic planes long. At this length scales a DW produces a rather strong spin-dependent scattering potential and large magneto-induced effects are somehow expected. In this context it is important to report that such an extreme confinement has been already achieved by contacting two magnetic grains with different orientation [163]. Unfortunately, these theoretical predictions are unable to account for HGMR. The MR values are usually two or three orders of magnitude lower even in the best case scenario (largest scattering).

Since these seminal works, a number of theoretical works on transport through magnetic domain walls have been presented [185, 186, 187]. These, as well as the two previously mentioned, consider equilibrium transport in the spirit of the Landauer-Büttiker formalism [84]; current induced effects such as charging of the point contact and, quite possibly, movement of the domain wall have not been taken into consideration. However, in low dimensional systems such as MPCs the introduction of small biases might cause charge accumulation inside the MPC, changing its transport properties [188].

The aim of this chapter is to provide a fully quantitative description of the origins of the reported LGMR and HGMR values and to understand whether they arise solely from electronic mechanisms. In order to do so one must consider an accurate description of the electronic structure of these MPCs which lead us into DFT-based

Hamiltonians and ultimately to *Smeagol*. *Smeagol* was used to calculate the zero bias transmission probabilities of different atomic and magnetic configurations of our system.

Recently it has been suggested that the presence of oxygen in Ni MPCs could lead to HGMR [158]. This suggestion follows from the insulating ground state of bulk NiO. Therefore it is also interesting to address the issue of impurities in the MPCs and their effects on the transport properties.

In all cases we model the magnetoresistance in MPC using the typical spin-valve scheme: we assume that in the absence of a magnetic field, the magnetisation vectors of the two leads are aligned opposite to each other - antiparallel alignment (AA). Therefore in the zero field situation a sharp DW is formed inside the MPC. Then, when a magnetic field is applied, the magnetic moments of the leads align parallel to each other and the wall is eliminated - parallel alignment (PA).

Furthermore we only consider collinear spins. This is justified by a recent calculation from Imamura *et al.* [185] who have used a Heisenberg model in a mean field approximation to show that, in the case of a domain wall pinned in a constriction, there is no spin precession and minority and majority bands can be treated separately.

3.2 Magnetoresistance in Nickel point contacts: an *ab initio* study

Hence the question raised in section (3.1) of this chapter still remains: is it possible to obtain huge giant-magnetoresistance (in excess of 100,000 %) solely from electronic effects [11, 157, 163, 179] ?

In order to address this raised in section (3.1), we need to model our point contact using a realistic description of the electronic structure while choosing an atomic arrangement that best describes the experimental conditions. *Smeagol* is the ideal tool for this task.

In the case of atomically thin Ni MPCs, Viret *et al.* have shown by molecular dynamics simulations that the last step in the stretching of a Ni break junction experiment forms two Ni pyramids joined at the neck by two atoms, without forming a single atom chain [159]. This particular configuration is shown in Fig. (3.1). Transmission electron microscopy experiments have confirmed that metallic quantum point contacts retain their crystallographic arrangement even at the limit of atomically thin junctions for a range of different metals [146, 149, 92, 152, 168]. Hence,

the two pyramids maintain the bulk lattice structure.

3.2.1 Impurity-free MPCs: relaxation and transport I

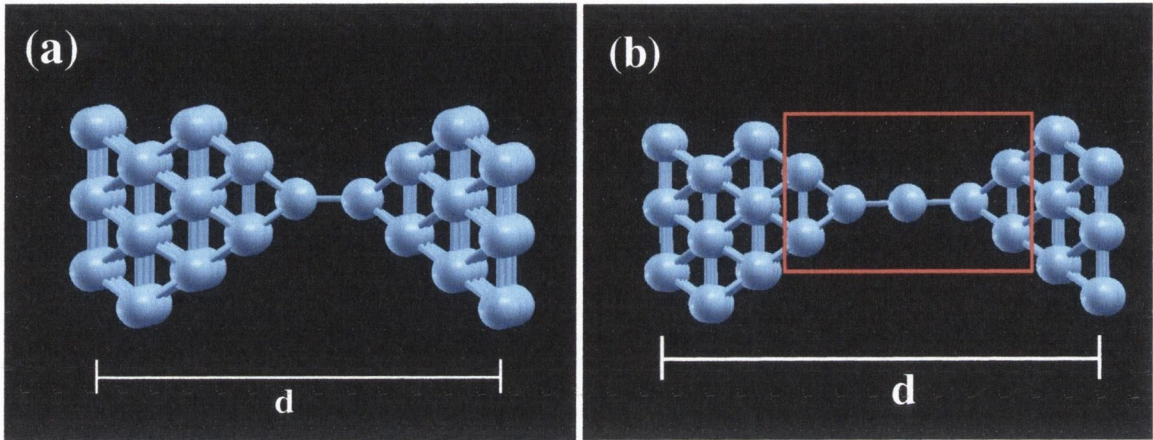


Figure 3.1: Ball-and-stick representation of a nickel point contact formed by two pyramidal tips joined together. a) The pyramids are directly connected at the end points (MPC-2), b) the tips are bridged together by a single atom (MPC-3). The eleven atoms enclosed in the red rectangle correspond to the tip atoms (three atoms forming the atomic chain and four atoms on either side forming the apices).

Our simulations are performed on atomic size point contacts with an arrangement similar to those proposed by Viret *et al.* [159]. The structure of a Ni break junction close to the rupture point is modelled as two Ni pyramids oriented along the [001] direction. At first, the geometry of the two tips follows the crystallographic structure of fcc bulk Ni as obtained by DFT.¹ We considered two possible cases: 1) the tips are directly bridged together (MPC-2 geometry) or 2) one nickel atom is placed between the two pyramids to form a single-atom chain (MPC-3). These two arrangements are shown in figure (3.1). The structures consist of 55 and 56 nickel atoms respectively.

The equilibrium position of the Ni atoms are expected to change due to relaxations (specially for the atoms closest to and at the tip). Hence we performed structure relaxations of the MPCs using SIESTA to obtain the lowest energy arrangement for both configurations. The atoms are allowed to relax following standard conjugate gradient (CG) methods [40]. Two of the left-most and two of the right-most planes were kept fixed at the Ni fcc bulk positions, while the middle atoms are free to move. Once convergence for a particular arrangement is obtained we then increase the size

¹Lattice constant $a \sim 3.46 \text{ \AA}$.

of the cell, d (the distance between the pyramids along the z direction) by slightly separating the planes. Then another relaxation is performed.

The basis set is chosen as a double- ζ (DZ) s with polarised orbitals and a double- ζ p and d .² The resulting total energy curve as a function of the cell size is presented in figure (3.2).³ In both cases there we can see a clear energy minimum. Hereafter, all the calculations shown were performed using the relaxed coordinates at this energy minimum.

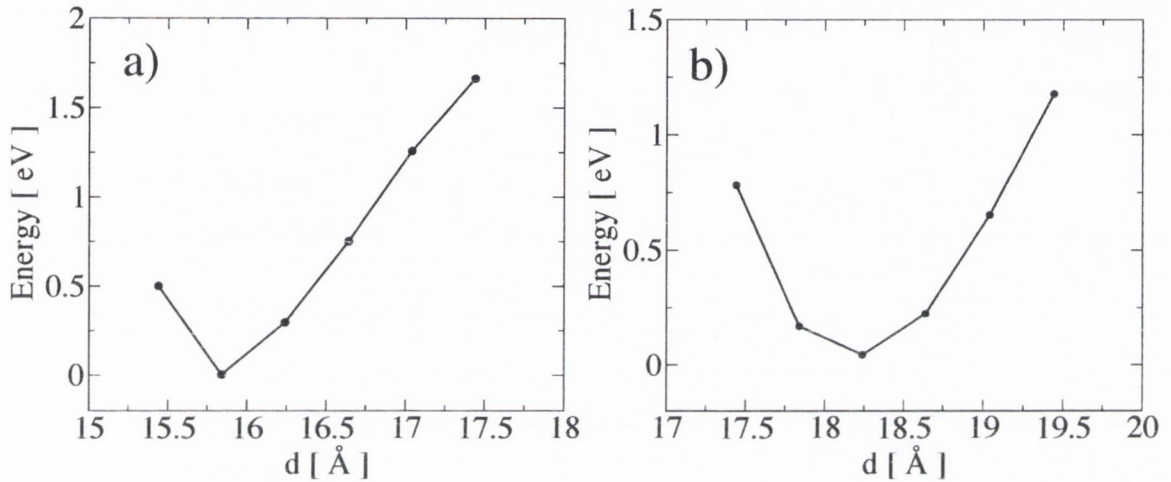


Figure 3.2: Total energy curves for different tip separations in the a) MPC-2 and b) MPC-3 structures shown in Fig. (3.1)). The atoms in the central region are allowed to relax while the last two slices to the left and to the right are kept at fixed coordinates. The positions of the atoms at the apexes are kept at their respective bulk fcc arrangement. The tips are oriented along the [001] direction.

The projected density of states (PDOS) can provide some insight into the character the states lying close to the Fermi level. In figure (3.3) we present the density of states projected onto the s and d orbitals of the entire MPC and the PDOS of the tip atoms. We can see that the density of states for the entire MPC is similar to the one of the apexes (four atoms to the left and to the right of the three-atom chain), but for a scaling factor (which account for the number of atoms in the relative region). It clearly resembles the density of states of bulk nickel. On the other hand, the PDOS for the three-atom chain (Fig. (3.3d)) clearly shows the effects of low-coordination, the density of states is much sharper than in the rest of the MPC (and in that of bulk). This in turn will result in some sharp features in the transmission probabilities of the point contact, specially for minority spins.

²Note that the p orbitals used here are not semi-core states, but the $4p$ orbital of Ni (empty valence orbitals).

³Our relaxations are performed in a collinear ferromagnetic alignment. We have assumed that

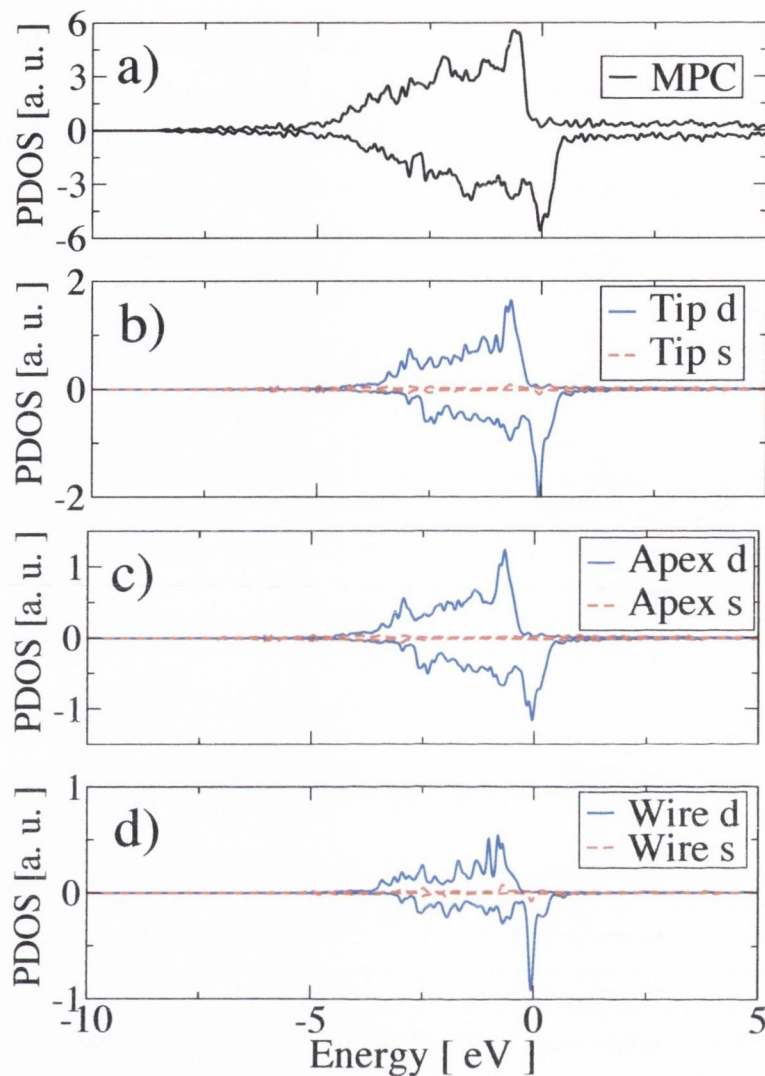


Figure 3.3: Projected density of states for the MPC-3 structure in figure (3.1b). a) Whole MPC, b) 11 atoms in the central region, three atoms forming the wire and four apex atoms on either side (shown inside the red box in Fig. (3.1b)). c) Apex atoms on the left and on the right. d) The 3 Ni atoms in the monoatomic chain.

The low bias magnetoresistance values for these MPCs can be obtained by calculating the zero-bias transmission coefficients. Figure (3.4) shows the energy-dependent transmission coefficients for the parallel (a) and anti-parallel (b) spin configurations of the MPC-2 arrangement.

We can clearly see that in the parallel configuration the conductance at the Fermi level is dominated by the minority spins ($G \sim 2.5 G_0$) whereas the conductance for the majority lies close to $1 G_0$. This behaviour can be explained by the presence

magnetic contributions to the forces will not significantly influence the final structure.

of partially empty d states at the Fermi level for the minority spins and completely filled states below the Fermi energy for the majority. At energies $(E - E_F) > 0$, the conductance is governed by the unpolarised s orbitals and it is quite similar for both up and down spins. For s orbitals one would expect a single channel for each spin component, but given the small distance between the pyramids we also observe direct transmission across the apexes of the pyramids, hence a larger conductance. In the anti-parallel case the system the DW is positioned between the two tips, so we see a mirror symmetric system and the transmission coefficients for majority and minority spins are identical. The GMR ratio for the MCP-2 was calculated to be approximately -5 %. Note that the GMR is not only very small, but also negative. This means that the conductance in the anti-parallel case is higher than that in the parallel one.

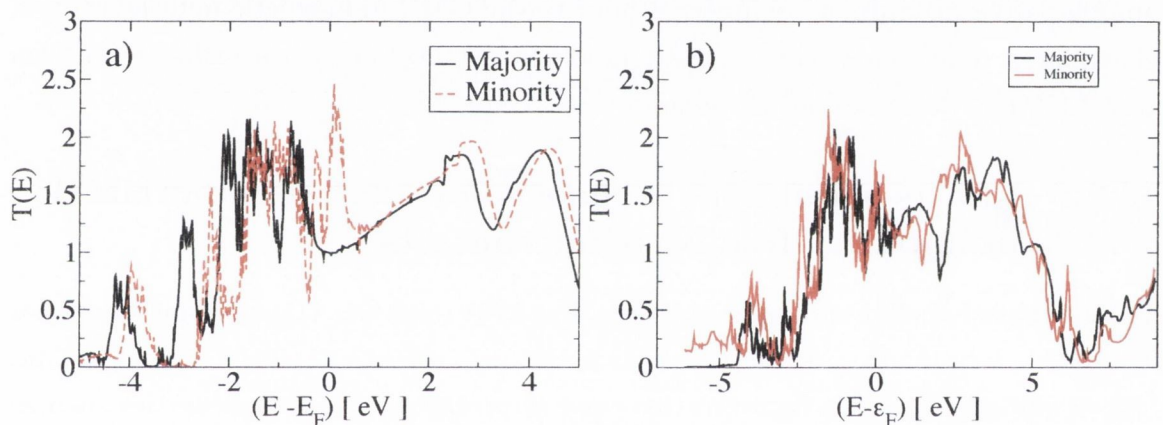


Figure 3.4: Transmission coefficients as a function of energy for Ni point contacts for the MPC-2 structure in the (a) parallel and (b) anti-parallel configuration. The majority (minority) spins are represented by solid (dashed) lines.

For the single-atom chain the picture changes slightly. Figure (3.5) shows the transmission coefficients for the MPC-3 as a function of energy. In the PA configuration we still see minority-dominated transmission, but with a slightly higher conductance. Most importantly, the introduction of an extra atom drastically reduces the conductance above the Fermi level corroborating our interpretation of direct transmission across the pyramids. In fact, we see a reasonably flat plateau around $1 G_0$ for $\epsilon > E_F$, a contribution from the unpolarised s electrons. In the AA configuration we placed the DW between the first and the second atom of the chain, hence the symmetry is broken. The GMR for this case is slightly higher ($\sim 20\%$).

Unfortunately, in both cases presented here s electrons strongly contribute to the transmission coefficients for both majority and minority spins. The presence of nearly

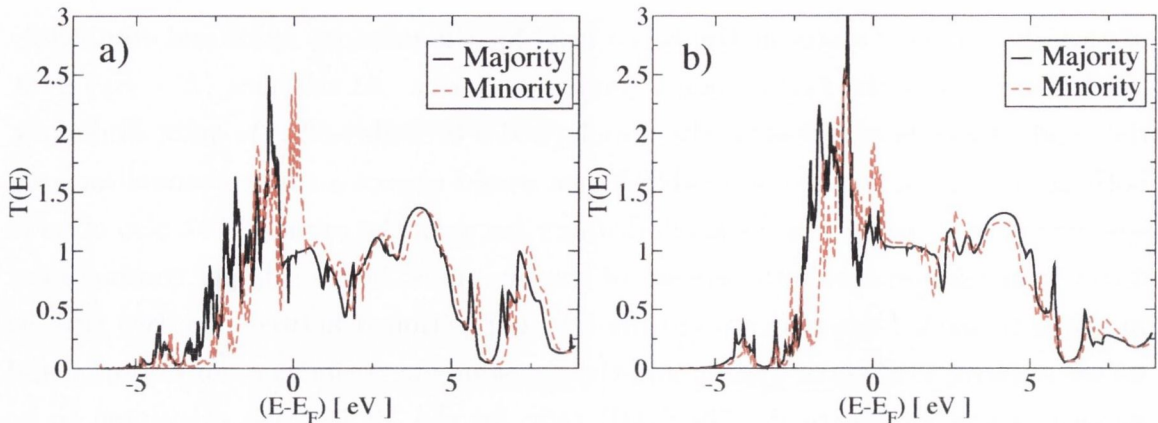


Figure 3.5: Transmission coefficients as a function of energy for Ni point contacts for a single atom chain in the (a) parallel and (b) anti-parallel configuration. The majority (minority) spins are represented by solid black (dashed red) lines.

unpolarised s orbitals set an inherent limit to the GMR in magnetic multilayers too. Therefore, so far, our results seem to indicate that huge magnetoresistance (or even just LGMR) effects are not possible in these systems.

3.2.2 Effects of different exchange-correlation potentials (V_{XC}) in impurity-free Ni point contacts

Although extremely useful in many cases, the LDA (and GGA) gives poor results for a variety of systems, specially those where strong correlation effects are important. Albeit bulk Ni does not figure in this class of problems (in fact, properties such as the magnetic moment are extremely well described by LDA), the same cannot be said about low-coordinated systems such as atomic-size chains.

In transition metals the d orbitals figure close to or at the Fermi level. The bands formed by these atoms are highly directional and in an one-dimensional system, one would expect a lift of the degeneracy. Let's take an infinite Ni chain for example. In figure (3.6) we present a schematic representation of the d orbitals in an mono-atomic wire. While orbitals d_{z^2} , d_{yz} and d_{xz} are oriented along the chain, orbitals d_{xy} and $d_{x^2-y^2}$ are perpendicular to it axis. Because d orbitals are quite short the coupling between adjacent orbitals, in the case of d_{xy} and $d_{x^2-y^2}$, is rather small which in turn will lead to localisation and strong $e - e$ interaction.⁴

Hence, in order to describe the electronic structure it is necessary to use exchange and correlation functionals which account for strong correlation. Unfortunately, most

⁴Note that in noble metals such as gold and silver the valence orbitals have s character which do not have any angular dependence. One would expect in this case LDA to yield a good description of the atomic chains (see section (2.5.2)).

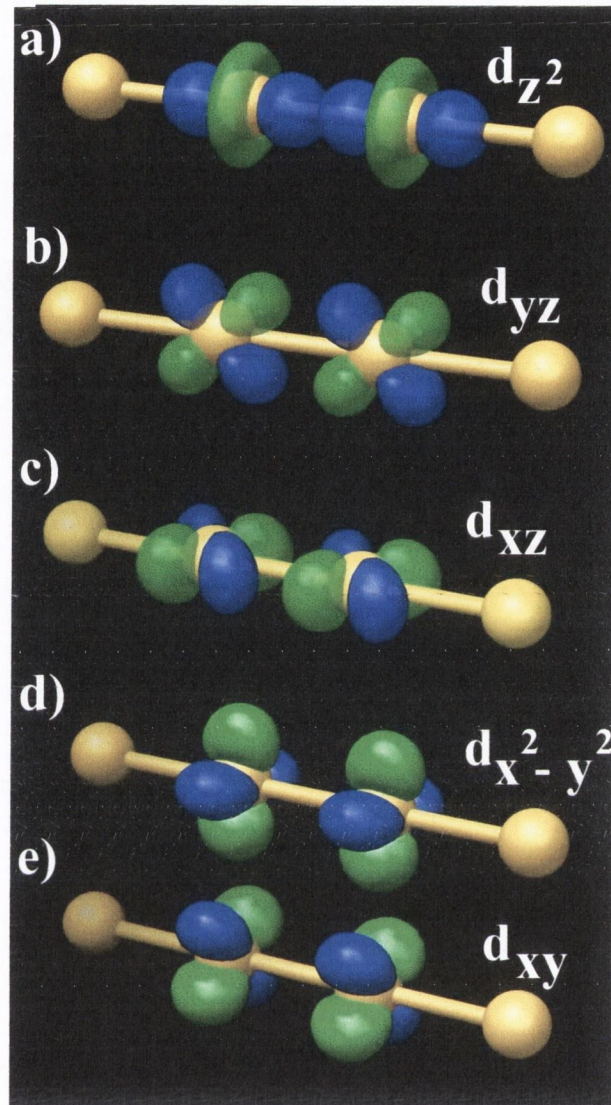


Figure 3.6: Schematic representation of the atomic orbitals in an infinite Ni mono-atomic wire oriented along z . a) d_{z^2} , b) d_{yz} , c) d_{xz} , d) $d_{x^2-y^2}$ and e) d_{xy} . The $d_{x^2-y^2}$ and d_{xy} are perpendicular to the axis of the wire and therefore weakly coupled.

functionals that correct over LDA tend to over-correct metallic systems, where usually LDA gives good results. The problem then becomes that of finding a good functional for the low connectivity apex region which does not alter the electronic structure of the planes at the edges of the cell which resemble bulk Ni.

The LDA+U is particularly suited for this purpose. Albeit based on empirical parameters one can choose to correct a set of d orbitals on a particular group of atoms preserving the LDA description for the rest of the system. The LDA+U functional was implemented in SIESTA [129] and Smeagol [85].

In order to gauge the effect of the LDA+U approximation on the transport prop-

erties we first performed calculations on an infinite one-dimensional nickel chain. This way we find the values of U and J for which the band structure of our chain is correctly described. We consider a linear chain of Nickel atoms $\sim 2.24 \text{ \AA}$ apart oriented along the z direction and in the ferromagnetic alignment. This lattice spacing corresponds to the approximate interatomic distance between atoms in the three atom chain of the MPC. We then performed calculations using different types of exchange-correlation potentials namely: standard LSDA, LDA+U [129] and ASIC. The latter was implemented in SIESTA by Pemmaraju *et al.* [86].

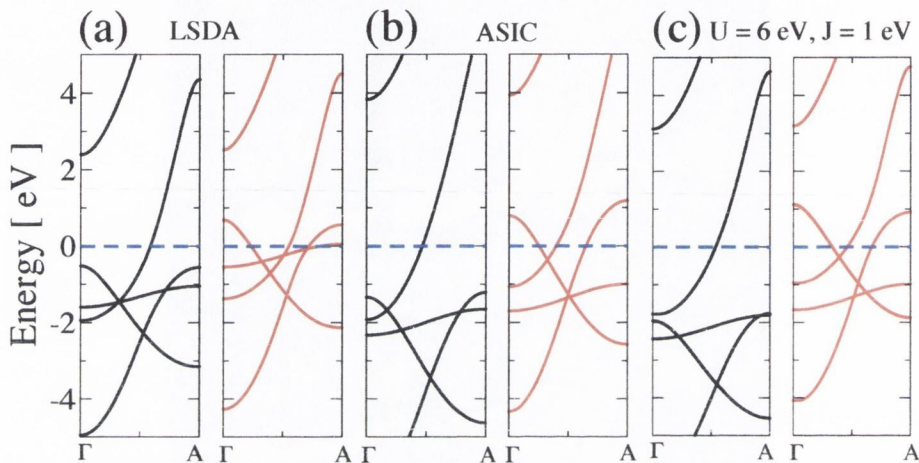


Figure 3.7: Band structures around the Fermi level for a one-dimensional infinite nickel chain. a) LSDA, b) atomic self-interaction correction and c) LDA+U with $U=6 \text{ eV}$ and $J=1 \text{ eV}$. The black (red) curves correspond to majority (minority) spin bands.

Atomic SIC, which is fully *ab initio* (it does not require empirical parameters) was taken as our benchmark for LDA+U. In figure (3.7) we present the band structure along the chain axis and demonstrate the effects of low dimensionality on Nickel. When compared to standard LSDA, we can clearly see that the more localised filled d bands are shifted down in energy, away from the Fermi level; more prominently the minority d_{xy} and $d_{x^2-y^2}$ states which are perpendicular to chain axis and present a very loose interatomic coupling lie close to the Fermi level for LSDA and are shifted downwards in ASIC and LDA+U.

Comparing our calculations for LDA+U and ASIC we can settle on a set of values for U and J which correctly describe the band structure of the infinite chain including corrections for the occupied orbitals,

$$U = 6 \text{ eV} \quad , \quad J = 1 \text{ eV}. \quad (3.1)$$

These values were used for all our calculations.

We assume that the atomic arrangement is not significantly affected by the Hubbard- U correction over LDA, hence we have kept the same arrangement from the previous section (Fig. (3.1)). The transmission coefficients as a function of energy for the MPC-3 are shown in figure (3.8). From the figure we can see that the total transmission in the PA close to the Fermi level is enhanced (particularly for minority spins) compared to the LSDA calculation presented in the previous section. We can also see that the transmission for the majority spins is close to unity for a wide range of energies indicating less hybridisation between s and d states. This is also clear when we see that the conductance due to d orbitals starts to play a role at lower energies when compared to our LSDA calculations.

The results for the parallel case can be directly correlated to the band structures of figure (3.7). The majority spins present a single broad s band (the first d band is approximately 3 eV below). For the minority spins there is a doubly degenerate d state (d_{yz} and d_{xz}) and one hybridised $s - d_{z^2}$ state (note the anti-crossing at the Fermi level) which in turn results in a conductance of about $2.5 G_0$.

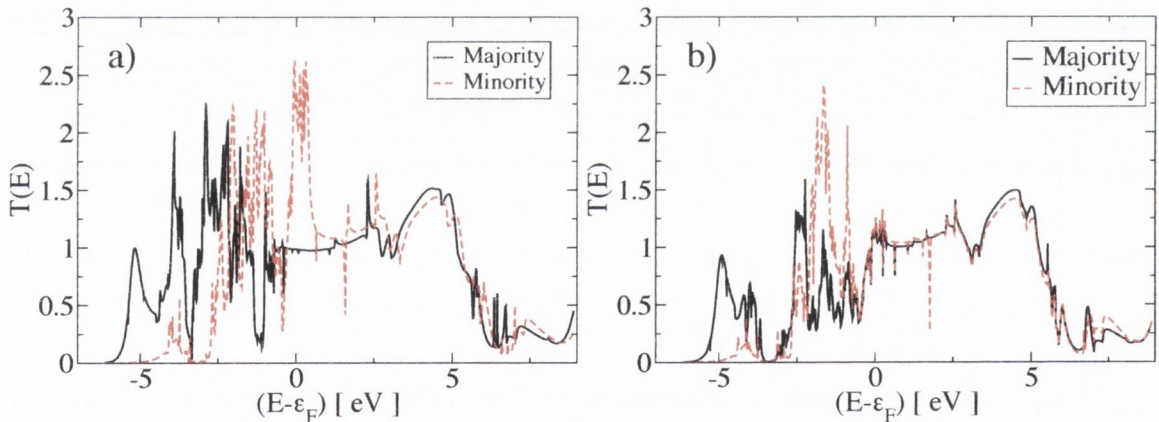


Figure 3.8: Transmission coefficients as a function of energy using LDA+ U for Ni point contacts with using LDA+ U . (a) Parallel and (b) anti-parallel cases for the single-long chain. The values of U and J were set to 6 eV and 1 eV respectively.

We can also use Fig. (3.7) to understand the AA. Let us assume that the three atom chain can be considered as two semi-infinite Ni wires separated by a DW. In that case the band structure on the right-hand-side is swapped (up spins \rightleftharpoons down spins) compared to the left-hand-side one. For Minority spins coming from the left have three open channels: one hybridised $s - d_{z^2}$ band and the degenerate d_{yz} and d_{xz} orbitals. When they flow across the domain wall they must propagate as majority states. For majority spins there is only a single sd_{z^2} band. Hence the other two states Bloch states are completely backscattered and the transmission is approximately 1

G_0 . Moreover, if electrons are coming from the left on the majority spin channel there is only one accessible band at the Fermi level which is also available for minority spins once the electrons flow across the DW. Hence, for both up and down spins this simple picture gives a conductance of $1 G_0$.

The total GMR in this case goes up considerably to approximately 60 %, in agreement with similar calculations using performed with alternative *ab initio* methods [189, 190]. However, this value is at least two orders of magnitude smaller than the ones observed in some of the experiments where HGMR was measured [11, 157, 163].

Although LDA+U significantly changes the electronic structure of the wire close to the Fermi level, the overall effect on the transmission coefficients is not enough to give rise to HGMR. This is mostly because the d_{xy} and $d_{x^2-y^2}$ bands which are removed from the Fermi level when we use LDA+U have little of no influence on the transport properties of the MPC.

On one hand, the GMR values obtained above show that it is possible to have useful nanoscale spintronics devices. We have observed that it is possible to obtain GMR in atomic point contacts with a magnetoresistance ratio at least similar to that of multilayer materials. This can lead to smaller technology preserving the same sensitivity of standard read/write heads in computer hard drives. On the other hand, despite larger GMR ratios, the introduction of the LDA+U exchange-correlation functional to correct for localisation does not qualitatively change the picture. Most notably, we have been unable to account for HGMR from solely electronic arguments. This is mostly because the d_{xy} and $d_{x^2-y^2}$ bands which are removed from the Fermi level when we use LDA+U have little of no influence on the transport properties of the MPC.

Hence, one must conclude that impurity free MPCs do not present HGMR for the arrangements we have studied. Other mechanisms might be playing a role. One possibility is that impurities are present in the MPC.

3.2.3 Oxygen-rich MPCs: relaxation and transport II

Recently García *et al.* [158] have proposed that the presence of impurities, in particular oxygen might be related to HGMR (values exceeding 1,000 %). These experiments are performed in air, but it is observed that even experiments in ultra high vacuum conditions can become contaminated after a couple of hours [92]. Therefore, it is reasonable to speculate that impurity atoms may be lying close to the constricted region in MPCs. It is also very likely that at the atomic scale even a single impurity may have a large effect on the current flowing through the device.

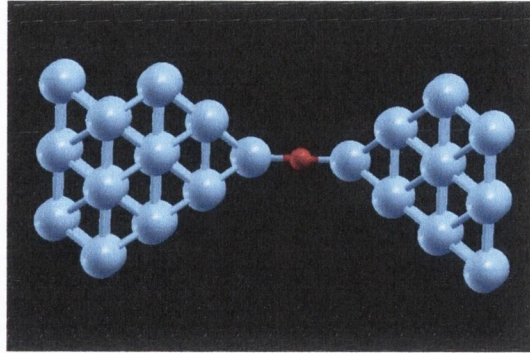


Figure 3.9: Ball-and-stick representation of the converged atomic arrangement of a nickel point contact with one oxygen atom bridging the gap between the two tips. Colour code: blue - Ni; red - O.

It is also well known that Ni is extremely reactive to oxygen and that bulk NiO is an insulator. If we position a single oxygen impurity bridging the two Ni [001] pyramids, the central region will resemble a one-dimensional NiO nanowire. If this system is insulating as its bulk counterpart it is possible that the contribution coming from the non-spin-polarised s bands will be removed from the Fermi level. In turn, this could lead to larger MR ratios. In many aspects this 1D system is the smallest conceivable tunnelling junction.

Tunnelling junctions are made of two magnetic layers intercalated with a non-magnetic tunnel barrier. For Fe/MgO tunnelling junctions, Parkin *et al.* [191] and Yuasa *et al.* [192] have shown that GMR ratios can reach in excess of 300 %. Furthermore, theoretical calculations have shown that the conductance is highly sensitive to the position on the transverse Brillouin zone [140]. In particular, minority spins present high conductance in small regions away from the Γ point and low conductance everywhere else in the BZ.

The same argument used for molecules in the introduction can be applied here. That is, at such a small scale the BZ collapses into a single point. Hence, by appropriately tailoring the MPC, we can probe different points in the BZ and considerably increase the GMR (possibly reaching HGMR values).

Hence we must answer the question of whether the 1D NiO wire is still insulating. If that is the case, then we also need to address the possibility of finding HGMR for this system.

We can start our analysis by using simple LSDA. As it was done with the impurity-free Ni MPC, we also need to find the most energetically favourable arrangement for the device. Using the same method already discussed, *ab initio* atomic relaxations are performed on the system presented in figure (3.9). Whilst the ba-

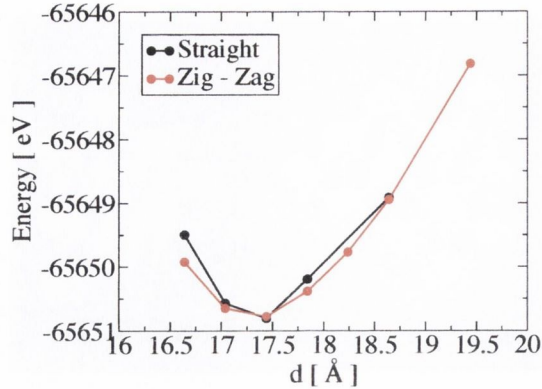


Figure 3.10: Total energy curves using LSDA for different tip separations of a nickel point contact with one oxygen atom between the tips. We started from two different configurations, a straight configuration (black curve) in which the oxygen atom lies along the axis of the two pyramids and a zig-zag configuration (red curve) where the oxygen is initially displaced from the axis. Note that there is a single energy minimum independent of the starting configuration.

sis set for Ni is the same as the previous calculation we use a double- ζ basis with polarisation for oxygen s and p orbitals.

We performed our calculations with two different initial arrangements of the oxygen atom. In the first case we placed the oxygen atom along the axis of the two pyramids while in the second it was displaced perpendicular to the axis. In both configurations the oxygen atom as well as some of the Ni atoms were allowed to relax to their preferred arrangement. The total energy curve as a function of the elongation (distance d between the bases of the two pyramids) is shown in figure (3.10). Despite initially different, at the energy minimum ($d = 17.04 \text{ \AA}$), both arrangements have an energy minimum for a straight configuration. In contrast, at smaller separations (compressive strain), in order to obtain better bond distances, the oxygen atom prefers a zig-zag arrangement.

By using the atomic positions at the energy minimum we proceed to calculate the zero-bias conductance which are shown in figure (3.11). The transmission coefficients for the PA configuration show a high conductance for the minority and low conductance for the majority spins (approximately $0.5 G_0$ and $2.5 G_0$ respectively). This is clearly an indication that we have suppressed part of the contribution to the conductance close to E_F which come from the s states.

In the AA the majority and minority spins are identical given the mirror-symmetric nature of the system (see figure (3.11b)). The conductance in this case is equal to $G^\uparrow = G^\downarrow = 1.75 G_0$. The overall conductance is larger in the antiparallel case which in turn yields a negative magnetoresistance ratio of approximately -6.3% .

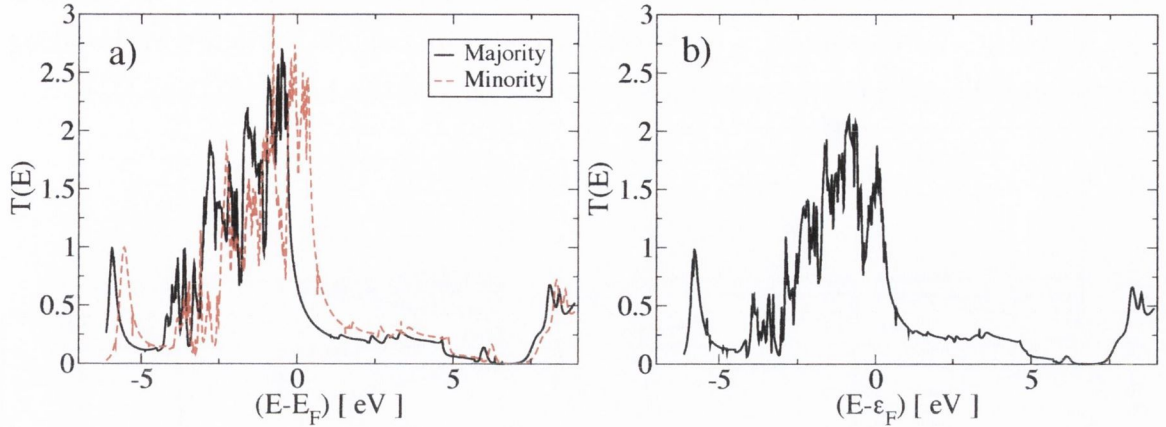


Figure 3.11: Zero bias transmission coefficients of Ni point contacts with oxygen in the LDA approximation for a) parallel and b) anti-parallel cases. The solid (dashed) lines represent the majority (minority spins). In the anti-parallel case, due to the mirror symmetry of the MPC, the transmission coefficients for majority and minority spins are identical.

Although we have shown that the s orbitals seem to be partially removed from the region around E_F , the desired insulating behaviour, specially for the AA case, seems to be still missing. At first, it might seem that the prospect of MPC-based tunnelling devices is dreary. However one must remember that LDA fails in describing bulk NiO correctly and one needs a different exchange and correlation functional.

3.2.4 Effects of different exchange-correlation potentials (V_{XC}) for oxygen-rich Ni point contacts

We have shown earlier (see section (2.2.1)) that the LDA+U is a much more appropriate exchange and correlation functional to treat bulk NiO. It is only natural to use the same method with a one-dimensional NiO chain. In this case correlation effects are very likely enhanced by low-coordination (2-fold instead of the 6-fold in bulk NiO).

We have also shown, in section (2.5.2), that the band structure of an infinite chain can give some insight into the character of the transport properties in quantum point contacts (albeit the final transmission coefficients are given by a combination of factors including the alignment of the Fermi energy and the coupling to the electrodes). Therefore, we can start exploring the Ni-O-Ni tip shown in figure (3.9) by looking at a one-dimensional infinite NiO chain.

We performed calculations using both LDA and LDA+U for an infinite NiO chain with a fixed Ni-O distance of 1.8 \AA . Let us first focus on the LDA. Our results for the band structure and PDOS for these two alignments are shown in figure (3.12). The

total energy difference between these two configurations is small, *i. e.*, the chain is not magnetic. Furthermore, in both cases we see a metallic behaviour corroborating the results obtained for the transmission coefficients of the MCP (Fig. (3.11)).

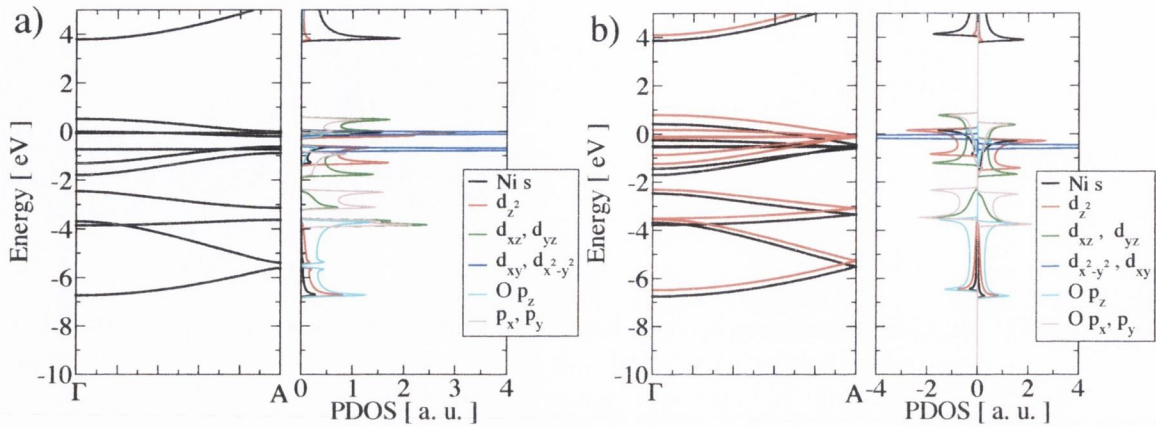


Figure 3.12: Band structures (left panels) and projected density of states (right panels) for an infinite one-dimensional NiO wire using LDA in the (a) antiferromagnetic and (b) ferromagnetic alignments. Black (red) lines indicate majority (minority) spin bands. In the AA case majority and minority spin bands and the projected density of states are identical.

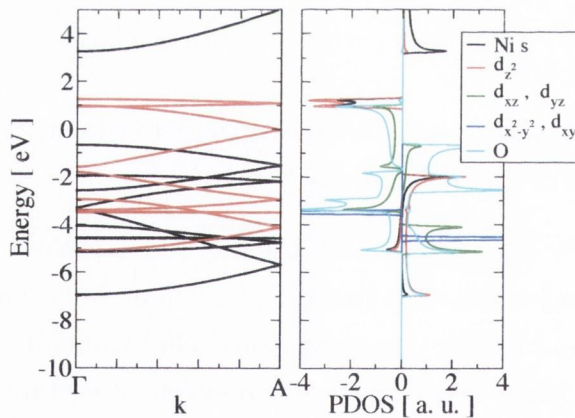


Figure 3.13: Band structures (left hand-side panel) and projected density of states (right hand-side panel) for an infinite one-dimensional NiO wire using LDA+U in the ferromagnetic alignment. The values of U and J are set to 6 eV and 1 eV respectively.

The electronic structure of the nanowire changes significantly with LDA+U. For the ferromagnetic alignment the band structure shown in figure (3.13) is that of a half-metal, *i. e.*, the majority spin states are completely filled and do not present DOS at $E - F$. Therefore the band-structure is that of an insulator. In contrast the minority spin bands lie close to the Fermi level and are partially filled. Differently

from the pure nickel chain there is no signature of the s band around E_F . The Fermi surface is mostly due to oxygen p and Ni d_{xz} and d_{yz} .

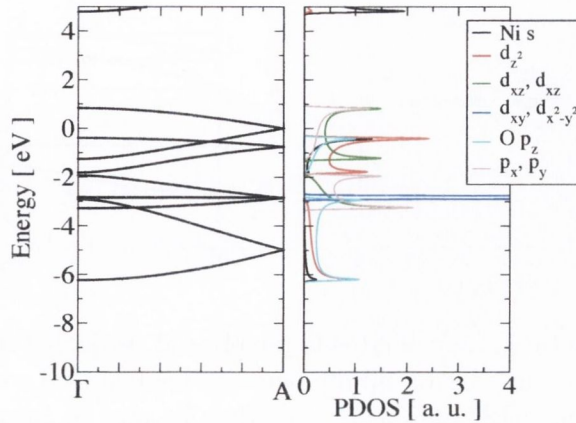


Figure 3.14: Band structures (left hand-side panel) and projected density of states (right hand-side panel) for an non-magnetic infinite one-dimensional NiO wire using LDA+U. The values of U and J are set to 6 eV and 1 eV respectively. Majority and minority spin bands are identical.

However, the lowest energy configuration (in LDA+U) for an infinite NiO chain is non-magnetic.⁵ This means that the occupation in each Ni atom for up and down spins is identical. The band structure and PDOS for this solution are shown in figure (3.14) and it is clearly metallic.

Finally, if starting from the anti-ferromagnetic alignment, we will observe that the results are very sensitive to the initial choice of orbital occupation. The results which are shown in figure (3.15) range from an insulator to a conductor.⁶ The band structure for the insulating AF nickel oxide wires is similar to those obtained using all-electron density functional theory with the B3LYP exchange-correlation potential.⁷ It was not possible to converge the conducting system with this latter functional.

When we attach the pyramids to the chain to form the MPC we are unable to converge the non-magnetic solution. The much larger pyramids which resemble bulk Ni, and therefore magnetic, strongly influence the two Ni atoms forming the chain. Hence, the final configuration can only be either the PA or AA the configuration.

⁵The non-magnetic solution is the most favourable one for a range of values of U ranging from 2 eV to 8 eV (J was kept constant at 1 eV).

⁶For an 1D system one would expect that a Peierls [193] distortion gives rise to a gap at the Fermi level and consequently prevents a conducting state to appear. Here we are only considering a hypothetical scenario in order to compare with the real transport calculations where the electrodes break translational symmetry and a conducting state becomes possible.

⁷The calculations were performed using CRYSTAL 2003 [194] and the all-electron basis sets provided in [195, 196].

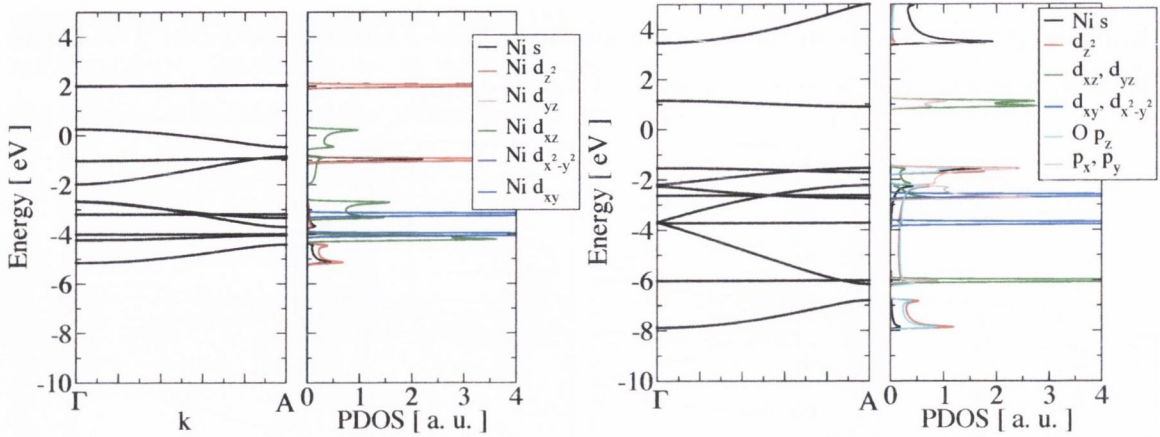


Figure 3.15: Band structures (left hand-side panel) and projected density of states (right hand-side panel) for an infinite one-dimensional NiO wire using LDA+U with anti-ferromagnetic alignment. a) Metallic and b) insulating solutions. The values of U and J are set to 6 eV and 1 eV respectively. We have used different starting orbital occupations for these antiferromagnetic calculations.

The transmission coefficients calculated using LDA+U are shown in figure (3.16). For the PA configuration we can see a qualitative agreement with the LDA case (figure (3.11a)). The transmission for minority spins is slightly higher and that for majority spins is lower ($\sim 0.2 G_0$). The majority d states are shifted downwards compared to the LDA case and although the transmission coefficients at E_F are non-zero, it does resemble the half-metal behaviour observed for the infinite chain. For the AA we have chosen to work with the insulating state. In that case a completely different picture arises: the conductance for both parallel and antiparallel is approximately $0.2 G_0$ because the s states are driven away from the Fermi energy. The resulting magnetoresistance reaches the much higher value of 450 %.

Recently calculations using B3LYP [197] in oxygen-rich MPC's have shown GMR ratios of approximately 600 % . The discrepancy in the results are probably due to differences in the anti-parallel configuration. The authors of the aforementioned work use the B3LYP functional on all the atoms of the point contact although it has been shown to over-correct the properties of bulk Ni resulting in a considerably larger magnetic moment when compared to the experimental value. Furthermore, they also describe the electrodes using a model Hamiltonian which can lead to extra scattering processes when one tries to match the leads' self-energies to the pyramids [82]. In metallic systems that is not so important, but in the tunnelling regime small differences in the electronic structure might lead to large changes in the conductance. Nevertheless, these results are within the same range as those from our calculations.

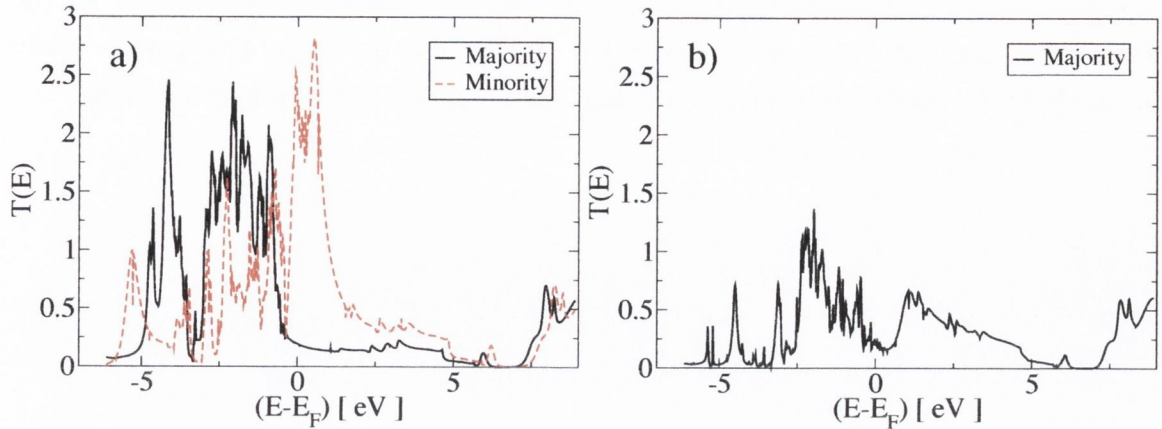


Figure 3.16: Zero bias transmission coefficients of Ni point contacts with oxygen in the LDA+U approximation for a) parallel and b) anti-parallel cases. The solid (dashed) lines represent the majority (minority spins)

3.3 Conclusion

In summary, in this chapter we have studied different aspects of magnetic point contacts and their applications as possible electronic devices. We have investigated, using NEGF's within a tight-binding approach, rôle of the position of the DW inside the junction and its effect on the I - V curves. Our main result is that largely asymmetric I - V curves can be found when the DW is asymmetrically placed inside the point contact, although the whole structure does not present any structural asymmetry. We have interpreted this result in terms of the charging properties of the junction and of spin-dependent HOMO/LUMO alignment. This asymmetric behaviour can only be obtained using a non-equilibrium approach to transport.

We have also studied MPCs using a more accurate DFT approach. Using *Smeagol* we addressed the issue of LGMR and HGMR in atomically sharp MPCs. In the case of impurity-free Ni MPCs we observe higher MR ratios when we use the LDA+U exchange and correlation functional. These results are comparable to calculations performed on similar systems [189, 190]. However, the observed increase is not able to account for HGMR (MR in excess of 10,000 %). We have speculated about the presence of oxygen impurities in the constriction forming an atomic size NiO tunnel barrier. In this case the use of LDA+U considerably changes the picture. For the benchmark structure formed by a NiO infinite chain LDA gives a metallic state for both PA and AA, whereas this may become insulating with the inclusion of corrections to the exchange and correlation functional. The magnetoresistance increases considerably to values close to 500 %.

This result is still at least one order of magnitude smaller than experimentally

observed values [189, 190]. From our calculations we must conclude, at least for the configurations that were studied here, that HGMR can not possibly originate solely from electronic means in contrast to what has been previously suggested [158].

Chapter 4

Giant Magnetoresistance in Organic Spin Valves

4.1 Introduction

Advances in nanoscale science are paving the way towards an entire new family of devices. It is now possible to envision systems where a single molecule comprising only a handful of atoms can perform the same type of task that is at present performed by significantly larger solid-state devices. We are now faced with endless possibilities.

As described before, the seminal work by Reed *et al.* [4] has shown one possible way to produce devices based on organic-molecule technology. Since then, other publications in the field have delivered a series of exciting results [4, 25, 26, 198] that show a wide range of phenomena ranging from switching and memory [25, 199] to rectification [200]. Some of these recent developments present real potential for applications.

The use of organic molecules for electronics has recently found its way into the field of magnetotransport [88]. The use of the spin degree of freedom opens new and interesting possibilities. In this area, the spin valve is the model device: two magnetic materials sandwiching a non-magnetic one. The mechanism determining the spin-transport properties derives from the interplay between the orientation of the electrodes' magnetic moments and the coupling of the different spin components to the spacer.

Recent work by Petta *et al.* [49] and Xiong *et al.* [50] has both shown magnetoresistance effects in organic molecules sandwiched between magnetic current/voltage electrodes. In the former, the authors have studied spin transport through organic tunnelling junctions formed by layering octane-dithiolate between nickel leads, whereas in the latter, aromatic molecules were intercalated in between cobalt and LaMnO₄.

In both cases the authors have shown that magnetoresistance is possible although perfect reproducibility of the results is still absent. In the case of Petta and coworkers the authors found a maximum GMR ratio of approximately 18 % , with a large sample to sample variation of MR which also included negative values.

In this chapter *Smeagol* is used to thoroughly study magneto-transport in molecular spin valves. We have considered two different families of molecules that present distinct transport mechanisms, namely coherent tunnelling and ballistic conductance. We give a detailed account of the states participating in the conductance. We also present the underlying effects driving the magnetoresistance and propose a way of engineering new devices using different anchoring groups between molecules and electrodes. Finally we use the idea of asymmetry-induced charging effects to simulate spin polarised STM-like experiments where an organic molecule is adsorbed on a surface and is probed by an STM tip, both of which magnetic.

In the following sections we present our *ab initio* transport calculations using the typical spin valve configuration. We consider two possible alignments of the leads' magnetisation: antiparallel (AA) or parallel (PA). Figure (4.1) shows a ball and stick sketch of one such molecule (1,4-benzene-dithiolate in this case) with the arrows pointing in the direction of the local magnetisation. The sulphur atom is used as the standard anchoring group due to strong bonding to gold [174, 175] and, in our case, nickel [201].

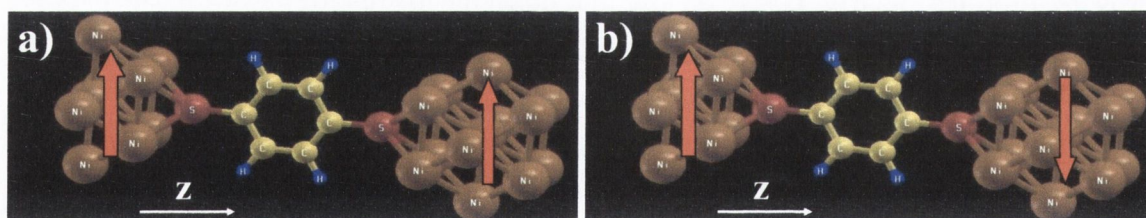


Figure 4.1: 1,4-benzene dithiolate (one benzene ring functionalised by two sulphur atoms at positions 1 and 4) attached via sulphur atoms to two [001]-oriented nickel electrodes. The orientation of the magnetic moments can be either a) parallel or b) anti-parallel.

Going to the details of our calculations, we always construct the unit cell of the extended molecule including four nickel atomic planes on each side. We use standard scalar relativistic pseudopotentials with the following reference configurations: H $1s^1 2p^0$, C $2s^2 2p^2 3d^0$, S $3s^2 3p^4 3d^0$ and Ni $4s^1 4p^0 3d^9$. Furthermore, for good convergence we need to consider a rather rich basis set. For both the molecules we have used a single zeta basis for H, C and S *s* orbitals, double zeta for Ni *s*, *p* and *d*, and double zeta polarised for C and S *p* orbitals [40]. This basis gives us a Hamiltonian

with over a thousand degrees of freedom. The LSDA exchange-correlation functional is used throughout. Finally the charge density is obtained by integrating the non-equilibrium Green function over 50 imaginary and 600 real energy points according to the scheme described in chapter (1) and references [70, 71].

4.2 Triphenyl-dithiolate: metallic regime

First we consider 1,4-[3]-phenyl-dithiolate (tricene) consisting of three benzene rings functionalised by thiol groups at both ends. A description of the molecule is presented in figure (4.2a). The molecule is attached to a Ni [001] surface terminated with a pyramid of nickel atoms. The molecule is connected to the hollow site of the nickel surface by the thiolate group. Although a multitude of other anchoring situations may be present in actual samples, this seems to be the most stable for the thiolate group on [001] Ni [201]. We always relax the atomic coordinates of the molecule on the surface using a conjugate gradient method within DFT [40] with a tolerance on the forces of $0.01 \text{ eV}\text{\AA}^{-1}$. The relaxations were performed taking a single surface of nickel and attaching the molecule via S-Ni bonds. These were then allowed to relax in a super cell with no periodic boundary conditions. The final relaxed distance between the Ni surface and the S atom was found to be 1.26 \AA . We then attached the other surface to the remaining sulphur atom to form the actual junction.

Before calculating the transport properties of this system it is interesting to understand the electronic configuration of the isolated molecule. The density of states and the charge-density iso-surfaces of the highest occupied and lowest unoccupied molecular orbital (HOMO and LUMO) for the isolated molecule are presented in Fig (4.2b). We can see that the HOMO-LUMO gap is approximately 2.5 eV. Moreover the HOMO and LUMO states of tricene are delocalised throughout the whole molecule with charge density concentrated both on the end-groups and on the central phenyl groups. We can clearly see from the iso-surface plots that all the states close to E_F consist of delocalised π orbitals (carbon $2p_z$ and sulphur $3p_z$ states). However the symmetry of these states is notably different as one can see from the position of the nodes and crests in the local charge density plots.

Figure (4.3) shows the current and zero-bias transmission coefficients for triphenyl-dithiolate. We can see that the transport is through extended states delocalised over the entire molecule and the typical transmission coefficients approach unity. The low-bias resistance of such a device is therefore in the $10 \text{ k}\Omega$ range. In the parallel case the zero-bias conductance is dominated at the Fermi level by majority spins,

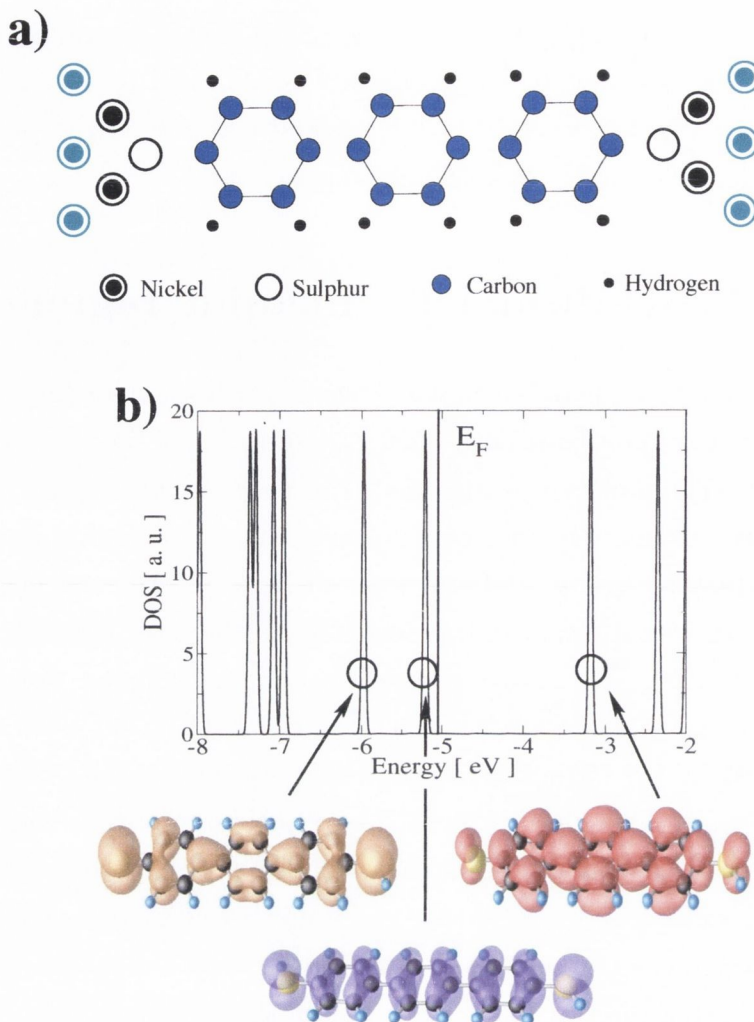


Figure 4.2: Structural and electronic properties of a Ni[001]/tricene/Ni[001] spin-valve. a) Schematic structure of the molecule attached to [001] Ni surfaces. b) Density of states and charge-density iso-surface plots for the relevant molecular orbitals of the isolated tricene-dithiol molecule. The highest "circled" state is the LUMO while the state closest to the Fermi level is the HOMO. A third state is also highlighted (shown in yellow). Because isolated levels correspond to delta functions in the DOS, for display purposes and to aid comparison with Figs (4.3) and (4.5) we have artificially broadened the DOS by 0.1 eV.

with negligible contribution from the minority electrons. The minority spin conduction starts at about 0.1 eV above E_F and is dominant for energies up to 0.6 eV. At higher energies the transmission coefficients become spin-independent because only the unpolarised s electrons are available in the leads. In the antiparallel case there is a general suppression of the transmission coefficients at any energy. For energies

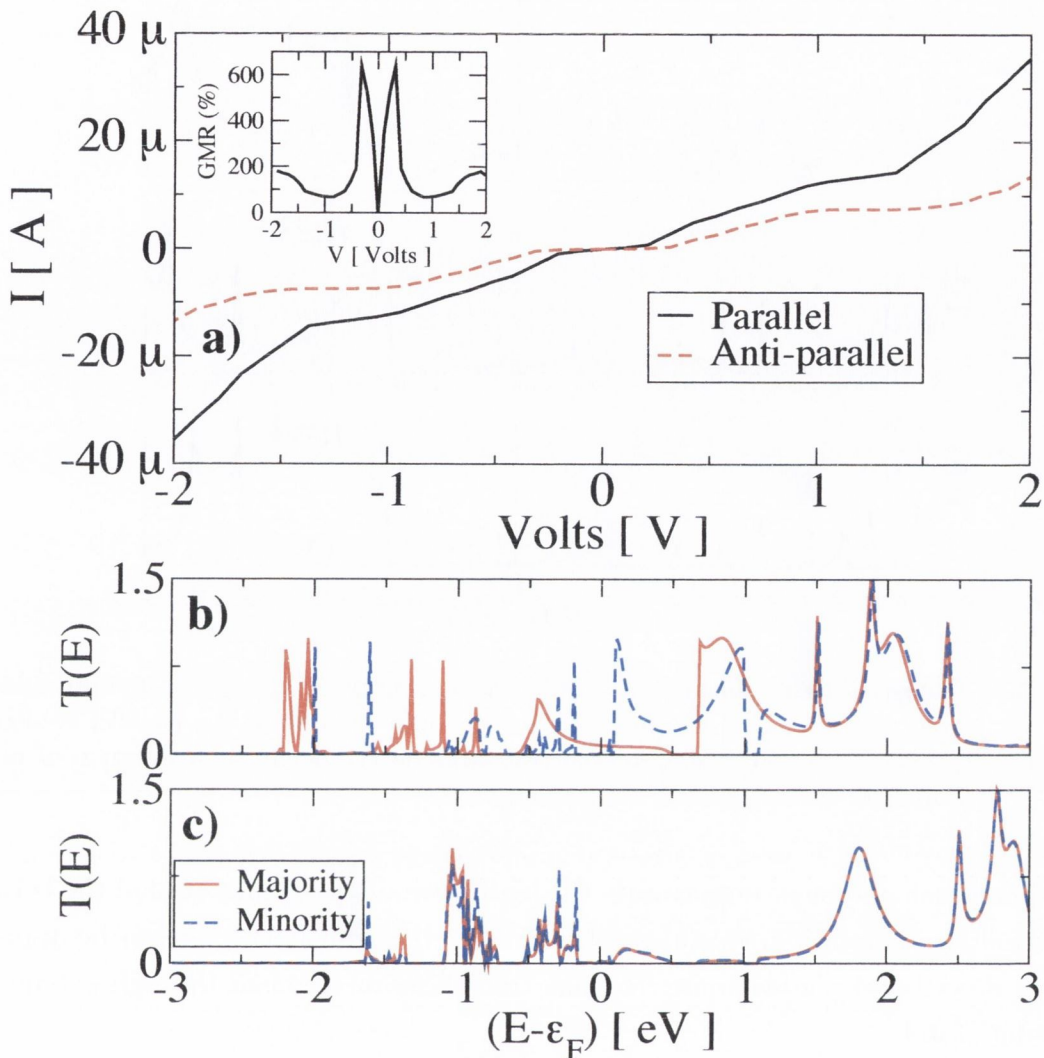


Figure 4.3: a) I-V characteristics for tricene. b) Transmission coefficients at zero bias for majority (solid) and minority (dashed) spins. The inset shows the magnetoresistance as a function of bias.

close to the Fermi level, this appears as a convolution of the transmission in the majority and minority spins in the parallel case. The conductance at the Fermi level is therefore small, and the current shows a tiny zero conductance plateau around zero bias with a consequent very large magnetoresistance ratio, exceeding 600 % close to zero-bias.

We have made additional calculations for various 1,4-[n]-phenyl-dithiolate molecules with different n ($n = 1, 2, 3, 4$). These curves are presented in figure (4.4) for the PA configuration. We can see that, in general, the features of the zero-bias transmission coefficients are similar and not strongly dependent on the length of the molecule. There is a reduction of the transmission with length, although the decay is certainly

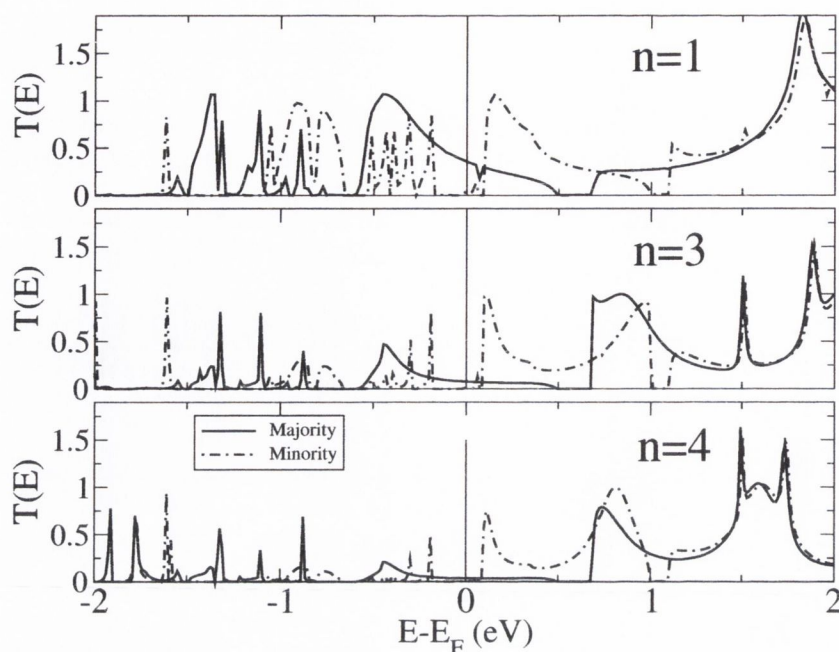


Figure 4.4: Transmission coefficient as a function of energy for 1,4-[n]-phenyl-dithiolate molecules with $n=1, 3$, and 4 . Here the spin-valve is in the parallel configuration. A similar scaling of the transmission coefficient as a function of n is found for the antiparallel configuration.

not exponential, and most importantly the high transmission peaks around the Fermi level remain. Therefore in this class of molecules the transport seems to be appropriately described by a coherent resonant tunnelling mechanism through extended molecular states.

In general one would expect the conductance to be dominated by resonant transport either through the HOMO or the LUMO state of the molecule [173]. This results in peaks in the zero bias transmission coefficient as a function of energy, and usually one is able to identify those corresponding to the HOMO and LUMO gap. In the case of 1,4-phenyl-dithiolate with gold electrodes, the HOMO-LUMO peaks are clearly visible and well separated [173]. In contrast, for the 1,4-tricene-dithiolate with nickel studied here the situation seems different. In fact the transmission coefficients for the parallel case show two peaks respectively for majority and minority spins with a separation of only 0.5 eV, not corresponding to the HOMO-LUMO gap. To identify these states we have followed the evolution of the orbital-resolved density of states (DOS) for a tricene molecule attached to nickel as a function of the Ni-S separation. In particular we have investigated the dependence of the carbon $2p$ and sulphur $3p$ DOS, because these are the relevant orbitals for the bonding to the nickel surface. This is presented in Fig. (4.5). From the figure one notices that the two sulphur p

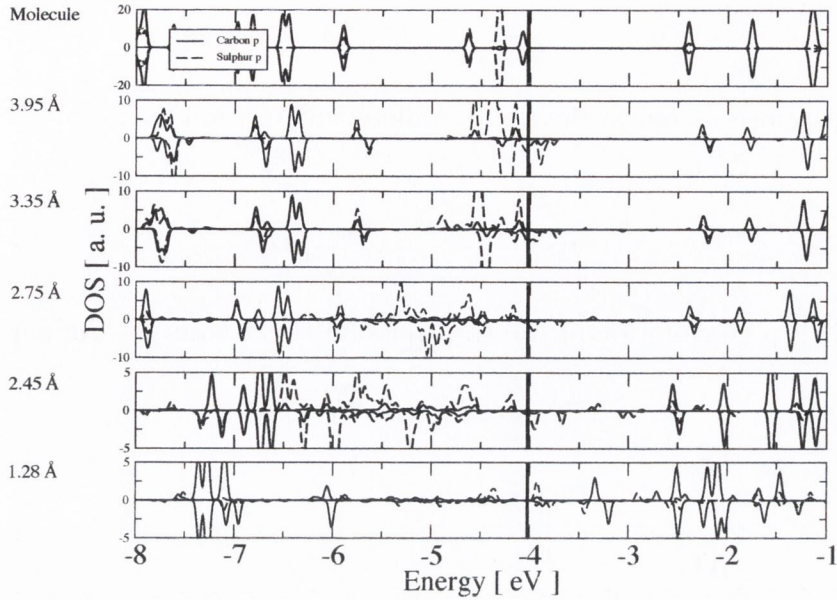


Figure 4.5: Orbital resolved density of states for tricene as a function of the distance between the sulphur end group and the plane of Ni atoms forming the leads. The solid (dashed) line represents the p orbital of carbon (sulphur).

HOMO states of the isolated tricene molecule steadily spin-split and broaden as the Ni-S distance is decreased. At the equilibrium position (1.28 Å) the broadening is large, although at the Fermi level one can still identify two sulphur p states for the majority spin (-0.5 eV and 0.1 eV from E_F) and one for the minority (0.1 eV from E_F). We can then conclude that the transport is through a very broadened HOMO which also includes some contribution from the state 1 eV below the HOMO (shown as a yellow surface in Fig. (4.2)). Also, in tricene molecules, the sulphur atoms possess a tiny spin-polarisation, which is a further indication of strong coupling ($\sim 0.05\mu_B$).

An interesting feature is that, in first approximation, the transmission coefficient at zero bias for the antiparallel state appears to be a convolution of those for the majority and minority spin in the parallel case. This finding can be qualitatively understood in terms of transport through a single molecular state (see figure 4.6). Let $t^\uparrow(E)$ be the majority spin hopping integral from one of the leads to the molecular state, and $t^\downarrow(E)$ the same quantity for the minority spins. Then, neglecting multiple scattering (i.e. all interference effects), the total transmission coefficients of the entire spin-valve in the parallel state can be written as

$$T^{\uparrow\uparrow}(E) = (t^\uparrow)^2 \quad \text{and} \quad T^{\downarrow\downarrow}(E) = (t^\downarrow)^2, \quad (4.1)$$

respectively for the majority and minority spins. The total spin in the parallel

configuration is then

$$T_{\text{Total}}^{\text{PA}} = T^{\uparrow\uparrow} + T^{\downarrow\downarrow}. \quad (4.2)$$

Similarly the transmission in the anti-parallel configuration is

$$T^{\uparrow\downarrow}(E) = T^{\downarrow\uparrow}(E) = t^{\uparrow}t^{\downarrow}, \quad (4.3)$$

$$T_{\text{Total}}^{\text{AA}} = 2T^{\uparrow\downarrow}. \quad (4.4)$$

Thus $T^{\uparrow\downarrow}(E)$ is a convolution of the transmission coefficients for the parallel case

$$T_{\text{Total}}^{\text{AA}} = 2T^{\uparrow\downarrow} \propto 2\sqrt{T^{\uparrow\uparrow}T^{\downarrow\downarrow}}. \quad (4.5)$$

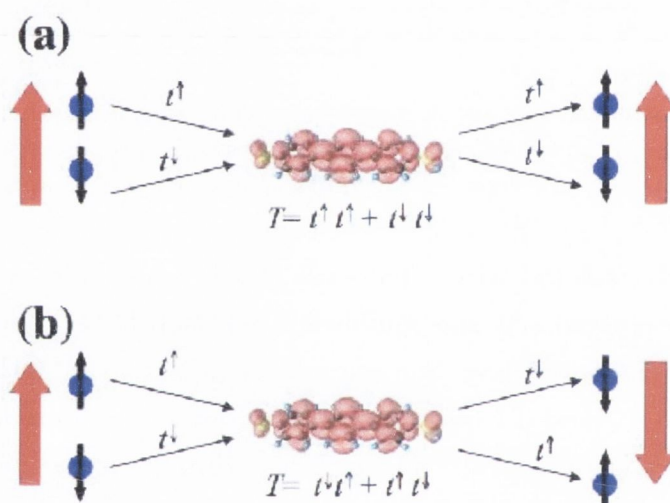


Figure 4.6: Scheme of the spin-transport mechanism through a single molecular state. $t^{\uparrow}(E)$ ($t^{\downarrow}(E)$) is the majority (minority) spin hopping integral from one of the leads to the molecular state. Neglecting quantum interference, in the parallel case (a) the total transmission coefficient is simply $T = (t^{\uparrow})^2 + (t^{\downarrow})^2$, while in the antiparallel (b) $T = 2t^{\uparrow}t^{\downarrow}$. Note that if either t^{\uparrow} or t^{\downarrow} vanishes, the current in the antiparallel configuration will also vanish (infinite GMR).

To further corroborate this picture we can turn our attention to the local charge density between energies E_{\min} and E_{\max} ,

$$\Delta n(\vec{r}) = \sum_l^{E_{\min} \leq E \leq E_{\max}} |\Psi_l(\vec{r})|^2. \quad (4.6)$$

Let us first analyse the PA configuration. Figure (4.7Aa-b) shows the local charge density iso-surfaces for both minority and majority for single particle states with energies comprised in $[-0.5, 0.0]$ eV. We can see that for majority spins there is

charge centred on the carbon atoms along the entire molecule whereas for minority spins the central part of the molecule is essentially charge-free. This metallic state state for majority spins can be associated with the peak in the conductance seen in Fig. (4.3) slightly below E_F . In the case of higher energies, the minority spins become conducting. In fact, the charge density for minority spins in the $[0.0, 0.5]$ eV energy interval (see fig. (4.7Bb)) is strikingly similar to the one presented in fig. (4.7Aa), which leads us to conclude they correspond to the same molecular state with a spin polarisation induced by the leads.

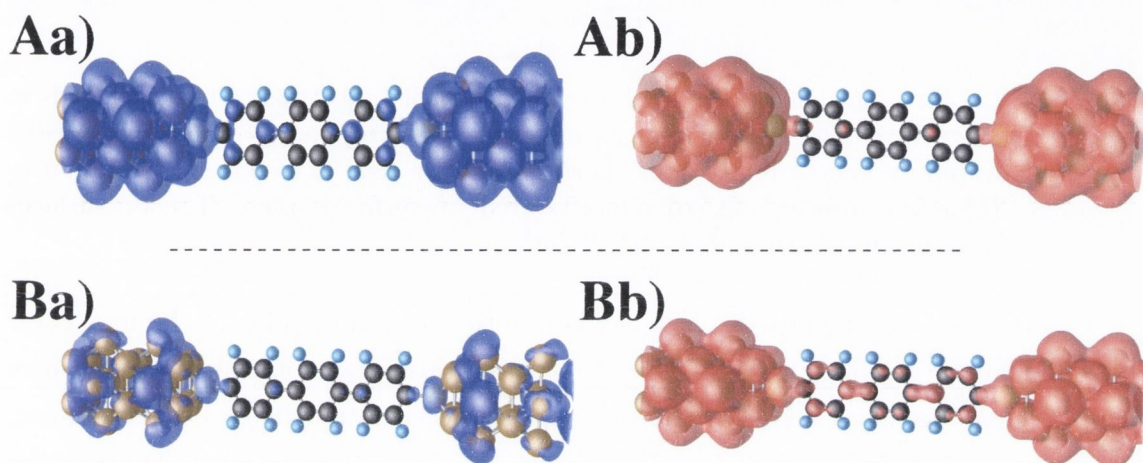


Figure 4.7: Local charge density Δn , for 1,4-triphenyl-dithiolate attached to nickel leads in the parallel alignment of the electrodes. The top panels are for the (A) -0.5 to 0.0 eV energy interval and bottom part for (B) 0.0 to 0.5 eV: (a) majority (blue iso-surface) and (b) minority (red iso-surface) spins. The iso-surfaces were taken for $\Delta n = 0.004 |e|/\text{Bohr}^3$.

Turning our attention to the anti-parallel case we can understand the reasons for the smaller conductance seen in fig. (4.3c). On the right hand-side lead, majority electrons turn into minority and *vice-versa*. Hence, we can think of the states in Fig. (4.8) as being formed by exchanging the majority (minority) spins from the left hand-side with the minority (majority) spins from the right hand-side. If we divide our system in two parts, we can clearly see that the left hand-side of the molecules in Fig. (4.8) are identical to the ones in Fig. (4.7) whereas a and b are interchanged for the right hand-side.

In essence the molecule can be split into two disjoint sides. The total transmission is determined by the interplay between the energy-dependent transmission probabilities for each side separately as presented in figure (4.6). In the PA configuration it leads to high (low) conductance for the majority (minority) at E_F while it results in a convolution in the AA alignment.

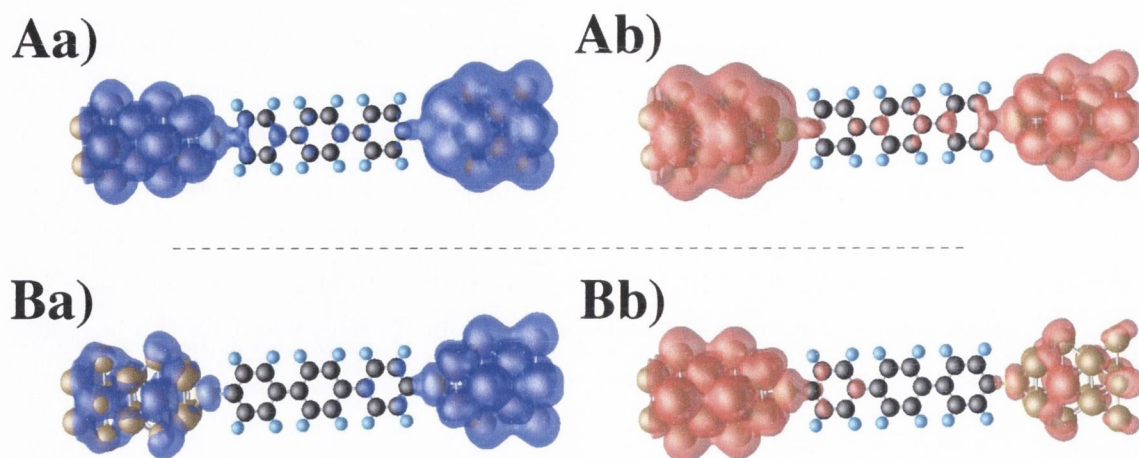


Figure 4.8: Local charge density, Δn for 1,4-triphenyl-dithiolate attached to nickel leads in the anti-parallel alignment of the electrodes. The top panels are for the (A) -0.5 to 0.0 eV energy interval and bottom part for (B) 0.0 to 0.5 eV: (a) majority (blue iso-surface) and (b) minority (red iso-surface) spins. The iso-surfaces were taken for $\Delta n = 0.004 |e|/\text{Bohr}^3$.

An extreme - and idealised - case is when only one spin couples to the molecular state. Then the total transmission in the antiparallel case is identically zero since either t^\uparrow or t^\downarrow vanishes. This is the most desirable situation in real devices since, in principle, an infinite R_{GMR} can be obtained. Note that in this situation the system leads+molecule behaves as a half-metal although the two materials forming the device are not half-metals themselves. An even more extreme situation is when for a particular energy window the transport is through two distinct molecular states, which are respectively coupled to the majority and minority spin only. This may happen for instance due a particular symmetry of the molecular anchoring groups. Then in this energy window (see figure 4.9)

$$T^{\uparrow\uparrow}(E) \neq 0 \quad , \quad T^{\downarrow\downarrow}(E) \neq 0 \quad (4.7)$$

$$T_{\text{Total}}^{\text{PA}} = T^{\uparrow\uparrow} + T^{\downarrow\downarrow} \neq 0 \quad (4.8)$$

but

$$T_{\text{Total}}^{\text{PA}} = 2T^{\uparrow\downarrow} = 2t^\uparrow t^\downarrow = 0. \quad (4.9)$$

One possible way to achieve this situation (of infinite GMR) is to change the functional group that links the molecule to the surface, leading to different bonding properties specially in materials with highly directional coupling. Transition metals where d orbitals play an important *role* are likely candidates as opposed to noble metals where the chemical bonding is dominated by s orbitals with no angular

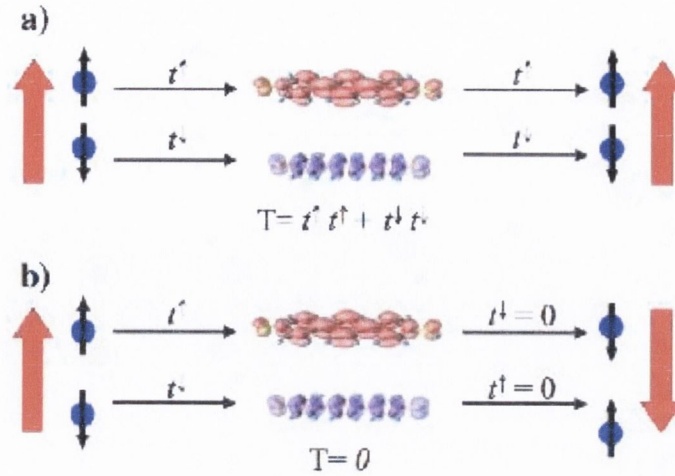


Figure 4.9: Scheme of the spin-transport mechanism through two energetically closely spaced molecular states. The first state (red) couples only to the majority spin band, while the minority spin couple only to the purple state. In the parallel case one finds $T^{\uparrow\uparrow}(E) \neq 0$ and $T^{\downarrow\downarrow}(E) \neq 0$ but in the antiparallel $T^{\uparrow\downarrow}(E) = 0$. We then expect an infinite GMR for such an energy window.

dependence [173]. The other possibility is to change the electrode itself. This is somewhat more complicated, but one can use an STM tip positioned at different lateral positions to probe different coupling configurations between the molecule and the tip itself. We will address these possibilities further on in this chapter.

4.3 Octane-dithiolate: tunnelling regime

The other family of molecules we have considered is the alkane family. Alkanes are single bond CH_2 groups that form a zigzag structure. Figure (4.10a) shows one such alkane with eight carbon atoms (octane) terminated with sulphur groups at both ends and connected to nickel electrodes in a similar fashion to the tricene molecule. These molecules have been recently used in pioneering molecular spin valve experiments by Petta *et al.* [49] although a theoretical description is still lacking.

As a starting point we performed DFT atomic relaxations on this molecule attached to nickel leads in the same way described in the previous section. The first difference from the tricene molecule presented in the previous section is the arrangement on surface; the preferred configuration of octanes on a [001] Ni surface is at an angle of approximately 36° from the normal to the surface.

The two molecules also present rather different electronic properties. Figure (4.10b) shows the density of states and local charge density for octane-dithiol. The HOMO-LUMO gap is now approximately 5 eV, almost double than that of tricene-

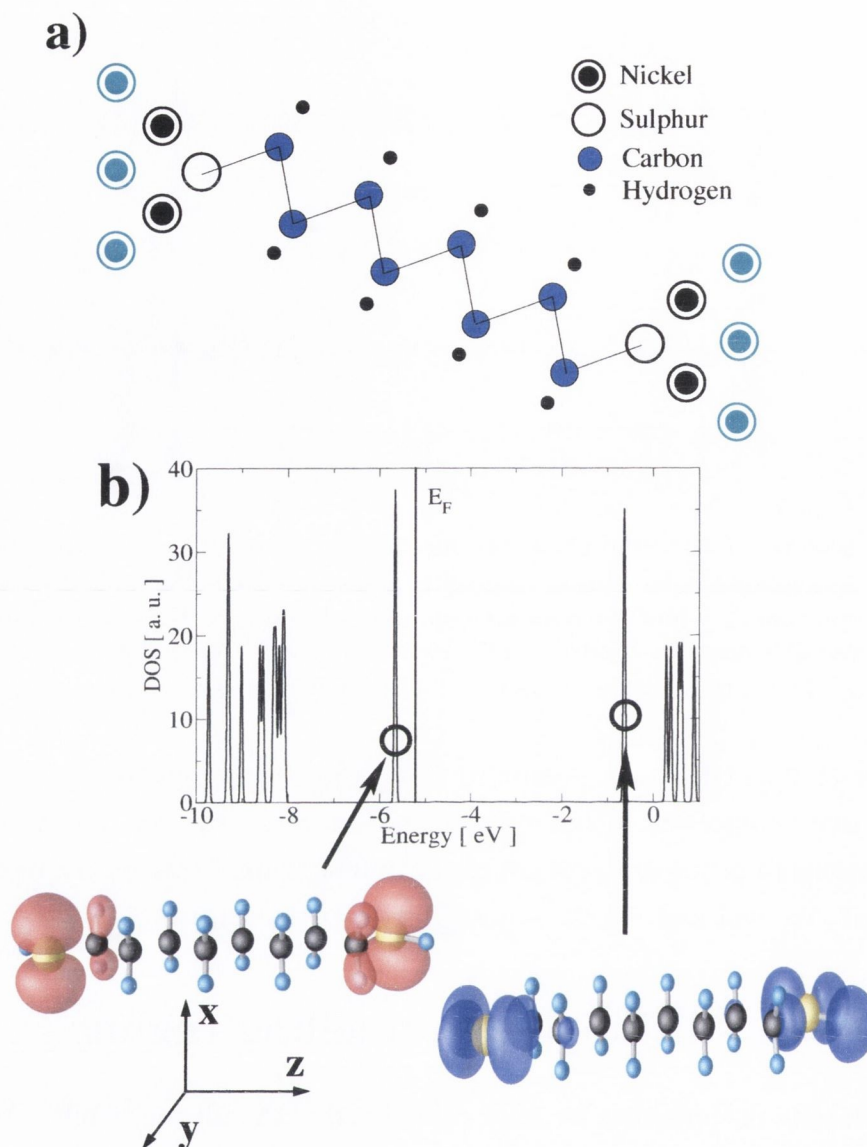


Figure 4.10: Structural and electronic properties of a Ni[001]/octane/Ni[001] spin-valve. a) Schematic structure of the octane molecule attached to [001] Ni surfaces. b) Density of states and charge-density iso-surface plots for the relevant molecular states of the isolated octane-dithiol molecule. The highest (lowest) “circled” state is the LUMO (HOMO) for such an isolated molecule. Because isolated levels correspond to delta functions in the DOS, for display purposes and to aid comparison with Fig. (4.11) we have artificially broadened the DOS by 0.1 eV.

dithiolate. The local charge density shown in the same figure also present considerably different behaviour. For the previous molecule the charge density was delocalised over the entire backbone whereas in octane the charge is concentrated mostly on the two sulphur atoms at either end of the molecule. The HOMO and LUMO also have significantly different orbital characters. While tricene could be understood in term

of bonding and anti-bonding states of the same π orbitals, for octane the HOMO is dominated mostly by the S $3p_x$ (and some contribution from the outermost C atoms) and the LUMO is a combination of sulphur p_z and p_y atomic orbitals.

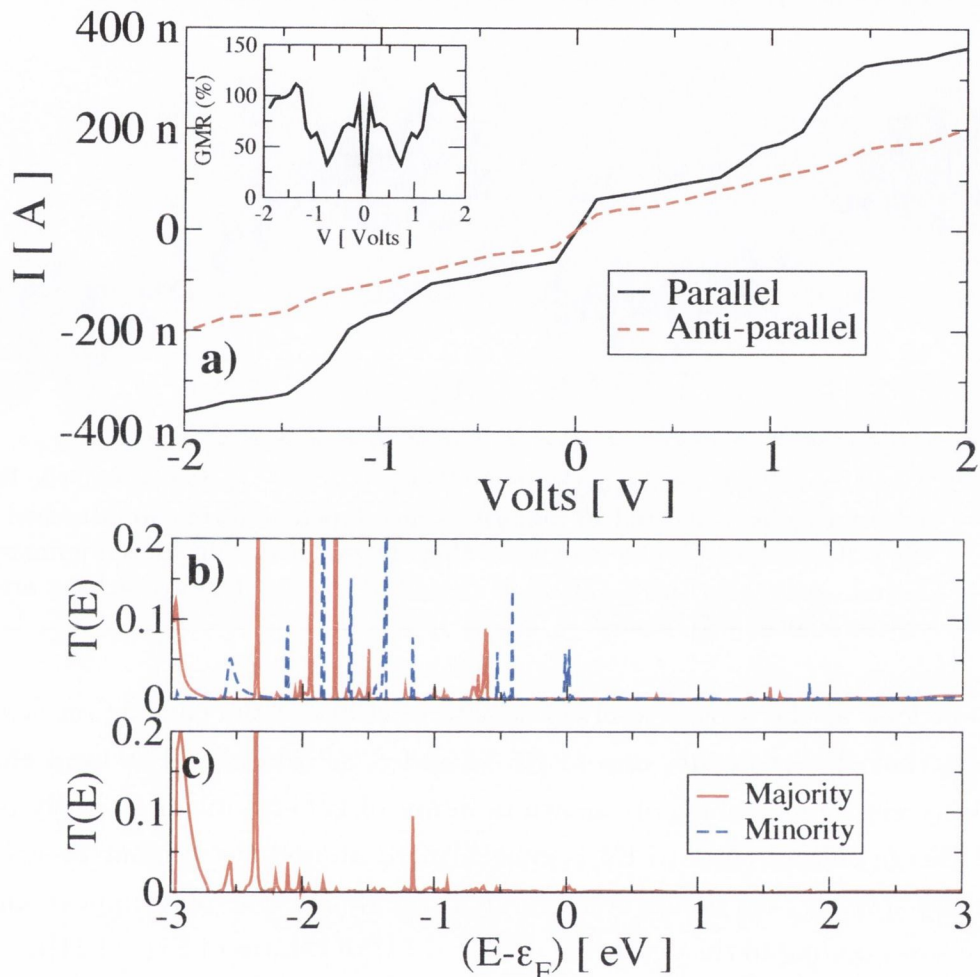


Figure 4.11: a) I-V characteristics for octane-dithiolate. b) Transmission coefficients at zero bias for majority (solid) and minority (dashed) spins. The inset shows the magnetoresistance as a function of bias.

The transport properties of octane-dithiolate are presented in Fig (4.11). At a more detailed level, it is clear that the two molecules possess rather different transport characteristics as well. In the case of octane the resistance is of the order of $10 \text{ M}\Omega$ with a current of about 150 nA at 1 V . This is in the same range as in recent experiments [49], although a direct comparison is difficult because the precise number of molecules bridging the two electrodes is unknown. However, the good agreement in terms of resistance gives us confidence in the ability of our method to describe these devices. The largest contribution to the current comes from a sharp resonance of the transmission coefficient at the Fermi level (see Fig. (4.11b)). This is mainly

given by minority electrons and it is strongly suppressed in the antiparallel case. Because in the antiparallel configuration the transmission coefficients are essentially zero at any energy around the Fermi energy E_F , we can conclude that the suppression of the aforementioned peak is the main reason for the magnetoresistance.

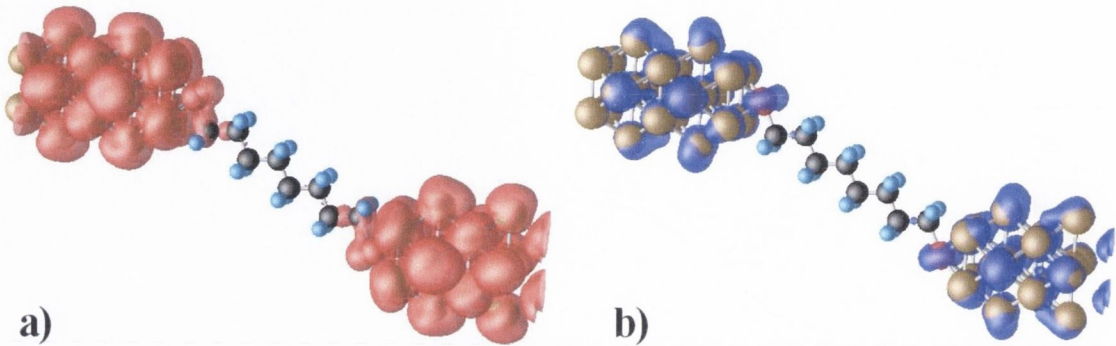


Figure 4.12: Local charge density Δn in the $[E_F-0.25, E_F+0.25]$ eV region around the Fermi level for a) minority and b) majority spins in octane-dithiolate attached to a Ni [001] surface. We can clearly see that the minority spin spins dominate the Fermi energy and the backbone is devoid of charge. The iso-surfaces are cut at $\Delta n=0.00015 |e|/Bohr^3$.

A closer look at the orbital-resolved density of states of the conduction peak at E_F reveals that this is mainly due to Ni $3d$ and S $3p$ orbitals. The local charge density iso-surface plots which are shown in figure (4.12) also unambiguously prove that the charge density close to E_F is concentrated around the sulphur atoms and little density spreads over the carbon molecular backbone. The plots appear similar to those corresponding to the octane HOMO and LUMO states of Fig. (4.11b). This suggests that the transport is tunnelling-like through a Ni- $3d$ /S- $3p$ surface state.

To further sustain this hypothesis we have calculated the transmission coefficients $T(E)$ at zero bias for various n-alkane molecules as a function of the number of carbon atoms n ($n = 4, 6, 8$ and 10). This reveals an exponential decay

$$T \propto e^{-\beta n} \quad (4.10)$$

with exponent $\beta = 0.88$, which clearly demonstrates that we are in a tunnelling regime. It is interesting to note that such an exponent is similar to the one found for the same molecule attached to gold [111] surfaces [202]. In addition we observe that the S atoms anchoring the octane molecule present an induced magnetic moment of $\sim 0.07\mu_B$ oriented in the same direction as the nickel magnetisation. The presence of charge density at the sulphur atoms is also a feature found for 8-alkane-dithiolate

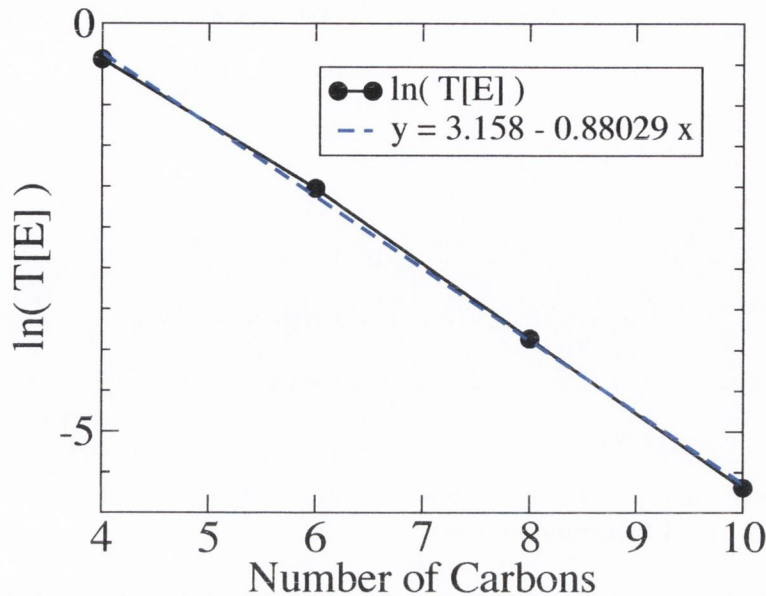


Figure 4.13: Distance dependence of the zero-bias transmission coefficients of octanedithiolate; calculations (solid + filled circles) and linear regression (dashed).

on [111] gold surfaces, and it is related to the fact that the Fermi level lies in the molecular HOMO-LUMO gap [202].

The GMR in this case is significantly smaller than tricene, between 40% and 100%. This result is slightly larger than experimental results obtained for actual devices [49], however one expects that the geometry of the leads, orientation of the magnetisation and short circuiting through pin-holes might account for the discrepancy.

4.4 1,4-benzene-(S, Se, Te): end-group engineering

In the previous two sections we have shown how two different molecules can give different magneto-transport properties and GMR. Following the idea of appropriately selecting the molecule to enhance the magnetoresistance, one interesting aspect that calls our attention is the possibility to tailor the GMR according to the anchor group (AG).

We have explored this avenue [71, 88] by replacing the standard thiol group on phenyl-type molecules with either a Se or a Te atom. We considered the shorter 1,4-benzene molecules. As we can see from figure (4.4) the qualitative transport properties remain essentially unchanged independent of the number of phenyl rings even though the actual values of the transmission coefficients are different. This

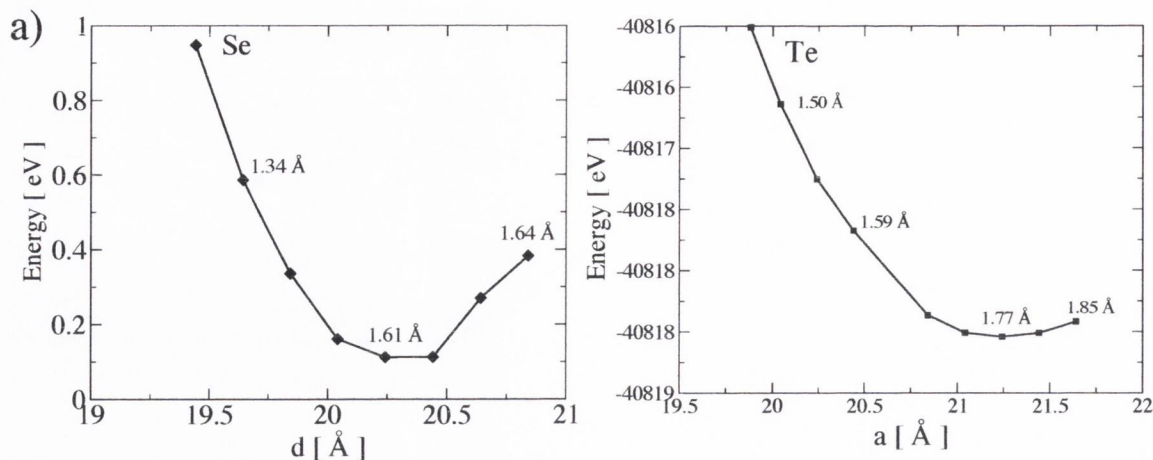


Figure 4.14: Total energy curve as a function super-cell size in a) 1,4-benzene-Selenium and b) 1,4-benzene-Tellurium.

result justifies our analyses of benzene-type molecules as a whole.

We considered three different anchoring groups, namely: sulphur (the standard AG in molecular electronics), Selenium and Tellurium. It is no coincidence that these three atoms belong to the same family of the periodic table. One would expect they have similar chemical and bonding properties, but different atomic radius.

In order to study the effects of different end-groups we first performed atomic relaxations to determine the arrangement of these new molecules on the magnetic surface. The initial configuration was similar to the one presented in figure (4.1) upon substitution of the sulphur atom - represented by the red sphere - by either Selenium or Tellurium. The CG relaxations were performed keeping the two outermost layers on either side of the super-cell fixed. The remaining central region was allowed to relax. We then vary the length of the cell d to minimise the total energy of the system. This method was applied in similar fashion as in chapter 3.

The selenium and tellurium atoms were modelled using respectively $3d^{10}4s^24p^4$ and $4d^{10}5s^25p^4$ as the initial atomic configurations. In both cases we used a DZ basis set for s and d and DZP for the p orbitals to account for the bonding properties.

The total energy curves for 1,4-benzene-selenium and -tellurium as a function of the total super-cell length are shown in figure (4.14). In the case of Tellurium the distance between the AG and the Ni surface is approximately 1.77 Å compared to 1.61 Å for Selenium and 1.26 Å for sulphur. Theoretical predictions of the transport properties of phenyl-tellurium and -selenium molecules attached to gold electrodes have been considered previously [203]. However the authors did not take into account the atomic relaxations due to changes in AG and the significant changes in the distance to the electrodes.

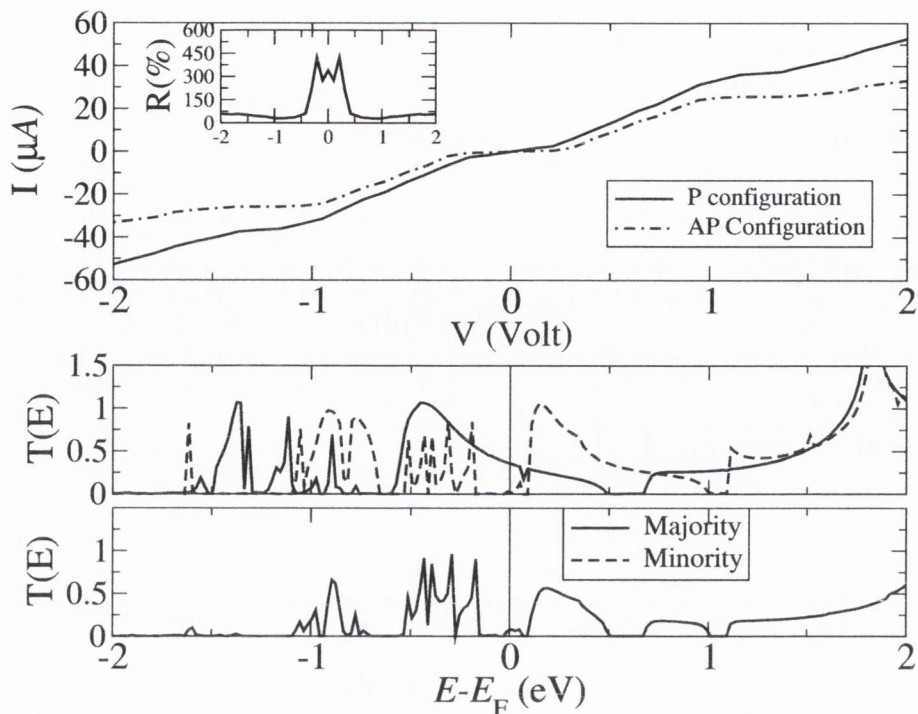


Figure 4.15: Transport properties for a 1,4-phenyl molecule attached to Ni (100) surfaces through a S group. The top panel shows the I - V characteristics for both the parallel and antiparallel alignment of the leads and the inset the corresponding GMR ratio. The lower panel is the transmission coefficient at zero bias as a function of energy. Because of spin-symmetry, in the antiparallel case we plot only the majority spin.

The transport properties of the three different molecules are presented in figures (4.9), (4.15) and (4.16). We can clearly see that the current as well as the transmission decreases as we go from sulphur down to selenium and then tellurium. As the molecules become more loosely coupled, the GMR increases reaching in excess of 450 % (figures' insets).

Albeit the higher GMR ratios the main transport properties are remarkably similar. In the PA alignment the HOMO is spin-split with the majority spin below and the minority spin above the Fermi level. We observe an overall reduction of the transmission coefficients for both majority and minority spins. However, for majority spins, given the strong hybridisation, the quenching of the transmission coefficients is not as significant as for the minority spins. Transmission probabilities for minority spins close to E_F are mostly due to tunnelling through Ni d states which are fairly localised. When we consider the AA configuration the convolution between majority and minority spins leads to much lower conduction because minority spins set the

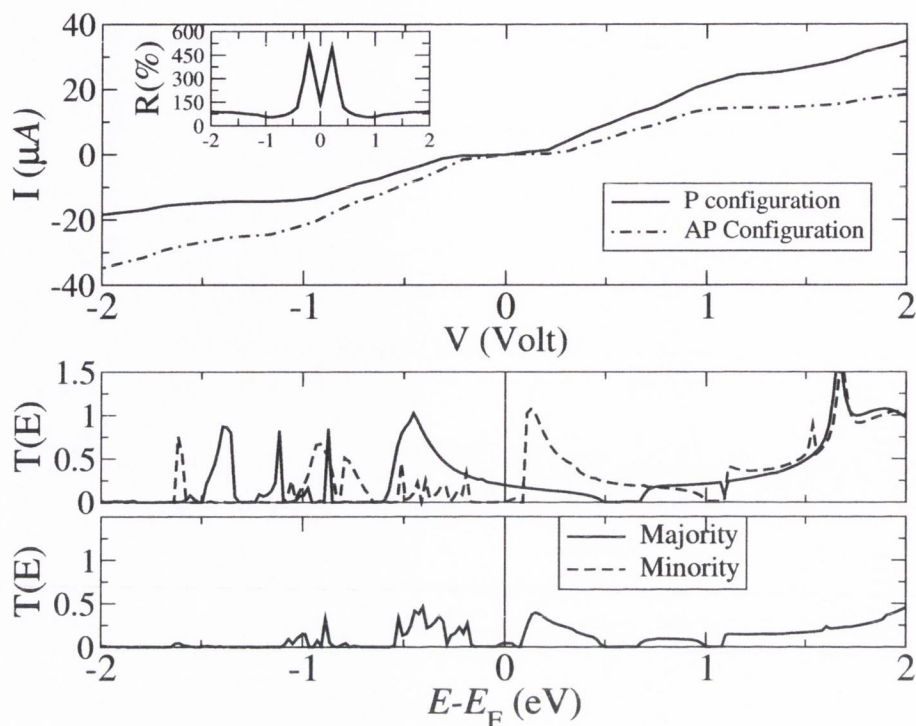


Figure 4.16: Transport properties for a 1,4-phenyl molecule attached to Ni [001] surfaces through a Se group. The top panel shows the I - V characteristics for both the parallel and antiparallel alignment of the leads and the inset the corresponding GMR ratio. The lower panel is the transmission coefficient at zero bias as a function of energy. Because of spin-symmetry, in the antiparallel case we plot only the majority spin.

bottleneck.

Essentially, the overall increase in the R_{GMR} is mainly due to an increase in the radius of the AG. Conduction through minority states which is mostly d -dominated is reduced more drastically than majority spin states.

4.5 Asymmetric molecules

In section (1.7) we used a simple one-energy-level model to show that charging effects on molecular states combined with asymmetric coupling to the electrodes can lead to asymmetries in the $I - V$ characteristics. This effect can be combined with a more realistic transport theory to design molecular devices which present highly asymmetrical characteristic curves. Ideally one can envisage a molecular substitute to standard solid-state diodes where current flows for forward bias, but is completely blocked for negative ones (or *vice versa*). In the case of spin-transport we can obtain

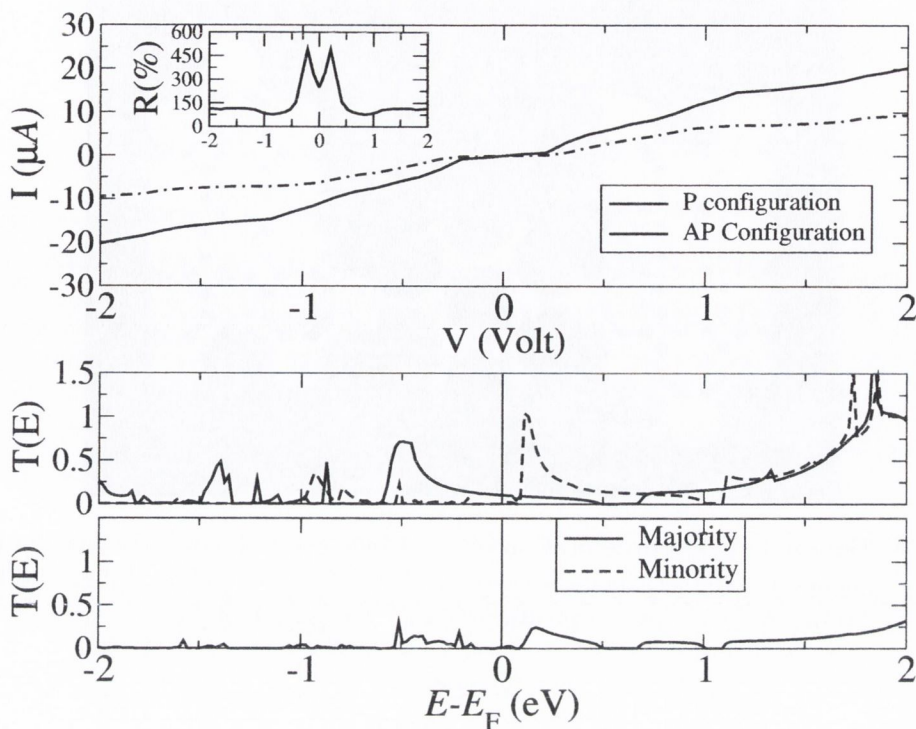


Figure 4.17: Transport properties for a 1,4-phenyl molecule attached to Ni [001] surfaces through a Te group. The top panel shows the I - V characteristics for both the parallel and antiparallel alignment of the leads and the inset the corresponding GMR ratio. The lower panel is the transmission coefficient at zero bias as a function of energy. Because of spin-symmetry, in the antiparallel case we plot only the majority spin.

devices for which one spin channel is completely blocked for forward bias, but not for negative voltages thus making a spin diode. We can then take the idea of end-group engineering one step further by using different AGs for either side.

The molecule we used is 1,4-benzene-tellurium-thiolate. It consists of a benzene ring terminated by a sulphur and a tellurium atom. The molecule is attached via sulphur and tellurium to two Ni [001] surfaces. Here we used periodic boundary conditions along the transverse direction with a 3×3 k -point mesh. A sketch of our system is shown in figure (4.18). The introduction of periodic boundary conditions in the transverse direction provides the correct description of the surface, more importantly we avoid mini-gaps in the band structure of the electrodes which can lead to spurious results. A possible drawback of this approach is that we are in fact modelling a monolayer of organic molecules between two Ni surfaces. In order to suppress inter-molecular interaction we make the lateral size of the super-cell rather big.

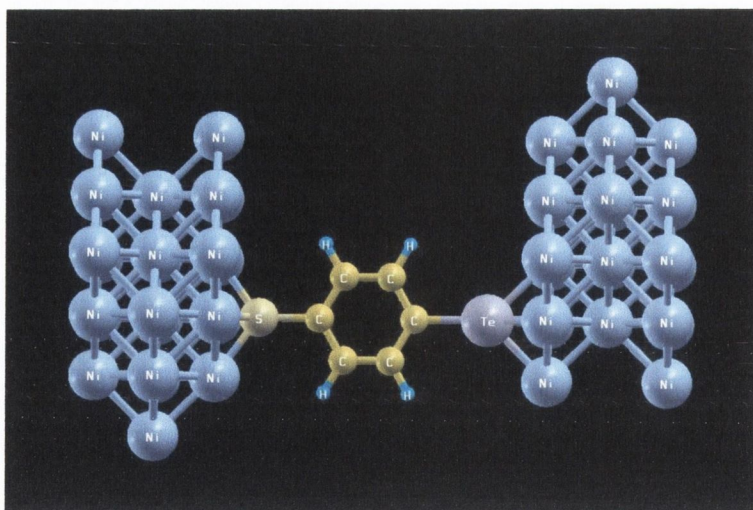


Figure 4.18: Ball-and-stick representation of a 1,4-benzene-tellurium-thiolate molecule attached to Ni [001] surfaces through the hollow site. The sulphur and tellurium atoms are attached to positions 1 and 4 respectively.

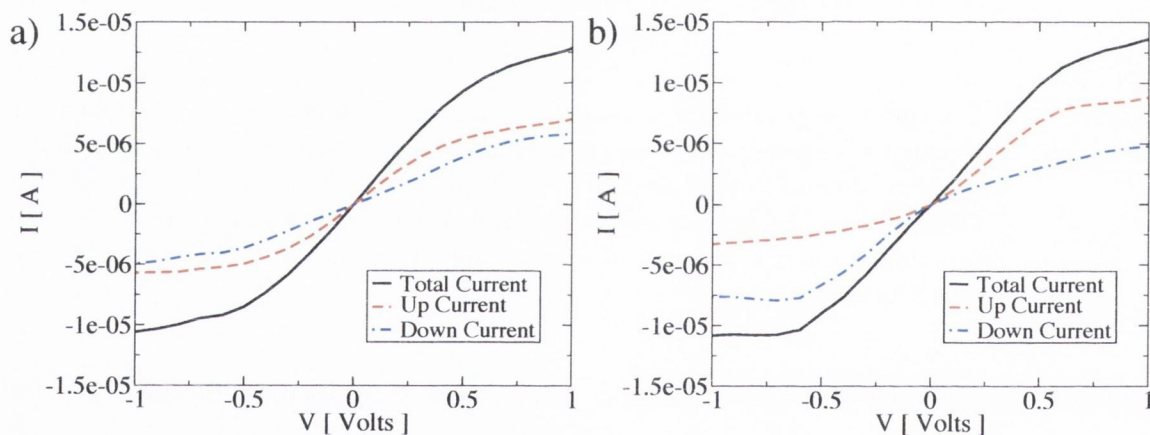


Figure 4.19: $I - V$ characteristics of 1,4-benzene-tellurium-thiolate molecule sandwiched between two Ni [001] surfaces. a) Parallel and b) anti-parallel configurations.

In figure (4.19) we analyse the $I - V$ characteristics our device. As we can see both the PA and AA configurations are reasonably asymmetric (the current for forward bias is only 20-25 % higher). Besides, the polarisation, P (defined in equation (3)) for the antiparallel case is also significant reaching approximately -50 % at -0.5 V (in the case of backward bias the minority spin current is larger in absolute terms than majority spin one).

The GMR ratio for this molecule is presented in Fig. (4.20) and it also shows some interesting features. The spin-resolved magnetoresistance ratios are calculated

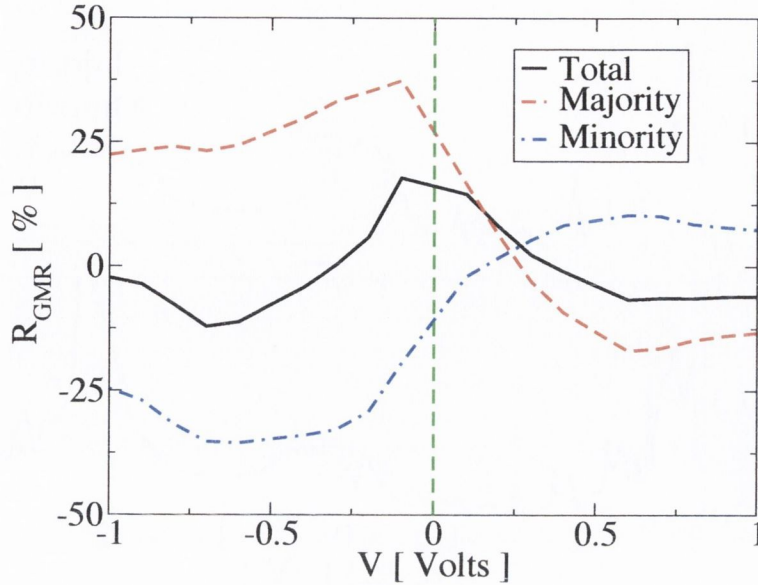


Figure 4.20: Giant-magnetoconductance ratio as a function of applied bias for BDTT molecule. The spin resolved GMR is calculated according to equations (4.11) and (4.12).

using

$$R_{\text{GMR}}^{\uparrow} = \frac{I_{\text{PA}}^{\uparrow} - I_{\text{AA}}^{\uparrow}}{I_{\text{AA}}^{\uparrow} + I_{\text{AA}}^{\downarrow}}, \quad (4.11)$$

$$R_{\text{GMR}}^{\downarrow} = \frac{I_{\text{PA}}^{\downarrow} - I_{\text{AA}}^{\downarrow}}{I_{\text{AA}}^{\uparrow} + I_{\text{AA}}^{\downarrow}}, \quad (4.12)$$

so that

$$R_{\text{GMR}}^{\text{Total}} = R_{\text{GMR}}^{\uparrow} + R_{\text{GMR}}^{\downarrow}. \quad (4.13)$$

The total GMR oscillates between positive and negative values depending on the applied bias, but it does not exceed 20 %. The individual spin components of the GMR can in fact exceed that value. We can clearly see from figure (4.20) that $R_{\text{GMR}}^{\uparrow}$ and $R_{\text{GMR}}^{\downarrow}$ have opposite signs for the entire bias range considered here. For forward bias the minority spins dominate the transport whereas for backward bias the majority sets the final sign of the total GMR. Therefore we can conclude that the total GMR is a balancing act between the two spin components.

Finally figure (4.21) shows the zero-bias transmission coefficients as a function of energy. We can see that the molecule is conducting both for the PA and AA alignments of the electrodes. This metallic behaviour prevents the molecule from charging once bias is applied. In that case the asymmetries are not as large as one might wish.

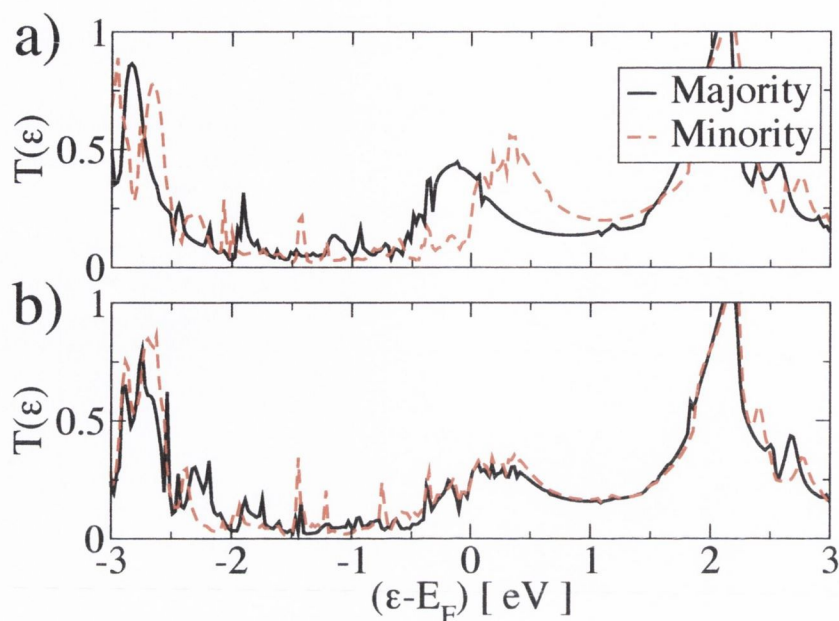


Figure 4.21: Transmission coefficients as a function of energy for 1,4-benzene-tellurium-thiolate sandwiched between Ni [001] surfaces: a) parallel and b) anti-parallel configurations.

4.6 Modelling scanning tunnelling microscopy with *Smeagol*

Instead of changing the anchoring groups as we did in the previous section it is also possible to tune the transport properties of organic molecules by attaching them to different sites [204]. In gold and other noble metals the bonds have mostly *s* character and have no angular dependence. In transition metals, on the other hand, *d* orbitals play an important role and the coupling of the molecule to different orbitals might lead to significant changes in the transport properties of a molecular device

The perfect tool for probing these properties is a STM [1]. In an STM one uses a metallic tip to measure the tunnelling current between a surface and the metallic tip itself. These tunnelling currents (usually ranging between nA and pA) can then be used to produce atomic resolution images of the surface and of molecules deposited on them [205]. The magnetic properties of surfaces can also be measured by using spin polarised STM [206, 207, 208]. Standard theory of STM's uses a convolution of the local density of states of the tip and the surface to describe the imaging process. In essence, the images produced are a fingerprint of the local density of states of the surface. It is usually assumed that tip and surface do not interact an approximation that has recently been called into question [209, 210].

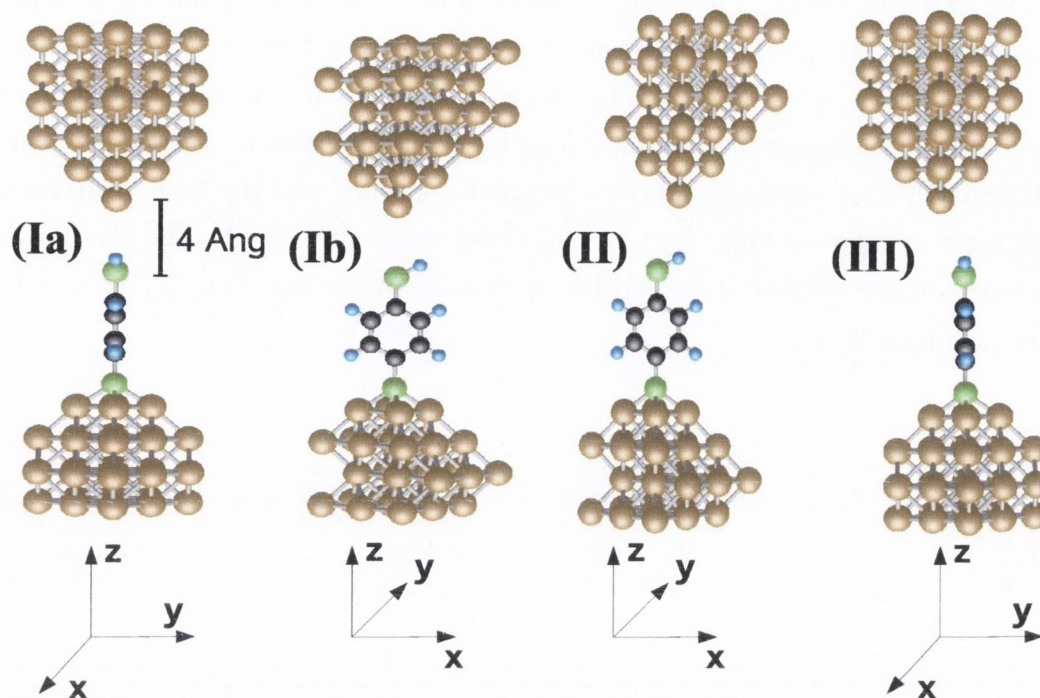


Figure 4.22: Ball-and-stick configurations of a 1,4-benzene-thiol-thiolate molecule in an STM setup. (Ia) side view; the tip is in the plane of the molecule on top of the sulphur atom, $\vec{r}_{\text{tip}} = (0, 0, 4) \text{ \AA}$. (Ib) top view for the same configuration as (Ia). (II) Side view; the tip is in the plane of the molecule on top of the hydrogen atom, $\vec{r}_{\text{tip}} = (1.18, 0, 4) \text{ \AA}$ (III) side view; the tip is shifted upwards with respect to the molecular plane, $\vec{r}_{\text{tip}} = (0, 1.18, 4) \text{ \AA}$. In all cases we consider that positive bias is applied from the bottom - the surface. Legend: carbon - black, sulphur - green, hydrogen - light blue and nickel - brown.

More recently the STM has been used for measuring transport properties of nanoscale devices. Onishi and coworkers have used STM's to produce monoatomic metallic wires and to measure conductance quantisation [146].

In principle, an atomically sharp STM tip can be used to probe different orbitals of a single molecule. Hence, a theoretical description capable of describing the transport properties of STM in contact mode as well including tip/surface interactions in standard STM experiments is potentially useful in the field of nanoscience.

As a proof-of-concept we performed calculations on a benzene-dithiol molecule adsorbed on a nickel [001] surface. As the molecule approaches the surface the hydrogen atom bonded to the sulphur is removed, thus becoming a thiolate group, whereas the free standing thiol group at position 4 remains unchanged. The resulting

molecule is known as 1,4-benzene-dithiol-dithiolate (BDTT).

In order to model the magnetic STM tip we assumed a pyramid of Ni atoms along the [001] direction. The base of the pyramid consists of a nine-atom square cross section and the apex is represented by a single nickel atom. Our calculations correspond to three possible positions of the STM tip with respect to the BDTT molecule. The configurations are shown in figure (4.22) and are referred hereafter as I, II and III. The planar distance between the sulphur and the final atom on the tip was kept at 4 Å (see Fig. (4.22a)).¹ In other words, if we let \vec{r}_{tip} be the position vector between the sulphur atom and the apex atom of the tip, then $\vec{r}_{\text{tip}} = (x, y, 4)$ Å for every configuration.

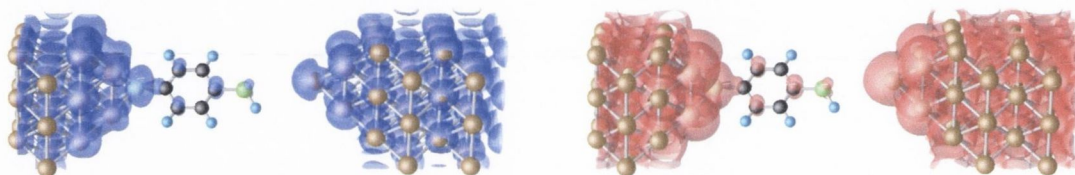


Figure 4.23: Local charge density of a 1,4-benzene-thiol-thiolate molecule attached a Nickel [001] surface probed by a Ni STM tip in configuration III. a) Majority and b) minority spins in the parallel configuration.

In configuration I (Fig. (4.22Ia-Ib)) the apex of the tip is positioned along the axis of the molecule, over the sulphur atom: $\vec{r}_{\text{tip}} = (0, 0, 4)$ Å. In arrangement II the tip shifts along the x axis to probe the H atom. In this case $\vec{r}_{\text{tip}} = (1.18, 0, 4)$ Å. Finally the tip is moved 1.18 Å away from the plane of the molecule, $\vec{r}_{\text{tip}} = (0, 1.18, 4)$ Å.

The calculations were performed with periodic boundary conditions in the lateral directions with a k -point sampling of 3×3 in the transverse Brillouin zone. The local charge density around E_F ($[E_F - 0.25, E_F + 0.25]$ eV) for configuration III is shown in figure (4.23). We can see that the molecular orbitals on BDTT around this energy range are mostly carbon and sulphur π states. The local charge on the nickel surface and tip is higher in minority spin as expected. Changing the position of the tip does not significantly change the local charge density neither on the molecule nor on the tip.

In figure (4.24) we present the $I - V$ characteristics for all the tip configurations. We adopt the substrate as our reference electrode. In other words, positive bias means we shift the potential on the substrate upwards by $V/2$ and the potential on the tip downwards by $V/2$ (current from the substrate to the tip).

¹We also performed calculations with distances of 2.5 Å and 3.0 Å with qualitatively similar

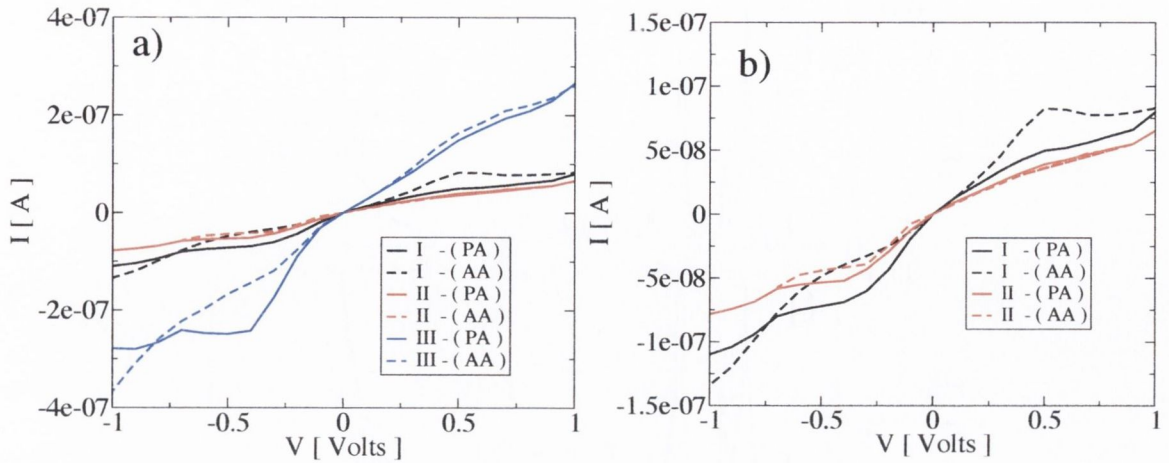


Figure 4.24: $I - V$ characteristics of BDTT attached to a Ni [001] surface through the hollow site and for different configurations of the STM tip. (a) arrangements I, II and III. (b) Focusing on arrangements I and II.

Although the absolute values of the $I - V$ characteristics are significantly different, we see a general trend in all curves, most notably the sign changes in the magnetoresistance ratios (when the current for the PA and AA configurations swap) occur at similar voltages. This is an indication that independently of the position of the tip, the states responsible for the transport properties are the same. Most notably in configurations I and II the transmission coefficients are very similar (see Fig. (4.25)). One notes that there is an overall reduction of the transmission coefficients, but the main features are the same.

The GMR ratio as a function of the applied bias is shown in figure (4.26). We can clearly see that the giant magnetoresistance ratio varies from approximately 80 to -50 % depending on bias and tip position.

The $I - V$ for configuration III deserves greater attention. Notably the current for this configuration is around twice as large as the other two arrangements, even though the distance between tip and molecule has effectively increased; $r_{\text{tip}}^{\text{III}} = r_{\text{tip}}^{\text{II}} > r_{\text{tip}}^{\text{I}}$.

This effect can be explained using the simple picture presented in figure (2). In essence the STM probes the π orbitals of the BDTT shown in Fig. (4.23). When the tip lies along the axis the coupling is smaller due to symmetry compared to the case where the tip is at an angle (above the plane of the molecule), consequently we see an enhancement of the conduction. The GMR for this device reaches approximately 60 %. Furthermore, it presents potential for rectification. Up to 0.4 Volts the current for negative voltages is approximately twice as large as the current for positive ones. On the other hand for higher negative bias the $I - V$ characteristics reaches a plateau

results.

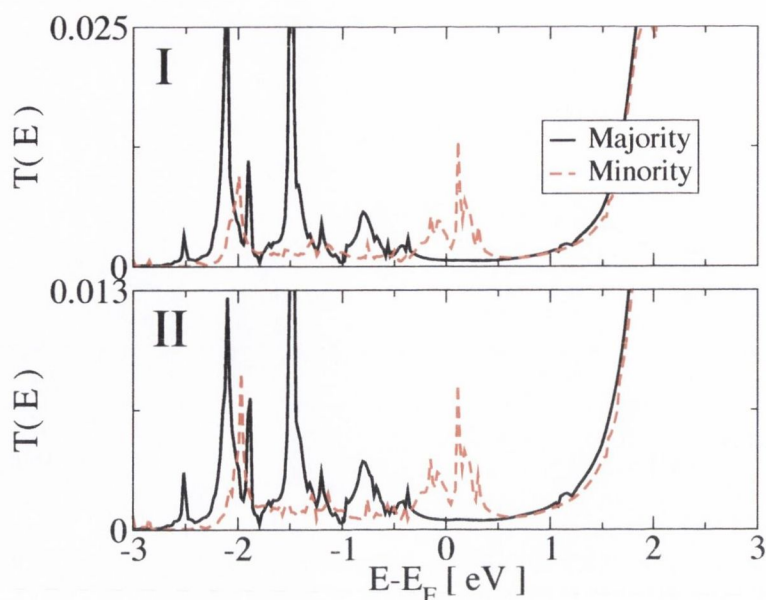


Figure 4.25: Transmission coefficients as a function of energy for the parallel configuration and different positions of the STM tip on the molecule. Note that the scales on the two graphs are different.

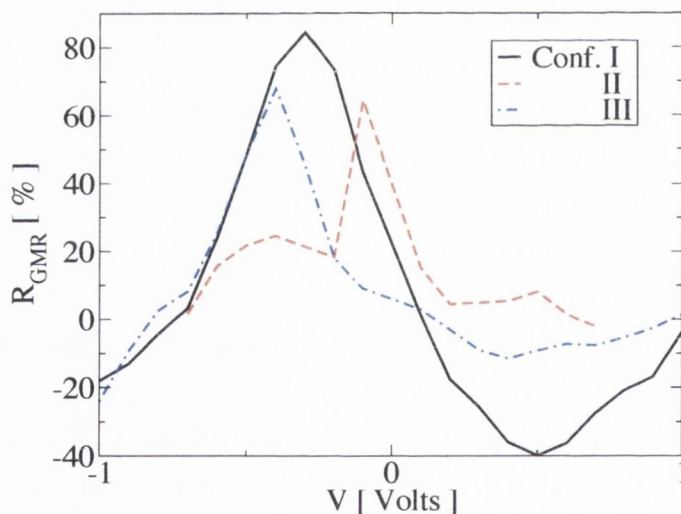


Figure 4.26: Giant magnetoresistance ratio as function of bias for different arrangements of the STM tip.

around and remains unchanged up to 1 Volt.

In order to analyse this curve we turn to the bias-dependent transmission coefficients. For positive bias the results are shown in Fig. (4.27).

At zero bias we can clearly see two crests slightly below the Fermi level for majority spins and one above and another below the E_F for minority spins. The nature of these crests can be understood by looking at the projected of states of the entire system - Ni-surface/molecule/Ni-STM. We can see in figure (4.28) that there

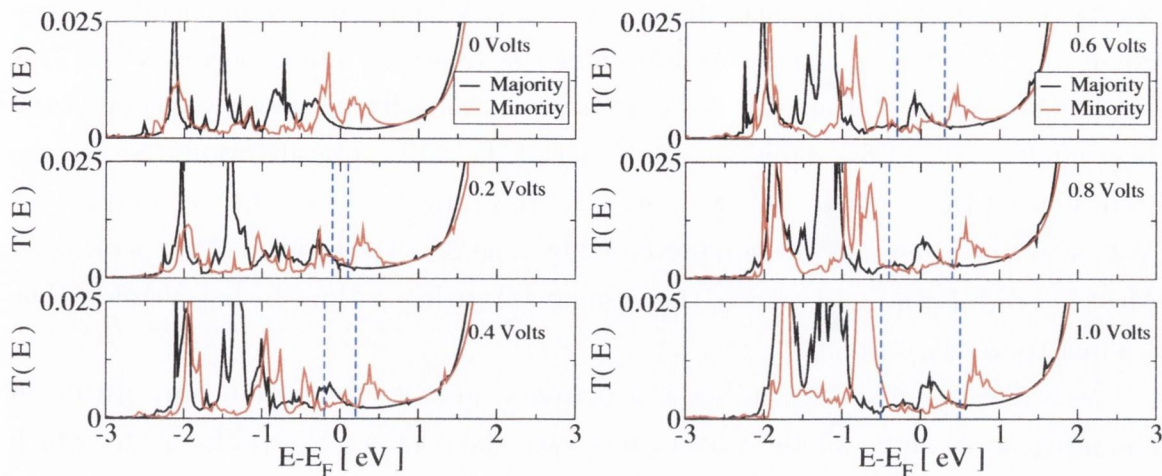


Figure 4.27: Transmission as a function of energy for BDTT attached to a Ni [001] surface for forward bias in configuration III.

are two states - for both majority and minority spins - which are close in energy to the zero-bias conductance peaks. The first state corresponds to a surface state on the nickel substrate which hybridises with the sulphur atom adsorbed on it. The second state is slightly lower in energy and is localised on the low-coordinated atoms of the tip. The existence of surface states usually lead sharp but high conductance peaks, but because the two contacts with the molecule present different electronic properties, these states lie at different energies in the PDOS: the system is off-resonance.²

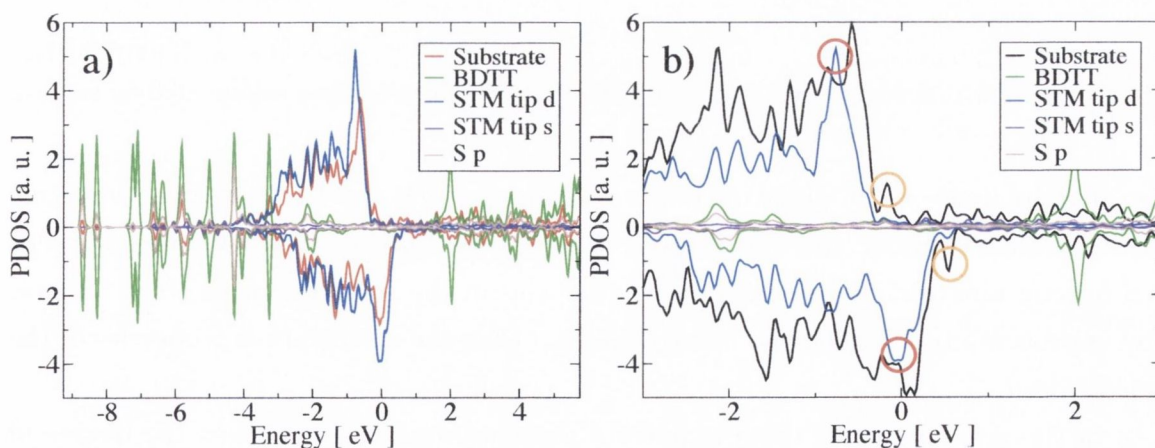


Figure 4.28: Projected density of states of the combined system surface/BDTT/tip. The states accounted for the transport in the surface and tip are circled in blue and red respectively. The bias window is indicated by vertical dashed blue lines.

²Resonant surface states have been observed in theoretical studies of point contacts [211] and tunnelling junctions [140] where both electrodes are similar. Usually impurities and the introduction of bias lead to a quenching of these states in experiments.

As we apply a positive bias the surface state, which is higher in energy (orange circle in Fig. (4.28)), moves upwards and the tip state moves downwards. This means they never overlap and the current monotonically increases as we open the bias window. When we apply a negative electric field the opposite occurs, we can see from figure (4.29) that these states move within range of each other at around -0.4 Volts creating a resonant state represented by a peak in the transmission coefficients. Most notably, for minority spins, this resonant state lies within the bias window thus leading to higher currents.

As we keep increasing the bias, the states come off resonance again. Although the integration range for the current increases the conductance peaks shrink which in turn results in the current *plateau* of figure (4.24a).

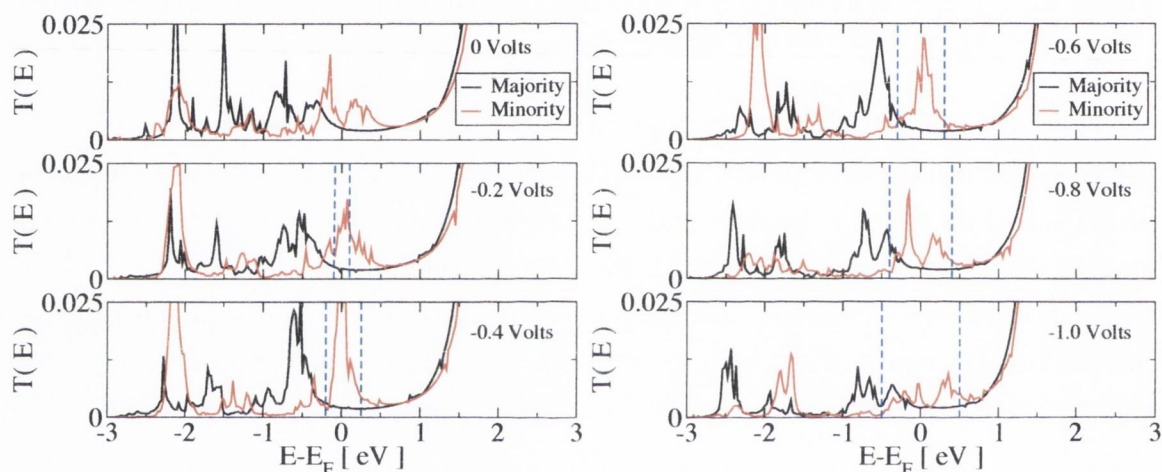


Figure 4.29: Transmission as a function of energy for BDTT attached to a Ni [001] surface for backward bias in configuration III. The bias window is indicated by vertical dashed blue lines.

This plateau will remain unchanged until we reach the LUMO of the molecule (around 1 eV above the Fermi level) whereas for forward bias the current keeps increasing monotonically. This leads to a swap in the rectification process. Hence, by appropriately selecting the voltage one can tune the rectification properties of the molecule.

In the AA alignment there is never a resonant state, nevertheless the degree of rectification is also large. At 1 Volt it is approximately 30 %.

Hence we have shown that by changing the position of the spin polarised STM tip with respect to an organic molecule we can obtain an enhancement of the current by probing different molecular orbitals as well as highly asymmetric $I - V$ characteristics. The correct description of the bias ramp results in interesting phenomena such as resonance states and current rectification.

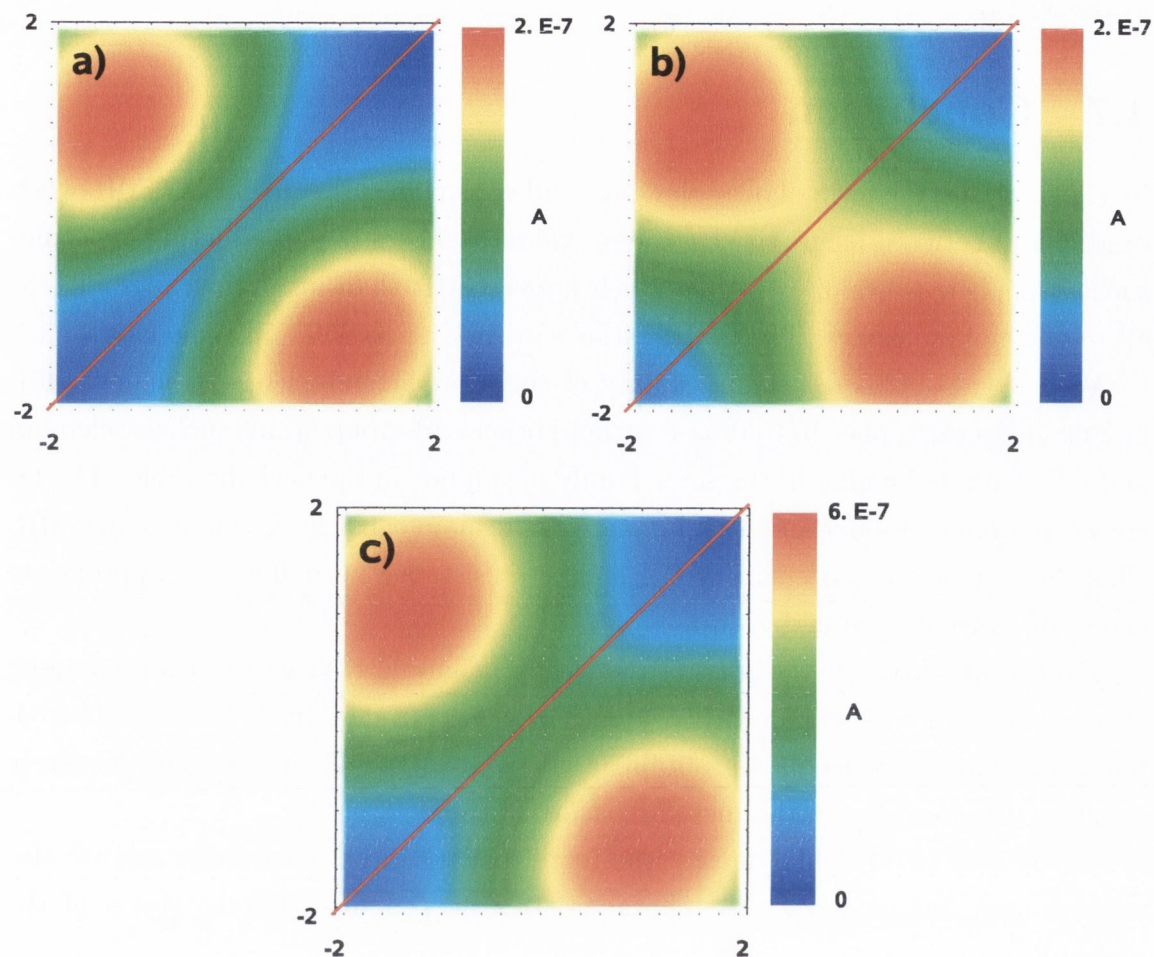


Figure 4.30: Theoretically calculated STM image of a benzene-thiol-thiolate molecule attached to a Ni surface probed by a Ni STM tip. a) Majority spin current, b) minority spin current and c) total current. The molecule lies along the diagonal depicted by the red line.

We can go one step further and calculate an STM image using the NEGF approach. By calculating the non-equilibrium steady current at different lateral positions of the tip (keeping the distance between the apex Ni atom and the sulphur at 4 \AA) we can reproduce the image of an STM experiment including the interaction between sample and tip, an effect usually neglected in simulations of this type [210]. In figure (4.30) we show a surface plot resulting from calculating the current at an applied bias of 500 mV between sample and tip. We considered here only the AA configuration. The plane of the benzene molecule lies along the diagonal (the red line). Hence, we observe higher currents above and below the plane of the molecule. This is an indication that we are imaging the delocalised π orbitals of the benzene molecule. Most notably there is no signature of the hydrogen atom even though it lies closer

to the Ni tip.

4.7 Conclusion

In this chapter we have shown that molecules can give rise to large GMR when sandwiched between magnetic electrodes. We have shown that conducting molecules such as triphenyl-dithiol can show much larger GMR than insulating ones such as alkane-dithiol molecules. The GMR ratios can vary up to 650% in some cases.

We have also explored the possibility to engineer the end-groups to achieve optimal magnetoresistance. In that case we used other end-group atoms such as selenium and tellurium, belonging to the same family of sulphur in the periodic table. The increase in atomic number and atomic radius is the main cause in the increase in GMR. This shows how we can engineer the magnetoresistance by making an appropriate choice of molecule and end-group.

Finally we explored the idea of diode-like magnetic devices by using charging effects combined with asymmetric coupling to the electrodes. In the case of a phenyl-tellurium-thiolate molecule we obtain large polarisation of current, but relatively small rectification due to the metallic nature of the device.

In the case of STM-like devices the rectification can be much large and we also showed how change the $I - V$ characteristics by probing different states of the molecule.

Chapter 5

Transport through DNA: where physics and biology meet

5.1 Introduction

In chapter 4 we have discussed the possibility of using organic molecules as spacers for GMR devices. We have shown that it is possible to obtain large GMR ratios as well as asymmetries in the $I - V$ characteristics that might lead to a diode-effect. In many aspects this is an attempt to reproduce at the nanoscale effects already observed in metallic multilayers or in microscaled devices.

An interesting possibility is to produce all-molecular devices. Based on this idea Bandaru *et al.* [212] have recently shown that it is possible to create logic gates using carbon nanotubes without the need of an external metallic gate. Another interesting idea is that of Cobaltocene molecules as both spin injector and spin detector in molecular spin valves [213]. Finally the transport properties of molecular magnets [214] have been shown to be intrinsically coupled to the internal degrees of freedom of the molecule, most notably to its spin state [215, 216].

A tantalising prospect for nanoscale electronics lies in a seemingly unrelated field: genetics, and in particular DNA research [18, 217].

In all cases described above, be it magnetic molecules or DNA, numerical simulations of electronic transport play an important role in predicting their properties and suitability for possible applications. Most of the systems described above fall into the category of macro-molecules. In other words we must move away from systems comprising only a handful of atoms towards larger organic molecules (still at the nanoscale) which are made of a few hundred constituent particles.

For that reason working with DNA as a possible building block for nanoscale electronics is both exciting and challenging. A computational tool for dealing with these large systems with a high degree of accuracy is necessary.

5.1.1 What is DNA?

Deoxyribonucleic Acid (DNA) is a polymeric chain of nucleotides.¹ Each nucleotide has three constituent parts: a phosphorous backbone, a sugar molecule (a pentose in the case of DNA)² and a nitrogenated base. The first two are the same for every nucleotide while the nitrogenated base is one of four possible choices: Adenine, Guanine, Thymine and Cytosine. Their structural formulas are shown in figure (5.1). These are aromatic compounds with delocalised π bonds.

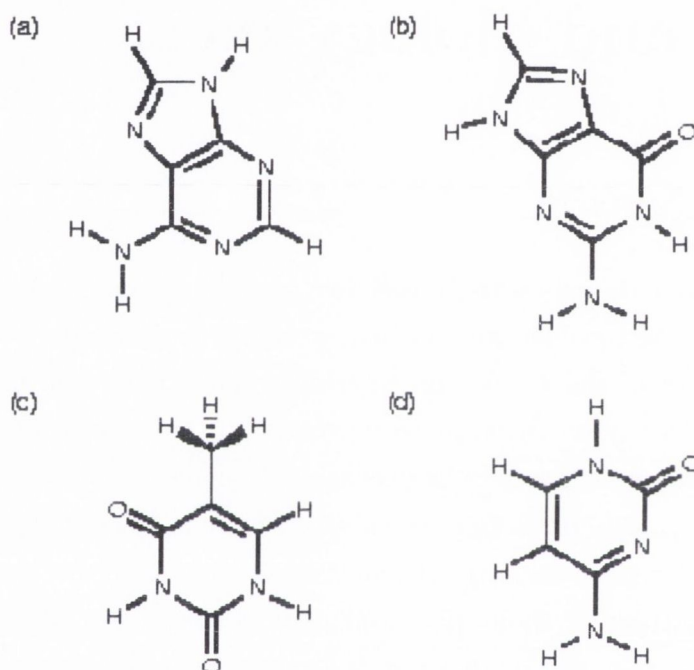


Figure 5.1: Sketch of the four nitrogenated basis that form DNA: (a) Adenine, (b) Thymine, (c) Guanine and (d) Cytosine.

The final structural formula of a nucleotide is shown in Fig. (5.2). Nucleotides bond together via hydrogen bonds between the basis to form pairs. Interestingly, although there are four basis, each one can only bond to a single complimentary counterpart.³ As we can see from figure (5.3) each base pair is coupled through

¹Nucleotides are also the building blocks of other important biological molecules such as ribonucleic acid (RNA) and molecules associated with energy production and signalling inside a living cell.

²A five-carbon sugar.

³There are interesting new structures as G4-DNA which can be derived from single strands of DNA. In G4-DNA four Guanine molecules bond in-plane and the subsequent stacking forms a four stranded DNA-like structure (tetra-helix structure). In this work we will only concern ourselves with DNA itself, we refer the reader to the relevant references to G4-DNA [218].

hydrogen bonds; Guanine to Cytosine, Adenine to Thymine. Pairs of nucleotides are subsequently stacked to form a double stranded structure bonded through the phosphate backbone.

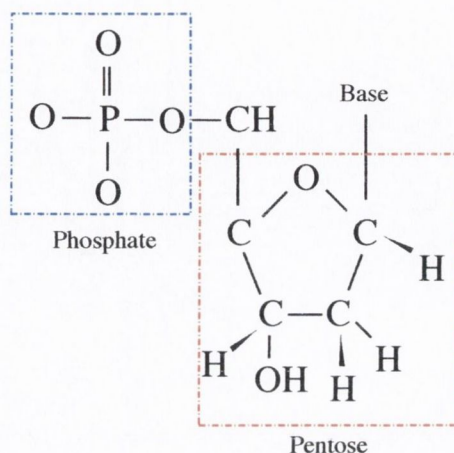


Figure 5.2: Structural formula for a nucleotide showing the phosphate backbone and the pentose. The base is one of (a-d) in figure (5.1).

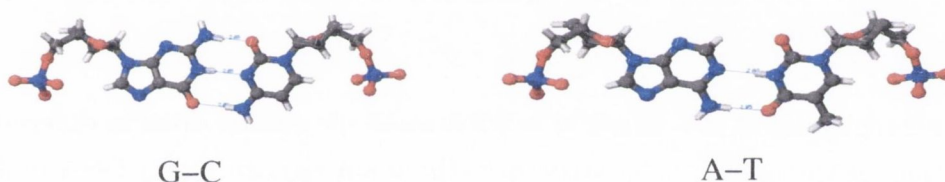


Figure 5.3: The molecular selectivity properties of DNA nitrogenated basis'; the hydrogen bond coupling of (a) Adenine to Thymine and (b) Guanine with Cytosine. Colour code: white - hydrogen, grey - carbon, red - oxygen, blue - nitrogen and dark blue - phosphorus.

Furthermore, because strands of the backbone are aligned anti-parallel to each other the planar stacking of these aromatic compounds is at an angle. This leads to a helical structure. Such an arrangement was first proposed by Watson and Crick [219] based largely on x-ray data by Franklin [220] and Wilkins [221]. Their work was considered so important that Watson, Crick and Wilkins were awarded the Nobel prize in Physiology or Medicine in 1962 [222].⁴ The structure shown as a ball-and-stick model in Fig. (5.4) - the structure of DNA - is probably the most recognisable image in the biological sciences today.

⁴Until Watson and Crick's proposal the structure of DNA was one of the most sought after results in crystallography and the biological sciences. Models had been proposed by Pauling and Corey [223, 224] as well as others. For an interesting yet highly personal and one-sided account of the discovery of the DNA structure one should refer to Ref. [225]

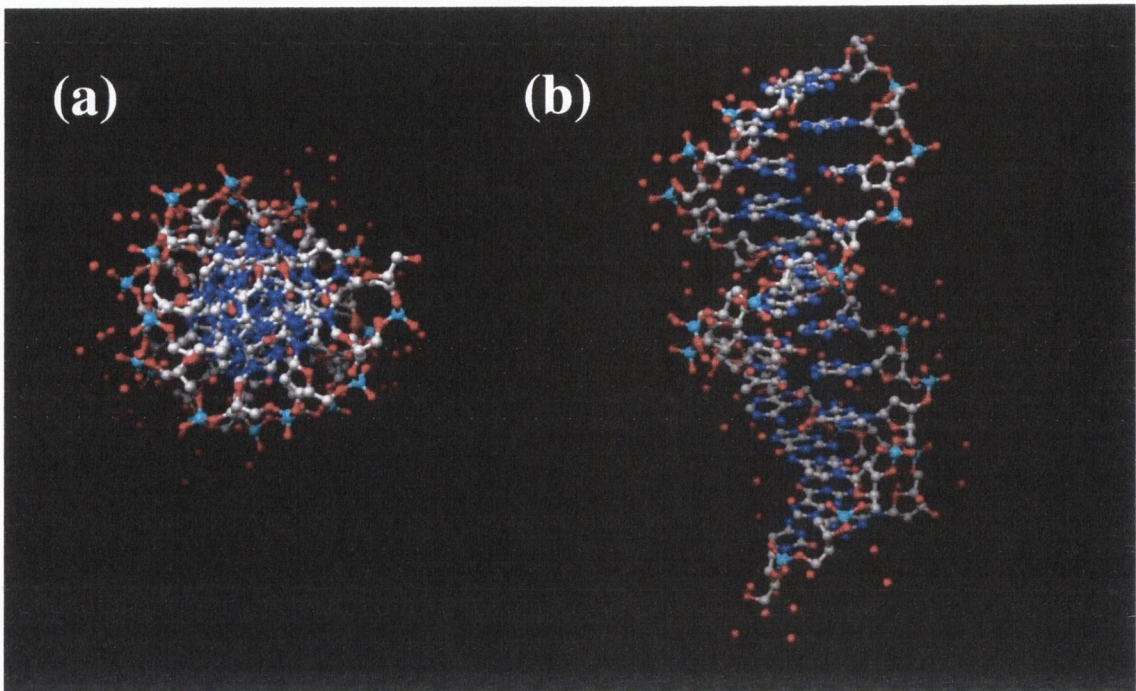


Figure 5.4: (a) Side and (b) top views of one full turn (10 base pairs) for B-DNA. Red spheres following the backbone denote possible counter-ions. Colour code: white - hydrogen, grey - carbon, red - oxygen, blue - nitrogen and cyan - phosphorus.

The arrangement of the atoms in a DNA molecule can be done in different ways while retaining the double helix structure (the main signature of a DNA molecule). The two main forms of DNA we are interested in are known as A-DNA and B-DNA [226, 227, 18]. B-DNA is found under physiological conditions, *i. e.*, in the presence of water molecules and when humidity levels are above 90 % [18]. When humidity levels drop below 75 % we have dry DNA and the structure of the molecule changes into the A form. In figure (5.4a-b) we show side and top views for one full turn of B-DNA and in Fig. (5.5a-b) we have the same for A-DNA.

We can note that the atomic arrangements are significantly different. Firstly, the stacked nitrogenated basis are aligned perpendicular to axis of the helical structure in B-DNA and at an angle in the case of A-DNA. Secondly, the twisting angle has also changed. In the case of B-DNA the angle between stacked base-pairs is 36° whereas in A-DNA it is 32.7° . This means that we need ten base pairs in the former case and eleven in the latter in order to have one full turn of the double helix structure (a periodic cell) in the solid state sense.

The interest in DNA from a biological perspective arises because it contains the complete information about each living being, *i.e.* it regulates the transcription of

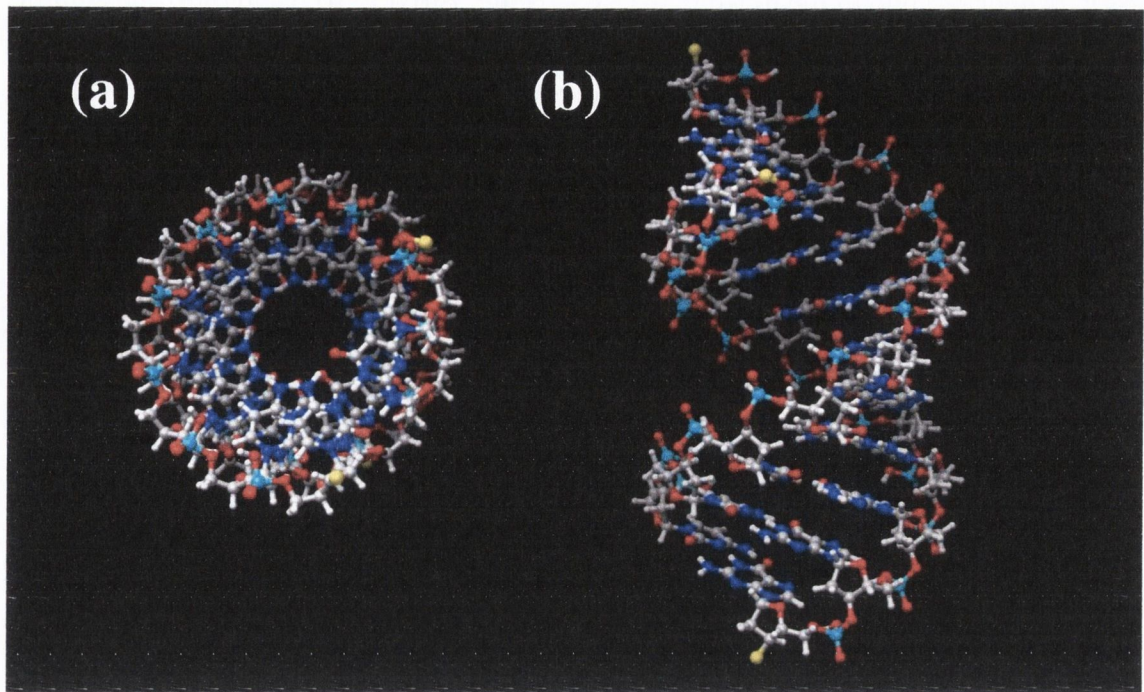


Figure 5.5: (a) Side and (b) top views of one full turn (11 base pairs) for A-DNA. The water molecules and counter-ions have not been included. Colour code: white - hydrogen, grey - carbon, red - oxygen, blue - nitrogen and cyan - phosphorus. The yellow spheres denote the sulphur atoms which anchor the molecule to a metal. In infinite strands it is not present.

proteins which are responsible for our metabolism. It also determines our physical appearance and many aspects of our health. In essence DNA can be considered as the ultimate memory device. Understanding the structural and functional aspects of this molecule has led to a number medical breakthroughs and a deeper understanding of living organisms as a whole [228]. Although a great deal has been done in that aspect an insurmountable amount of work still remains and there many exciting questions remain unanswered [228].

5.1.2 Is DNA a conductor?

But why are physicists and materials' scientists interested in DNA for electronics applications? One of the reasons is due to its molecular recognition properties. In other words its ability to bond with specific molecules (Guanine to Cytosine and Timine and Adenine) can lead to self-assembled devices at the molecular level.

Braun *et al.* [19] explored this idea by attaching different types of nucleotide sequences to two separate gold electrodes. These single stranded oligonucleotides

work as hooks, while in mean time, λ -DNA⁵ is deposited in solution onto the sample. The 16- μm -long λ -DNA then hybridises with specific nucleotides; only those which provide a specific matching combination. Subsequently the authors coat the DNA molecule which has attached to the electrodes with Ag clusters, using the DNA strands as a template for metallic interconnects.

One can clearly see the amazing possibilities. Integrated circuits can be designed by marking electrodes with a specific (or combination of) basis. The desired connections are immediately made once DNA in aqueous solution is deposited onto the sample.

More interestingly still is whether it would possible to use DNA itself as the device instead of merely as a template. This in turn leads to the issue of DNA conductivity. This is no doubt a contentious one.

The first proposal in favour of DNA conductivity was made as early as 1962 by Eley and Spivey [229]. The authors proposed that the $\pi - \pi$ bonds between stacked basis could create a delocalised state along the double helix that would lead to conducting behaviour. Indeed, other similar stacked aromatic crystals present metallic character [230], although some crucial differences with DNA are evident. Most notably DNA is not, strictly speaking, a polymer because the arrangement of the stacked basis is not necessarily periodic. This can possibly lead to localisation effects which might hinder the conduction.

Unfortunately, experimental results so far seem unable to answer this question unambiguously. Braun *et al* [19] in their work on DNA-templated metallic wires measured the conductance of 11- μm -long DNA molecules deposited on a glass substrate and sulphur-bound to gold electrodes. They show that DNA in solution (B-DNA) is insulating up to 10 Volts of externally applied bias; no conductance is seen over this bias range. This result seems to suggest that DNA is insulating. Experiments performed by de Pablo *et al.* [231] also show no conductance (resistances of at least $10^{12} \Omega$) on 1- μm -long λ -DNA double strands deposited on mica surfaces.

In contrast, Fink *et al.* [21] used a low-energy electron point source (LEEPS) to image bundles of DNA molecules approximately 600 nm long. These ropes were deposited on a conducting sample holder with holes. The measurements were then performed using a manipulating tip that approaches the bundles until contact is made. The $I - V$ characteristics suggest that DNA conducts as efficiently as a good semiconductor (its behaviour is Ohmic). However, these results have been challenged

⁵ λ -DNA is simply the genetic material of the bacteriophage virus *Enterobacteria phage* λ . It can be easily isolated in the laboratory and therefore is a good candidate in experiments. In our work, for practical purposes we consider λ -DNA simply as a random sequence of nucleotides.

by de Pablo *et al.* [231]. It has been argued that even the low-energy electrons used in the imaging process can cause damage to the DNA structure and lead to higher conductivity.

Kasumov *et al.* [232] obtained some striking results. They suggested that DNA deposited on Re/C electrodes on a mica substrate is metallic down to 1K - of the order of one resistance quantum. Below such temperature the Re/C contacts undergo a superconducting transition and the DNA molecules become superconducting as well due to proximity effect. Since these results have never been reproduced, we should consider them the least reliable ones and we shall not address them here.

This brings us to the last set of results for conductivity in DNA. Experiments on short DNA strands (between 26-30 base pairs) were performed by Porath *et al.* [20] and subsequently by Cohen *et al.* [233, 234]. In both cases, the authors performed conduction experiments on short suspended DNA strands - between 26 and 30 base pairs. Porath and collaborators used a suspended Platinum bridge with an 8 nm gap where a 10.4-nm-long poly(G)-poly(C) DNA oligomer was deposited. The corresponding $I - V$'s present a voltage gap that varies from sample to sample from about 1.5 up to 2.5 Volts and the currents obtained were about 1.5 nA at 4 Volts. Cohen *et al.* took this experiment further by depositing a thin film of DNA short strands 5'-thiolated on both ends on a single gold substrate. Subsequently a gold nanoparticle is allowed to bond to the remaining sulphur at the other end of the strand. The authors then use a conducting AFM tip to measure the conductance of, what the authors claim is, a single DNA molecule. The results show the same voltage gap from the previous experiment, but much higher currents: of the order of 100 nA even in the case of complex nucleotide combinations. Besides double stranded DNA (dsDNA) the authors also considered single stranded (ssDNA) and systems where the sulphur anchoring group was removed. In all cases except for dsDNA bonded through S groups no conducting behaviour was observed. Finally, in both articles, the authors suggest that transport is mediated by molecular energy bands and that DNA behaves as a wide-gap semiconductor.

More recently Xu and coworkers [23] performed break junction experiments on DNA molecules in aqueous solution (the molecules were shorter, containing only 8 base pairs). Their results show no conductance gap and also high currents.

Other experiments deal with charge transfer in free standing (in the absence of electrodes) DNA molecules in solution. For these experiments, an electron is photo-excited and allowed to relax. It is usually accepted that the excited electrons move towards guanine nucleotides which are regarded as acceptors [235, 236]. In these

experiments a number of mechanisms have been proposed for the observed charge transfer depending on the energetics of the of the base sequence [237, 238, 239, 240]. These experiments are conceptually different to direct conductance measurements where the molecule is contacted between two electrodes (a source and a drain) and an external bias is applied. According to Porath *et al.* [20] none of the mechanisms for these setups can account for the results in direct conductance measurements.

At first it appears that the plethora of results shed no light on our initial question. But if we take a closer look, we will see a general picture arising from these seemingly conflicting conclusions. The experiments that show low conduction or insulating behaviour were performed on mica or glass surfaces. It has been shown that the interaction with the substrate leads to significant changes in the DNA molecule [241]. Most importantly, results showing semiconductor behaviour were obtained in short DNA strands (between 8-30 base pairs). These observations suggest that at these length scales the electronic transport is coherent, whereas for larger length scales (the micrometre range) inelastic effects may dominate.

Some theoretical work has been performed on DNA molecules. Taniguchi and Kawai [242] performed DFT calculations on A- and B-Poly(dA)-Poly(dT) and A- and B-Poly(dG)-Poly(dC) molecules.⁶ The authors showed that the HOMO in both A and B forms is largely adenine- (for Poly(dA)-Poly(dT)) or guanine-dominated (for Poly(dG)-Poly(dC)). De Pablo *et al.* [231] also performed DFT calculations on a periodic Poly(dG)-Poly(dC) A-DNA molecule. In this case the authors also considered base swaps at a concentration of one per every 11 pairs to show the effects of Anderson localisation and to argue that random DNA sequences are insulating.

Endres *et al* [243] have performed DFT calculation to show that the effective coupling between stacked basis is close to zero in the case of A-DNA and up to 0.1 meV for B-DNA. Firstly, this results show that the twisting angle has an influence on the inter-base coupling along the helix. Secondly, in principle, one should expect little or no conductance even in the case of a periodic double strand because the state at the Fermi level can be considered as a collection of isolated molecular orbitals for the base pairs.

All these calculations were performed using standard equilibrium DFT. The effects of the electrodes have been completely neglected and the conductivity can only be inferred by looking at the band structure. Transmission curves or $I - V$ characteristics thus far have only been calculated with model Hamiltonians [244].

⁶A periodic sequence of adenine-thymine (Poly(dA)-Poly(dT)) or guanine-cytosine (Poly(dG)-Poly(dC)) base pairs.

One important issue that has been neglected in all previous DFT calculations is the role of the electrodes. The alignment of the molecular orbitals with the Fermi level of the semi-infinite leads will greatly influence the transport properties of these systems.

5.2 Calculations

Fully *ab initio* transport calculations on DNA, although computationally demanding, seem to be the only way of unambiguously assessing the conductivity of DNA molecules. *Smeagol* is the perfect tool for this task, being fully parallelised and capable of treating systems in excess of 1000 atoms (see section 2.4.1).

In all our calculations the DNA molecule was modelled using the following basis set

Atom	<i>s</i>	<i>p</i>	<i>d</i>
H	1 <i>s</i> ¹ DZ	-	-
C	2 <i>s</i> ² DZ	2 <i>p</i> ² DZ	-
N	2 <i>s</i> ² DZ	2 <i>p</i> ³ DZ	-
O	2 <i>s</i> ² DZ	2 <i>p</i> ⁴ DZ	-
P	3 <i>s</i> ² DZ	3 <i>p</i> ³ DZP	-
S	3 <i>s</i> ² DZ	3 <i>p</i> ³ DZP	3 <i>d</i> ⁰ SZ
H'	1 <i>s</i> ¹ DZP	-	-
O'	2 <i>s</i> ² DZ	2 <i>p</i> ⁴ DZP	-
N'	2 <i>s</i> ² DZ	2 <i>p</i> ³ DZP	-

Table 5.1: Initial atomic configurations and their respective basis sets for each element in the DNA calculation. Elements denoted by prime are involved in hydrogen bonds.

For those atoms where H-bonds are involved we use extra polarisation orbitals: *s* orbitals in hydrogen and *p* orbitals in nitrogen and oxygen. This basis is the same used in previous calculations [231, 245] with satisfactory results.

We considered two DNA molecules both in the A form, namely a molecule containing 2 base pairs and another one containing 11 base pairs (one full turn of the double helix structure). The molecules are attached on the hollow site of two gold [001] surfaces via thiolate end-groups. Figure (5.6) shows ball-and-stick models of the these two arrangements. The gold electrodes were modelled as 10x5x4 finite clusters (the introduction of self-energies turn them into semi-infinite quasi-1D wires). For the gold atoms bonded to the S end-groups we used *s*, *p* and *d* in the valence with

a double- ζ basis and soft-confinement potentials [40]. For the remaining gold atoms we use a single $5s$ orbital and we placed the filled d orbitals in the core.

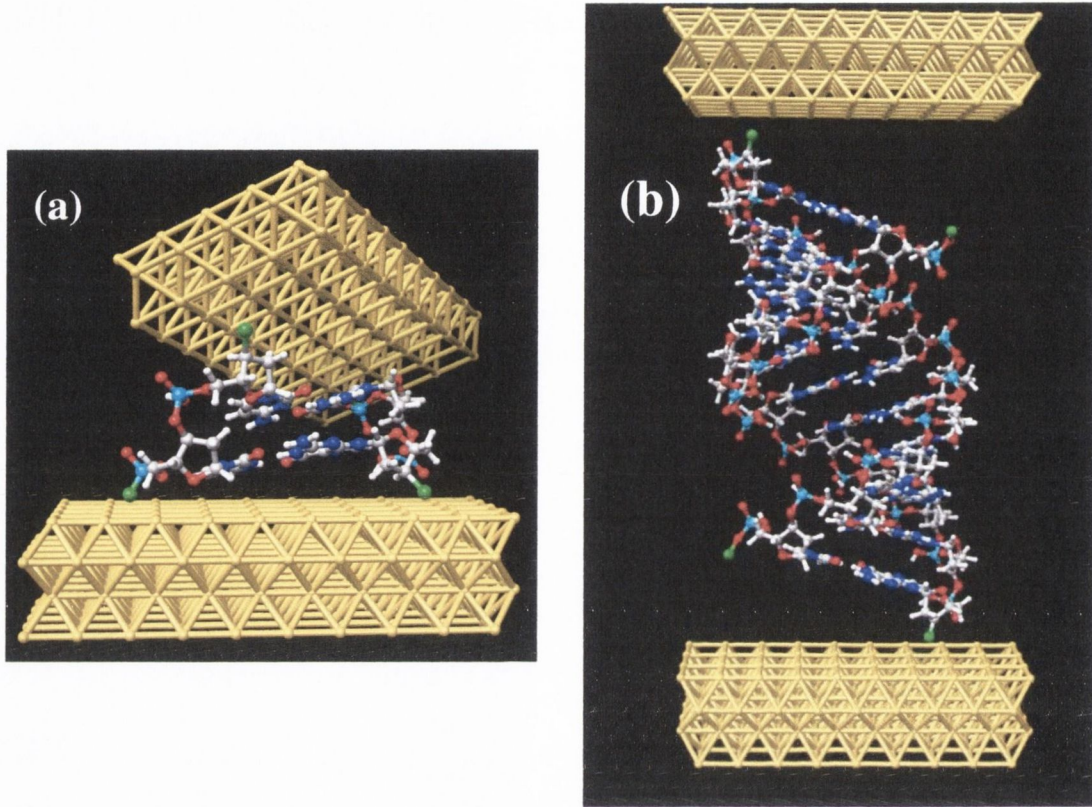


Figure 5.6: Ball-and-stick model of a) a two-base-pair, and b) an eleven-base-pair A-DNA arrangements. Color code: Au - gold; C - grey; H - white; O - red; N - blue; P - cyan; S - green

5.2.1 Describing Au in DFT with s orbitals only

In the case of bulk gold, LDA gives a good description of the electronic properties if we include the filled $5d^{10}$ and half filled $6s^1$ states in the valence and the remaining filled orbitals in the core (described by the pseudopotential).⁷

Figure (5.7a) shows the band structure along symmetry lines for a fully converged calculation of bulk gold at the DFT equilibrium lattice constant (4.09 \AA) with a rich basis set (double- ζ with soft-confinement potentials). We can see that the Fermi level, as it would be expected, is largely dominated by a broad s band. The d and p orbitals start to play a role at energies 3 eV below and 3 eV above E_F respectively.

The inclusion of $5d$ and $6p$ orbitals in the gold electrodes of our DNA transport calculation would make the problem intractable since the total number of basis func-

⁷The atomic configuration of Au is $[\text{Xe}] 4f^{14} 5d^{10} 6s^1$.

tions will exceed the amount of memory available. Fortunately the description of the leads in the transport problem depends largely on the band structure which are much more resilient basis set choice than total energy calculations. In other words, the band structure of the electrodes can be satisfactorily described by a simpler basis set without sacrificing the overall precision.

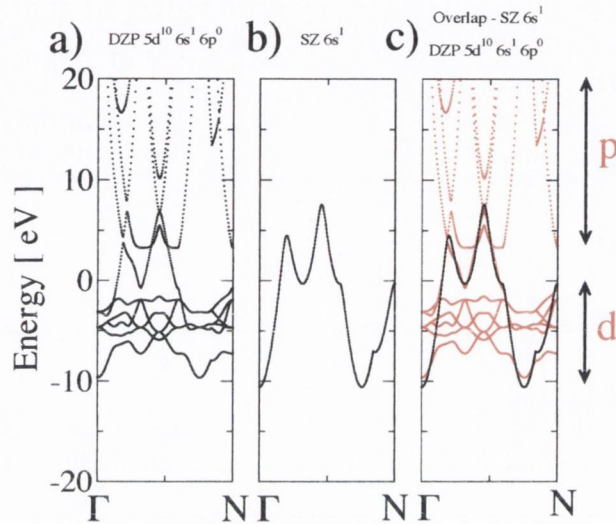


Figure 5.7: Band structures obtained using SIESTA with different types of basis sets and pseudopotentials for gold. a) double- ζ spd with polarisation orbitals, b) single zeta s with core correction and c) graphs (a) - red - and (b) - black - have been superimposed to show the similarity.

In fact, we performed band structure calculations (shown in Fig. (5.7b-c)) where the $5d$ orbitals were included in the core. We can clearly see that the band structures for this simpler case is very similar to the more precise calculation in the region ± 3 eV around E_F . Therefore, for voltages within this window we can expect adequate results.⁸ On the other hand, the description of the DNA molecule itself whose transport properties we are calculating is done in an accurate way, *i.e.* with a much richer basis set.

5.2.2 Infinite DNA strands

Before we actually start looking at the transport properties of double stranded DNA molecules attached to external leads it is interesting to consider the isolated molecule (without the effects of the electrodes). In figure (5.8) we show the total density of states and the PDOS projected onto the Guanine and the Cytosine basis. We can see

⁸It is important to notice here that the total energy and forces calculated using this configuration cannot be considered accurate.

that the HOMO (A in figure (5.8)) is clearly dominated by the Guanine states (~ 1 eV below E_F). One can notice that the broad occupied molecular orbital (BOMO) identified as (B) in the figure includes some contribution from the backbone and the pentose. Finally the LUMO is mostly dominated by Cytosine and the HOMO-LUMO gap is approximately 2 eV.

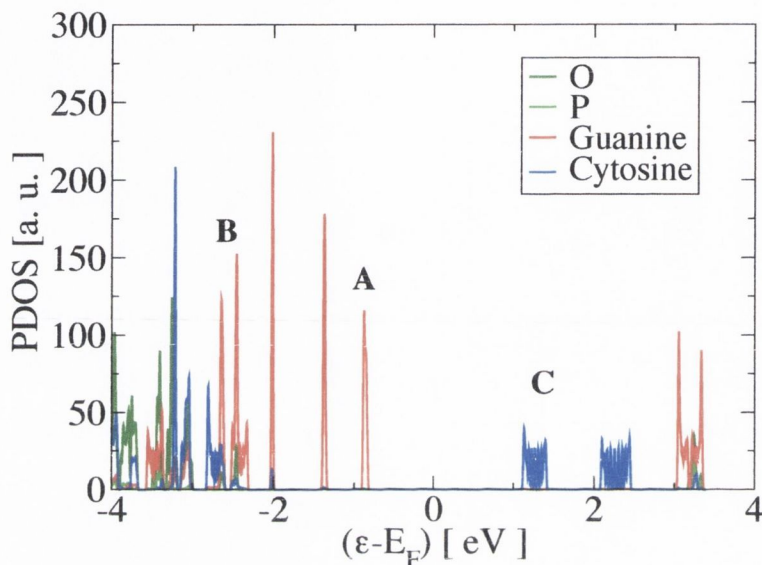


Figure 5.8: Total and partial density of states for infinite double-stranded Poly-(dC)-Poly-(dG) A-DNA. The partial density of states has been projected on either the Guanine or the Cytosine basis. Three states have been indicated: A) the HOMO, B) broad occupied molecular orbital (BOMO), and C) the LUMO.

This can be further corroborated by looking at the charge density projected onto these states. These are plotted in figure (5.9). Notably the delocalised π states over the Guanine are accountable for the HOMO while we see some charge density on the pentose and the phosphate backbone for the BOMO.

These results are similar to those obtained by Taniguchi and Tomoji [242] for infinite DNA double strands.

5.2.3 Two-base-pair DNA

We start our transport calculations *per se* by considering the small DNA complex. We performed extensive atomic conjugate gradient relaxations to obtain the optimised structure. In particular we are interested in obtaining the correct position of the sulphur atoms on the gold surface. We found that the distance between the S atoms and the surface is 2.5 Å, similar to those obtained for simpler thiolated

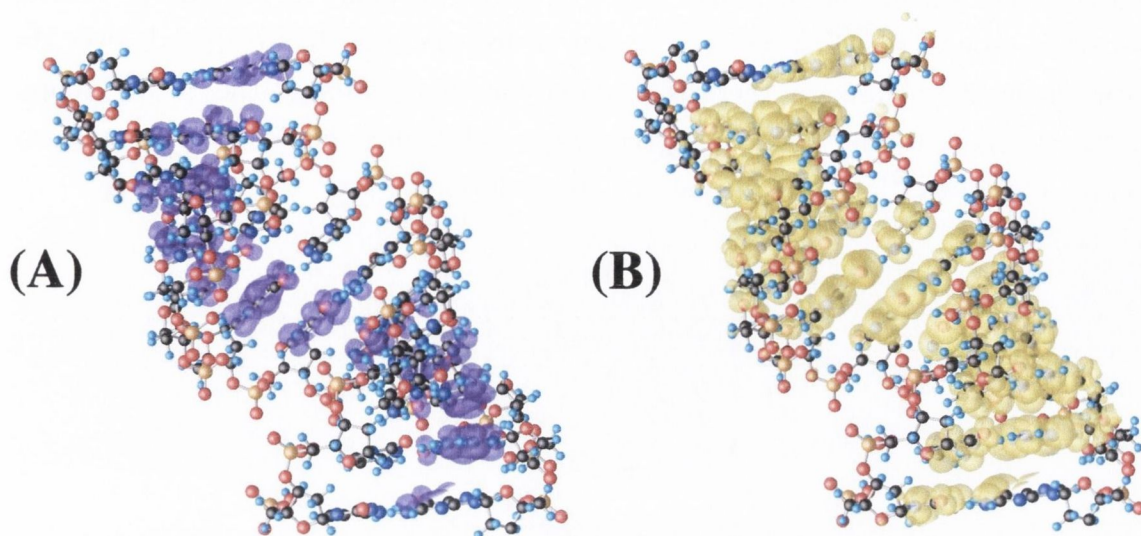


Figure 5.9: Iso-surfaces for local charge density for the (A) HOMO and (B) BOMO as highlighted in figure (5.8). For display purposes we have include one extra base pair totalling 12 base pairs.

compounds [174, 175].⁹

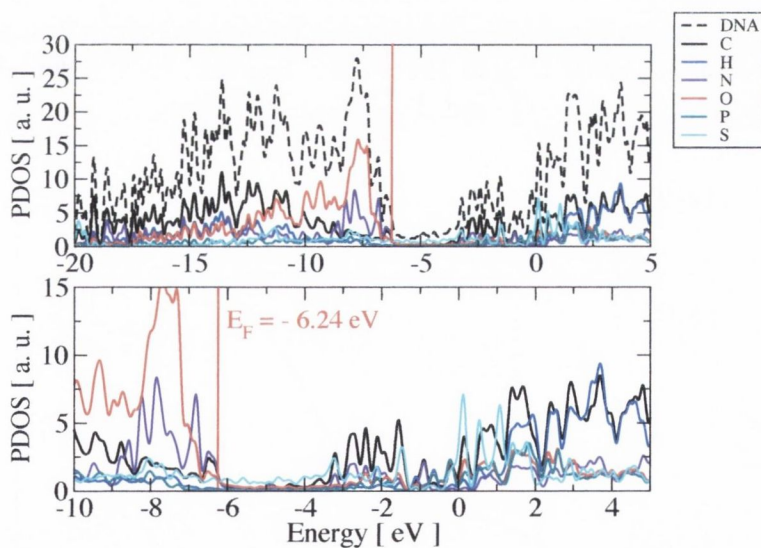


Figure 5.10: (a-b) Projected density of states of a thiolated two-base-pair structure attached to gold electrodes. Top and bottom panels represent the same PDOS with different energy ranges. The vertical red line indicates the position of the Fermi level, $E_F = -6.24$ eV.

From the projected density of states (Fig. (5.10)) we can clearly see the presence of broad states around the Fermi level. We also note the presence of a broad

⁹For the atomic relaxations we included the $5d$ and empty $6p$ orbitals of gold in the valence for all the atoms in the leads.

sulphur state within the molecular gap. By further looking at the charge density projected around E_F (Fig. (5.11)) we can notice that the charge spreads over the entire molecule. Moreover there is considerable charge around the S end-groups. From this analysis one would to expect large conductance, however one cannot say so for sure unless transport calculations are performed.

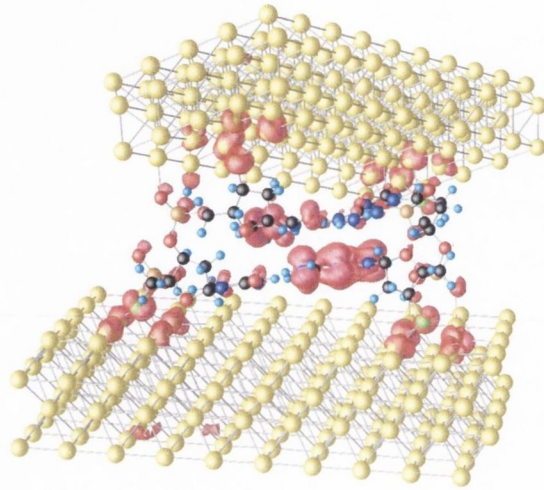


Figure 5.11: Projected charge density around the Fermi level for a two-base-pair DNA molecule attached to gold electrodes. Legend: Au - yellow, C - black, H - light blue, N - blue, O - red, P - orange, S - green.

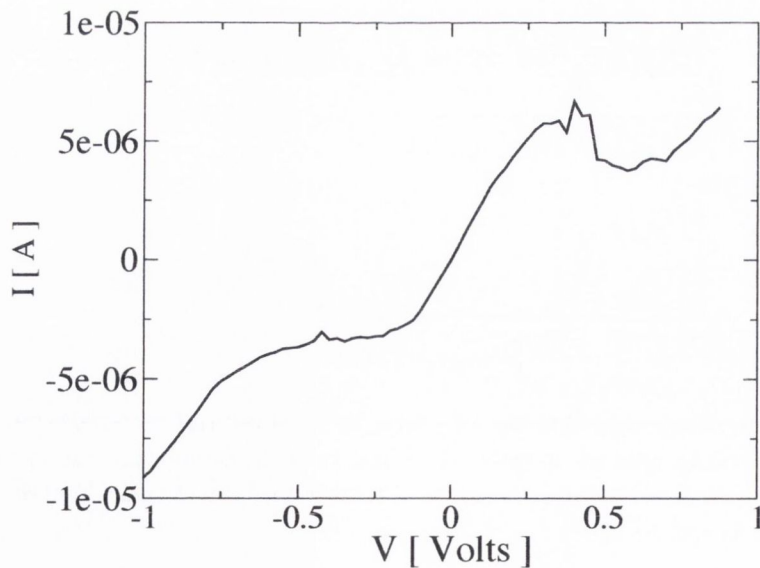


Figure 5.12: Current as a function of bias for a two-base-pair DNA strand. The $I - V$ is quite asymmetric and the current reaches $10 \mu\text{A}$ at 1 Volt.

The current as a function of bias for this short DNA strand is shown in figure

(5.12). We can see that the current is close to $-10 \mu\text{A}$ at -1 V (and $\sim 7 \mu\text{A}$ at 1 V) and is highly asymmetric. Moreover there is no gap in the $I - V$. This behaviour can be understood from inspecting the transmission coefficients as a function of energy for zero bias (Fig. (5.13)). There are two broad resonances close to E_F and the transmission for these resonances is close to unity. These two resonances can be associated with the pinning of the HOMO to the Fermi level. As we can see from the projected density of states for the entire system, this state is broadened by the interaction with the electrodes. In the presence of an external electric field these resonances will immediately contribute towards the conductance which in turn results in an absence of conduction gaps around zero bias.

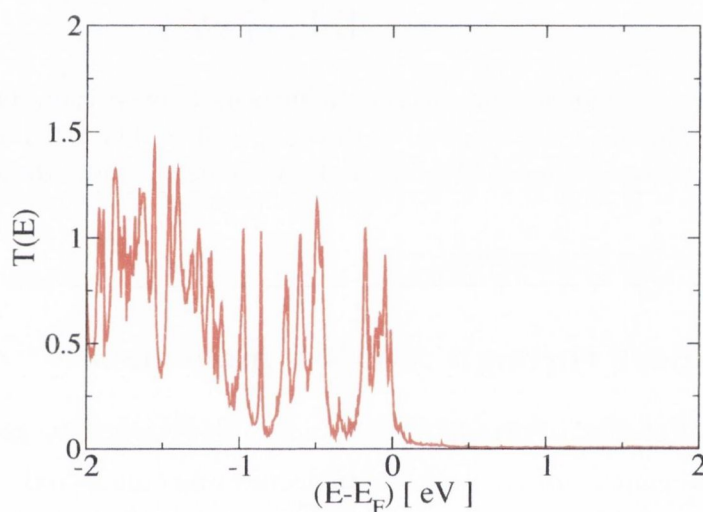


Figure 5.13: Transmission as a function of energy for a two-base-pair attached to gold electrodes.

Since the molecule is so short this behaviour can be associated to direct tunnelling between sulphur surface states. We consider this possibility by performing a calculation where the two-base-pair molecule was entirely removed from the contact region. In order to correctly model the vacuum region where we removed the molecule from we introduced ghost atoms [40].¹⁰ The results for the transmission coefficients at zero bias are shown in figure (5.14). From the figure we can note the presence of a peak slightly below the Fermi level associated to a gold-sulphur surface state. Hence we can conclude that the transport is mainly through sulphur and the molecule merely acts as a medium that effectively lowers the dielectric constant of

¹⁰The charge density in the vacuum region is usually poorly described by localised-basis-set approaches to DFT because these are usually atom centred. By introducing ghost atoms we include in the calculation extra basis functions in the vacuum region. These extra empty states have the same symmetry of the LCAO's used for the real atoms without including the pseudopotential.

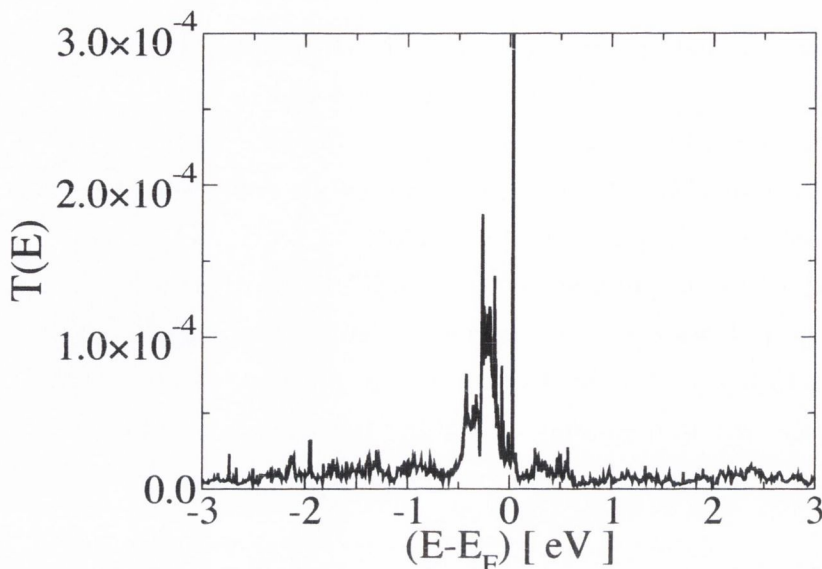


Figure 5.14: Energy dependent transmission coefficients between two [001] gold surfaces with sulphur atoms attached to the hollow sites. The DNA molecule has been removed but we have introduced ghost atoms to model the vacuum region.

the region between the two surfaces.

5.2.4 Transport through A-DNA molecules

For the longer A-Poly(dG)-Poly(dC) DNA molecule attached to gold, the fully relaxed atomic arrangement of the isolated molecule was considered. Those positions were kept fixed while S atoms were attached to the 5' and 3' sites at both ends of the molecule. This arrangement was then allowed to relax in a super cell with no boundary conditions. Subsequently the sulphur end-groups were attached to the hollow site of the [001] Au surface using the sulphur/surface distance obtained in the previous calculations of section (5.2.3).

The projected density of states of the eleven-base-pair A-DNA molecule is shown in figure (5.15). The picture shows features reminiscent of the isolated molecule. Most notably signatures of the HOMO, the LUMO and the gap remain largely unaffected after attachment to the electrodes. While we saw a broad sulphur state across the entire gap in section (5.2.3), here region identified as the HOMO-LUMO gap of the isolated molecule ($[-5.14, -2.8]$ eV) is practically devoid of states.

As it was the case with the two-base pair molecule the Fermi level is pinned to the HOMO of the isolated molecule. However, we can clearly see that that state is now much sharper. In other words, not as strongly coupled. The PDOS starts to broaden ~ 1.5 Volts below the Fermi level where oxygen states become important.

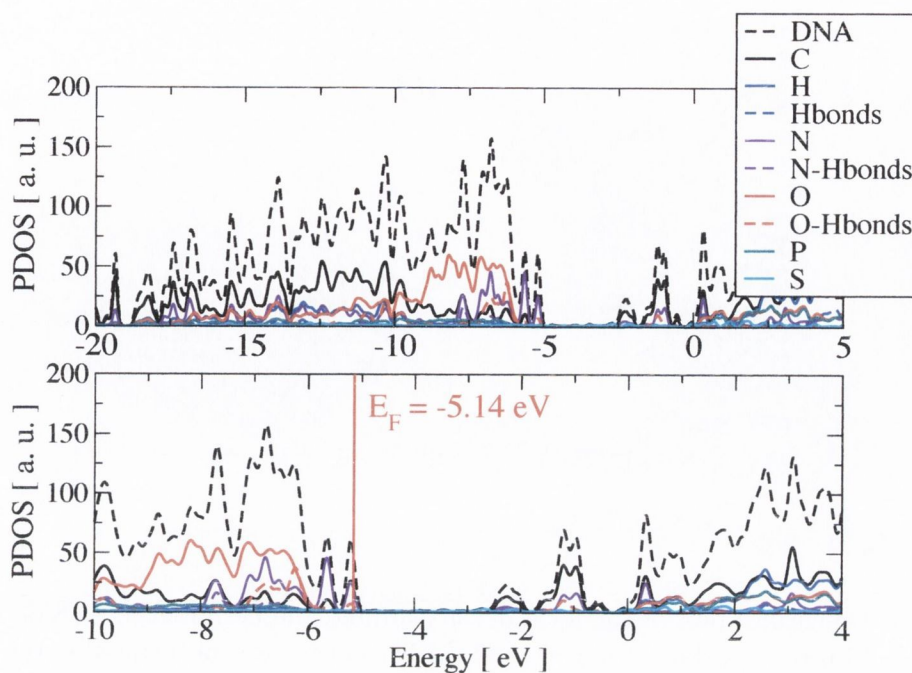


Figure 5.15: Projected density of states of a thiolated A-DNA structure attached to gold electrodes. Top and bottom panels correspond to the same system with different energy range.

By projecting the charge density around the Fermi level we can clearly see that most of the contribution to this energy region comes from the HOMO of the isolated molecule with some effect from the anchoring sulphur atoms.

The total transmission coefficients show some interesting behaviour. While the PDOS shows that the Fermi level is pinned to the HOMO we find very little conductance around E_F .

The HOMO is almost completely decoupled. In other words, although the HOMO is mostly due to the Guanine π states, the coupling between planes is close to zero as suggested by [233]. We can see that the transmission starts to be significant around 1.5 eV below the Fermi level. In the Landauer-Büttiker approach this would mean that an external applied bias of approximately 3 Volts would lead to coherent band conduction.

Hence, while calculations for the isolated molecule give some indication of the transport properties of these systems, only fully *ab initio* transport calculations where the effects of the electrodes are taken into consideration can elucidate the full quantum mechanical transport properties of these macromolecules.

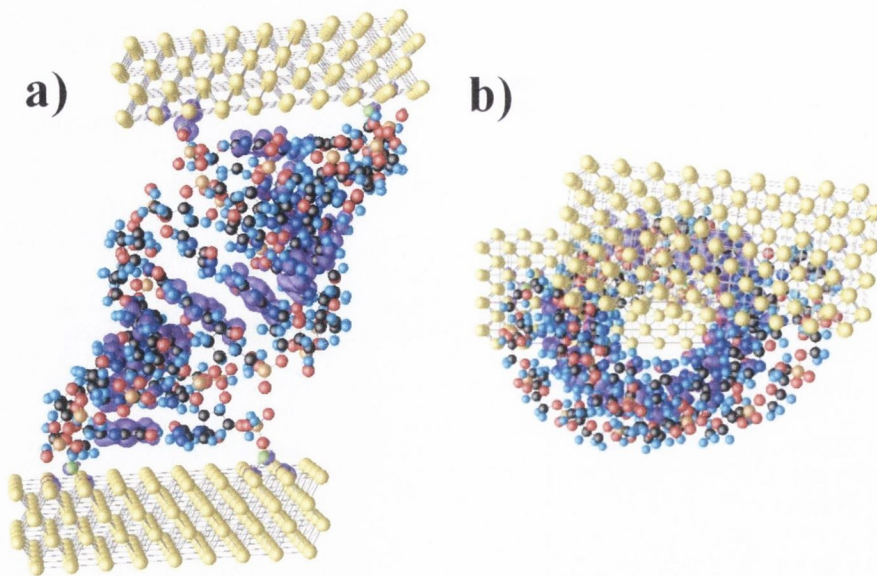


Figure 5.16: Iso-surface plot of the local density around the Fermi level. a) Side view and b) top view. The charge around the Fermi level is concentrated in the Guanine basis. Legend: Au - yellow, H - light blue, C - black, N - blue, O - red, P - orange, S - green.

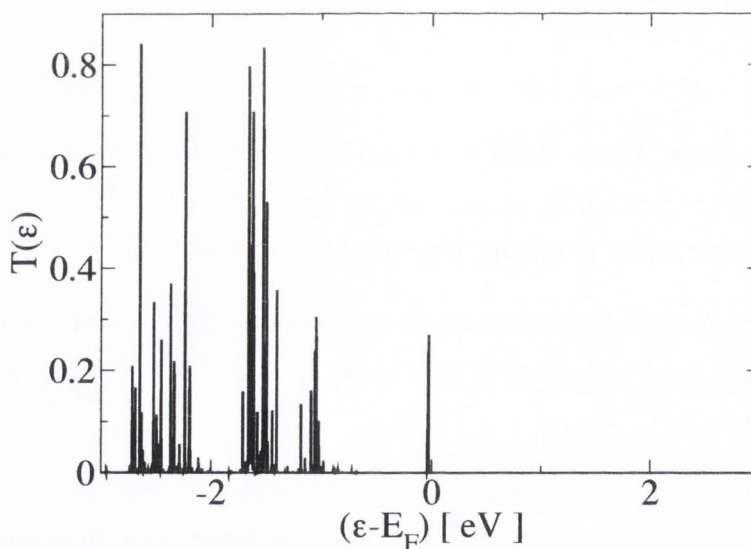


Figure 5.17: Transmission as a function of energy for a 11-base pair DNA strand attached to gold electrodes.

5.3 Conclusions

As we have seen, for both the short and long DNA molecules, the Fermi level is pinned to the HOMO as soon as we attach the electrodes. However, while in the short DNA the HOMO is broadened by coupling to the electrodes, the largely Guanine-

dominated HOMO level in the long DNA molecule is very localised. In that case, the HOMO is represented by a series of uncoupled states sitting in each of the Guanine bases.

Previous calculations [243] have shown that this effect would be present due to symmetry in A-DNA corroborating our results.

The broadened states in the short DNA molecule leads to high conductance even at zero bias, so once the bias is increased we see a large current response. On the other hand, the transmission coefficients of the long DNA show a clear gap up to 1.5 eV around the Fermi level. The gap leads to a flat $I - V$ characteristics up to 3 Volts. After that we clearly see conductance. This result is in agreement with a band transport mechanism through a wide band-gap semiconductor.

This result is completely consistent with experimental results in dry short DNA double strands performed by Cohen *et. al.*. We can clearly see that the states responsible are not the HOMO neither they correspond to the LUMO. The broader states responsible for the conductance lie below the HOMO in the so called BOMO state. This is related to the backbone instead of the basis. This leads us to believe that the transport properties of DNA are largely independent of our basis choice. In that case, it is also very robust with respect to localisation effects.

Conclusion

In summary, we have presented the theoretical framework of the non-equilibrium Green function formalism coupled to the Kohn-Sham Hamiltonian provided by DFT. This symbiosis can yield accurate transport properties of nanoscale devices, from surfaces to molecular spin valves. The non-equilibrium transport formalism can be understood in terms energy and bias-dependent transmission coefficients in a manner analogous to the Landauer-Büttiker scattering formalism for the linear regime [84]. We have also showed, using a single energy level model, that the steady state current through a one dimensional device can be thought of as a balancing act between current flowing from (into) the left electrode into (out of) a molecule or into (from) the right electrode and out of (into) the molecule. These two descriptions have been shown to be part of a more general formalism for transport (the NEGF formalism) which can be combined with the DFT-KS Hamiltonian to form *Smeagol* [71, 72]. *Smeagol* is our state of the art electronic transport code for nanoscale devices. It was specially designed for magnetic materials. It includes a procedure for regularising the self-energies in order to remove singularities brought about the localised states (specially *d* orbitals).

In chapter 2 we present how *Smeagol* can be efficiently parallelised up to 128 processors and we showed a number of tests which provide some insight into *Smeagol*'s capabilities. Most importantly we show how it can treat the transport properties of a variety of nanoscale systems under bias, from surfaces to molecular electronics devices, from systems with simple gold electrodes to more complicated ones where magnetism is present - for example Ni - and even non-collinear spins.

In terms of applications, we have analysed the possible existence of large GMR in magnetic point contacts using both a simple tight-binding Hamiltonian with NEGF and our more accurate *Smeagol* code. In the case of our simple tight-binding model we found the possibility of asymmetric $I - V$ characteristics arising from an asymmetric DW, but with no structural asymmetry in the electrodes. This shows the possibility of purely electronic asymmetries driven by charging effects. This is an effect that cannot be accounted for in the linear regime. Using *Smeagol* we also investigated the

possible occurrence of LGMR and HGRM (in excess of 10,000 % [11, 157, 163]) in magnetic point contacts. Our calculations showed no sign of such high values even after introducing corrections to the LDA exchange-correlation functional and oxygen impurities. This led us to conclude that the observed values cannot be accounted for from a purely electronic mechanism and other effects such as magnetostriction might be playing a role [159].

Still in the field of magnetism we introduced the concept of organic spin valves [87, 88], *i.e.* the idea of using the spin degree of freedom as the information carrier. We showed that it is possible to select the type of molecule (metallic or insulating) to maximise the MR ratio as well as engineer the anchoring groups connecting the molecule to the nickel electrodes. We have also used different anchoring groups to design asymmetric molecules which present spin-diode characteristics. Finally we also showed the possibility of accurately calculating tunnelling currents in spin-polarised STM-like experiments. Here a magnetic tip probes an organic molecule over a surface which is also magnetic. It was noted that the position of the tip with respect to the molecule can lead to current enhancement as one probes different orbitals. The presence of surface states in these devices was also shown. Due to the asymmetry of the electrodes these states are off-resonance. They are bias-dependent and only come into resonance for negative bias (current flowing from the tip to the substrate). This leads to large asymmetries in the current as well.

Finally we have showed that DNA molecules present semiconducting behaviour by calculating the transport properties of A-DNA molecules attached to gold. Our calculations reveal that the main state responsible for transport is neither the HOMO nor the LUMO as it is usually assumed in organic molecules [173]. In fact, the main contribution to transport comes from a broad state lower in energy than the HOMO which contains some contribution from the molecular backbone. While the HOMO which is pinned to the Fermi level is formed by Guanine states that follow the double helix, but are decoupled, the BOMO is largely basis-independent and lies approximately 1.5 eV below E_F . This results in band conduction with a gap of approximately 3.0 Volts corroborating the wide band-gap semiconductor picture.

Future work

Using the work presented here as a stepping stone a number of issues deserve greater attention in the future.

Firstly, the inclusion of spin orbit (SO) [53, 108] effects can lead to interesting

phenomena, from the correct treatment of the transport properties in GaAs/AlGaAs heterojunctions with *ab initio* techniques to the assessment of the transport mechanisms in certain classes of organic molecules where it has been claimed SO effects play an important role [58, 246]. Recently a method has been proposed using LCAOs which introduces an on-site correction to the LSDA Hamiltonian to account for spin orbit effects [108]. This approach gives accurate results for a range of semiconductors and is justified by the short range nature of the SO interaction which is largely an atomic effect [53].

Furthermore, inelastic effects might play an important role at the nanoscale [247]. A fully non-equilibrium inelastic approach to transport might be needed in many cases. In fact, in metallic gold nanowires Agraït and coworkers observe distinct drops in the conductance which the authors associate with scattering due to atomic vibrations [248]. Moreover, Smit *et al.* [169] used inelastic electron tunnelling spectroscopy (IETS) [247] to measure the phonon modes of a H₂ molecule between Pt electrodes (see section (2.5.4)) and to determine the relative orientation of the molecule bridging the contacts. Hence, inelastic effects can be used to probe molecular properties. Finally, in long polymer chains there is evidence for phonon-assisted transport [?]. Inelastic effects have been neglected in this thesis. A few methods have been proposed in this direction [249, 250, 251, 252] and implementing them in *Smeagol* might be in order [253].

It is also becoming increasingly clear, that local exchange-correlation potentials are not enough for calculating the electronic transport properties of certain molecular electronic devices [178, 254]. In this thesis we have presented some results where we correct for LDA using the Coulomb U term from the Hubbard model [127, 128]. Atomic SIC [131, 86] has also been implemented in *Smeagol* and will be the scope of future work [255]. The so called third generation exchange-correlation functionals [256] are becoming increasingly popular in solid state physics and materials science as computers become ever faster and the numerical overheads for these corrections start to be acceptable for small-to-medium sized systems. Thus far these methods are orbital-dependent. In other words, one must store the KS-eigenvectors as well as the charge density. This proves to be a problem for the NEGF approach where the calculation of the KS states is bypassed in favour of the Green function for the system. In order to implement these third generation exchange and correlation functionals a new method needs to be devised either by recasting these functionals in terms of Green functions or possibly by calculating the orbital-resolved Green function.

It is also been argued that a fully time-dependent approach is necessary [257,

258, 259]. Density functional theory is only valid for ground-state properties and the current does not fit into this category. A possible approach to transport based on time-dependent density functional theory was proposed by Kurth *et al.* [258], but no robust package is available as of yet.

Finally a new technique must be devised to treat large scale problems. The methods presented in section (2.4.1) and appendix A can lead to parallelisation up to 128 and 4096 CPUs respectively. However for modelling solid-state devices such as transistors at the boundary between micro and nanoscale one would require numerical simulation packages capable of dealing with hundreds of thousands of atoms. Macromolecules such as DNA and magnetic molecules (e.g. $\text{Mn}_12\text{O}_{12}(\text{CH}_3\text{COO})_{16}(\text{H}_2\text{O})_4$ [214, 215, 216]) are already testing the limit of present numerical tools for both standard DFT and more importantly for NEGF+DFT methods. Real life devices in a future molecular-electronics-based society will most likely not be made of small benzene thiolated molecules. These simpler molecules are important to enhance our understanding of phenomena at the molecular scale. Macromolecules which perform complex tasks combining self-assembly, molecular recognition and perhaps magnetism will dominate molecular electronics. For numerical simulations of these devices, new tools are necessary.

To conclude, it is clear that a lot of work has been done in the field of nanoscience, and of molecular electronics in particular, over the past ten years. However, this is a field much in its infancy. The experiments performed by Reed *et al.* [4] in 1997 were among the first and many questions remain unanswered ten years on. There is still a lack of control over experimental set ups and full scale production of working devices remains a dream. Yet, the challenges posed by this new field are extremely exciting and the possibilities endless.

Bibliography

- [1] G. Binnig, H. Rohrer, C. Gerber, and E. Wihel, *Phys. Rev. Lett.* **50**, 120 (1983).
- [2] C. Joachim, J. K. Gimzewski, and A. Aviram, *Nature (London)* **408**, 541 (2000).
- [3] A. Aviram and M. A. Ratner, *Chem. Phys. Lett.* **29**, 277 (1974).
- [4] M. A. Reed, C. Zhou, J. Muller, T. P. Burgin, and J. M. Tour, *Science* **278**, 252 (1997).
- [5] J. Chen, M. A. Reed, A. M. Rawlett, and J. M. Tour, *Science* **286**, 1550 (1999).
- [6] Z. Yao, H. W. C. Postman, L. Balents, and C. Dekker, *Nature (London)* **402**, 273 (1999).
- [7] S. J. Tans, A. R. M. Verschueren, and C. Dekker, *Nature (London)* **393**, 49 (1998).
- [8] P. Kuekes, J. Heath, and R. S. Williams (2000), US Patent (Hewlett-Packard) # 6128214.
- [9] C. Collier, E. Wong, M. Belohradsky, F. Raymo, J. Stoddart, P. Kuekes, R. Williams, and J. Heath, *Science* **285**, 391 (1999).
- [10] Y. Huang, X. Duan, Y. Cui, L. Lauhon, K.-H. Kim, and C. Lieber, *Science* **294**, 1313 (2001).
- [11] N. García, M. Muñoz, and Y. W. Zhao, *Phys. Rev. Lett.* **82**, 2923 (1999).
- [12] J. J. Versluijs, M. A. Bari, and J. M. D. Coey, *Phys. Rev. Lett.* **87**, 26601 (2001).
- [13] P. Qi, O. Vermesh, M. Grecu, A. Javey, Q. Wang, H. Dai, S. Peng, and K. Cho, *Nano Lett.* **3**, 347 (2003).

- [14] J. P. Novak, E. S. Show, E. J. Houser, D. Park, J. L. Stepnowski, and R. A. McGill, *Appl. Phys. Lett.* **83**, 4026 (2003).
- [15] F. Patolsky, G. Zheng, O. Hayden, M. Lakadamyali, X. W. Zhuang, and C. M. Lieber, *Proc. Natl. Acad. Sci. USA* **101**, 14017 (2004).
- [16] Y. Cui, W. Qingqiao, P. Hongkun, and C. M. Lieber, *Science* **293**, 1289 (2001).
- [17] J. P. Heath, M. E. Phelps, and L. Hood, *Mol. Im. Biol.* **5**, 312 (2003).
- [18] J. D. Watson, T. A. Baker, S. P. Bell, A. Gann, M. Levine, and R. Losick, *Molecular Biology of the Gene* (Benjamin Cummings, Menlo Park, 1987), 4th ed.
- [19] E. Braun, Y. Eichen, U. Sivan, and G. Ben-Yoseph, *Nature (London)* **391**, 775 (1998).
- [20] D. Porath, A. Bezryadin, S. de Vries, and C. Dekker, *Nature (London)* **403**, 635 (2000).
- [21] H.-W. Fink and C. Schönenberger, *Nature (London)* **398**, 407 (1999).
- [22] I. L. Garzón, E. Artacho, M. R. Beltrán, A. García, J. Junquera, K. Michaelian, P. Ordejón, C. Rovira, D. Sánchez-Portal, and J. M. Soler, *Nanotechnology* **12**, 126 (2001).
- [23] B. Xu, P. Zhang, X. Li, and N. Tao, *Nano Lett.* **4**, 1105 (2004).
- [24] S. Datta, *Nanotechnology* **15**, S433 (2004).
- [25] J. Chen and M. A. Reed, *Chem. Phys.* **281**, 127 (2002).
- [26] W. Wang, T. Lee, and M. A. Reed, *Phys. Rev. B* **68**, 035416 (2003).
- [27] X. Y. Xiao, B. Q. Xu, and N. J. Tao, *Nano Lett.* **4**, 267 (2004).
- [28] L. Venkataraman, J. E. Klare, C. Nuckolls, M. S. Hybertsen, and M. L. Steigerwald, *Nature (London)* **442**, 904 (2006).
- [29] A. P. Sutton, *Electronic Structure of Materials* (Oxford University Press, Oxford (UK), 1996).
- [30] P. S. Krastic, D. J. Dean, X. G. Zhang, D. Keffer, Y. S. Leng, P. T. Cummings, and J. C. Wells, *Comp. Mat. Sci.* **28**, 321 (2003).

- [31] M. N. Baibich, J. M. Broto, A. Fert, F. N. V. Dau, F. Petroff, P. Etienne, G. Creuzet, A. Friederich, and J. Chazelas, *Phys. Rev. Lett.* **61**, 2472 (1988).
- [32] G. Binasch, P. Grünberg, F. Saurenbach, and W. Zinn, *Phys. Rev. B* **39**, 4828 (1989).
- [33] S. A. W. and, *Science* **294**, 1488 (2001).
- [34] G. Prinz, *Science* **282**, 1660 (1998).
- [35] G. Prinz, *Phys. Today* **48**, 58 (1995).
- [36] J. M. Kikkawa and D. D. Awschalom, *Phys. Rev. Lett.* **80**, 4313 (1998).
- [37] J. M. Kikkawa and D. D. Awschalom, *Nature (Londo)* **397**, 139 (1999).
- [38] D. P. D. Vincenzo, *Science* **270**, 255 (1995).
- [39] J. M. D. Coey and S. Sanvito, *Physics World* **7**, 33 (2004).
- [40] J. M. Soler, E. Artacho, J. D. Gale, A. García, J. Junquera, P. Ordejón, and D. Sánchez-Portal, *J. Phys.: Condens. Matter* **14**, 2745 (2002).
- [41] T.-S. Choy, J. Naset, J. Chen, S. Hershfield, and C. Stanton, *Bulletin of The American Physical Society* **45(1):L36**, 42 (2000), URL <http://www.phys.ufl.edu/fermisurface/>.
- [42] N. Mott, *Proc. Roy. Soc. A* **153**, 699 (1936).
- [43] I. I. Mazin, *Phys. Rev. Lett.* **83**, 1427 (1999).
- [44] S. P. Lewis, P. B. Allen, and T. Sasaki, *Phys. Rev. B* **55**, 10253 (1997).
- [45] B. Nadgorny, I. I. Mazin, M. Osofsky, R. J. Soulen-Jr., P. Broussard, R. M. Stroud, D. J. Singh, V. G. Harris, A. Arsenov, and Y. Mukovskii, *Phys. Rev. B* **63**, 184433 (2001).
- [46] D. Singh, *Phys. Rev. B* **55**, 313 (1997).
- [47] J. M. D. Teresa, A. Barthélémy, A. Fert, J. P. Contour, and F. M. P. Seneor, *Science* **286**, 507 (1999).
- [48] K. Tsukagoshi, B. W. Alphenaar, and H. Ago, *Nature (London)* **401**, 572 (1999).

- [49] J. R. Petta, S. K. Slater, and D. C. Ralph, *Phys. Rev. Lett.* **93**, 136601 (2004).
- [50] Z. H. Xiong, D. Wu, Z. V. Vardeny, and J. Shi, *Nature (London)* **427**, 821 (2004).
- [51] V. Dediu, M. Murgia, F. Maticcotta, C. Taliani, and S. Barbanera, *Solid State Commun.* **122**, 181 (2002).
- [52] M. Ouyang and D. D. Awschalom, *Science* **301**, 1074 (2003).
- [53] J. H. Davies, *The Physics of Low-dimensional Semiconductors : An Introduction* (Cambridge University Press, Cambridge (UK), 1997).
- [54] J. Serrano, M. Cardona, and T. Ruf, *Solid State Commun.* **113**, 411 (2000).
- [55] A. Khaetskii, D. Loss, and L. Glazman, *Phys. Rev. B* **67**, 195329 (2003).
- [56] G. Salis, D. T. Fuchs, J. M. Kikkawa, D. D. Awschalom, Y. Ohno, and H. Ohno, *Phys. Rev. Lett.* **86**, 2677 (2001).
- [57] M. Julliere, *Phys. Lett. A* **50**, 225 (1975).
- [58] S. Pramanik, C.-G. Stefanita, S. Bandyopadhyay, N. Harth, K. Garre, and M. Cahay, unpublished, cond-mat/0508744 (2005).
- [59] C. K. Chiang, C. R. Fincher-Jr., Y. W. Park, A. J. Heeger, H. Shirakawa, E. J. Louis, S. Gau, and A. MacDiarmid, *Phys. Rev. Lett.* **39**, 1098 (1977).
- [60] D. Gatteschi, R. Sessoli, and J. Villain, *Molecular Nanomagnets* (Oxford University Press, Oxford (UK), 2006).
- [61] S. Datta, *Electronic Transport in Mesoscopic Systems* (Cambridge University Press, Cambridge, UK, 1995).
- [62] H. Haug and A. P. Jauho, *Quantum Kinetics in Transport and Optics of Semiconductors* (Berlin, 1996).
- [63] C. Caroli, R. Combescot, P. Nozieres, and D. Saint-James, *J. Phys. C* **5**, 21 (1972).
- [64] J. Ferrer, A. Martín-Rodero, and F. Flores, *Phys. Rev. B* **38**, 10113 (1988).
- [65] S. Sanvito, C. J. Lambert, J. H. Jefferson, and A. M. Bratkovsky, *Phys. Rev. B* **59**, 11936 (1999).

- [66] N. D. Lang, Phys. Rev. B **36**, 8173 (1987).
- [67] N. D. Lang, Phys. Rev. B **52**, 5335 (1995).
- [68] M. D. Ventra, S. T. Pantelides, and N. D. Lang, Phys. Rev. Lett. **84**, 979 (2000).
- [69] S. Sanvito, *Ab-initio methods for spin-transport at the nanoscale level in Handbook of Computational Nanotechnology* (American Scientific Publishers, Stevenson Ranch, California, 2005), also in cond-mat/0503445.
- [70] A. R. Rocha and S. Sanvito, Phys. Rev. B **70**, 94406 (2004).
- [71] A. R. Rocha, V. M. G. Suárez, S. W. Bailey, C. J. Lambert, J. Ferrer, and S. Sanvito, Phys. Rev. B **73**, 085414 (2006).
- [72] A. R. Rocha, V. M. G. Suárez, S. W. Bailey, C. J. Lambert, J. Ferrer, and S. Sanvito, *Smeagol - non-equilibrium electronic transport*, www.smeagol.tcd.ie (2004).
- [73] C. Beenakker, Phys. Rev. B **44**, 1646 (1991).
- [74] R. Gebauer and R. Car, Phys. Rev. B **70**, 125324 (2004).
- [75] B. Muralidharan, A. Ghosh, S. Pati, and S. Datta (2006), cond-mat/0505375.
- [76] G. Stefanucci and C. O. Almbladh, Phys. Rev. B **69**, 195318 (2004).
- [77] P. Hohenberg and W. Kohn, Phys. Rev. **136**, B864 (1964).
- [78] W. Kohn and L. Sham, Phys. Rev. **140**, A1133 (1965).
- [79] M. Brandbyge, J.-L. Mozos, P. Ordejón, J. Taylor, and K. Stokbro, Phys. Rev. B **65**, 165401 (2002).
- [80] J. Taylor, H. Guo, and J. Wang, Phys. Rev. B **63**, 245407 (2001).
- [81] Y. Xue, S. Datta, and M. Ratner, Chem. Phys. **281**, 151 (2002).
- [82] J. J. Palacios, A. J. Pérez-Jiménez, E. Louis, E. SanFabián, and J. A. Vergés, Phys. Rev. B **66**, 035322 (2002).
- [83] A. Pecchia and A. D. Carlo, Rep. Prog. Phys. **67**, 1497 (2004).

- [84] M. Büttiker, Y. Imry, R. Landauer, and S. Pinhas, *Phys. Rev. B* **31**, 6207 (1985).
- [85] T. Archer, private communication.
- [86] C. D. Pemmaraju, T. Archer, D. Sanchez-Portal, and S. Sanvito, *Phys. Rev. B*, accepted; also cond-mat/0609325 (2006).
- [87] A. R. Rocha, V. M. G. Suárez, S. W. Bailey, C. J. Lambert, J. Ferrer, and S. Sanvito, *Nature Materials* **4**, 335 (2004).
- [88] S. Sanvito and A. R. Rocha, *J. Comp. Theo. Nanosci.*, in press (2006).
- [89] L. Kadanoff and G. Baym, *Quantum Statistical Mechanics* (W.A. Benjamin, Menlo Park, CA, 1962).
- [90] L. V. Keldysh, *Sov. Phys. JETP* **20**, 1018 (1965).
- [91] E. Emberly and G. Kirczenow, *Phys. Rev. B* **58**, 10911 (1998).
- [92] L. G. C. Rego, A. R. Rocha, V. Rodrigues, and D. Ugarte, *Phys. Rev. B* **67**, 045412 (2003).
- [93] N. W. Ashcroft and N. D. Mermin, *Solid State Physics* (Saunders College Publishing and Harcourt Brace College Publishing, Fort Worth, 1976).
- [94] D. Fisher and P. Lee, *Phys. Rev. B* **23**, 6851 (1981).
- [95] T. Todorov, *J. Phys. Condens. Matter* **13**, 10125 (2001).
- [96] T. Todorov, *J. Phys. Condens. Matter* **14**, 3049 (2002).
- [97] Y. Meir and N. S. Wingreen, *Phys. Rev. Lett.* **68**, 2512 (1992).
- [98] A. R. Williams, P. J. Feilbeman, and N. D. Lang, *Phys. Rev. B* **26**, 5433 (1982).
- [99] J. W. Brown and R. V. Churchill, *Complex Variables and Applications*, Series in Science and Engineering (Mc Graw-Hill, New York, 2003).
- [100] W. H. Press, B. P. Flannery, S. A. Teukolsky, and W. T. Vetterling, *Numerical Recipes in Fortran* (Cambridge University Press, Cambridge (UK), 1992), 2nd ed., URL <http://library.lanl.gov/numerical/bookfpdf.html>.

- [101] N. Mott, Proc. Roy. Soc. A **153**, 699 (1936).
- [102] F. Bloch, Z. Phys. **74**, 295 (1932).
- [103] L. Néel, C. R. Acad. Sci. (Paris) **241**, 533 (1955).
- [104] J. J. Sakurai, *Modern Quantum Mechanics* (Addison-Wesley Publishing Company, Reading, Massachusetts, 1994).
- [105] E. Merzbacher, *Quantum Mechanics* (John Wiley & Sons Inc., New York, 1998).
- [106] T. Burkert, O. Eriksson, P. James, S. I. Simak, B. Johansson, and L. Nordstrom, Phys. Rev. B **69**, 104426 (2004).
- [107] P. Y. Yu and M. Cardona, *Fundamentals of Semiconductors: Physics and Materials Properties* (Springer, Berlin, 2005).
- [108] L. Fernandez-Seivane, M. A. Oliveira, S. Sanvito, and J. Ferrer, J. Phys C: Cond. Matt. **18**, 7999 (2006).
- [109] M. Nardelli, Phys. Rev. B **60**, 7828 (1999).
- [110] E. Anderson, Z. Bai, C. Bischof, S. Blackford, J. Demmel, J. Dongarra, J. D. Croz, A. Greenbaum, S. Hammarling, A. McKenney, and D. Sorensen, *Lapack Users Guide* (Society for Industrial and Applied Mathematics, 1999), 3rd ed.
- [111] R. G. Parr and W. Yang, *Density-Functional Theory of Atoms and Molecules*, vol. 16 of *The International Series of Monographs on Chemistry* (Oxford University Press, Oxford (UK), 1989).
- [112] J. P. Perdew and S. Kurth, *Density Functionals for Non-relativistic Coulomb Systems in the New Century*, in *Density Functionals: Theory and Applications* (Springer, Berlin, 1998), vol. 500 of *Lecture Notes in Physics*.
- [113] A. Szabo and N. S. Ostlund, *Modern Quantum Chemistry: Introduction to Advanced Electronic Structure Theory* (Collier MacMillan, New York, 1982).
- [114] M. Springborg, ed., *Density-Functional Methods in Chemistry and Materials Science*, Wiley Research Series in Theoretical Chemistry (John Wiley & Sons Ltd., Chichester (UK), 1997).

- [115] R. P. Feynman and A. R. Hibbs, *Quantum Mechanics and Path Integrals* (Mc Graw-Hill, New York, 1964).
- [116] E. Runge and E. K. U. Gross, Phys. Rev. Lett. **52**, 997 (1984).
- [117] M. Marques, A. Castro, G. F. Bertsch, and A. Rubio, Comput. Phys. Commun. **151**, 60 (2003).
- [118] U. von Barth and L. Hedin, J. Phys. C: Cond. Matt. **5**, 1629 (1972).
- [119] D. C. Langreth and M. J. Mehl, Phys. Rev. B **28**, 1809 (1983).
- [120] J. P. Perdew, Phys. Rev. Lett. **55**, 1665 (1985).
- [121] J. P. Perdew, K. Burke, and M. Ernzerhof, Phys. Rev. Lett. **77**, 3865 (1996).
- [122] J. Perdew and A. Zunger, Phys. Rev. B **23**, 5048 (1981).
- [123] J. Perdew and Y. Wang, Phys. Rev. B **45**, 13244 (1992).
- [124] *The gaussian 03 package*, URL <http://www.gaussian.com>.
- [125] R. Ahlrichs, M. Bar, M. Häser, H. Horn, and C. Kölmel, Chem. Phys. Lett. **162**, 165 (1989).
- [126] N. F. Mott and R. Peierls, Proc. Phys. Soc. (London) **49**, 72 (1937).
- [127] V. I. Anisimov, J. Zaanen, and O. K. Andersen, Phys Rev B **44**, 943 (1991).
- [128] V. I. Anisimov, F. Aryasetiawan, and A. I. Lichtenstein, J. Phys. C: Cond. Matt. **9**, 767 (1997).
- [129] M. Wierzbowska, D. Sánchez-Portal, and S. Sanvito, Phys Rev B **70**, 235209 (2004).
- [130] J. Hubbard, Proc. Roy. Soc. (London) **A276**, 238 (1963).
- [131] A. Filippetti and N. A. Spaldin, Phys. Rev. B **67**, 125109 (2003).
- [132] J. R. Chelikowsky, L. Kronik, I. Vasiliev, M. Jain, and Y. Saad, *Using Real Space Pseudopotentials for the Electronic Structure Problem* (Elsevier Sciences, Amsterdam, 2006), Handbook of Numerical Analysis, URL <http://www.ices.utexas.edu/parsec/>.

- [133] X. Gonze, J.-M. Beuken, R. Caracas, F. Detraux, M. Fuchs, G.-M. Rignanese, L. Sindic, M. Verstraete, G. Zerah, F. Jollet, M. Torrent, A. Roy, *et al.*, *Comp. Mat. Sci.* **25**, 478 (2002).
- [134] G. B. Arfken and H. J. Weber, *Mathematical Methods for Physicists* (Harcourt Academic Press, San Diego, 2001), 5th ed.
- [135] J. M. Soler, E. Artacho, J. D. Gale, A. García, J. Junquera, P. Ordejón, and D. Sánchez-Portal, *SIESTA: Spanish Initiative for Electronic Structure Calculations with Thousands of Atoms* (2006), URL <http://www.uam.es/departamentos/ciencias/fismateriac/siesta>.
- [136] R. M. Martin, *Electronic Structure: Basic Theory and Practical Methods* (Cambridge University Press, Cambridge (UK), 2004).
- [137] L. Kleinman and D. M. Bylander, *Phys. Rev. Lett.* **48**, 1425 (1982).
- [138] S. Huzinaga, ed., *Gaussian Basis Sets for Molecular Calculations* (Elsevier Publishing Company, Amsterdam, 1991), 1st ed.
- [139] N. Maron, A. R. Rocha, S. Sanvito, and L. Kronik (2006), unpublished.
- [140] I. Rungger, A. R. Rocha, O. Mryasov, O. Heinonen, and S. Sanvito, in *Magnetic Thin Films, Heterostructures, and Device Materials*, edited by C. Ross (Mater. Res. Soc. Symp. Proc., Warrendale, PA, 2006), pp. 0941–Q01–03, URL http://www.mrs.org/s_mrs/sec_subscribe.asp?CID=6456&DID=173869.
- [141] M. Snir, S. Otto, S. Huss-Lederman, D. Walker, and J. Dongarra, *MPI: The Complete Reference*, Scientific and Engineering Computation Series (The MIT Press, Cambridge, Massachusetts, 2000), URL <http://www.netlib.org/utk/papers/mpi-book/mpi-book.html>.
- [142] L. S. Blackford, J. Choi, A. Cleary, E. D’Azevedo, J. Demmel, I. Dhillon, J. Dongarra, S. Hammarling, G. Henry, A. Petitet, K. Stanley, D. Walker, *et al.*, *ScaLAPACK Users’ Guide* (Society for Industrial and Applied Mathematics, Philadelphia, PA, 1999).
- [143] PathScale Inc., *Pathscale compiler*, URL <http://www.pathscale.com/>.
- [144] D. Pettifor, *Bonding and structure of molecules and solids* (Oxford University Press, Oxford, 2002).

- [145] D. J. Griffiths, *Introduction to Electrodynamics* (Prentice Hall, New Jersey, 2000), 3rd ed.
- [146] H. Onishi, Y. Kondo, and K. Takayanagi, *Nature (London)* **395**, 780 (1998).
- [147] J. M. van Ruitenbeek, *Metal Cluster at Surfaces* (Springer-Verlag, Berlin, 2000), Cluster Series, edited by K. H. Meiwes-Broer.
- [148] N. Agrat, A. Levy-Yeyati, and J. van Ruitenbeek, *Phys. Rep.* **377**, 81 (2003).
- [149] V. Rodrigues, T. Fuhrer, and D. Ugarte, *Phys. Rev. Lett.* **85**, 4124 (2000).
- [150] B. J. van Hees, H. van Houten, C. W. J. Beenaker, J. G. Williamson, L. P. Kouwenhoven, D. van der Marel, and C. T. Foxon, *Phys. Rev. Lett.* **60**, 848 (1988).
- [151] D. Wharam, T. Thornton, R. Newbury, M. Pepper, H. Ahmed, J. Frost, D. Hasko, D. Peacock, D. Ritchie, and G. Jones, *J. Phys. C: Cond. Matt.* **21**, L209 (1988).
- [152] V. Rodrigues and D. Ugarte, *Rev. Sci. Inst.* (2004).
- [153] P. Z. Coura, S. B. Legoas, A. S. Moreira, F. Sato, V. Rodrigues, S. O. Dantas, D. Ugarte, and D. S. G. ao, *Nano Lett.* **4**, 1187 (2004).
- [154] H. Häkkinen, R. N. Barnett, and U. Landman, *J. Phys. Chem. B* **103**, 8814 (1999).
- [155] V. Garcia-Suarez, A. R. Rocha, S. W. Bailey, C. J. Lambert, S. Sanvito, and J. Ferrer, *Phys. Rev. Lett.* **95**, 256804 (2005), also available as cond-mat/0505487.
- [156] V. Garcia-Suarez, A. R. Rocha, S. W. Bailey, C. J. Lambert, S. Sanvito, and J. Ferrer, *Phys. Rev. B* **72**, 045437 (2005), also available as cond-mat/0412726.
- [157] N. García, M. M. noz, G. G. Qian, H. Rohrer, I. G. Saveliev, and Y. W. Zhao, *Appl. Phys. Lett.* **79**, 4550 (2001).
- [158] N. García, M. R. Ibarra, C. Hao, R. F. Pacheco, and D. Serrate (2005), cond-mat/0502046.
- [159] M. Viret, S. Berger, M. Gabureac, F. Ott, D. Olligs, I. Petej, J. F. Greeg, C. F. nd G. Francinet, and G. L. Goff, *Phys. Rev. B* **66**, 220401 (2002).

- [160] M. Gabureac, M. Viret, F. Ott, and C. Fermon, *Phys. Rev. B* **69**, 100401 (2004).
- [161] M. Gabureac, M. Viret, F. Ott, and C. Fermon, *Phys Rev B* **69**, 100401 (2004).
- [162] P. Bruno, *Phys. Rev. Lett.* **83**, 2425 (1999).
- [163] S. Z. Hua and H. D. Chopra, *Phys. Rev. B* **67**, 060401 (2003).
- [164] O. Céspedes, A. R. Rocha, S. Lioret, M. Viret, C. Dennis, J. Gregg, S. van Dijken, S. Sanvito, and J. Coey, *J. Mag. Mag. Mat.* **272**, 1571 (2003).
- [165] S. R. Bahn and K. W. Jacobsen, *Phys. Rev. Lett.* **87**, 266101 (2001).
- [166] M. Stamenova, S. Sanvito, and T. Todorov, *Phys. Rev. B* **72**, 134407 (2005).
- [167] V. Rodrigues, J. Bettini, L. G. C. Rego, A. R. Rocha, and D. Ugarte, *Phys. Rev. B* **65**, 153402 (2002).
- [168] V. Rodrigues, J. Bettini, P. C. Silva, and D. Ugarte, *Phys. Rev. Lett.* **91**, 096801 (2003).
- [169] R. H. M. Smit, Y. Noat, C. Untiedt, N. D. Lang, M. C. van Hemert, and J. M. van Ruitenbeek, *Nature (London)* **419**, 906 (2002).
- [170] J. C. Cuevas, J. Heurich, F. Pauly, W. Wenzel, , and G. Schön, *Nanotechnology* **14**, R29 (2003).
- [171] D. Djukic, K. S. Thygesen, C. Untiedt, R. H. M. Smit, K. W. Jacobsen, and J. M. van Ruitenbeek, *Phys. Rev. B* **71**, 161402 (2005).
- [172] K. S. Thygesen and K. W. Jacobsen, *Phys. Rev. B* **72**, 033401 (2005).
- [173] M. D. Ventura, S. T. Pantelides, and N. D. Lang, *Phys. Rev. Lett.* **84**, 979 (2000).
- [174] H. Basch and M. A. Ratner, *J. Chem. Phys.* **119**, 11926 (2003).
- [175] H. Basch and M. A. Ratner, *J. Chem. Phys.* **119**, 11943 (2003).
- [176] T. Dadosh, Y. Gordin, R. Krahné, D. Mahalu, V. Frydman, J. Sperling, A. Yacoby, and I. Bar-Joseph, *Nature (London)* **436**, 677 (2005).
- [177] C. Toher and S. Sanvito, unpublished.

- [178] C. Toher, A. Filippetti, K. Burke, and S. Sanvito, *Phys. Rev. Lett.* **95**, 146402 (2005).
- [179] O. Cespedes, M. A. Bari, C. Dennis, J. Versluijs, G. Jan, J. O'Sullivan, J. F. Gregg, and J. M. D. Coey, *J. Magn. Magn. Mat.* **492**, 242 (2002).
- [180] S. H. Chung, M. Muñoz, N. García, W. Egelhoff, and R. D. Gomez, *J. App. Phys.* **93**, 7939 (2003).
- [181] J. E. Wegrowe, T. Wade, X. Hoffer, L. Gravier, J. M. Bonard, and J. P. Ansermet, *Phys. Rev. B* **67**, 104418 (2003).
- [182] J. B. A. N. van Hoof, K. M. Schep, A. Brataas, G. E. W. Bauer, and P. J. Kelly, *Phys. Rev. B* **59**, 138 (1999).
- [183] G. Tatara, Y. W. Zhao, M. M. noz, and N. Garcá, *Phys. Rev. Lett.* **83**, 2030 (1999).
- [184] L. D. Landau and E. M. Lifshitz, *Z. Phys. Sowjetunion* **8**, 153 (1935).
- [185] H. Imamura, N. Kobayashi, S. Takahashi, and S. Maekawa, *Mat. Sci. and Eng.* **B86**, 107 (2001).
- [186] H. Imamura, N. Kobayashi, S. Takahashi, and S. Maekawa, *Phys. Rev. Lett.* **84**, 1003 (2000).
- [187] K. Nakanishi and Y. O. Nakamura, *Phys. Rev. B* **61**, 11278 (2000).
- [188] S. K. Nielsen, M. Brandbyge, K. Hansen, K. Stokbro, J. M. van Ruitenbeek, and F. Besenbacher, *Phys. Rev. Lett.* **89**, 066804 (2002).
- [189] A. Bagrets, N. Papanikolaou, and I. Mertig, *Phys. Rev. B* **70**, 064410 (2004).
- [190] D. Jacob, J. Fernández-Rossier, and J. J. Palacios, *Phys Rev B* **71**, 220403(R) (2005).
- [191] S. S. P. Parkin, C. Kaiser, A. Panchula, P. M. Rice, B. Hughes, M. Samant, and S.-H. Yang, *Nature Materials* **3**, 862 (2004).
- [192] S. Yuasa, T. Nagahama, A. Fukushima, Y. Suzuki, and K. Ando, *Nature Materials* **3**, 868 (2004).
- [193] R. F. Peierls, *Quantum Theory of Solids* (Oxford University Press, Oxford (UK), 1955), p. 108.

- [194] V. R. Saunders, R. Dovesi, C. Roetti, R. Orlando, C. M. Zicovich-Wilson, N. M. Harrison, K. Doll, B. Civalleri, I. Bush, P. D'Arco, and M. Llunell, *CRYSTAL2003 User's Manual*, University of Torino, Torino (2003), URL <http://www.crystal.unito.it/Manuals/crystal03.pdf>.
- [195] M. D. Towler, N. L. Allan, N. M. Harrison, V. R. Saunders, W. C. Mackrodt, and E. Aprà, *Phys. Rev. B* **50**, 5041 (1994).
- [196] K. Doll, *Surface Science* **544**, 103 (2003).
- [197] D. Jacob, J. Fernández-Rossier, and J. J. Palacios, *Phys. Rev. B* **74**, 081402 (2006), cond-mat/0606727.
- [198] X. D. Cui, A. Primak, X. Zarate, J. Tomfohr, O. F. Sankey, A. L. Moore, T. A. Moore, D. Gust, L. A. Nagahara, and S. M. Lindsay, *J. Phys. Chem.* **106**, 8609 (2002).
- [199] E. G. Emberly and G. Kirczenow, *Phys. Rev. Lett.* **91**, 188301 (2003).
- [200] P. E. Kornilovitch, A. M. Bratkovsky, and R. S. Williams, *Phys. Rev. B* **66**, 165436 (2002).
- [201] R. D. Mullins, T. Tang, X. Chen, V. Shneerson, D. K. Saldin, and W. T. Tysoe, *Surf. Sci.* **372**, 193-201 (1997).
- [202] J. K. Tomfohr and O. F. Sankey, *Phys. Rev. B* **65**, 245105 (2002).
- [203] M. D. Ventra and N. D. Lang, *Phys. Rev. B* **65**, 045402 (2002).
- [204] R. B. Pontes, F. D. Novaes, A. Fazzio, and A. J. R. da Silva, *J. Am. Chem. Soc.* **128**, 8996 (2006).
- [205] D. M. Eigler and E. K. Schweizer, *Nature (London)* **344**, 524 (1990).
- [206] R. Wiesendanger, H. J. Güntherodt, G. Güntherodt, R. J. Gambino, and R. Ruf, *Phys. Rev. Lett.* **65**, 247 (1990).
- [207] M. Johnson and J. Clarke, *J. Appl. Phys.* **67**, 6141 (1990).
- [208] S. F. Alvarado, *J. Appl. Phys.* **73**, 5816 (1993).
- [209] A. R. Champagne, A. N. Pasupathy, and D. C. Ralph, *Nano Lett.* **5**, 305 (2005).

- [210] B. Naydenov, P. Ryan, L. C. Teague, and J. J. Boland, *Phys. Rev. Lett.* **97**, 098304 (2006).
- [211] H. Dalglish and G. Kirczenow, *Phys Rev B* **72**, 155429 (2005).
- [212] S. J. P. R. Bandaru, C. Daraio and A. M. Rao, *Nature Materials* **4**, 663 (2005).
- [213] R. Liu, S.-H. Ke, H. U. Baranger, and W. Yang, *Nano Lett.* **5**, 1959 (2005).
- [214] D. Gatteschi and R. Sessoli, *Angew. Chem. Int. Ed.* **42**, 1268 (2003).
- [215] H. B. Heersche, Z. de Groot, J. A. Folk, H. S. J. van der Zant, C. Romeike, M. R. Wegewijs, L. Zobbi, D. Barreca, E. Tondello, and A. Cornia, *Phys. Rev. Lett.* **96**, 206801 (2006), cond-mat/0510732.
- [216] M.-H. Jo, J. E. Grose, K. Baheti, M. M. Deshmukh, J. J. Sokol, E. M. Rumberger, D. N. Hendrickson, J. R. Long, H. Park, and D. C. Ralph (2006), cond-mat/0603276.
- [217] B. A. Pierce, *Genetics: A Conceptual Approach* (W. H. Freeman and Company, New York, 2006), 2nd ed.
- [218] I. G. Panyutin, I. Kovalsky, E. I. Budowsky, R. E. Dickerson, M. E. Rikhirev, and A. A. Lipanov, *Proc. Nat. Acad. Sci. (U.S.)* **87**, 867 (1990).
- [219] J. Watson and F. Crick, *Nature (London)* **171**, 737 (1953).
- [220] R. Franklin and R. G. Gosling, *Nature* **171**, 740 (1953).
- [221] M. H. F. Wilkins, A. R. Stokes, and H. R. Wilson, *Nature (London)* **171**, 738 (1953).
- [222] *The Nobel Foundation*, URL <http://www.nobelprize.org>.
- [223] L. Pauling and R. B. Corey, *Nature (London)* **171**, 346 (1953).
- [224] L. Pauling and R. B. Corey, *Proc. Nat. Acad. Sci. (U.S.)* **39**, 84 (1953).
- [225] J. D. Watson, *The Double Helix: A Personal Account of the Discovery of the Structure of DNA* (Touchstone, New York, 2001), 1st ed.
- [226] R. E. Franklin and R. G. Gosling, *Acta Crystallographica* **6**, 673 (1953).
- [227] R. E. Franklin and R. G. Gosling, *Acta Crystallographica* **6**, 678 (1953).

- [228] C. Dennis and P. Campbell (editors), *Nature* **421**, 396 (2003).
- [229] D. D. Eley and D. I. Spivey, *Trans. Faraday Soc.* **58**, 411 (1962).
- [230] S. Roth and D. Carroll, *One Dimensional Metals* (Wiley-VCH, Weinheim, Germany, 2004), 2nd ed.
- [231] P. J. de Pablo, F. Moreno-Herrero, J. Colchero, J. G. Herrero, P. Herrero, A. M. Baró, P. Ordejón, J. M. Soler, and E. Artacho, *Phys. Rev. Lett.* **85**, 4992 (2000).
- [232] A. Y. Kasumov, M. Kociak, S. Guéron, B. Reulet, V. T. Volkov, D. V. Klinov, and H. Bouchiat, *Science* **291**, 280 (2001).
- [233] H. Cohen, C. Nogues, R. Naaman, and D. Porath, *Proc. Nat. Acad. Sci. (U.S.)* **102**, 11589 (2005).
- [234] H. Cohen, C. Nogues, D. Ullien, S. Daube, R. Naaman, and D. Porath, *Faraday Discussions* **131**, 367 (2006).
- [235] M. W. Grinstaff, *Angew Chem Int Ed* **38**, 3629 (99).
- [236] P. F. Barbara and E. J. C. Olson, *Adv Chem Phys* **107**, 647 (1999).
- [237] C. J. Murphy, M. A. Arkin, Y. Jenkins, N. D. Ghatlia, S. Bossman, N. J. Turro, and J. K. Barton, *Science* **262**, 1025 (1993).
- [238] M. Bixon, B. Giese, S. Wessely, T. Langerbacher, M. E. Michel-Beyerle, and J. Jortner, *Proceedings of the National Academy of Sciences U.S.A.* **96**, 11713 (1999).
- [239] G. B. Schuster, *Acc. Chem. Res.* **33**, 253 (2000).
- [240] E. M. Conwell and S. V. Rakhmanova, *Proc. Nat. Acad. Sci. U. S. A.* **97**, 4556 (2000).
- [241] M. Zwolak and M. D. Ventra, *Nano Lett.* **5**, 421 (2005).
- [242] M. Taniguchi and K. Tomoji, *Phys. Rev. E* **70**, 011913 (2004).
- [243] R. G. Endres, D. L. Cox, and R. R. P. Singh, *Rev. Mod. Phys.* **76**, 195 (2004).
- [244] R. Gutierrez, S. Mohapatra, H. Cohen, D. Porath, and G. Cuniberti (2006), cond-mat/0604435.

- [245] S. S. Alexandre, E. Artacho, J. M. Soler, and H. Chacham, *Phys. Rev. Lett.* **91**, 108105 (2003).
- [246] A. Hernando, P. Crespo, and M. A. Garcia, *Phys. Rev. Lett.* **96**, 057206 (2006).
- [247] B. C. Stipe, M. A. Rezaei, and W. Ho, *Science* **280**, 1732 (1998).
- [248] N. Agraït, C. Untiedt, G. Rubio-Bollinger, and S. Vieira, *Phys. Rev. Lett.* **88**, 216803 (2002).
- [249] N. Jean and S. Sanvito, *Phys Rev B* **73**, 094433 (2005).
- [250] M. Galperin, A. Nitzan, and M. A. Ratner, *Phys. Rev. B* **73**, 045314 (2004).
- [251] P. Hyldgaard, S. Hershfield, J. H. Davies, and J. W. Wilkins, *Annals of Physics* **236**, 1 (1994).
- [252] T. Frederiksen, M. Brandbyge, N. Lorente, and A.-P. Jauho, *Phys. Rev. Lett.* **93**, 256601 (2004).
- [253] W. L. Rodgers and S. Sanvito, unpublished.
- [254] S.-H. Ke, H. U. Baranger, and W. Yang (2006), cond-mat/0609637.
- [255] C. Toher, A. R. Rocha, S. C. D. Pemmaraju, and S. Sanvito, unpublished.
- [256] A. Gorling and M. Levy, *Phys. Rev. A* **50** (1994).
- [257] M. D. Ventra and T. N. Todorov, *Phys. Rev. Lett.* **92**, 176803 (2004), cond-mat/0407534.
- [258] S. Kurth, G. Stefanucci, C. O. Almbladh, A. Rubio, and E. K. U. Gross, *Phys Rev B* **72**, 035308 (2005).
- [259] C. Sanchez, M. Stamenova, S. Sanvito, D. Bowler, A. Horsfield, and T. Todorov, *J. Chem. Phys.* **124**, 214708 (2006).

Appendix A

Extensions to Smeagol: scaling to large systems and high performance computing

In section (2.4.1) we presented the main features of the parallel version of *Smeagol*. In *Smeagol*, one needs to perform an integral over the energy (see equations (1.57) and (1.58)). Numerically, this integral is discretised and becomes a sum over energy points weighted using Gauss-Legendre polynomials [100]. The Green function for a subset of energies (obtained by inverting equation (1.33)) is calculated in serial in each processor (POE method). Subsequently the partial sums for are gathered to obtain the full density matrix. This method is very efficient since the number of communication between CPUs is rather small - the Hamiltonian at the beginning of each self-consistent cycle is distributed over all the CPUs. Each CPU then works independently to calculate parts of the integrals and finally all the segments are added to obtain the total density matrix.

Although the scalability is good for the POE method, the equilibrium part of the density matrix (equation (1.57)) can be performed with a reasonably small number of points (between 50-150 depending on the system)¹ and with good precision. Therefore increasing the number of CPUs would not increase the overall speed up of the code (we could only increase the total number of energy points in the integral despite the need for more points) and we still need to perform the calculation of the Green function - a matrix inversion - in series for each energy point.

Hence the POE method only allows for parallelism up to approximately 128 processors. Albeit respectable for small clusters, the present form of parallelism implemented in *Smeagol* is not scalable to a higher number of processors. More

¹the number of points for equation (1.57) is usually smaller than the one of (1.58) and therefore it defines the bottleneck of our calculation.

importantly, until recently great effort was placed in increasing the speed of individual processing units, but there has been a shift towards distributed architectures where the overall time for a calculation decreases by increasing the actual number of CPUs. In other words, instead of improving the performance of a single processor (a task hindered by technological barriers), computer companies are increasing the number of CPUs performing the same task. This change in paradigm is not only the realm of high performance computing, but has also made its way into desktops and laptops with the advent Duo Core technology.

Furthermore *Smeagol* needs to store in memory the Green function (and other auxiliary matrices). In DNA molecules attached to Au electrodes (see chapter 5) the number of degrees of freedom is in excess of 5,000 ($5,000 \times 5,000$ matrices). At its present state we are reaching the limit of available memory per single compute node in state-of-the-art facilities for high performance computing.²

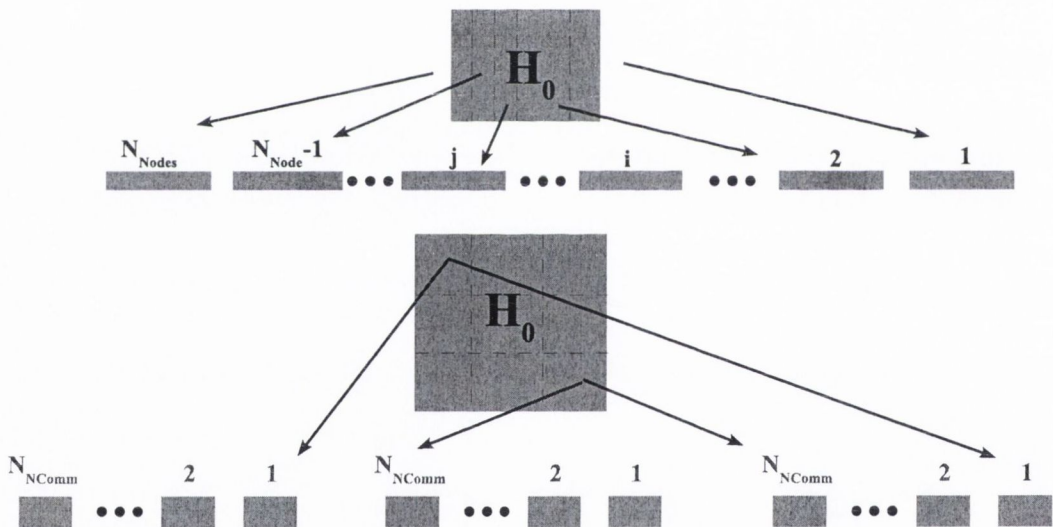


Figure A.1: Schematic representation of redistribution of the Hamiltonian into groups of communicators. The Hamiltonian is initially distributed over N_{Nodes} processors. It is then regrouped and redistributed N_{NComm} times over groups of CPUs comprising N_{NComm} processors each.

Facilities where a few thousand processors can be accessed at a time are becoming increasingly available to the scientific community. Numerical tools that can be used in such systems, however, remain relatively few, specially within the materials science community. Importantly, no electronic transport code as far as we know, has been

²Blue Gene architectures deserve special attention. In favour of low power consumption and scalability the memory available per CPU is approximately 500 Mb, *i.e.*, rather small. Therefore one must ensure that memory usage is small as possible while ensuring scalability.

designed to run in such facilities and no way of accurately treating the transport properties of large systems (in excess of 10,000 atoms) is yet available.

Charge transport in macromolecules for example present exciting potential for future applications in molecular electronic devices. Furthermore, with the present computing hardware we can start to calculate electronic transport properties of quantum dots and the new generation of transistors from first principles. The numerical tools for such tasks, however, as mentioned earlier are still lacking.

A new approach is needed to deal with these two issues: 1) scalability up to thousands of CPUs and 2) memory storage of large matrices. One possible way to deal with this problem is to have a mixed scheme. In other words use the POE scheme already implemented in *Smeagol* together with the POO approach (discussed in section (2.4.1)). In the latter case the orbitals are distributed over the processors without the need to store the entire matrices in one single processor. This can ensure better memory usage.

The way to do this is by using sets of communicators [141]. A communicator is nothing more than a subset of CPUs within a parallel task. Let N_{Nodes} be the number of CPUs available. Initially SIESTA distributes the Hamiltonian (the overlap matrix and the density matrix) over all processors. We then set N_{Comm} groups of CPUs, each group comprising

$$N_{\text{NComm}} = \frac{N_{\text{Nodes}}}{N_{\text{Comm}}} \quad (\text{A.1})$$

compute nodes.³ The total Hamiltonian is then redistributed using the POO scheme over N_{NComm} .

Figure (A.1) shows a schematic representation of this procedure. To increase performance even further we split each group into a two-dimensional grid [142],

$$N_{\text{NComm}} = N_x \times N_y \quad (\text{A.2})$$

instead of the one-dimensional strips used by SIESTA. This ensures better scalability for parallel inversion algorithms specially if

$$N_x \sim N_y. \quad (\text{A.3})$$

This approach ensures better memory management overall. On average, we can increase memory availability (and system size) by approximately a factor N_{NComm} .

³We must ensure that N_{Nodes} is a multiple of N_{Comm} .

⁴The one dimensional grid is a special case with $N_y = 1$. As the number of processors increases $N_x \gg N_y$ and scalability becomes poor.

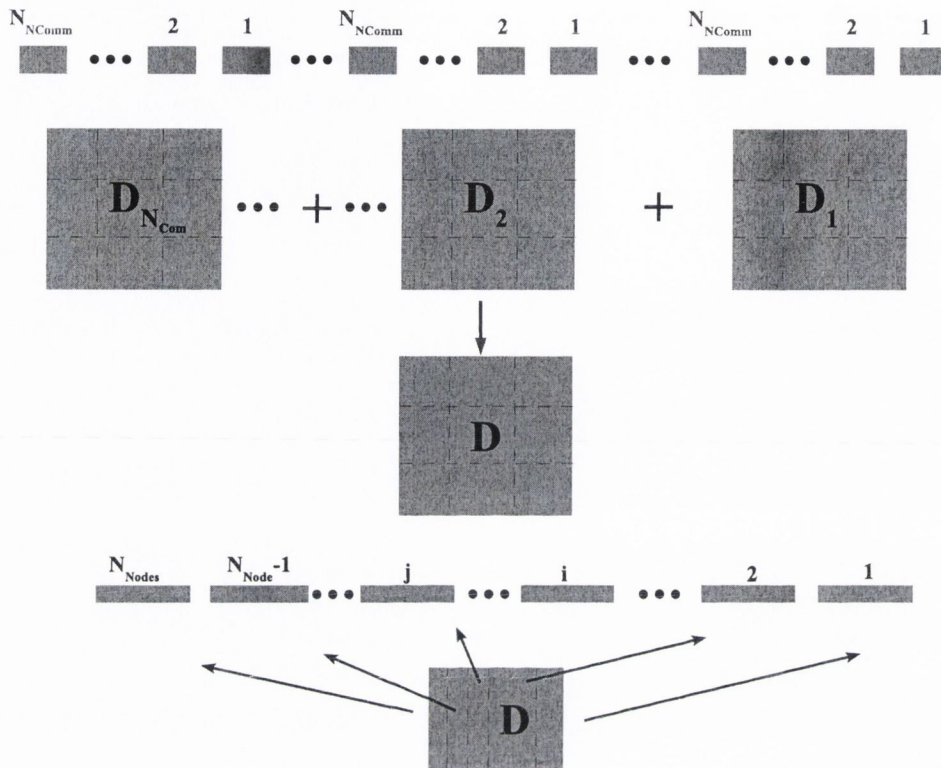


Figure A.2: Schematic representation of the calculation of the density matrix. Each group of communicators calculates the inversion of the Green function in parallel for a different set of energies. The partial density matrices are then summed and collected to form the final density matrix which is subsequently redistributed over the initial N_{Nodes} processors.

Once this is done we can consider each set of communicators as a separate entity. Each group performs the inversion of equation (1.33) for a set of energies. Note that within each group the inversion is performed in parallel instead of in series as the standard POE method. But if we take the subset collectively the operations performed resemble the POE method. For that reason we call our new approach the mixed parallel over energy method (MPOE).

Because we work with groups of communicators each inversion is performed within N_{NComm} processors. Usually $N_{NComm} \leq 32$ processors which ensures good scalability of the inversion subroutine if we have good interconnects. Moreover, we can use the power of the POE method to scale up to 128 processors/communicators.

Therefore using the MPOE approach we can not perform calculations over

$$N_{Nodes} = N_{Comm} \times N_{NComm} \sim 128 \times 32 = 4,096 \text{ CPUs,} \quad (\text{A.4})$$

while increasing memory availability by a factor of

$$N_{\text{NComm}} \sim 32. \tag{A.5}$$

This means that while previously we could do calculations with 1,000 atoms, the MPOE method allows us to break the 10,000 atom barrier. Furthermore, with more efficient inversion algorithms one can increase N_{NComm} even more and consequently so can the system size.

The MPOE method has been implemented in *Smeagol* and tests have been performed on a 1024-processor BlueGene solution located at HPCC Edinburgh. While it is hard to compare these results with other benchmarks for *Smeagol* (see section (2.4.1)) given the peculiarities of the BlueGene architecture, the results look promising.

Appendix B

Publications stemming from this work

- Molecular-Spintronics: the art of driving spin through molecules, Stefano Sanvito and Alexandre Reily Rocha, submitted to *J. Comp. Theo. Nano.* Also [cond-mat/0605239](#).
- Spin and Molecular Electronics in Atomically-Generated Orbital Landscapes, Alexandre Reily Rocha, Victor Garcia-Suarez, Steve W. Bailey, Colin J. Lambert, Jaime Ferrer and Stefano Sanvito, *Phys. Rev. B.* **73**, 085414 (2006), Also [cond-mat/0510083](#).
- Towards Molecular Spintronics, Alexandre Reily Rocha, Victor Garcia-Suarez, Steve W. Bailey, Colin J. Lambert, Jaime Ferrer and Stefano Sanvito, *Nature Materials* **4**, 335 (2005).
- Conductance oscillations in zigzag platinum chains - suppression of parity effects, Victor Garcia-Suarez, Alexandre Reily Rocha, Steve W. Bailey, Colin J. Lambert, Stefano Sanvito and Jaime Ferrer, *Phys. Rev. Lett.* **95**, 256804 (2005), Also [cond-mat/0505487](#).
- Single channel conductance of H₂ molecules attached to platinum or palladium electrodes Victor Garcia-Suarez, Alexandre Reily Rocha, Steve W. Bailey, Colin J. Lambert, Stefano Sanvito and Jaime Ferrer, *Phys. Rev. B.* **72**, 045437 (2005). Also [cond-mat/0412726](#).
- Asymmetric I-V characteristics and magnetoresistance in magnetic point contacts, Alexandre Reily Rocha and Stefano Sanvito, *Phys. Rev. B* **70**, 094406 (2004). Also [cond-mat/0403351](#).

- Computational Spintronics in highly confined systems, Stefano Sanvito and Alexandre R. Rocha, CMSM 2004.

Appendix C

The Smeagol Manual

USER'S GUIDE

SMEAGOL (version 1.0)

June 29, 2005

Alexandre Reily Rocha and Stefano Sanvito

Department of Physics, Trinity College Dublin, IRELAND

Víctor Manuel García Suárez and Jaime Ferrer Rodríguez

Departamento de Física, Universidad de Oviedo, SPAIN

Steve Bailey and Colin J. Lambert

Department of Physics, Lancaster University, Lancaster, LA14YB, UK

smeagol@tcd.ie

<http://www.smeagol.tcd.ie>

Contents

1	INTRODUCTION	2
2	THE SYSTEM SET UP	2
3	THE LEADS CALCULATION	3
3.1	Input files	3
3.2	Input flags	3
3.3	Output files	4
4	<i>I-V</i> CALCULATION	5
4.1	Input files	5
4.2	Input flags	6
4.2.1	Matching of the Hartree Potential	10
4.2.2	Flags specific of k -point calculations	11
4.2.3	Flags specific of Γ point calculations	12
4.3	Output files	12
5	HOW TO RUN SMEAGOL	13
6	PROBLEM HANDLING	14
7	ACKNOWLEDGEMENTS	14

1 INTRODUCTION

This is a comprehensive user's guide to the quantum electronic transport code SMEAGOL (Spin and Molecular Electronics Algorithm on a Generalized atomic Orbital Landscape) [1, 2]. SMEAGOL is based on the non-equilibrium Green's function (NEGF) formalism for one-particle Hamiltonian. In its present form it uses density functional theory (DFT) with the numerical implementation contained in the code SIESTA [3, 4]. However, SMEAGOL's computational scheme is very general and can be implemented together with any electronic structure methods based on localized basis sets. Alternative implementations are currently under investigation.

In the next sections we will explain how to set up a typical calculation and we will describe the various options. The reader of this user guide is supposed to have familiarity with the non-equilibrium Green's function formalism [5, 6, 7, 8, 9, 10, 11, 12] and with density functional theory [13]. In addition a good knowledge of SIESTA and the SIESTA's input files is necessary since only the SMEAGOL's commands are described here, although a complete input file needs the setting of flags proper of SIESTA. For these we refer to the SIESTA user's guide [4].

2 THE SYSTEM SET UP

SMEAGOL is designed for calculating two probe I - V characteristics. The typical system investigated is described in figure 1. It comprises two semi-infinite leads (left and right) and an extended molecule, which includes the region of interest and a few atomic layers of the leads. The electronic structure of the leads is not affected by the potential drop and it is computed only once at the beginning of the calculation.

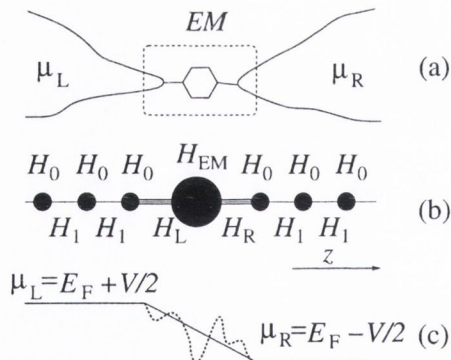


Figure 1: (a) Schematic two terminal device. Two leads are kept at the chemical potentials μ_L and μ_R and the transport is through the extended molecule EM . (b) The Hamiltonian is an infinite matrix comprising two block diagonal parts describing the leads and a part (finite) describing the extended molecule H_{EM} . (c) Typical potential profile.

There are two fundamental steps in setting up a SMEAGOL's calculation: 1) calculating the electronic structure for the leads, and 2) calculating the I - V curve for a given system. The evalu-

ation of the electronic structure of the leads is essential and must be performed before attempting the calculation of the I - V . The files: `SystemLabel.HSL`, `SystemLabel.DM`, `bulk1ft.DAT` and `bulkrgt.DAT` are generated during the evaluation of the electronic structure of the leads. These are necessary for calculating the I - V characteristic.

3 THE LEADS CALCULATION

Here SMEAGOL evaluates the Hamiltonian \mathcal{H} , the overlap \mathcal{S} and the density ρ matrices of the current/voltage probes (the leads). The self-energies for the semi-infinite electrodes can be obtained from the knowledge of the Hamiltonian and the overlap matrices of an infinite system, and therefore only a DFT calculation for a bulk system is needed. \mathcal{H} and \mathcal{S} should be written in the tridiagonal form described by Sanvito *et al.* [1, 14]. Figure (2) shows the typical setup for the electrodes.

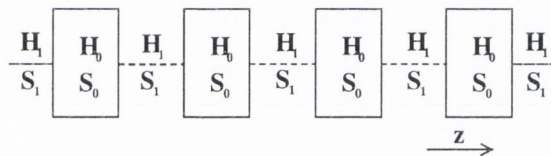


Figure 2: Periodic structure of the leads. H_0 and S_0 are the Hamiltonian and overlap matrix describing the interaction within one unit cell and H_1 and S_1 are the coupling and overlap matrix describing the interaction between adjacent unit cells. The arrow shows the direction of transport (z direction)

The same procedure is used for calculating the matrix elements of the Hamiltonian and overlap matrix in the case of k -points calculation (along the direction orthogonal to transport).

3.1 Input files

There are no additional input files than those used by SIESTA for an ordinary DFT calculation (input file, pseudopotentials ...). For these we refer to the SIESTA user's guide.

3.2 Input flags

The following input flags must be supplied to the `input.fdf` file in order to perform the bulk calculation.

BulkTransport (*Boolean*):

When this flag is set to true the leads Hamiltonian and overlap matrix will be written to the file `SystemLabel.HSL`. Moreover the files `bulk1ft.DAT` or `bulkrgt.DAT` (or both) will be created. These contain information about the system (Fermi energy, System label, unit cell, non-zero elements of the Hamiltonian and information about the super cell).

Default value: F

BulkLeads (*String*):

Define whether the calculated electronic structure should be used for the left-hand side lead, for the right-hand side lead or for both. In practise it defines the names and the extensions of the output files. There are three possible options

- LR or RL (the same output files will be used for both left- and right-hand side lead)
- R (the output files will be used for the right-hand side lead only)
- L (the output files will be used for the left-hand side lead only)

Default value: LR

3.3 Output files

bulkft.DAT :

File containing information about the left-hand side lead (number of states, Fermi energy, number of k -points, etc)

bulkrgt.DAT :

File containing information about the right-hand side lead (number of states, Fermi energy, number of k points, etc)

Systemlabel.HSL :

File containing the Hamiltonian and overlap matrices of the leads. The string **Systemlabel** is read from either **bulkft.DAT** or **bulkrgt.DAT**. If the two leads are the same one can use the same **Systemlabel.HSL** file to read the information for both the left and right leads (set the flag **BulkLeads** to LR). If the two systems are different, then two files with different names must be provided from two different leads calculations (set the flag **BulkLeads** to either L or R).

Systemlabel.DM :

File containing the density matrix of the leads. It is needed for calculating the I - V . The string **Systemlabel** is read from either **bulkft.DAT** or **bulkrgt.DAT**. If the two leads are made from the same materials and have the same geometrical arrangement one can use the same **Systemlabel.DM** file to read the information about both the left- and right-hand side lead (set the flag **BulkLeads** to LR). If the two leads are different, then two files with different names must be provided from two independent leads calculations (set the flag **BulkLeads** to either L or R). The **Systemlabel.DM** file is used to set the boundary condition at the interface between the scattering region and the electrodes.

4 I-V CALCULATION

Once the initial calculation for the leads has been performed we can proceed with computing the non-equilibrium transport properties of our system.

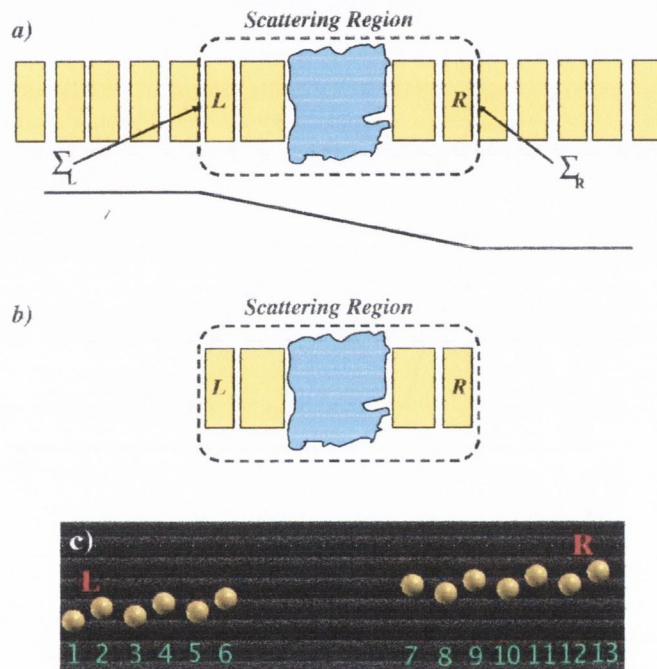


Figure 3: a) Sketch of a typical system simulated using SMEAGOL: two semi-infinite electrodes connected to a central scattering region. b) The typical unit cell for a SMEAGOL calculation. The reader must note that we include at least one layer of the leads both to the left- and to the right-hand side of the scattering region. The order of the atoms in the input file is only important in these two layers. The first atoms of the list (see `AtomicCoordinatesAndAtomicSpecies` in the SIESTA user's guide) must be those contained in the left-hand side lead unit cell, and they should be input with the same order than in the bulk leads calculation. In an analogous way, the last atoms of the list must conform with the input file for the right-hand side lead. c) An example of a system setup for two semi-infinite zig-zag wires separated by a vacuum region. The numbers for each atom have been indicated as well as the two atoms on either side corresponding to the the unit cells for the left- and right-hand side lead.

4.1 Input files

Several files generated during the construction of the leads must be used. These are: `bulkleft.DAT`, `bulkrigt.DAT`, `Systemlabel.HSL` and `Systemlabel.DM`.

4.2 Input flags

The following input flags must be supplied to the file `input.fdf` in order to perform the transport (I - V) calculation. If any of these values is not supplied, the default value will be assumed. Special care should be taken for the variables that control the real and contour integrals, when calculating the non-equilibrium density matrix.

EMTransport (Boolean):

When `EMTransport` is set to `T`, SMEAGOL will perform a NEGF calculation (transport). Otherwise, the code will perform a standard SIESTA equilibrium ground state calculation for either a periodic system or a molecule.

Default value: `F`

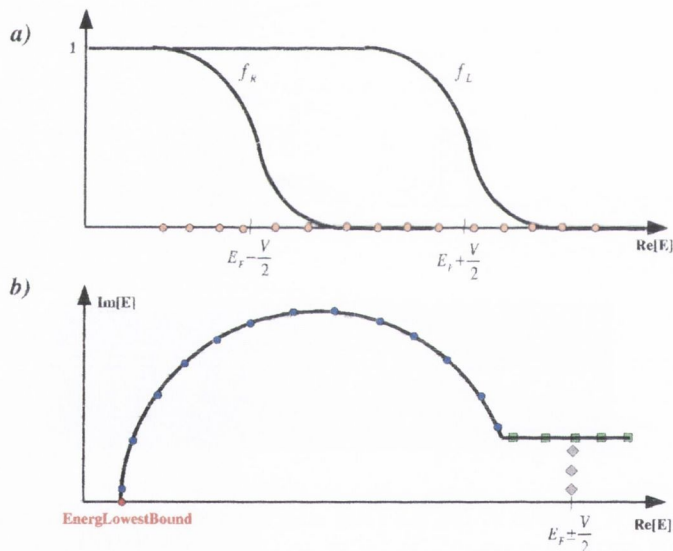


Figure 4: Sketches for the Green Function integration leading to the non-equilibrium charge density [1, 2]. a) The non-equilibrium part must be performed along the real energy axis, but is bound by the left- and right-hand side Fermi distributions functions, f_L and f_R . b) The equilibrium component is performed over a semicircular path in the complex energy plane. Here we show the starting position `EnergLowestBound`, the energy mesh along the two segments of the curve and the poles of the Fermi distribution.

NEnergyReal (Integer):

Number of energy points along the real axis for the integration of the non-equilibrium part of the Green's function. The number of points is extremely sensitive to the type of calculation performed. The points are distributed between $-(\frac{V}{2} + 30.0 k_B T)$ and $(\frac{V}{2} +$

$30.0 k_B T$). The number of points determines how fine the mesh is. Since the Green's function on the real axis can be ill-behaving (large number of singularities), a very fine mesh might be necessary. For equilibrium calculations, `NEnergReal` can be set to zero. In Fig. (4a) the real axis energy points are sketched as orange circles and `NEnergReal`= 15.

Default value: 0

NEnergImCircle (*Integer*):

Number of energy points along the semi-circle in the complex plane (equilibrium part of the Green's function integral). The circle starts at the energy `EnergLowesBound` and finishes at the complex point energy point $(E_F - 30.0 k_B T, 2 N_{\text{Poles}} \pi k_B T)$. The values for the energy points are calculated using a Gauss-Legendre algorithm along a semicircle. Fig. (4b) shows a sketch of the points along the contour in the complex energy plane. In this example, the points along the circle are represented by blue circles and `NEnergImCircle`= 13.

Default value: 15

NEnergImLine (*Integer*):

Number of energy points along the line in the complex plane where the integral of the equilibrium contribution to the density matrix is performed. This straight line starts at the point $(E - 30.0 k_B T, 2 N_{\text{Poles}} \pi k_B T)$ and finishes at point $(E_F + 30.0 k_B T, 2 N_{\text{Poles}} \pi k_B T)$ (green squares in Fig. (4b), `NEnergImLine`= 5). The position of the energy points is determined by a Gauss-Legendre algorithm.

Default value: 20

NPoles (*Integer*):

Number of poles in the Fermi distribution used to compute the contribution to the equilibrium charge density. The Fermi distribution is given by:

$$f(\epsilon) = \frac{1}{e^{\frac{\epsilon - \mu}{k_B T}} + 1} \quad (1)$$

The poles of $f(\epsilon)$ all lay on the complex plane with $i_n = \mu + (2 * n + 1) i \pi$ being the n -th pole. The number of poles specifies how far from the real axis the contour integral will be performed. The furthest away from the real axis the more well-behaving the Green's function is.

In Fig. (4b) the position of the poles are represented by grey diamonds (`NPoles`= 3).

Default value: 5

VInitial (*Physical*):

Value of the initial bias for the I - V calculation.

Default value: 0.0 eV

VFinal (*Physical*):

Value of the final bias for the I - V calculation.

Default value: 0.0 eV

NIVPoints (*Integer*):

Number of bias steps considered between the two limits V_{initial} and V_{final} . The current will be calculated only for these biases.

Default value: 0

Delta (*Double precision*):

Small imaginary part δ that accounts for the broadening of the localized energy levels of Green Function, $G = [\epsilon + i\delta - H_S - \Sigma_L - \Sigma_R]^{-1}$.

Default value: 10^{-4}

EnergLowestBound (*Physical*):

Energy that specifies the beginning of the contour integral in the complex plane for the equilibrium contribution to the charge density. **EnergLowestBound** must be below both the lowest band of the leads and the lowest energy level of the scattering region. Red dot in Fig. (4b).

Default value: -5.0 Ry

NSlices (*Integer*):

Number of slices of the bulk Hamiltonian substituted into the left- and right-hand side part of scattering region. The Hamiltonian of these slices is not recalculated self-consistently and these “buffer” layers help the convergence, in particular when the two leads are different.

Default value: 1

AtomLeftVCte (*Integer*):

Number of the atom used to determine the onset of the bias ramp on the left-hand side. The number of the atom is taken from the order in which the atoms are specified in the SIESTA block **AtomicCoordinatesAndAtomicSpecies** (refer to the SIESTA manual for a description of this block).

Default value: 1

AtomRightVCte (*Integer*):

Number of the atom that is used to determine the onset of the bias ramp on the right-hand side. The number of the atom is taken from the order in which the atoms are specified in the SIESTA block **AtomicCoordinatesAndAtomicSpecies** (refer to the SIESTA manual for a description of this block).

For $z < z_{\text{AtomLeftVCte}}$ and $z > z_{\text{AtomRightVCte}}$, the potential added to the Hartree potential is a constant equal to $+\frac{V}{2}$ and $-\frac{V}{2}$ respectively. For $z_{\text{AtomLeftVCte}} < z < z_{\text{AtomRightVCte}}$

a bias ramp $V(z - z_0)$ is introduced, where z_0 is the midpoint between $z_{\text{AtomLeftVCte}}$ and $z_{\text{AtomRightVCte}}$.

Default value: Last Atom

TrCoefficients (*Boolean*):

If set to true the transmission coefficients as a function of energy $T(\epsilon, V)$ will be calculated and printed to the file `SystemLabel.TRC` (see section 4.3 below) for any bias point. Although the current is defined as

$$\frac{e}{h} \int_{-\infty}^{\infty} T(\epsilon, V) (f_L - f_R) d\epsilon \quad (2)$$

we can calculate the Transmission coefficients for a wider range of energy values and a different number of energy points by using the variables `InitTransmRange`, `FinalTransmRange` and `NTransmPoints` which are defined below.

Default value: F

InitTransmRange (*Physical*):

Initial energy for the calculation of the transmission coefficients

Default value: -5.0 Ry

FinalTransmRange (*Physical*):

Final energy for the calculation of the transmission coefficients

Default value: 5.0 Ry

NTransmPoints (*Integer*):

Number of energy points uniformly distributed between `InitTransmRange` and `FinalTransmRange` for which the transmission coefficients are calculated. If `TrCoefficients` is set to false, this flag is ignored.

Default value: 100

PeriodicTransp (*Boolean*):

If the two electrodes are equal one may use periodic boundary conditions over the supercell. This procedure improves convergence and decreases the size of the unit cell. If the two leads are different then `PeriodicTransp` must be set to F.

Default value: T

SaveBiasSteps (*data block*):

Block containing information for printing the Hartree potential (`Systemlabel.VH`), the charge density (`Systemlabel.RHO`), the difference between the self-consistent and the atomic charge densities (`Systemlabel.DRHO`) and the total DFT potential

(`SystemLabel.VT`) at a specified bias step. The arguments in the block are integers indicating the bias steps at which to print these files. They range from 0 up to `NIVpoints`. The appropriate SIESTA flag for printing any of these files must also be set to true.

Example :

```
% block SaveBiasSteps
0 2 3
% endblock SaveBiasSteps
```

SMEAGOL will print the requested file (for instance `SystemLabel.VT` if the SIESTA flag `SaveElectrostaticPotential` is set to true) at the bias steps 0, 2 and 3.

Default value: No Default

4.2.1 Matching of the Hartree Potential

One important information needed from the leads calculation is the average value of the Hartree Potential. SMEAGOL uses a Fast Fourier Transform (FFT) algorithm to solve the Poisson equation in reciprocal space (refer to the SIESTA manual for more details). The $\vec{k} = 0$ term is ignored resulting in a Hartree Potential that is defined up to a constant. This might lead to a mismatch between the Hartree potential of the leads and that at the edges of the scattering region. This mismatch is better illustrated in Fig. 5 where we have plotted the average Hartree potential on the plane orthogonal to transport for the electrodes and two semi-infinite wires separated by 12 Å (our scattering region; see Fig. (3c)) using the post-processing tool `Pot.exe` (included in the `Utils` directory).

In order to compensate for the arbitrary zero of the potential we shift the Hartree Potential of the scattering region by a constant (see variables `HartreeLeadsLeft`, `HartreeLeadsRight` and `HartreeLeadsBottom` described below). In this way we force the match of the potential at the scattering region/leads interface.

HartreeLeadsLeft (*Physical*):

Position in space in the left-hand side lead where the Hartree potential of the scattering region should match that of the bulk.

Default value: 0.0 Ang

HartreeLeadsRight (*Physical*):

Position in space of the right-hand side lead where the Hartree potential in the scattering region should match that of the bulk.

Default value: 0.0 Ang

HartreeLeadsBottom (*Physical*):

Average value of the Hartree potential in the leads over a plane perpendicular to the transport direction. This parameter should be evaluated from the bulk leads calculation.

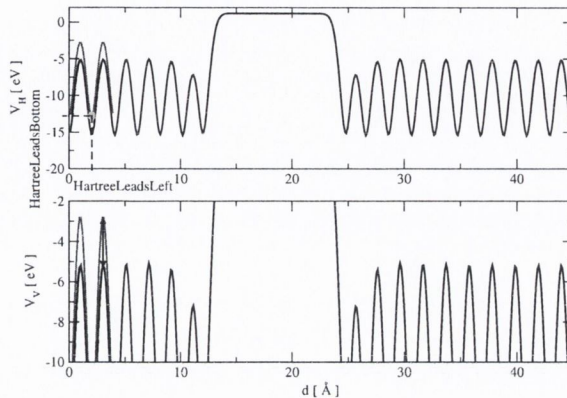


Figure 5: Shift of the Hartree potential between two SIESTA calculations: bulk gold (the leads) with two atoms in the unit cell (red line) and the parallel plate capacitor (scattering region) depicted in Fig. (3c). Note that the Hartree potential of the scattering region has converged to the bulk value after the first atomic layer except for a constant.

The fast Fourier Transform algorithm used in SMEAGOL to solve the Poisson's equation disposes the $k = 0$ term. This defines the Hartree potential up to an arbitrary constant. By defining `HartreeLeadsBottom` we shift the Hartree potential in the scattering region in order to match that of the leads.

Default value: 0.0 eV (no shift)

4.2.2 Flags specific of k -point calculations

These flags are used only when periodic boundary conditions in the direction orthogonal to the transport are considered.

`SaveMemTranspK` (*Boolean*):

By default, SMEAGOL calculates the self-energies during the first iteration and stores them in memory. There are two self-energies (one for the left- and one for right-hand side contact) for each energy point and each k -point. If the number of k -points and the size of the unit cell of the leads are large, large memory might be needed. In that case, `SaveMemTranspK` should be set to T, and the self-energies will be re-calculated after each iteration without the need for storing them in memory. Use with caution; this specification might increase considerably the time of the calculation.

Default value: F

`TransmissionOverk` (*Boolean*):

Allow to print the transmission coefficient as a function of both the k -vector in the transverse Brillouin zone and the energy. Note that the flag `TrCoefficients` provide only the

integral of the transmission coefficients over the k -points. `TrCoefficients` must be set to true. The file `SystemLabel.TRC.k.up` (down) contains the results (see section 4.3 below).

Default value: F

4.2.3 Flags specific of Γ point calculations

`UseLeadsGF` (*Boolean*):

If true the file `SystemLabel.LGF` is read from disk (see description of output files below). It is particularly useful when one wants to perform numerous calculations with the same set of leads and the same number of real energy points.

Default value: T

4.3 Output files

`SystemLabel.CUR` :

Four column vector containing the I - V characteristics. The first column corresponds to the bias in Rydberg, the second column corresponds to the total current and the third and fourth columns (in the case of a spin-dependent calculation) correspond to the spin-decomposed current.

`SystemLabel.TRC` :

Transmission coefficients as a function of energy for different biases. The first column corresponds to the energy, the second to the total transmission for both the spin direction and the following `nspin` columns are the spin-decomposed transmission coefficients.

`SystemLabel.TRC.k.up` (down) :

If `TransmissionOverk` is set to T, `SystemLabel.TRC.k.up` contains the transmission coefficients for each k point and energy for either up or down spins. The first two columns contain the perpendicular components of each k point, the third column contains the spin dependent transmission coefficient and the fourth column contains the energy.

`SystemLabel.LGF` :

For a Γ point serial calculation, this file contains the `NEnergReal` self-energies for both the right and left hand-side leads for all the energies lying on the real axis. This file might be useful when restarting a calculation. The user should note that, in this case, both `VInitial`, `VFinal` and `NEnergReal` must be the same as in a previous calculation.

`SystemLabel.CHR` :

File containing the total charge inside the scattering region after each iteration. The first column contains the iteration number, the second column contains the charge in units of e (the electron charge), the third column contains the bias in Rydberg and the fourth column contains the temperature also in Rydberg.

IV.SystemLabel.VH :

If `SaveElectrostaticPotential` is set to true (see SIESTA user's guide) and the block `SaveBiasSteps` is present, the file `IV.SystemLabel.VH` containing the Hartree potential for the biases specified in `SaveBiasSteps` will be generated.

IV.SystemLabel.VT :

If `WriteVT` is set to true (see SIESTA user's guide) and the block `SaveBiasSteps` is present, the file `IV.SystemLabel.VT` containing the total DFT potential for the biases specified in `SaveBiasSteps` will be generated.

IV.SystemLabel.RHO :

If `WriteRHO` is set to true (see SIESTA user's guide) and the block `SaveBiasSteps` is present, the file `IV.SystemLabel.RHO` containing the self-consistent charge density for the biases specified in `SaveBiasSteps` will be generated.

IV.SystemLabel.DRHO :

If `WriteDRHO` is set to true (see SIESTA user's guide) and the block `SaveBiasSteps` is present, the file `IV.SystemLabel.DRHO` containing the difference between the self-consistent and the atomic charge densities for the biases specified in `SaveBiasSteps` will be generated.

IV.SystemLabel.DMT :

If `SaveDMT` is set to true and the block `SaveBiasSteps` is present, the file `IV.SystemLabel.DM` containing the converged density matrix at each bias specified in `SaveBiasSteps` will be written.

5 HOW TO RUN SMEAGOL

Assuming that the user has already compiled SMEAGOL successfully and saved it as an executable (say `smeagol.1.0`), then we are ready to start a calculation. Initially the user must setup the input file for the left- and right-hand side leads. The input file must include the appropriate SIESTA and SMEAGOL flags as discussed in section (3.2) and in the SIESTA Manual. Let us assume, as a simple example, that the two leads are equivalent and the leads file is called `leads.fdf`. In the same directory where this file is, there must also be the pseudopotential files - either in `.psf` or `.vps` format. Then the user should type:

```
$ smeagol.1.0 < leads.fdf > leads.out
```


The calculation will yield the files `bulkleft.DAT`, `bulkright.DAT`, `Systemlabel.HSL` and `Systemlabel.DM`. These should be moved to the directory containing the input file for the scattering region - say `scattering.fdf`. This directory must also contain pseudopotential files for all the atomic species involved in the calculation. It is important to note that the user must be consistent with regards to pseudopotentials, they should be identical to the ones used for the leads calculation.

Before starting the I - V calculation we must obtain `HartreeLeadsBottom`. For that we use the post-processing tool `Pot.exe` contained in the `Utils` directory of the SMEAGOL distribution. The file `Potential.dat` should be edited in order to process the file `SystemLabel.VH` (for the leads). The resulting output `SystemLabel.VH.DAT` can be viewed using a plotting tool such as `gnuplot` or `xmgrace`.

We are interested in the first two columns of this data file. They contain the planar average of the Hartree potential as a function of the z direction. A value for the Hartree Potential (`HartreeLeadsBottom`) should be chosen (usually the edges of the unit cell) and the position in the unit cell should be recorded and matched with the equivalent position in the scattering region (`HartreeLeadsLeft` and `HartreeLeadsRight`). Once this is done, we are ready to calculate the I - V characteristics:

```
$ smeagol.1.0 < scattering.fdf > scattering.out
```

The resulting files can be processed using a variety of plotting programs such as `gnuplot` and `xmgrace` for 2D-plots and `OpenDX` for 3D-plots and isosurfaces.

6 PROBLEM HANDLING

The users are encouraged to report problems and bugs to the SMEAGOL's developers at `smeagol@tcd.ie`. Patches and fixes will be uploaded to the web-site <http://www.smeagol.tcd.ie/>

7 ACKNOWLEDGEMENTS

This work is sponsored by Science Foundation of Ireland under the grant SFI02/IN1/I175. JFR and VMGS thank the spanish Ministerio de Educación y Ciencia for financial support (grants BFM2003-03156 and AP2000-4454). SB and CJL thank the UK EPSRC and the EU network MRTN-CT-2003-504574 RTNNANO. ARR thanks Enterprise Ireland (grant EI-SC/2002/10) for financial support. Traveling has been sponsored by the Royal Irish Academy under the International Exchanges Grant scheme.

References

- [1] A. R. Rocha, V. M. García-Suárez, S. W. Bailey, C. J. Lambert, J. Ferrer and S. Sanvito, *Nature Materials* **4**, 335 (2005).
- [2] A. R. Rocha, V. M. García-Suárez, S. W. Bailey, C. J. Lambert, J. Ferrer and S. Sanvito, in preparation.
- [3] J. M. Soler, E. Artacho, J. D. Gale, A. Garcia, J. Junquera, P. Ordejón and D. Sanchez-Portal, *J. Phys. Cond. Matter* **14**, 2745-2779 (2002).
- [4] <http://www.uam.es/departamentos/ciencias/fismateriac/siesta/>
- [5] S. Datta, *Electronic Transport in Mesoscopic Systems*, Cambridge University Press, Cambridge, UK, 1995.
- [6] H. Haug and A. P. Jauho, *Quantum Kinetics in Transport and Optics of Semiconductors*, Springer, Berlin, 1996.
- [7] C. Caroli, R. Combescot, P. Nozieres, and D. Saint-James, *J. Phys. C: Solid State Phys.* **5**, 21 (1972).
- [8] J. Ferrer, A. Martín-Rodero, and F. Flores, *Phys. Rev. B* **38**, 10113 (1988).
- [9] J. Taylor, H. Guo, and J. Wang, *Phys. Rev. B* **63**, 245407 (2001).
- [10] M. Bradbyge, J. Taylor, K. Stokbro, J.-L. Mozos, and P. Ordejón, *Phys. Rev. B* **65**, 165401 (2002).
- [11] J. J. Palacios, A. J. Pérez-Jiménez, E. Louis, E. SanFabián, and J. A. Vergés, *Phys. Rev. B* **66**, 035322 (2002).
- [12] A. Pecchia and A. Di Carlo, *Rep. Prog. Phys.* **67**, 1497 (2004).
- [13] H. Hohenberg and W. Kohn, *Phys. Rev.* **136**, B864 (1964). W. Kohn and L.J. Sham, *Phys. Rev.* **140**, A1133 (1965).
- [14] S. Sanvito, C. J. Lambert, J. H. Jefferson, and A. M. Bratkovsky, *Phys. Rev. B*, **59**, 11936 (1999).